Abnormal Combustion in Spark Ignition Engines

Johannes Gerhard Mutzke

Magdalen College

A thesis submitted in partial fulfilment of the requirements

for the degree of Doctor of Philosophy

Department of Engineering Science

University of Oxford

Hilary Term 2018

Abnormal Combustion in Spark Ignition Engines

Johannes Gerhard Mutzke DPhil

Magdalen College, University of Oxford Department of Engineering Science

A thesis submitted in partial fulfilment of the requirements for the degree of Doctor of Philosophy, Hilary Term 2018

Abstract

Emissions from internal combustion engines are a major contributor to anthropogenic climate change. In order to decrease the amount of emissions, car manufacturers are investing in increasing the efficiency of spark ignition engines. Means for this include downsizing and turbocharging which come with an exacerbated risk of abnormal and harmful combustion phenomena, notably auto-ignition, knock and pre-ignition and thus pose a limit to the efficiency of the engines.

Abnormal combustion depends on the engine geometry, the operating conditions and the fuel. Industrial standard classification systems are outlined to be insufficient, misleading or non-existent for modern engines and fuels. This thesis aims to improve the understanding of the abnormal combustion phenomena through an experimental project which can be utilised for improved classification systems.

The vast majority of the experiments were conducted on a variable compression ratio engine which was fitted with modern control, measurement and data acquisition equipment to resemble an industrially-used test engine.

In a first study, methods of finding the ideal engine operating point were investigated. Knock was induced in the engine, and knock indicators and limitations of knock are discussed here. Enhanced humidity was passed into the heated air-inlet stream by means of a custom-built humidifying unit. Results showed that both the power output of the engine and the severity of knock were reduced with increased humidity. This was explained by the exclusion of combustible air. A fuel-vaporization unit allowed for experiments with fully vaporized fuel. It could be shown that this had an adverse effect on knock as the cooling effect of the enthalpy of vaporization was removed.

A second study employed a temperature-controlled glow plug to induce surface pre-ignition. A range of analysis techniques were tested and discussed which ranged from flame ionization detection to several in-cylinder pressure based methods. A cycle-by-cycle analysis with a maximum pressure method revealed an unexpected trend of surface pre-ignition tendency in sweeps of stoichiometry and fuels, with slightly weak of stoichiometric mixtures being the most susceptible to pre-ignition. Enhanced humidity had a negligible effect on surface pre-ignition under real world conditions.

A third study concerned itself with the analysis of knock-induced heat flux, which is both a major cause for damage to the engine and trigger for surface pre-ignition. A heat flux probe was fitted to the engine and results linking heat flux to knock could be obtained on cycle-by-cycle basis and cycle-averaged basis. A linear trend between heat flux and knock intensity was found.

Acknowledgements

My first and greatest thanks go to my supervisor Professor Richard Stone whose professional guidance, advice and support have been unparalleled. With his unlimited knowledge and expert training, he helped me on every step of the way that led to this thesis. I will be forever grateful to him.

I would further like to thank Dr. John Williams from BP not only for providing funding for this project but for the many in depth discussions and valuable suggestions that shaped this thesis.

I would like to thank Professor Martin Davy for assessing my project several times over the course of the last three years and the many good discussions and follow-on work that have resulted from this.

I am grateful for the very productive cooperation with the 4yp students Todd Slaughter, Robert Fordham and Blane Scott as well as the wider Oxford Internal Combustion Engine Group. Here, I am particularly appreciative to Dr. Joe Camm, Dr. Kun Liang and Dr. Felix Leach whose software training has proven invaluable for the success of this work.

I would further like to take the opportunity to thank several academics whose support and confidence in me led me to where I am today. These include Professors Wolfgang Arlt, Lars Zigan, Juergen Karl, Johann Jaeger and Stefan Will from the University of Erlangen-Nuremberg, Professor John Prausnitz from the University of California Berkeley, Professor C.K. Law from Princeton University as well as Professors Robin Cleveland and Ben Williams from the University of Oxford. I am indebted to all of them.

Special thanks further go to the UK Research Council and the late Mrs. Jane Ledig-Rowohlt, nee Scatcherd, for initiating the scholarship under her maiden name that provided for me during my time in Oxford.

Lastly, I want to extend my gratitude to my parents. None of this would have been possible without their loving support. They have given me both values and vision and have succeeded in, as Johann Wolfgang von Goethe held it on the duties of parents: ‘to give their children two things: roots and wings’.

Table of Contents

Table of Contents

Table of Contents

Notation

1. Acronyms

Acronym	Description
aTDC	After TDC
AFR	Air Fuel Ratio
AI	Analogue Input
AO	Analogue Output
bTDC	Before TDC
CCD	Charge-Coupled Device
COBRA	Combustion Burn Rate Analysis
CI	Compression Ignition
CR	Compression Ratio
CFR	Cooperative Fuels Research
DAQ	Data Acquisition
EGR	Exhaust Gas Recirculation
EVC	Exhaust Valve Closing
EVO	Exhaust Valve Opening
FIR	Finite Impulse Response
GUI	Graphical User Interface
HDAQ	High Speed DAQ card
IIR	Infinite Impulse Response
IVC	Inlet Valve Closure

Notation

IVO	Inlet Valve Opening
IMPO	Integral of the Modulus of Pressure Oscillations
IC	Internal Combustion
IEA	International Energy Agency
KLSA	Knock Limited Spark Advance
KLT	Knock Limited Torque
LKI	Logarithmic Knock Index
LDAQ	Low Speed DAQ Card
MAPO	Maximum Amplitude of Pressure Oscillation
MBT	Minimum Ignition Advance for Best Torque
MON	Motor Octane Number
NTC	Negative Temperature Coefficient
NOx	Nitrogen Oxides
OI	Octane Index
PI	Pre-Ignition
PIA	Pre-Ignition Analysis
PR	Pre-Ignition Resistance
PRF	Primary Reference Fuel
PV	Process Variable
PFI	Programmable Function Interface
PFO	Programmable Function Output
PID	Proportional Integral Derivative

PWM	Pulse Width Modulation
RON	Research Octane Number
RPM	Rounds per Minute
SP	Set Point
SI	Spark Ignition
TPRF	Toluene Primary Reference Fuels
TRF	Toluene Reference Fuels
TDC	Top Dead Center
TTL	Transistor Transistor Logic
UHC	Unburned Hydrocarbons
VI	Visual Interface

2. Parameters

Symbol	Description	Unit
ω	Absolute Humidity	[ ]
g	Acceleration due to Gravity	[m/s^2]
E	Activation Energy	[J/mol]
R_{AF}	Air Fuel Ratio	[ ]
λ	Air/Fuel Equivalence Ratio	[ ]
$\dot{q}_{\text{Ang}}$	Angle of Peak Heat Flux	[°ca bTDC]
ω	Angular Velocity	[rad/s]
A	Area	[m^2]

Notation

A	Arrhenius constant	[s]
a	August Roche Magnus Coefficient	[K]
b	August Roche Magnus Coefficient	[K]
$\tilde{p}$	Bandpass Filtered Pressure Signal	[bar]
$BMEP$	Brake Mean Effective Pressure	[bar]
$\overline{P_b}$	Break Mean Effective Pressure	[bar]
τ, *'CR'*	Compression Ratio	[ ]
Θ	Crank Angle	[°ca bTDC]
ρ	Density	[kg/m^3]
W	Duration of Knock Interval	[°ca]
μ	Dynamic Viscosity	[kg/m s]
k	E6 factor	[m]
E	Energy	[J]
Ω	Engine speed	[RPM]
h_{fg}	Enthalpy of Vaporization	[kJ/mol]
e	Error	[ ]
V_{evap}	Evaporative Cooling	[kJ/kg$_{air}$]
R_f	Flame Radius	[m]
$FMEP$	Friction Mean Effective Pressure	[bar]
ϕ	Fuel/Air Equivalence Ratio	[ ]
m	Fuel-dependent Exponent (1)	[ ]
n	Fuel-dependent Exponent (2)	[ ]

Notation

K	Gain	[ ]
R	Gas constant	[J/mol K]
$IMEPg$	Gross Indicated Mean Effective Pressure	[bar]
Q	Heat	[J]
c_p	Heat Capacity (isobaric)	[J/kg K]
c_v	Heat Capacity (isochoric)	[J/kg K]
$\dot{q}$	Heat flux	[W/m^2]
Q_{hr}	Heat release Through Combustion	[J]
Q_{ht}	Heat Transfer on the Cylinder Chamber Walls	[J]
τ_i	Ignition Delay	[s, °ca]
$IMEP$	Indicated Mean Effective Pressure	[ ]
$\dot{q}_{Int}$	Integral of Heat Flux	[W/m^2]
$IMPO$	Integral of the Modulus of Pressure Oscillations	[MPa]
U	Internal Energy	[J]
$KLSA$	Knock Limited Spark Advance	[°ca]
KLT	Knock Limited Torque	[Nm]
S_L	Laminar Burning Velocity	[m/s]
δ	Laminar Flame Thickness	[m]
L	Latent Heat of Vaporization	[J/mol]
l	Length	[m]
α	Length Compression and Expansion Stroke	[°ca]
Le	Lewis Number	[ ]

Notation

C	LKI Constant	[ ]
LKI	Logarithmic Knock Intensity	[ ]
m	Mass	[kg]
mfb	Mass Fraction Burned	[ ]
$MAPO$	Maximum Amplitude of Pressure Oscillation	[MPa]
ξ	Mean	[ ]
MBT	Minimum Ignition Advance for Best Torque	[°ca]
M	Molar Mass	[g/mol]
MON	Motor Octane Number	[ ]
V^-	Negative Voltage Output	[V]
$Q_{n\Theta}$	Net Heat Release per Degree Crank Angel	[J/°ca]
$IMEPn$	Net Indicated Mean Effective Pressure	[bar]
OI	Octane Index	[ ]
K	Octane Index Constant	[ ]
$\dot{q}_{Max}$	Peak Heat Flux	[W/m^2]
ω	Pitzer's Acentric Factor	[ ]
k	Polytropic Index	[ ]
V^+	Positive Voltage Output	[V]
D	Prandtl Number	[ ]
r_{PI}	Pre-ignition Ratio	[ ]
p	Pressure	[bar]
n	Pressure Exponent	[ ]

Notation

p_c	Pressure Rise through Combustion	[bar]
p_v	Pressure Rise through Compression	[bar]
γ	Ratio Of Heat Capacities	[ ]
ϕ	Relative Humidity	[ ]
RON	Research Octane Number	[ ]
S	Sensitivity	[ ]
x	Share of Evaporated Fuel	[ ]
ω	Specific Humidity	[kg / kg]
σ	Standard Deviation	[ ]
s	Stroke	[m]
PR	Surface Pre-Ignition Resistance Number	[ ]
T	Temperature	[K], [°C]
α	Temperature Coefficient	$[K^{-1}]$
D	Thermal Diffusivity	$[m^2/s]$
x_{PI}	Threshold Factor Pre-Ignition	[ ]
t_{pi}	Threshold of Pre-Ignition	[bar]
t	Time	[s]
T	Torque	[Nm]
p_{sat}	Vapour Pressure	[bar]
V	Volume	$[m^3]$
W	Work	[N]
β	Zeldovich Number	[ ]

R_f	Zeldovich' critical flame radius	[m]

3. Superscript

Superscript	Description
K	Gain
LKI	Logarithmic Knock Index
u	PID components

4. Subscript

Subscript	Description
a	Air
ang	Angle
c	Coolant
c	Critical
d	Derivative
d	Dewpoint
evap	Evaporation
f	Fuel
gp	Glow plug
ht	Heat Transfer
i,ign	Ignition (Timing)
I	Increment

Notation

i, int	Integral
L	Liquid
x	Location
max	Maximum
m, mix	Mixture
N	Net
pi	Pre-ignition
p	Proportional
ref	Reference
sat	Saturation
s	Steam
s	Swept
v	Vapour

1. Introduction and Literature Review

1.1. Trends in the Powertrains of Transportation Vehicles

The global consequences of the anthropogenic climate change are threatening the livelihoods of a large part of the world's population. Droughts, floods, severe weather and consequent crop failure can lead to hunger crisis, forced migration and conflict. The transport sector is a major contributor to the rising greenhouse gas emissions that are responsible for global warming. Governments around the world are therefore increasing the regulations on emissions of internal combustion powered passenger road vehicles. While alternative means of propulsion have successfully been deployed today, they still fall short of matching the many advantages of the internal combustion engine. The International Energy Agency (IEA) predicts that by 2050, 58% of cars will still be powered with gasoline or diesel engines, while 85% of these will have a hybrid propulsion system [1]. A quick, wide market penetration of electric cars is unlikely as manufacturers struggle with high prices for batteries [2]. A quick upscaling of a charging infrastructure is difficult in developed countries and much more so in the developing world [3-6]. Further, in many countries, notably in China, the greenhouse gas balance for the operation of electrical cars is far worse than for cars with internal combustion engines due to the carbon intense electricity generation. Internal combustion engines remain the powertrain of choice for the majority of vehicles and car manufacturers are therefore heavily invested in improving the efficiency and thus reducing the emissions of these propulsion systems [1, 2, 7, 8].

Internal combustion engines can be categorized in two classes: Spark Ignition (SI) engines and Compression Ignition (CI) engines. Spark ignition engines represent 60% of the fleet of the world's more than one billion vehicles. While CI engines are more efficient than SI engines due to higher pressures and temperatures, the latter can apply three-way catalysts

which clean the exhaust gas of hazardous components such as NOx (nitrogen oxides), CO (carbon monoxide) and UHC (unburned hydrocarbons). In order to control these emissions, the SI engine is always run stoichiometric ($\lambda = 1$) while the nature of the CI engine is a weak of stoichiometric, non-premixed operation ($\lambda >\sim 1.3$).

In SI engines the fuel and air are premixed in nearly all engine types. The energy is then released in a flame that is originating from ignition at the spark plug and is first laminar and then turbulent in nature. This change comes about because the flame front becomes wrinkled by the turbulence in the combustion chamber and after some 5 to 10 % of the fuel has burned (*5-10%mfb*, see Section 1.4), fully turbulent combustion has developed.

Car engines have to be able to operate over a large range of loads and speeds. While most passenger vehicles operate at low loads most of their lifetime, they still have to be fit to provide high load and speeds occasionally. The size of the engine is therefore traditionally determined by these peak load and speeds rather than the usual low load operation. In order for an engine to provide a non-maximum power output, the fuel burned and, given the fixed stoichiometric fuel/air ratio, the amount of intake air has to be reduced. The latter is realized by throttling the engine which reduces the efficiency of the engine dramatically. To address this inefficiency, car manufacturers are downsizing their engines to levels more appropriate to everyday use. When additional peak power is required, this can then be achieved by supercharging or turbocharging which forces extra air into the combustion chamber. This allows the downsized engine to be run with reduced throttle losses in normal operation while still providing the same maximum power output as requested by the driver in peak demand situations [9-11]. An example of performance maps for a regular and a downsized turbocharged engine can be seen in Figure 1.1.

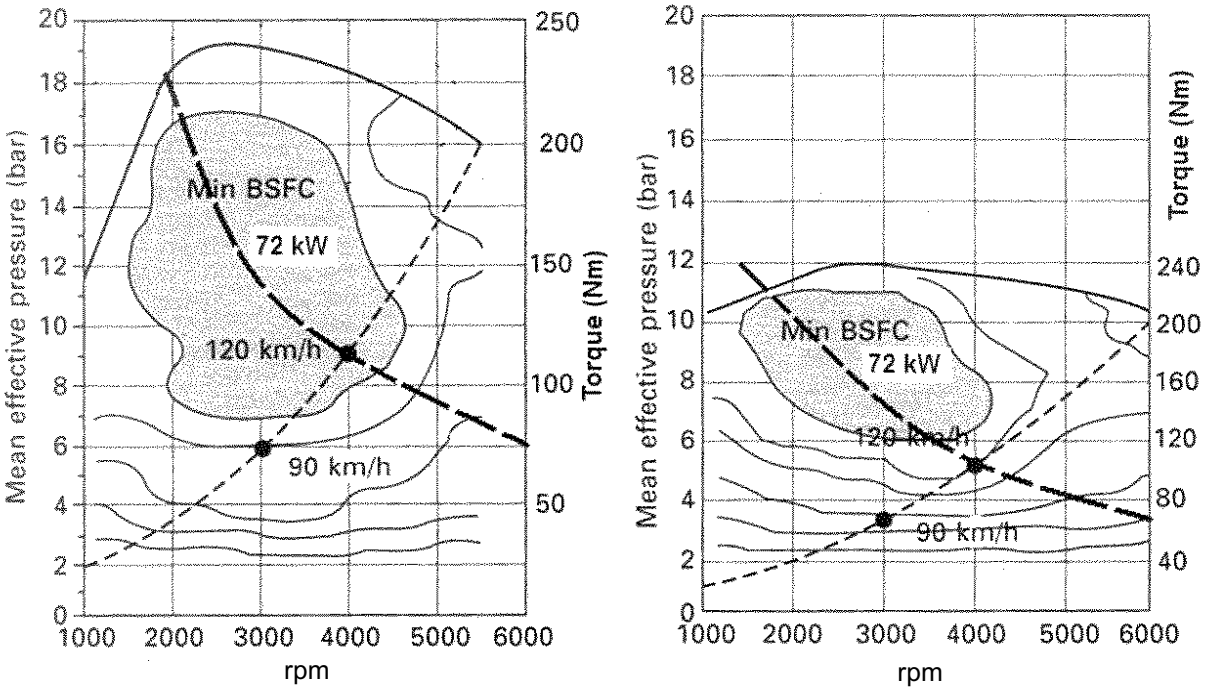

Figure 1.1. Performance maps for two 130 kW engines. Left: Naturally aspirated (2.5 L) engine. Right: Downsized, boosted (1.6 L) engine with the same maximum power. Adapted from Zhao [12].

The engine on the right hand side in Figure 1.1 is a 1.6 L boosted engine that has the same maximum power output as the naturally aspirated engine to its left with 2.5 L. As can be seen for the downsized engine, the road load operating points are in a more efficient region and the maximum torque is achieved at a lower speed. The overall efficiency and drivability of the downsized engine is greater. It can also be lighter and therefore the efficiency of the vehicle is further increased.

The downsized engine in Fig 1.1 requires a boost pressure ratio of about 2:1. The intake air is also cooled after compression to increase the charge density. The ideal gas equation (Eq. 1.1) states that at constant pressure p, a decrease in temperature T leads to an increased density ρ.

$$\rho = \frac{p}{R\,T} \tag{1.1}$$

The cooling has the additional benefit that the chance of auto-ignition and subsequent knock is reduced for a given compression ratio and fuel. These abnormal combustion phenomena are a major hurdle for the further improvement of modern car engines [9, 11]. This will be explained in more detail in the following section.

1.2. Auto-Ignition and Knock

1.2.1. Physical Background

Downsizing and turbocharging of spark ignition engines is being applied throughout the automotive industry. This comes with increased maximum pressures and temperatures and this exacerbates the vulnerability of the engines to auto-ignition and subsequent knock. These abnormal combustion phenomena can lead to destruction of engine components by means of pressure and thermal strain on the combustion chamber surface. Because of auto-ignition and knock, the optimal combustion phasing which would lead to the best thermal efficiency might not be reached and therefore knock limits the possible efficiency that can be obtained [9, 13]. This will be explained further in Section 1.5.

Auto-ignition and knock lead to an increased heat flux on the cylinder wall. The thermal strains from the temperature gradient caused by the heat flux can lead to damage, and the hot surfaces can cause surface pre-ignition. Surface pre-ignition has a similar effect to an over-advanced spark timing and cause heavy knock in subsequent cycles. This which will be discussed more in Section 1.3 and Chapters 4 and 5.

With the trend of increased boosting of engines, knock has become a focus of research in the past years. In the last decade, more papers have been published on knock than in all the years before [14]. The research is relevant beyond the work on efficiency as it also involves engine durability, power density, engine noise and composition of emissions.

Auto-ignition must be understood before knock can be addressed. During normal combustion, the flame front moves uniformly away from the spark plug across the combustion chamber. As the pressure rises the temperature of the burned and unburned gas rises. Due to turbulence and mixture irregularities, the end gas (unburned air/fuel mixture) is never completely homogeneous. In an auto-igniting cycle, the flame is developing non-uniformly as the air/fuel mixture ignites autonomously and is locally separated from the conventional spark-plug-ignited flame front [10, 15].

The expanding flame originating from the spark plug causes a pressure rise in the end gas region. The unburned mixture is compressed isentropically in the adiabatic core and its temperature increases swiftly. Here, chain reactions in the end gas further boost the temperature. Initiation reactions generate radicals from stable species first. Chain-branching reactions further increase the amount of radicals in the end gas. Termination reactions eventually decrease the number of radicals. These three types of reactions are thousands of separate discernible reactions with countless reaction products. The OH radical, which results from a decomposition reaction from H_2O_2 at temperatures between 900 and 1000 K is a key entity for auto-ignition [13, 16-18].

In Figure 1.2, an auto-igniting combustion cycle is shown in an optical engine. The six pictures are taken with a time difference of 0.5 ms each. The bright yellow areas show the very hot autoigniton ahead of the white flame front [15].

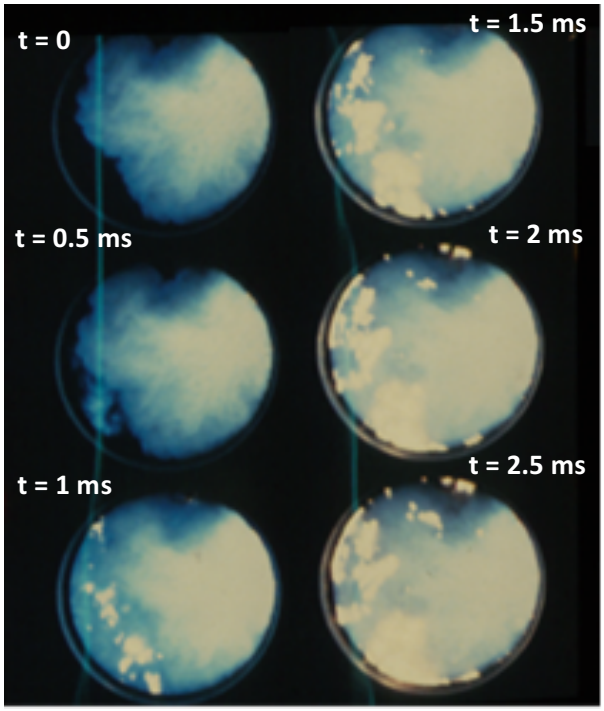

Figure 1.2. Auto-ignition; 0.5 ms intervals. Adapted from [15].

Auto-ignition is associated with a rapid increase in temperature and pressure in the combustion chamber. Pressure waves propagate through the engine block causing structural vibrations with frequencies of 5-10 kHz and causing the engine to resonate and to produce a characteristic 'pinging' noise, known as knock. Auto-ignition only leads to knock when the associated heat release is sufficiently high to cause pressure fluctuations [13, 18]. Both auto-ignition and knock are eclectic, stochastic processes and depend on the anti-knock quality of the fuel, the engine geometry, the mixture composition, the temperature and pressure history of the end gas and the engine operating point. The subsequent sections will elaborate on these parameters [9, 10].

A pressure record of a knocking and non-knocking cycle is plotted in Figure 1.3 where a non-knocking cycle with a modest compression ratio of $\tau = 8$ is compared to a knocking cycle with a compression ratio of $\tau = 9$.

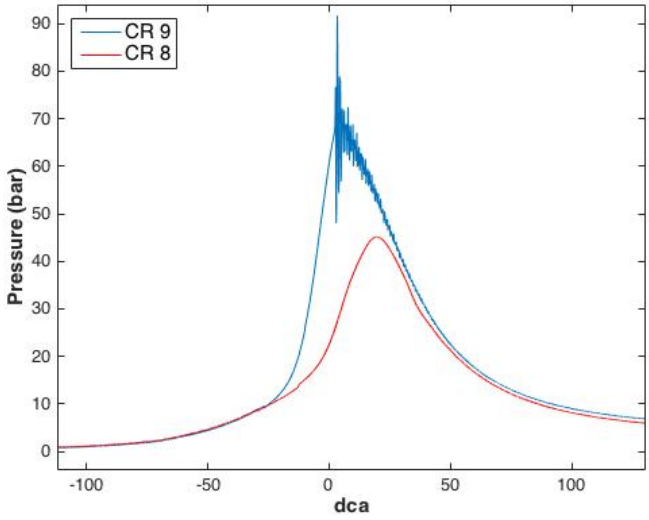

Figure 1.3. In-cylinder pressure trace. Knocking (blue, '*CR*' = τ = 9) and non-knocking (red, τ = 8) cycles. Fuel: iso-octane, Θ_i = 30°ca bTDC, λ = 1.0, T_c = 80°C, T_a = 30°C, Ω = 600 RPM

Knock occurs at the maximum of the pressure oscillation and at the peak heat release. In Figure 1.4, the heat flux is plotted for the same knocking and non-knocking cycles as in Figure 1.3.

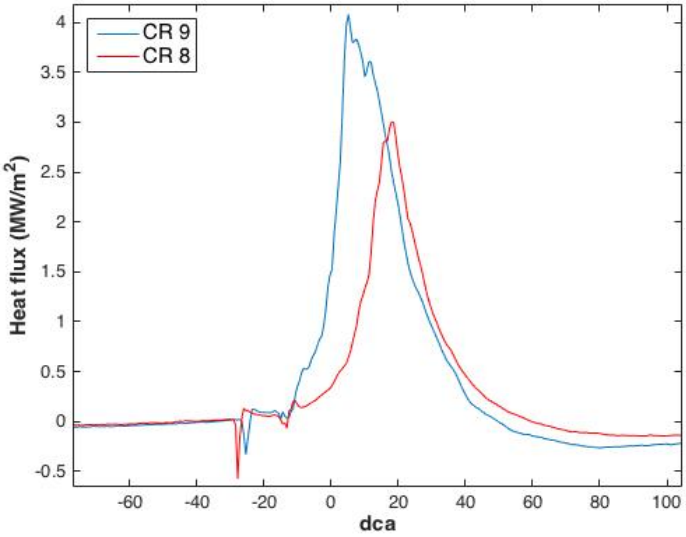

Figure 1.4. In-cylinder surface heat flux. Knocking (blue, τ = 9) and non-knocking (red, τ = 8) cycles for the same cycles as depicted in Figure 1.3. Fuel: iso-octane, Θ_i = 30°ca bTDC, λ = 1.0, τ = 8-9, T_c = 80°C, T_a = 30°C, Ω = 600 RPM

Knock leads to disturbance of thermal boundary layers. The potential damage to the engine is manifold. Erosion of the piston crown and cylinder head are possible as is the breakage of piston rings or melting of the piston as seen in Figure 1.5.

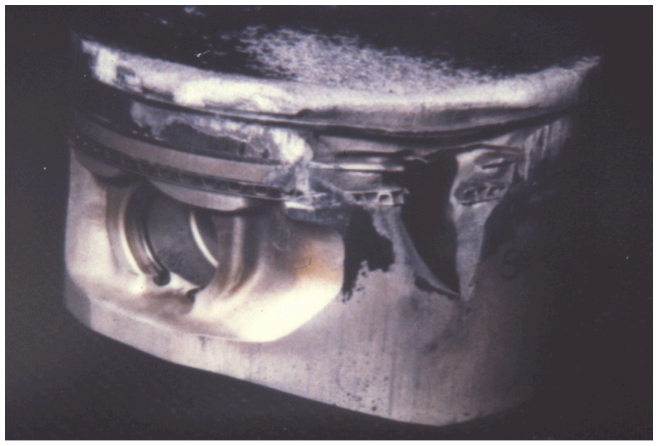

Figure 1.5. Knock-induced damage to a piston crown [19].

To decrease the probability of knock, several methods are viable. These include, where possible, the operation at higher engine speeds as this gives auto-ignition less time to occur. A retarded ignition timing decreases the chance of knock. A leaner air-fuel ratio leads to a decreased combustion pressure and lower temperature in the end-gas and therefore significantly decreases the chance of knock. However, there is little scope for change of the air fuel ratio as the engine has to run at near stoichiometric conditions for both efficiency and exhaust gas composition reasons as outlined before. The turbulence in the cylinder can be increased and the area the flame front has to travel can be made smaller to reduce knock [9, 11]. Operating the engine with fuels of a high anti-knock quality is an additional way to decrease knock and the effect of fuels on auto-ignition and knock will be discussed in detail in the next section.

1.2.2. Fuel Considerations for Auto-Ignition and Knock

In Figure 1.6, it can be seen that fuels have different ignition temperatures in respect to pressure.

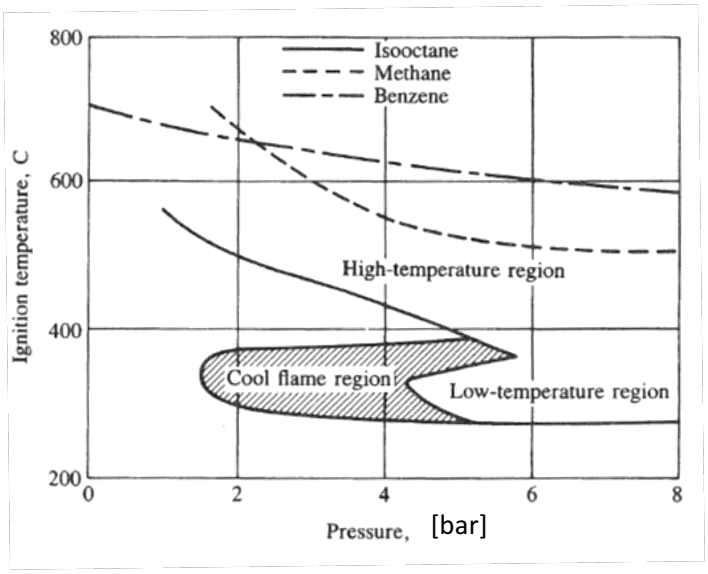

Figure 1.6. Auto-ignition graph for iso-octane, methane and benzene, λ = 1.0, adapted from Heywood [10].

At constant mixture strength, the ignition temperatures for methane and benzene decline with an increasing pressure. Auto-ignition therefore becomes more likely at higher pressures.

A cool-flame phenomenon has to be considered: Straight chain paraffins can ignite in a two stage process. In a low temperature region, a cool flame is established before a normal flame appears. The cool flame is associated with formaldehyde fluorescence which depends on the presence of peroxides of sufficient concentration. Peroxides do not play a role in the ignition in higher temperature zones. This cool flame phenomenon is less common among branched-chain paraffins and olefins [10, 20].

The structures of fuels vary for the different kinds of fuels [10, 21, 22]. For paraffins it was found that longer chained molecules increased the tendency of the fuel to knock and shortening the basic chain by incorporating side chains made knock less likely. Further,

adding methyl groups (CH_3) to carbon chains in the second from the end or centre position decreased the knocking tendency.

Napthenes (cyclo-alkanes) of the same carbon number as aromatics were found to knock more than the aromatics. For both types of fuels, double bonds reduced the knocking tendency as did decreasing the length of the side chain on a ring structure. With some exceptions (C_2H_4, C_2H_2, C_3H_6), the knocking tendency of olefins was decreased when two or more double bonds were added [10, 21, 22].

It is because of the complexity of the auto-ignition behaviour of the fuels that a fundamental quantification is impossible. For the automotive industry, the anti-knock quality of fuels is therefore determined with the Research and Motor Octane Number tests (RON and MON) [23]. The octane numbers rely on an empirical scale derived on the Cooperative Fuel Research (CFR) engine with specific parameters using blends of the two primary reference Fuels (PRFs) – n-heptane (*RON* = *MON* = 0) and 2, 2, 4-trimethylpentane (= iso-octane, *RON* = *MON* = 100). These fuels were selected because iso-octane has a high knock resistance, n-heptane shows very strong knocking behaviour and at the time both were easily producible in high purity. Some crucial test conditions for the octane tests are outlined in Table 1.1.

Table 1.1. MON/RON conditions according to D2770 and D2699 ASTM [23].

	RON	**MON**
Engine speed	600 RPM	900 RPM
Charge temperature	52°C	149°C
Spark advance	13°ca bTDC	14-26°ca bTDC
Humidity air	3.56-7.12 [g_{water}/kg_{air}]	3.56-7.12 [g_{water}/kg_{air}]

The fuel that is to be ranked in the octane scale is run in the CFR engine and its knocking behaviour is compared to that of blends of PRF fuels at identical conditions. The octane number of the fuel is then derived as the volumetric percentage of iso-octane in the PRF blend that matches the behaviour of the fuel.

The Octane Index (OI) is an additional measure that takes into account both *RON* and *MON*, as well as engine design and operating conditions [10, 13]:

$$\mathrm{OI} = (1 - K)'RON' + K * 'MON' = 'RON' - K * S \tag{1.2}$$

With K as an empirically derived constant depending on the engine design and operating conditions and with Sensitivity S:

$$S = 'RON' - 'MON' \tag{1.3}$$

$K = 1$ for the MON test and $K = 0$ for the RON test. This means that $OI = MON$ and $OI = RON$ in the MON and RON tests respectively. The octane index is thus a measure of how a non-PRF fuel compares to a PRF fuel which always by definition has a sensitivity of $S = 0$. European gasolines would usually have a *RON* in the range of 95-100 and a *MON* of 85-93 and a sensitivity of about $S = 10$. Shock tube measurements (see next section) reveal that the chemical kinetic response of the PRFs differs to that of industrial fuels as these are blends of hundreds of fuel components and include aromatics, olefins, paraffins and oxygenates.

Research and development on the octane scale has been executed from the 1920s to the 1950s [24]. Today, the refining and automotive industries rely on this standard. For manufacture and marketing of transportation fuels in these industries the RON and MON numbers are of highest significance [9, 24].

However, changed operating conditions as well the blending-in of non-paraffinic components into gasoline such as alcohols (notably ethanol and in some countries methanol [25]) question

the applicability of the RON/MON fuel ranking system to match today's demands. In Figure 1.7, the operating conditions for the RON and MON test and for a modern engine are displayed.

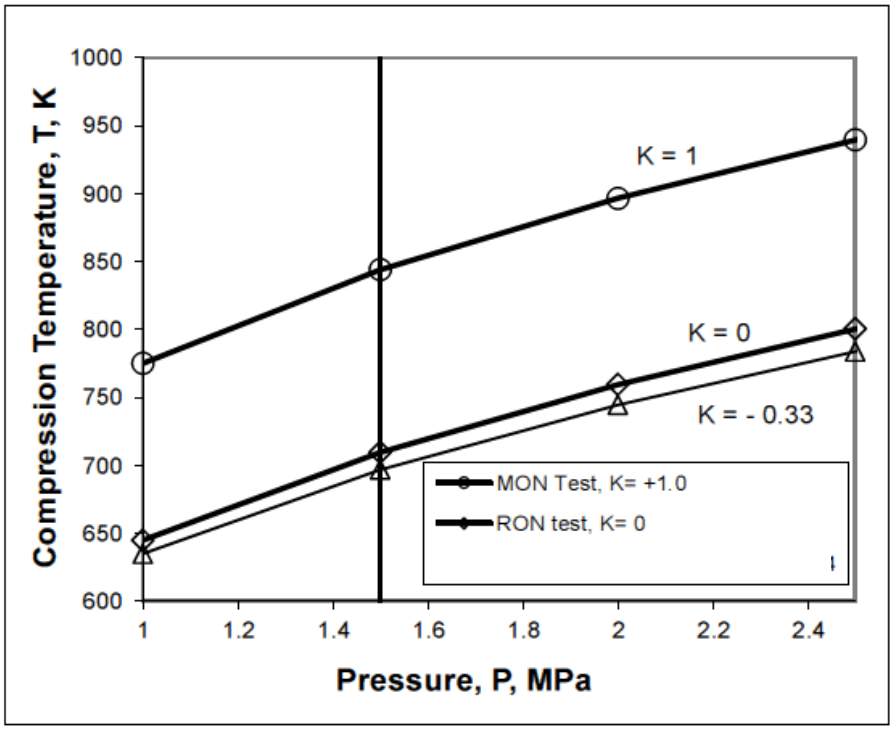

Figure 1.7. Unburned gas temperature vs. pressure in the RON and MON test and for a modern car engine. Adapted from [26].

Figure 1.7 shows the variation of unburned gas temperature with pressure in different operating conditions. It can be seen that the temperature is higher for a given pressure in the MON test compared to the RON test. The shown *T*/*P* trajectories are the conditions to which the end gas of a given fuel is exposed during an engine cycle. It depends on the design and the operating conditions of the engine which is expressed with the variable *K*.

K is 0 for the RON test, and 1 for the MON test. *K* can be higher than 1 if the temperatures for a given pressure is higher than MON and, importantly, it can be below 0 if conditions are 'lower' than at the RON test. This can be seen in Figure 2.7. Kalghatgi [27] established that if

the temperature of the end gas of an engine at p = 15 bar (indicated by vertical line in Figure 1.7) is lower than for the RON test, the test is considered to be 'beyond RON'.

As described in previous sections, to increase the power density and efficiency, development goals for SI engines have for long been increased pressures and reduced temperatures. Downsizing and turbocharging move the engine to negative values of K and thus beyond RON. This means that the MON test has become less and less relevant. Several studies show that negative K values are predominant in most modern downsized turbocharged car engines in conditions in which knock occurs [27-34].

This means that, according to equation 1.2, for a given *RON*, the smaller the *MON*, the higher the Octane Index (*OI*), which is counterproductive. Both the EU and the US have minimum MON-requirements for commercial fuels. With the prevalence of downsized and turbocharged engines, this is leading to a mismatch [27].

Potential solutions to the problem have been discussed. This includes the abrogation of the MON test (Japan) and the replacement of iso-octane with toluene as a PRF as toluene reference fuels (TRF) have sensitivities more comparable to real world gasolines [26]. Morgan et al [35] suggest a tri-component system to match both *RON* and *MON* of a gasoline. The suggested components are iso-octane, n-heptane and toluene. While mixtures of PRFs have the same *RON* and *MON* and thus the same sensitivity S, a third component makes it possible to match the sensitivity. Toluene is an aromatic which are common in commercial gasolines. The tri-component system is referred to as Toluene Primary Reference Fuels (TPRF). Figure 1.8 shows the ternary TPRF plots [36].

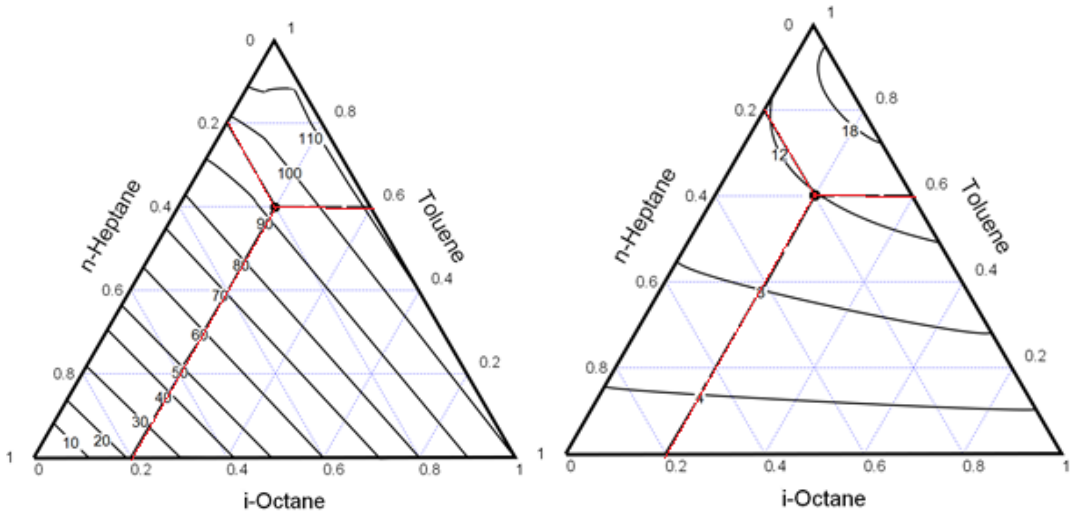

Figure 1.8. Ternary plots. Iso-octane, n-heptane and toluene of RON (left) and sensitivity (right) [36].

In Figure 1.8, a mixture point has been selected of 20% iso-octane, 20% n-heptane and 60% toluene. It can be seen on the left side that this blend has a RON of 92 and from the right side, a sensitivity of 12. The absence of linearity in both diagrams, particularly on the sensitivity side, but also in the very relevant area of higher *RON* values, shows that the conventional two component linear mixing models lead to significant errors.

It can be seen in Figure 1.9, how TPRF blends allow for control of *RON* and *MON*.

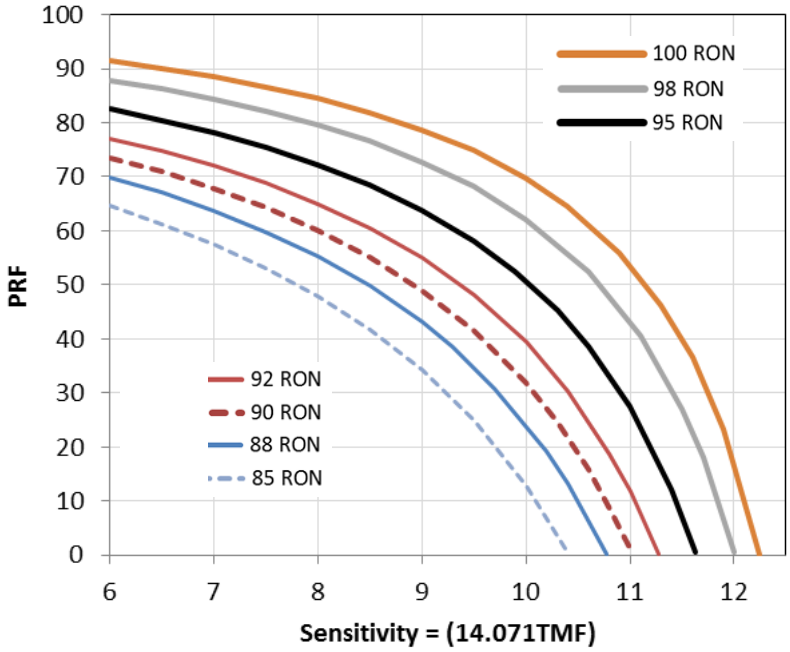

Figure 1.9. Octane number of the PRF required in the TPRF blend against *S* for a range of *RON* numbers in a TPRF blend [37].

Selecting a TPRF of 98 *RON* at a sensitivity of 10 (and thus a *MON* of 88) it can be seen in Figure 1.9 that this corresponds to a PRF (*RON* = *MON*) of 60. The toluene mass fraction can be calculated from the sensitivity and the volume percent of all three components of the TPRF can be calculated according to [37]. Figure 1.9 further shows that in order to increase the RON and the sensitivity of the TPRF, the toluene content has to be increased [37].

To further improve the understanding of the behaviour of toluene in abnormal combustion, it has been tested extensively in this thesis.

1.2.3. Quantification and Modelling of Knock

In order to quantify knock, experiments with shock tubes are commonly applied in research. In the tubes, the air/fuel mixture is compressed homogeneously and held at nominally constant temperature and pressure. The starting point of auto-ignition is then observed and the time between the end of the compression and the beginning of auto-ignition is recorded as

the ignition delay τ_i. The higher τ_i, the less prone to auto-ignition is the fuel. The ignition delay τ_i is a function of pressure, temperature and lambda.

It was suggested by Livengood and Wu, that auto-ignition occurs when the Livengood-Wu integral I of the reciprocal of τ_i reaches unity with time t [13, 38, 39].

$$I = \int_0^{t_e} \frac{1}{\tau_i(p,T)} dt = 1 \tag{1.4}$$

The time t_e is the time that is just sufficient for autoigniton to occur.

The rest of this section is dedicated to the understanding of the influence of pressure, lambda and temperature on the ignition delay and therefore on auto-ignition and knock.

Equation 1.5 expresses the ignition delay τ_i for an increase in pressure from p_0 (τ_{i0}) to p (at constant temperature T).

$$\frac{\tau_i}{\tau_{i0}} \propto \left(\frac{p}{p_0}\right)^{-n} T \tag{1.5}$$

On a molecular level, the constant temperature means that pressure rises due to an increase in density. The pressure exponent n varies with fuel and lambda. Literature reports of values for n show a discrepancy between PRF fuels (n = 1.64 for n-heptane, n = 1.5 for iso-octane) and non-paraffinic fuels (n < 1.0) [40, 41]. According to Equation 1.5, when pressure is being raised, τ_i grows less fast for PRFs than for non-PRFs. PRFs therefore are comparatively less resistant to auto-ignition, which challenges their relevance for a comprehensive fuel rating system.

A leaner mixture has been reported to lead to a larger ignition delay τ_i [41, 42]. Herzler et al. [42] reported a two-fold increase in ignition delay for a weak mixture compared to a stoichiometric mixture at p = 40 bar, T = 800°C. Additionally, exhaust gas recirculation

(EGR) in modern SI engines has been shown to have a negative effect on auto-ignition as it makes the end gas less combustible [43-45].

An Arrhenius equation can be used to describe the effect of temperature on the ignition delay τ_i [13].

$$\tau_{\mathrm{i}} = f(T) = A \exp\left(-\frac{E}{RT}\right) \tag{1.6}$$

With the activation energy E, the universal gas constant R and the Arrhenius constant A. E and A change for different fuels and lambda and they also depend on the temperature range. For most fuels, the ignition delay decreases with an increased temperature. However, the dependency on the temperature range makes the equation problematic to use outside high and low temperature regimes for some fuels. In the temperature range of 700 – 900 K, τ_{i} is almost independent of temperature for paraffins. Chevalier et. al [46] have demonstrated that τ_{i} actually increased with temperature for the PRF n-heptane in certain pressure regimes, a phenomenon known as negative temperature coefficient (NTC). This can be seen in Figure 1.10 [47].

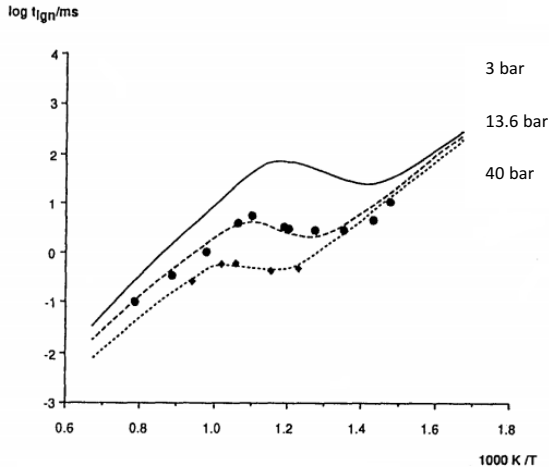

Figure 1.10. Ignition delay vs. reciprocal of temperature for stoichiometric combustion of n-heptane. Adapted from [46].

The temperature range-dependency of the PRF is additional evidence that the reliance on the PRFs for the prevalent octane ranking is problematic.

The Livengood-Wu integral can be used for accurate prediction of auto-ignition and knock if τ_i is well known for a given fuel through experiments, and if temperature and pressure of the unburned end gas can be calculated precisely [39]. But due to limited computational resources this will remain impossible for a wide range of fuels in the foreseeable future.

Chemical models that can be of use in IC engines face enormous challenges due to their complexity. There are thousands of reactions, thousands of educts and products, the complex turbulence, the influence of temperature and pressure, chemical kinetic rate constants, reactions paths, thermodynamic parameters and a vast range of different and very complex fuel compositions (a typical gasoline has more than 100 components) to be considered. This means that vast computational power is necessary even for reduced models with simplified assumptions. Only for pure components, such as paraffins with short chains, do chemical reaction schemes exist. Unfortunately, to accurately model the combustion behaviour of even these simple paraffins, turbulence, mixture composition and flame development have to be considered which makes calculations too strenuous to accurately model their combustion behaviour. Therefore the study of knock remains largely experimental [13, 48, 49].

1.3. Pre-Ignition

Pre-ignition is an abnormal combustion phenomenon that is discernible from auto-ignition. It is the name given to combustion that establishes itself before the spark-plug has fired. Ignition sources are hot spots either on the surface of the combustion chamber or self-igniting fuel/oil droplets. Until the 1950s pre-ignition was considered a major concern in the development of more modern car engines. Only recently, as car engines are downsized and

turbocharged, it has become a problem of increasing concern again. In a pre-igniting cycle, the pressure and temperature of the end-gas rise much higher compared to spark-igniting cycles. It can lead to a phenomenon known as super-knock which can be an order of magnitude more severe than regular knock. It can have most destructive consequences for the engine. The following outlines the major steps that are characteristic for pre-ignition and subsequent superknock in SI engines [13, 50].

Firstly a hot spot in the combustion chamber has to be formed. On the one hand these can be certain surfaces with augmented temperature such as the exhaust valve or combustion deposits on the cylinder wall. This process is referred to as surface pre-ignition. On the other hand oil/fuel droplets can self-ignite due to the very low octane numbers of their blends. Only the former way of pre-ignition, the surface pre-ignition, is considered in this thesis. Pre-ignition and auto-ignition are discernible phenomena and auto-ignition does not occur at timings as early as pre-ignition. The temperatures and pressures are too low at this point in the compression of the charge inside the combustion chamber [51, 52].

In a second step, the hot spot has to form a self-sustaining flame. An inverse relationship between the severity of pre-ignition and laminar burning velocity was reported for a range of fuels in the literature but there is no apparent relation to the octane rating (RON, MON) [53]. The combustion following on from pre-ignition then occurs at higher temperatures and pressures compared to auto-ignition. Super knock can then occur if the pressure wave from the initial pre-ignition couples up with an additional auto-ignition flame front. This has an amplifying effect and depends on the size of the hot spot, the temperature gradient and importantly, the auto-ignition resistance of the fuel (*RON*/*MON*). So, while the octane number has no influence on pre-ignition, the most severe consequence of pre-ignition, super-knock, can be contained with high octane fuels [54, 55]. Surface pre-ignition will be discussed in more detail in Chapter 4.

1.4. Fuel Evaporation Characteristics

The RON and MON tests differ in the way the mixture is prepared. For the RON test, the intake air is heated to 52°C. The charge temperature is then dependent on the fuel composition and the extent of its evaporative cooling characteristics. In the MON test the intake air is heated to 38°C, but the charge is then heated up to 149°C. This means that the state of the charge that enters the engine is independent of the fuel composition in the MON test [23]. This can be seen in Figure 1.11.

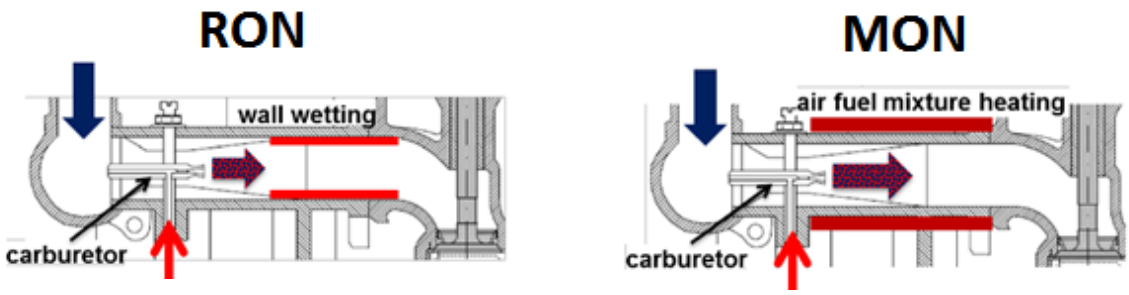

Figure 1.11. Mixture formation with the RON and the MON method in the CFR engine with carburetor, adapted from [56].

Alcohol fuels are highly knock resistant due to their high enthalpy of vaporisation. However, the positive cooling effect through the enthalpy of vaporisation is wiped out by the effect of the heating of the charge in the MON test to 149°C. The heat for the vaporisation of these fuels is coming from the wall of the inlet manifold, instead of the combustion chamber. The better knock resistance is not evident in the MON test.

In modern IC engines however, the charge in the combustion chamber is actually cooled down, further decreasing the chance and severity of auto-ignition and knock. Both the RON and MON tests are therefore obscuring the real-world behaviour with respect to fuels of moderate enthalpy of vaporization. The MON test is particularly unrealistic when it comes to fuels with high enthalpies of vaporization [56].

1.5. Engine Performance Parameters

This section outlines relevant engine performance and burn rate analysis parameters that have been used throughout this thesis. A common parameter to describe engine work is the torque. It can be measured with a load cell (see Chapter 2) that measures the rotational force of the engine's crankshaft. It is defined in Equation 1.7.

$$T = \overline{p_b} V_s \frac{\Omega}{120} \frac{1}{\omega} \tag{1.7}$$

With swept volume V_s and brake mean effective pressure $\overline{p_b}$and angular velocity ω:

$$\omega = 2\pi \frac{\Omega}{60} \tag{1.8}$$

The capacity of an engine to do work is the brake mean effective pressure ($\overline{p_b}$ or *BMEP*) which is independent of the engine size and the speed. It equals the difference between indicated mean effective pressure (*IMEP*) and friction mean effective pressure (*FMEP*). The net indicated mean effective pressure (*IMEPn*) is the *IMEP* over an entire engine cycle. The gross indicated mean effective pressure (*IMEPg*) is the *IMEP* over the compression and expansion stroke (360°ca) [9, 10]. *IMEPn* will be used throughout this thesis as the key parameter of engine performance.

The $IMEP_{\mathrm{n}}$ is calculated as Equation 1.9:

$$IMEP_{\mathrm{n}} = \frac{1}{V} \oint_{\text{cycle}} p\mathrm{d}V \tag{1.9}$$

The $IMEP_{\mathrm{g}}$ is described as Equation 1.10:

$$IMEP_{\mathrm{g}} = \frac{1}{V} \oint_{\alpha} p\mathrm{d}V \tag{1.10}$$

With α as the length in degrees crank angle of the compression and expansion stroke.

The maximum engine power is reached when as much oxygen as possible is burned. However, this likely results in unburned fuel and hence reduced fuel efficiency. For maximum efficiency the aim must be to burn as much of the fuel as possible. For this, additional oxygen should be present. This weakens the mixture. If the mixture becomes too weak, the combustion becomes incomplete and thus a trade-off must be found [10].

Operation at the optimum ignition timing is of high importance. Engines should be operated at the minimum ignition advance for best torque (*MBT*) for maximum power yield and best efficiency. The *MBT* lies ahead of TDC, so the spark is advanced. In a plot of *BMEP* vs. ignition timing (Figure 1.12), the *MBT* is found near the maximum of the curve at 99.9% of $BMEP_{Max}$.

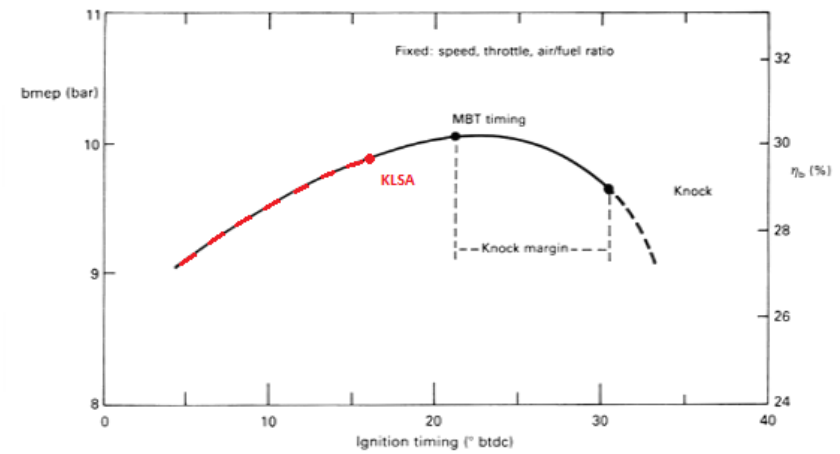

Figure 1.12. The effect of ignition timing on the output and efficiency of the engine and the onset of knock. Adapted from [9].

An advanced ignition timing leads to higher pressures, higher temperatures and increased efficiency. This makes auto-ignition and subsequent knock more probable. A retarded ignition consequently decreases the chance of auto-ignition but reduces the efficiency. In the

conditions where it occurs before MBT timing, knock therefore limits the thermal efficiency of the engine because it does not allow the spark to fire as far advanced as ideally required. An over-advanced ignition timing (θ_{ign} > 25°ca bTDC in the example of Figure 1.12) decreases the efficiency because of the magnified negative work on the piston during the compression stroke [10].

The Knock Limited Spark Advance (*KLSA*) is the operating point where a fuel of lower quality reaches its maximum torque due to limitations by knock. It is an important parameter and it diverges with different fuels of different octane ratings. A fuel of good anti-knock quality can reach a higher *IMEP* compared to a fuel of lower anti-knock quality at the same experimental conditions. The torque at *KLSA* is the knock limited torque (*KLT*). Modern engines equipped with knock sensors can detect knock and take action to reduce knock in consecutive cycles. This can be done by retarding the ignition timing and (if turbo-/supercharged) by reducing the boost pressure. Both measures can reduce the engine efficiency.

An important combustion engine parameter is the mass fraction burned *mfb*. Here the *mfb* is calculated with a burn rate analysis based on the Rassweiler and Withrow method [57]. The method considers that the pressure rise in the combustion chamber after firing during the compression stroke is a combination of two effects: The pressure rise through the piston Δp_v and the pressure rise due to combustion Δp_c [9, 57].

$$\Delta p = \Delta p_c + \Delta p_v \tag{1.11}$$

This is illustrated in in Figure 1.13.

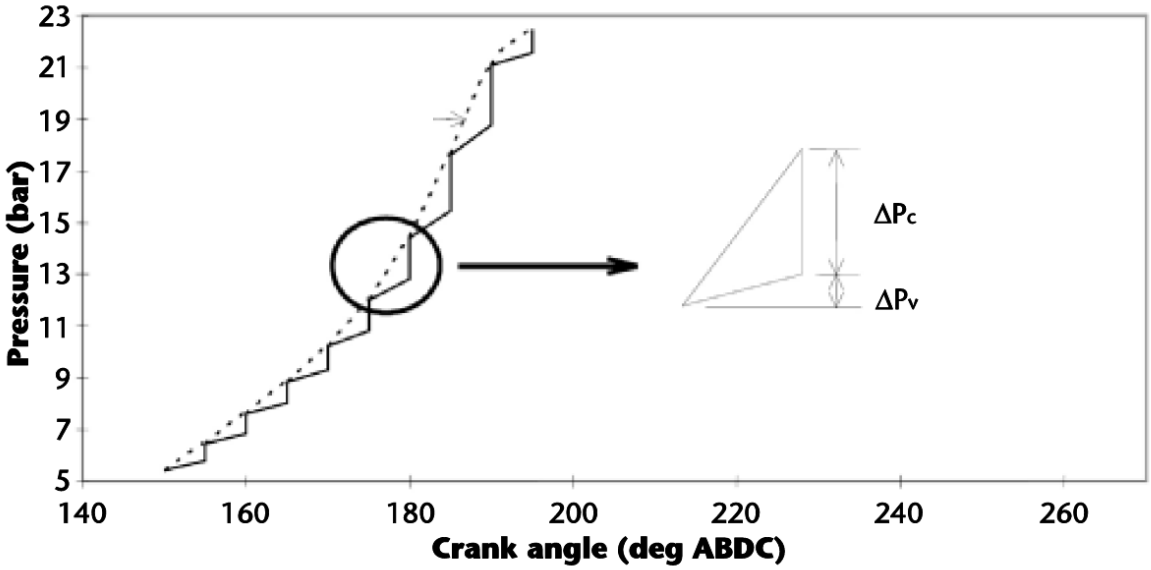

Figure 1.13. Rassweiler and Withrow method. Adapted from [9].

When advancing from crank angle θ_I to the next increment θ_{I+1}, the volume changes from V_I to V_{I+1} and the pressure from p_I to p_{I+1}. If a polytropic process for the change in pressure due to compression is assumed, Equation 1.11 can be written as:

$$p_{I+1} - p_I = \Delta p_c + p_I \left[\left(\frac{V_I}{V_{I+1}} \right)^k - 1 \right] \tag{1.12}$$

Equation 1.12 can then be solved for the pressure change due to combustion Δp_c.

$$\Delta p_c = p_{I+1} - p_I \left(\frac{V_I}{V_{I+1}} \right)^k \tag{1.13}$$

As combustion is not occurring at a constant volume, Δp_c has to be referenced to a constant volume such as the clearance volume V_c.

$$\Delta p_c^* = \Delta p_c \frac{V_i}{V_c} \tag{1.14}$$

After N increments, the pressure due to combustion Δp_c^* is zero. The mass fraction burned at the increment I ($N>I$) is then the ratio of summed up Δp_c^* at this increment over the sum of all Δp_c^* at the end of combustion. This can be seen in equation 1.15.

$$mfb = \sum_{0}^{I} \Delta p_c^* / \sum_{0}^{N} \Delta p_c^* \tag{1.15}$$

The calculation of *mfb* relies on the use of an appropriate value for the polytropic index k. The Rassweiler and Withrow method suggests to evaluate k before and after combustion and to then form an average value to use for the *mfb* analysis [57]. If k is only determined in the compression stroke, *mfb* actually decreases after reaching 100% *mfb* because k is lower during the expansion stroke. This is because combustion products are present in the expansion stroke and the heat transfer is elevated. For our analysis we nevertheless decided to calculate the polytropic index from the compression before combustion. A least squares straight line fit in a logarithmic plot of pressure and volume allows one to find k. Since this method is very sensitive to errors on the pressure data and since the pressure rise is very moderate during the early part of the compression, the initial part of the compression was disregarded. k was calculated from the halfway point between inlet valve closure (IVC) and ignition to ignition. Popular ranges for *mfb* that are reported in literature are 0-10%, 0-50% and 0-90% and all three have been used in this thesis.

A heat release analysis can be deployed to calculate how much heat would have been necessary in the combustion chamber to produce the measured in-cylinder pressure due to combustion. Assuming a fully mixed air/fuel mixture and, in a control volume, no mass transfer, the first law of thermodynamics states the heat release through combustion (δQ_{hr}) according to equation 1.16.

$$\delta Q_{\mathrm{hr}} = \mathrm{d}U + \delta W + \delta Q_{ht} \tag{1.16}$$

With δQ_{ht} as the heat transfer on the combustion chamber walls.

It is furthermore assumed that there are no differences in the properties of the reactants and products and that there is a uniform temperature distribution.

The work term in Equation 1.16 can then be formulated as:

$$\delta W = p\mathrm{d}V \tag{1.17}$$

The internal energy term in Equation 1.16 can be written as:

$$\delta U = mc_{\mathrm{v}}\mathrm{d}T \tag{1.18}$$

And with the ideal gas law in Equation 1.1:

$$m\mathrm{d}T = \frac{1}{R}(p\mathrm{d}V + V\mathrm{d}p) \tag{1.19}$$

Equations 1.18 and 1.19 can then be combined to:

$$\delta U = \frac{c_{\mathrm{v}}}{R}(p\mathrm{d}V + V\mathrm{d}p) \tag{1.20}$$

Equation 1.20 and 1.17 can then be substituted into Equation 1.16 and expressed per degree crank angle θ:

$$\frac{\mathrm{d}Q_{\mathrm{hr}}}{\mathrm{d}\theta} = \frac{c_{\mathrm{v}}}{R}\left(p\frac{\mathrm{d}V}{\mathrm{d}\theta} + V\frac{\mathrm{d}p}{\mathrm{d}\theta}\right) + p\frac{\mathrm{d}V}{\mathrm{d}\theta} + \frac{\mathrm{d}Q_{\mathrm{ht}}}{\mathrm{d}\theta} \tag{1.21}$$

Equation 1.21 can, with the assumption of semi-perfect gas behaviour: $c_{\mathrm{p}}/c_{\mathrm{v}} = \gamma$, $R = c_{\mathrm{p}} - c_{\mathrm{v}}$, be formulated as:

$$\frac{\mathrm{d}Q_{\mathrm{hr}}}{\mathrm{d}\theta} - \frac{\mathrm{d}Q_{\mathrm{ht}}}{\mathrm{d}\theta} = \frac{1}{\gamma - 1}\left(p\frac{\mathrm{d}V}{\mathrm{d}\theta} + V\frac{\mathrm{d}p}{\mathrm{d}\theta}\right) + p\frac{\mathrm{d}V}{\mathrm{d}\theta} \tag{1.22}$$

The net heat release $dQ_{n\theta}$ per degree crank angle θ can then be expressed as

$$Q_{n\Theta} = \frac{dQ_n}{d\theta} = \frac{\gamma}{\gamma - 1} p \frac{dV}{d\theta} + \frac{1}{\gamma - 1} V \frac{dp}{d\theta} \tag{1.23}$$

With $dV/d\theta$ as defined from the engine geometry and $dp/d\theta$ as the in-cylinder pressure data [9, 10].

1.6. Control Theory

The control system of the research engines required the application of several control devices, namely LabVIEW-implemented PID controllers which are introduced in this section. PID is the abbreviation for 'proportional integral derivative'. A process variable (PV) is measured and compared to a 'set-point' (SP), the desired value for that variable. The difference between PV and SP (error) is calculated by the PID and the controller constantly adjusts the variables in the process of reaching the SP.

The proportional component depends on the present error, the integral component on the past errors and the derivative component on the prediction of future errors. Since the PID controller only relies on the process variable, no information about the upstream process has to be included and it can therefore be used in a variety of applications.

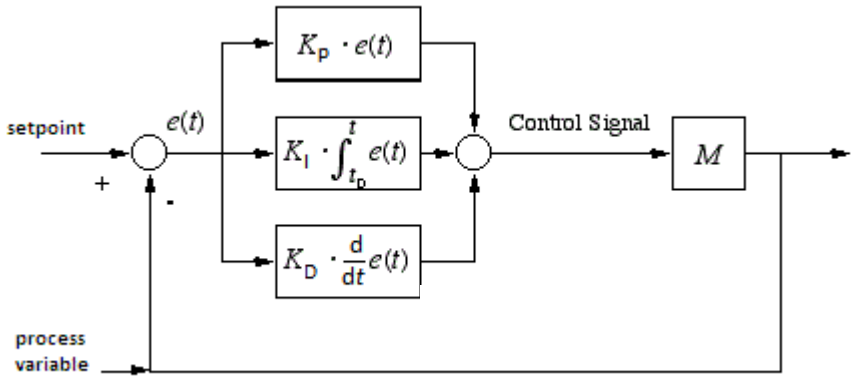

Figure 1.14. PID controller schematic

Figure 1.14 explains how the PID controller is implemented. The difference between the process variable and the set-point is the error which is used to calculate the proportional, integral and derivative action.

The proportional action is defined as in Equation 1.24.

$$u_p(t) = K_p * e(t) \tag{1.24}$$

With K_p as the controller gain and $e(t)$ as the error.

The controller gain is of high importance as it controls the speed of the response of the PID controller system. A large positive number (large negative in case of inverse proportionality) will result in a fast response. A fast response however has the disadvantage that the process variable might oscillate and make the system unstable. A small number improves stability but it means that it takes the controller a long time to reach the set point.

The integral component u_i is defined as in Equation 1.25.

$$u_i(t) = K_i \int_0^t e(\tau)\mathrm{d}\tau \tag{1.25}$$

The integral component takes account of the severity and the duration of the error. It contains the integral gain and the sum of the instantaneous errors over time. Hence it gives information on how the error should have been corrected in the past loops.

The derivative component is defined as in Equation 1.26.

$$u_d(t) = K_D \frac{\mathrm{d}}{\mathrm{d}t} e\,(t) \tag{1.26}$$

The derivative term takes the slope of the error and the derivative gain K_D. This term predicts how large the error will be in the future. If the process variable increases too quickly, the derivative component shrinks the output proportionally. A longer derivative time exacerbates the response of the PID controller to changes in the error and accelerates the speed of the PID controller. The derivative time is set to a small value because it is very sensitive to noise in the process variable. The derivative component applies only to changes in the local variable and not to changes in the set-point, as the latter is always abrupt and would influence the whole control system adversely.

The three components from Equations 1.24 – 1.26 are combined to the controller output $u(t)$ as in Equation 1.27.

$$u(t) = u_p(t) + u_I(t) + u_D(t) \tag{1.27}$$

The individual components can be auto-tuned for maximum system performance. A toolkit that uses the Ziegler-Nichols-Method to determine the PID control parameters in auto-tuning was applied. This requires an initial set of PID parameters to produce a stable control system [58, 59].

1.7. Summary of Thesis Project

In Chapter 1 it has been discussed how emissions from internal combustion engines contribute to anthropogenic climate change and how car manufacturers have therefore invested in increasing the fuel economy of these engines. Means to achieve higher efficiency include downsizing and turbocharging but these are limited by the increased chance and severity of the abnormal combustion phenomena auto-ignition, knock and pre-ignition. The

physical backgrounds of auto-ignition and knock were then discussed in detail and it was outlined how these abnormal combustion phenomena are influenced by the engine operating conditions and the fuel. The octane classification for fuels was introduced and great emphasis was put on expressing the numerous insufficiencies of this system for today's demands. Pre-ignition was introduced only briefly as it is germane, and therefore will be discussed in more depth, in Chapter 4. Fuel evaporation characteristics that are relevant for auto-ignition were outlined. Engine performance parameters that have been used throughout this thesis were introduced, the ideal engine operating point was explained and the calculation of burn rate analysis parameters was outlined. An introduction to control theory was given as this is pertinent for the control of the engine with PIDs.

The rest of this thesis is dedicated to investigating abnormal combustion phenomena in spark-ignition engines. The aim is to improve the understanding of these phenomena by means of predominantly experimental work. This work is then pertinent for an improved, modern classification system for fuels.

Chapter 2 introduces the experimental set-up, namely the Ricardo E6 variable compression ratio engine that was used in the vast majority of experiments. The instrumentation, control and data acquisition equipment are then described. The E6 engine resembles an industrial CFR test engine. Spray imaging of the fuel injector and calibration of relevant sensor equipment are also discussed.

Chapter 3 concerns itself with the investigation of knock, auto-ignition and how these abnormal combustion phenomena are influenced by engine operating point, humidity of the intake air and mixture preparation. The ideal engine operating point is investigated and knock parameters are introduced.

Chapter 4 presents a study of surface pre-ignition. Surface pre-ignition is a very important abnormal combustion phenomenon as it can exacerbate knock. This is because the increased heat flux on the cylinder wall during auto-ignition can be the ignition source of surface pre-ignition. Surface pre-ignition has an over-advancing effect on the ignition timing and this in turn exacerbates knock. The heavier knock leads to increased heat flux and the engine moves to runaway knock that cannot be stopped by turning off the ignition. The physical background of this abnormal combustion phenomenon is explained and attempts of classifications that are available in literature are reviewed. The lack of a correlation to the octane scale is presented. Several experimental techniques are assessed and deployed to measure surface pre-ignition and while only one method is adopted eventually, this is relevant to other researchers who might want to try different techniques. Pre-ignition is induced with the help of a temperature controlled glow plug.

Chapter 5 is then a study of the effect of auto-ignition and knock on the heat flux of the cylinder wall. A review of the relevant literature shows that no cycle-by-cycle correlations between knock and heat flux have been reported. I successfully demonstrate just this with a co-located heat flux and pressure sensor probe. A cycle-by-cycle resolution is of utmost importance as occasional peak heat flux events are the most disproportionately damaging (and relevant for surface pre-ignition) and this is disregarded in anything but a cycle-by-cycle analysis.

2. Experimental Equipment

2.1. Engine and Instrumentation

This chapter outlines the equipment relevant to the overall thesis. Chapter-specific experimental instrumentation is introduced and discussed in the respective chapters where the equipment is used. A Ricardo E.6/T variable compression ratio engine was deployed for the vast majority of the experiments in this thesis. The change of compression ratio does not affect the fixed valve timing which is a characteristic shared with the CFR engine.

The engine cross section can be seen in Figure 2.1. The E6 is a single-cylinder four stroke engine that can be operated as a spark ignition engine or as a compression ignition engine. The experimental setup was designed so that the E6 resembles a spark-igniting CFR engine [23].

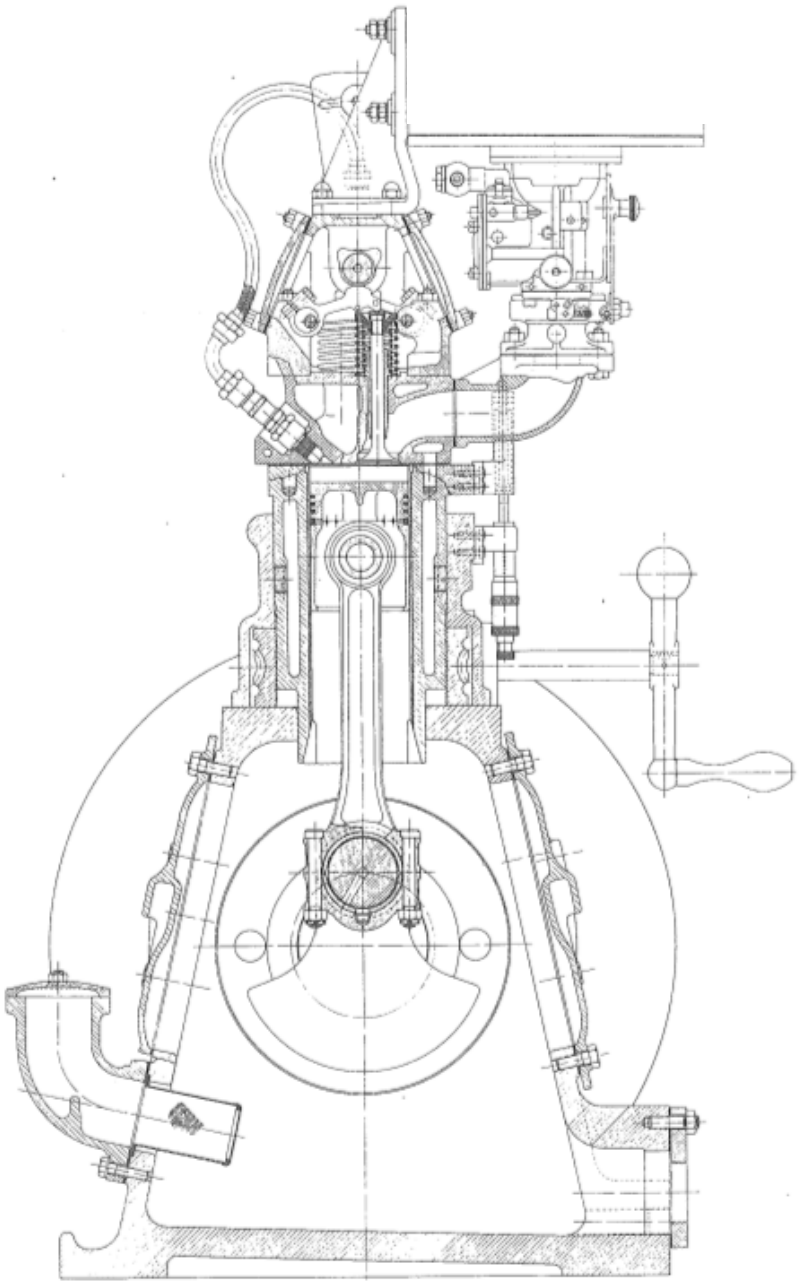

Figure 2.1. Engine cross-section adapted from original handbook

The dimensions and specifications of the E6 engine are summarized in Table 2.1.

Table 2.1. Engine specifications and dimensions

Property	**Specification**
Engine Type	Single Cylinder, 4-stroke
Fuel Injection Type	Port fuel injection
Bore	3 in (= 7.62 cm)
Stroke	4.375 in = (11.11 cm)
Swept Volume	507 cm^3
Speed Range	300 – 3000 RPM
Compression Ratio Range	4.5 - 20

The engine is equipped with overhead poppet valves. Table 2.2 outlines the valve timings.

Table 2.2. Valve timings

Operating point	**Timing**
Inlet Valve Opening (IVO)	9°ca bTDC
Inlet Valve Closing (IVC)	37°ca aBDC
Exhaust Valve Opening (EVO)	41°ca bBDC
Exhaust Valve Closing (EVC)	6°ca aTDC

In the following section, the individual parts of the experimental equipment are introduced. An overview of external transducers and control units is given in Table 2.3.

The coolant circuit of the engine is shown in Figure 2.2.

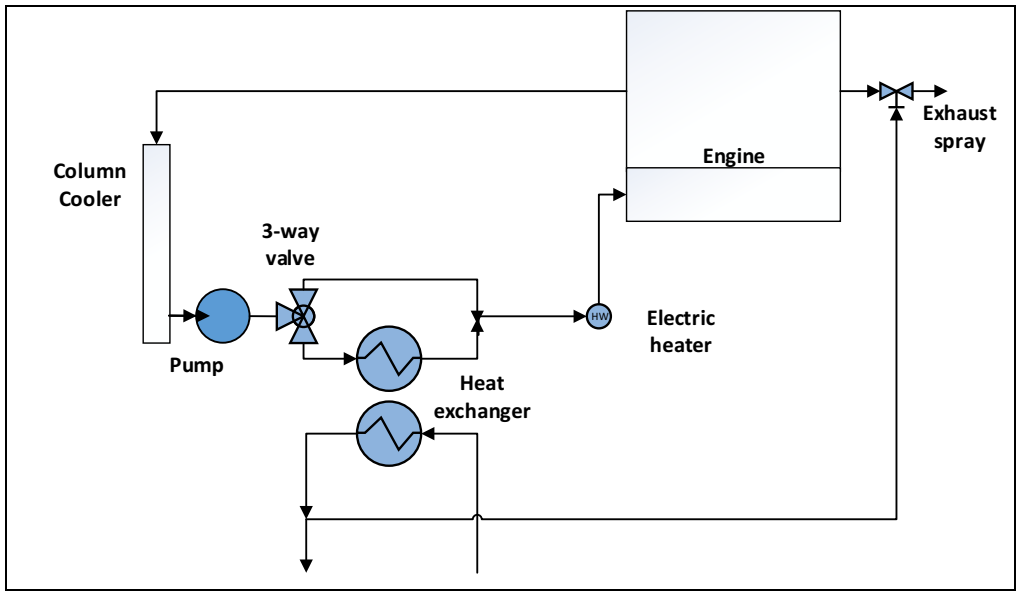

Figure 2.2. Engine coolant circuit

The coolant water is a 50:50% blend of water and anti-freeze [AFNOR NFR 15-601] with anti-corrosive properties. Hot coolant water exiting the engine is cooled in a column cooler before being pumped through a heat exchanger and subsequently re-entering the engine. By means of a PID-controlled 3-way valve [ESBE VRG 130], the coolant can bypass the heat exchanger and an electric heater [Carlton Technologies, 6 kW] can heat the coolant to the specified temperature. This was required in nearly all experiments as it was important that the engine coolant temperature is constant during the experiments. Water is sprayed into the exhaust gas stream of the engine to cool down the gas in order to protect the downstream exhaust pipes of the building.

The engine is connected to a swinging field dynamometer. [Laurence Scott Electromotors Ltd, 196]. It can absorb the peak mechanical power of 6.5 kW at Ω = 1500 RPM.

The compression ratio can be adjusted by raising or lowering the cylinder liner and barrel relative to the crankcase, by means of worm and wheel gearing. The outside of the cylinder liner has a screw thread to fit with the internal thread of the worm-wheel. Rotating the nut clockwise raises the cylinder, rotating it counter-clockwise lowers it, relative to the crankshaft. The compression ratio can be adjusted while the engine is motoring or firing. This way the experimental conditions can be changed quickly. The E6 is therefore an ideal engine for knock research. The engine is equipped with a micrometer that gives information about the clearance to the cylinder head from which the compression ratio can be calculated. A digital displacement transducer [RDP DCTH 500C] was fitted alongside the micrometer and connected to the instrumentation interface unit. This allowed for an easier and more precise way of adjusting the compression ratio. Furthermore, it gives real time information and allows for logging of the compression ratio.

A lambda sensor [Innovative Motorsports LM-1] was installed in the exhaust pipe 15 cm from the exit of the engine. It is connected to a readout device [Innovative Motorsports] with an analogue output that is connected to the data logging system. A delay in the response of 5-10 cycles was considered in the analysis.

Three fuel tanks have been installed on the engine with a capacity of 700 mL each. A variable-pressure N_2 supply allows for the fuel to be injected with a port fuel injection system into the combustion chamber. For injection, a TTL flag signal is generated by a slotted optical switch on the camshaft connected to the injection control unit. The control unit uses a potentiometer to define a voltage that determines the injection pulse duration, so a switch and BNC socket were added to allow a voltage to be set externally by LabVIEW in a Visual Interface (VI) on a computer; ‘PC 1’. This enables control of the voltage and thereby the injection duration directly from the computer. Within LabVIEW, the duration can be specified directly or a PID controller can automatically adjust the injection duration

according to a desired Lambda value. An analogue signal in the range 0 – 10 V generates a pulse to the injector of 0 – 20 ms duration. Section 2.2 will elaborate on the data-acquisition and control in extended detail.

A fuel switch controls solenoid valves on the fuel tanks and allows the operator to switch between the fuels easily and quickly. The 2100 mL supply is sufficient to fire the engine for approximately 60 min when run at stoichiometric conditions with a standard high octane fuel at Ω = 600 RPM.

Figure 2.3 shows an engine cross section and a superimposed picture of the fuel spray (fitted to scale).

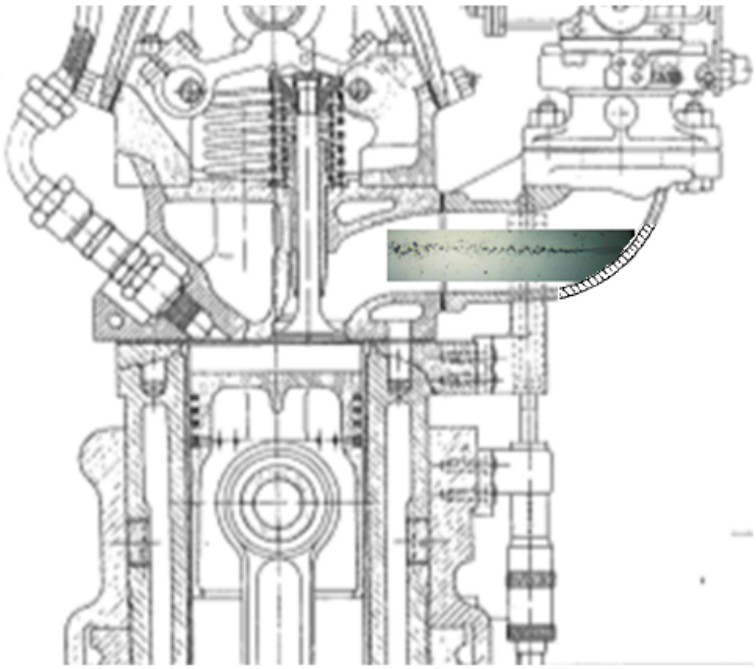

Figure 2.3. Engine cross section and fuel spray

The fuel spray impinges on the wall and the valve stem. This can be seen in the photograph in Figure 2.4. The spray pictures were made by fitting the fuel injector to a spray rig and taking high speed videos of the fuel injection.

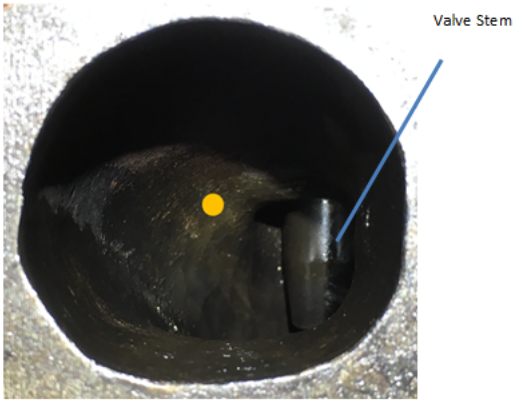

Figure 2.4. Photograph of inlet area. Yellow dot is used to mark the centre point where fuel impinges.

The surface of the inlet area was found to be wetted in oil. The lack of oil seals on the top of the valve stem were identified as the cause of this.

The combustion chamber of the engine has two bores for sensors or spark plugs. The engine is fitted with a spark plug [Champion N9YC] and a custom built ignition system. The ignition circuit board is fitted in an ignition control box that is powered with 5V. The ignition board picks up the engine flag from the shaft encoder, for processing in LabVIEW. The appropriate ignition timing is then fed back to the ignition circuit from where the signal is sent to a pulse generator [TTi, Thurlby Thandar insturments, TGP110, 10MHz] and from there to the spark plug. The pulse generator acts as a buffer to avoid interference pulses from the spark plug back to the instrumentation and control system. This is the result of a very time-consuming search for means to reduce spark interferences. Suggestions ranged from altering the injection flag sensor (from always high to always low) and shielding wires. The spark plug was further powered by a 12 V battery [APC, lead acid] rather than relying on grid-supply to further reduce interference.

A control techniques panel contains the electronics for the electric dynamometer. It manages the control of the engine speed and auxiliaries such as the coolant pump and heater. An

emergency stop switch is fitted to the outside of the panel. An additional instrumentation box contains crucial engine control equipment. As a safety feature, the engine is turned off if a pressure transducer in the exhaust signals an insufficient vacuum. An interface for the shaft encoder is located in this box which outputs an extended (with the help of a built-in flag pulse extender) cam flag and the crank angle signal. It is also fitted with an additional emergency stop button within the reach of the engine operator.

All temperature measurements were undertaken with K-Type thermocouples with the exception of a thermometer in the oil flow that did not need to be connected to the data acquisition system. The K-type thermocouples have a sensitivity of 41 μV/K and were amplified to give an output range of either 0-100°C or 0-1000°C in the case of the exhaust gas temperature measurement. The thermocouples have a 3 mm diameter outer sheath and are fitted using 1/8'' BSP compression fittings. Thermocouple 3, which measures the temperature of the air/fuel mixture as it enters the combustion chamber, is exposed to fuel deposition from the mixture stream. Subsequent evaporation of the fuel could lead to an underestimate of the mixture temperature. A special shrouded fitting was therefore built that shields the thermocouple from the stream. Additionally, the sheath was removed from the thermocouple so that it operates with an exposed junction so as to give a faster response.

The engine speed display is derived from an AC-generator that is coupled to the shaft at the back of the electrical dynamometer. A full bridge rectifier and smoothing capacitor led to a linear relation between voltage and crankshaft speed. The smoothing capacitors were a trade-off between having a steady reading when the engine was at a fixed speed, but also requiring a quick response when the engine speed changed.

The air flow is measured by the pressure drop across a viscous flow element. The pressure drop is measured with a pressure transducer that is connected to the E6 with ¼'' tubing.

Inside this transducer, the deflection of a stainless steel diaphragm changes the capacitance and a positive pressure moves the diaphragm towards an electrode which increases the capacity and *vice versa*. The air can be heated with an air heater [custom-build, 515 W] before entering the air plenum and combustion chamber. At the maximum speed of the engine (Ω = 3000 RPM) the heater would need 410 W to heat the air from room temperature to T_a = 50°C. Since most of our experiments were conducted at Ω = 600 RPM and T_a = 30°C, the power of the heater is well sufficient for our purposes.

Different in-cylinder pressure transducers depending on the experiment were used. The type Kistler 6051A would be fitted into the bore opposite the spark plug. When this bore had to be used for an additional sensor, a pressure sensor that was co-fitted to the spark plug [Kistler 6517a17 d14f-7d2] could be used. The pressure signals were then amplified with an amplifier [KIAG, Type 5001] for data logging and analysis.

Additional pressure transducers [UNIK 5000, GE, PTX 5072] were fitted to the inlet and exhaust streams, so the common pressure pulsations in the exhaust and inlet manifold could be closely monitored.

A load cell of the type [PCM, BD-ST-615 50 kg bi-directional S-type] was installed. The required load cell range was calculated from the expected torque at standard conditions according to Equation 1.7.

2.2. Data Acquisition

The data acquisition was realized on four separate data acquisition (DAQ) cards which allow for several different variable sampling rates:

The SHDAQ card [NI USB6251], the ‘super-high-speed DAQ card’ with a maximum sampling rate of 1.25 MS/s with 16 inputs was mostly used for logging the pressure data from the engine for knock and combustion analysis.

The HDAQ card [NI USB-6211], the ‘high-speed DAQ card’ with a maximum sampling rate of 250 kS/s. The card has 16 analogue inputs (Ai) 2 analogue outputs (Ao), 4 digital inputs (PFI) and 4 digital outputs (PFO). Always operated at a sampling rate of 720 S/cycle, this card was triggered by external clock from the crank angle signal after it had been extended in a pulse generator [TTi, Thurlby Thandar insturments, TGP110, 10Mhz]. This card was concerned with the operation of the injection and ignition system as well as data display and logging of the cylinder pressure and flag signals.

The LDAQ card [NI USB-6211], the ‘low speed DAQ card’ with a maximum sampling rate of 250kS/s was of the same type as the HDAQ card. This card was operated at a sampling rate of 1 sample per revolution and was triggered with an external clock by the pulse generator-extended (¼°ca-10°ca) crank flag signal [Thurlby Thandar insturments, TTi, TGP110, 10 Mhz]. This DAQ Card was used to display and log the data from a range of sensors installed on the engine. It was further used to operate the PID controllers for the coolant temperature, the heated air temperature, the mixture temperature and the humidity (Chapter 3).

The SLDAQ card [NI USB 6008], the ‘super low speed DAQ card’ with a maximum sampling rate of 10 kS/s was used exclusively for the pre-ignition experiments which will be discussed in Chapter 4.

The DAQ cards were connected to two computers ‘PC 1’ and ‘PC 2’, both equipped with LabVIEW [Version 2012 SPI, 32 bit]. The data was then processed in several LabVIEW VIs

for real time display, control and data logging for subsequent calculations in the combustion burn rate analysis software package.

An interface control box accommodated the HDAQ and LDAQ cards, much of the associated wiring and provided additional signal conditioning and power supplies. The DAQ cards operated on a 0-10 V basis, so the signals from the transducers and thermocouples had to be amplified accordingly. The SHDAQ and SLDAQ card were not fitted into the interface control box.

The interface control box is a 19 inch by 3 U rack case that contains the majority of the electrical wiring. The front and back panel of the control box can be seen in Figure 2.3 and Figure 2.4. The back panel of the interface control box was designed to accommodate the connectors for the incoming and outgoing signals from sensors, actuators and to the ignition/injection control box. Additional sockets were installed for devices that could be added later. All sockets were connected on the inside to the HDAQ and LDAQ cards which in turn are connected to ‘PC 1’ via USB cables. The front panel of the interface control box has BNC sockets that correspond to every input and output on the back panel. This was designed to enable us to check the incoming data independently from the LabVIEW system with the help of an oscilloscope [Tektronix DPO 2014, digital phosphor oscilloscope, 100 Mhz, 1 GS/s] or a voltmeter [DT – 2844, DIGITEK]. The front panel also contains green LEDs to signal if the +24 V, the + 12 V and the -12 V power sources are switched on. The thermocouple circuits were equipped with red LEDs that illuminate when the thermocouples are disconnected.

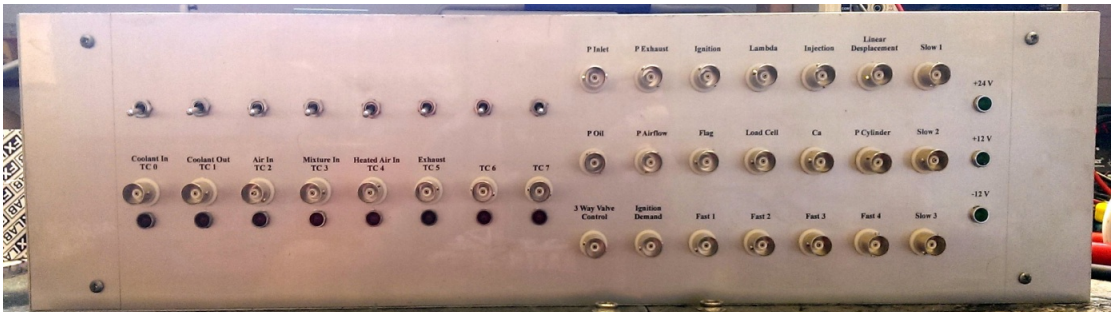

Figure 2.3. Interface control box front panel with LEDs at thermocouple ports

Figure 2.4. Interface control box back panel with clearance holes for DAQ-card cables

Table 2.3 summarizes the measurement and control parameters required to run and monitor the engine. It further gives details about the names of the devices, their specifications, power supply, signal conditioning and information about how the devices were wired up within the interface control box and connected to the DAQ card. Information was mostly derived from the data sheets of the components.

Table 2.3. Engine instrumentation; the connectors to the LDAQ card are labelled with 'L' and the connectors to the HDAQ card are labelled with 'H'.

Item	Sensor	Specification	Power Supply	Signal Conditioning	Channel	DAQ L/H-Pin	Connector Type	
							Front	Back
Temperature - Coolant In	Thermo-couple	• 1/8" BSP fixing • 3mm Diameter • 10 mV/°C • 1000 °C Range	12 V	• AD595 Amplifier – +5 to 15V Power supply • Buffer Amplifier • Filter	AI 1	L-17	BNC	K-Type Thermocouple
Temperature -Coolant Out	Thermo-couple				AI 9	L-18	BNC	K-Type Thermocouple

Temperature - Air In	Thermo-couple				AI 2	L-19	BNC	K-Type Thermocouple
Temperature - Mixture In	Thermo-couple				AI 10	L-20	BNC	K-Type Thermocouple
Temperature - Air In	Thermo-couple				AI 3	L-21	BNC	K-Type Thermocouple
Temperature - Exhaust	Thermo-couple				AI 11	L-22	BNC	K-Type Thermocouple
Temperature - Fuel	Thermo-couple				AI 4	L-24	BNC	K-Type Thermocouple
Temperature - TBD	Thermo-couple				AI 12	L-25	BNC	K-Type Thermocouple
Pressure – Airflow	Differential Pressure Transducer	RS Part No. 5351252 • 0-10 V output • 0-1 kPa • 1 s response time • 1% accuracy	24 V DC	Direct to DAQ	AI 5	H-26	BNC	4-pin
Pressure – Oil	Gauge Pressure Transducer	RS Part No. 4554624 • 4-20 mA output • 0-10 Bar • 1 ms response time • 0.25% accuracy	24 V DC	Output in series with 500 Ω (2 x 250 Ω resistors), connected to a 24 V supply gives 2-10 V output.	AI 13	L-27	BNC	3-pin
Pressure - Inlet Manifold	Pressure Transducer	RS Part No. 7463600 • 4-20 mA output • -1 to 1.6 bar • 10 ms response time • 0.1% accuracy	24 V DC	Output in series with 500 Ω (2 x 250 Ω resistors), connected to a 24 V supply gives 2-10 V output.	AI 8	H-16	BNC	3-pin
Pressure – Exhaust	Pressure Transducer	RS Part No. 7463600 • 4-20 mA output • -1 to 1.6 bar • 10 ms response time • 0.1% accuracy	24 V DC	Output in series with 500 Ω (2 x 250 Ω resistors), connected to a 24 V supply gives 2-10 V output.	AI 0	H-15	BNC	3-pin
Pressure - Cylinder	Pressure Transducer	• 0-250 bar • Sensitivity 38.21 pC/bar • Linearity < ± 0.3 % • Max 400 ℃	24 V DC	Output converted and calibrated to 10 bar/V by charge amplifier	AI 13	SH DAQ	BNC	BNC
Compression Ratio	Displace-ment Transducer	RDP Product Code DCTH500C • ±12.5 mm (25 mm travel) • 4-20 mA / DC output • <±0.5 % Linearity • 5 mV/V Output	24 V DC		AI 6	L-29	BNC	BNC
Lambda	Lambda Sensor	Innovate Motorsports With 3737 Bosch O_2 Sensor LSU 4.2	12 V DC		AI 14	L-30	BNC	BNC
Ignition Timing	Cussons	• From Department - See Manual	N/A	Take output from Eurocard pin 31, 0-9V	CTR 1	H-7	BNC	BNC
Engine Speed	Counter-Timer	• 1 Pulse / °ca			AI 8	L-16	BNC	BNC

Engine Flag		• Shaft encoder		Also on AI-10(HDAQ) and AI-7(LDAQ)	PFI 1	H-2	BNC	BNC
Crank Angle		• Shaft encoder			PFI 2	H-3	BNC	BNC
Air Heater Controller		RS Part No. 720 4048 SSR • AC operated	24V AC (Min)	Using input from TC 4, LabVIEW output to DAQ D/O, 0-10 V signal to solid state relay	PFI 4	L-6	BNC	BNC
Mixture Temperature Controller		RS Part No. 720 4048 SSR • AC operated	24V AC (Min)	Using input from TC 3, LabVIEW output to DAQ D/O, 0-10 V signal to solid state relay	PFI 5	L-7	BNC	BNC
Injection Duration				Counter-timer	AO 1	L-13	BNC	BNC
3 Way Valve Control				LabVIEW output to DAQ A/O 0-10 V signal to valve	AO 1	H-17	BNC	5-pin 240^{o}
3 Way Valve Control				Status signal to LabVIEW	AO 1	H-13	BNC	BNC
Fast 1 (Spare)					AI 2	H-19	BNC	BNC
Fast 2 (Spare)					AO 0	H-12	BNC	BNC
Fast 3 (Spare)					AI 9	H-18	BNC	BNC
Fast 4 (Spare)					PFI 7	H-9	BNC	BNC
Slow 1 (spare)					AO 0	L-12	BNC	BNC
Slow 2 (spare)					PFI 0	L-1	BNC	BNC
Air Heater					CTR 0	L-6	BNC	BNC
Engine Torque	Load Cell	PCM (BD-ST-615 50 kg Bi-directional S-type)		Differential Amplifier	AI 15	L-32	BNC	5-pin

In Table 2.3, ‘AO’ refers to Analogue Output, ‘AI’ to Analogue Input, ‘PFI’ refers to Programmable Function Interface, ‘CTR’ refers to Control.

Figure 2.5 gives an additional overview as to how the different devices were connected to the HDAQ and LDAQ cards.

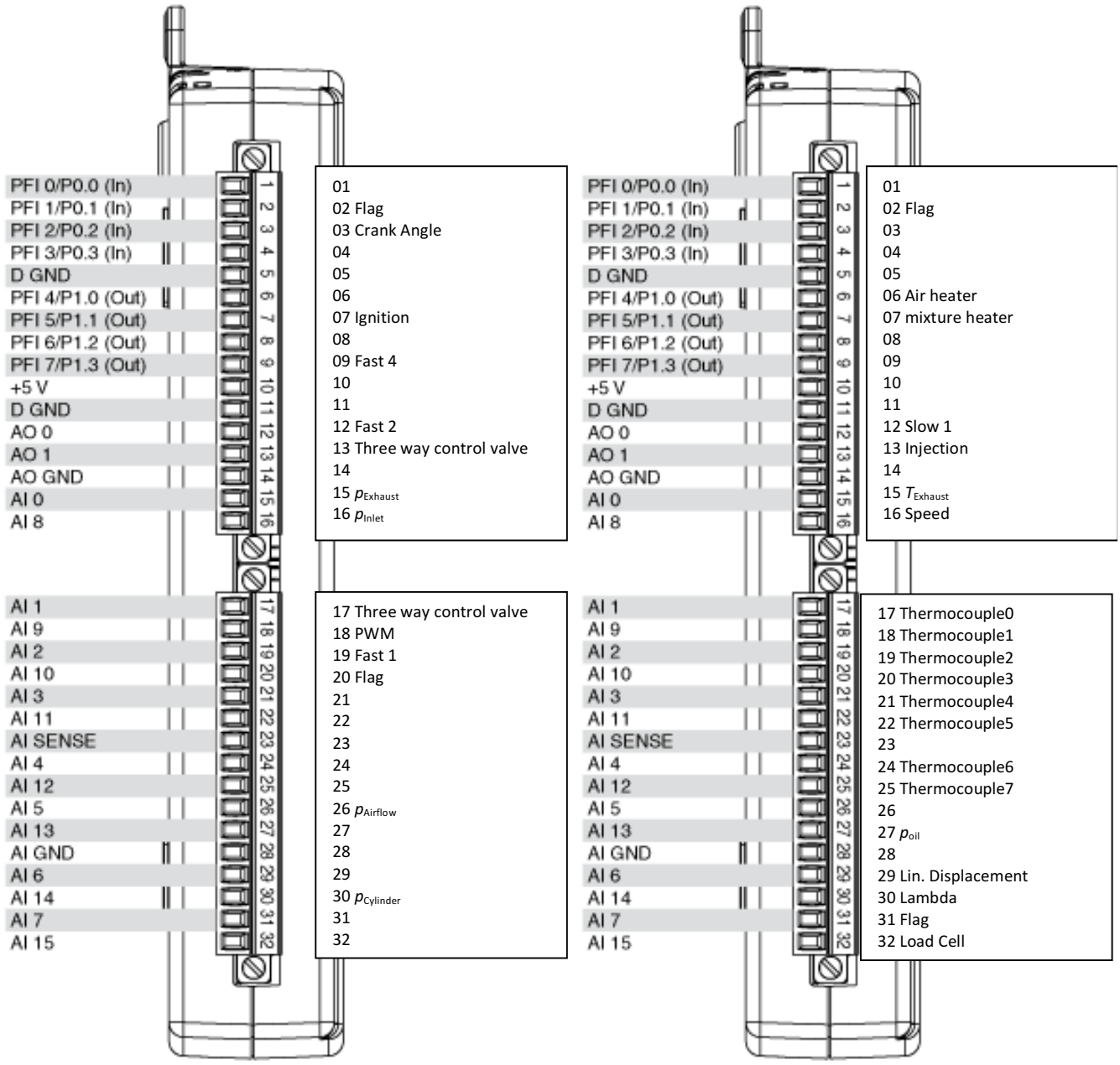

Figure 2.5. DAQ cards. HDAQ on the left, LDAQ on the right.

The main LabVIEW VI to control the engine is explained briefly in the following section. Several boxes were set up to help the user with orientation around the VI. On the top left, the user can switch on and off a button to log data for both DAQ cards. In a field above, the name of the data file can be edited. The rest of this box is made up of indicators of the measurements from the LDAQ card. This includes all the thermocouples, the lambda value,

the oil pressure, the compression ratio, torque, the speed, the ignition timing and the airflow. In the box on the top right corner the HDAQ values of intake and exhaust pressure are displayed.

In the other boxes key parameters of the engine are controlled. The occurrence of the spark before TDC and the injection duration can be adjusted. For the latter, a switch can turn the injection on and off and a desired duration can be entered manually. Another switch overwrites the manually entered duration and activates the lambda PID controller, which will adjust the injection duration in a way for a desired lambda value to be established.

For the repeatability of our experiments, it was essential that the temperature of the intake air and the coolant remained constant. PID controllers were deployed to control the air heater for a default air temperature of 30-70°C and to control the three way valve for a default coolant temperature of 80°C. The respective PIDs are also shown in the VI and the respective set-points can be entered by the user before the experiment. Both the air and the coolant heater have warning lights if the temperature exceeds a user-specified limit beyond the set point. Additionally, the air heater turns itself off when the engine speed is below a set point. The humidity of the intake air was also controlled in this VI. The humidifier equipment will be introduced in Chapter 3.

An additional box on the bottom left of the VI shows the real-time cylinder pressure data from the HDAQ card.

A tab in the background allows for a quick change of input and output channels without having to consult the block diagram. Furthermore, on this tab the parameters for the PID controllers can be adjusted.

2.3. Calibration

All transducers used for the experiments were calibrated. The K-Type thermocouples were calibrated at two different temperatures. An experimental setup was designed for this purpose. An insulated container was prepared with large pieces of ice in water and the temperature monitored with a mercury thermometer. The thermocouples (connected to the LDAQ and LabVIEW) were then held into the ice water pool and allowed to adjust to the temperature. From the LabVIEW VI the values of the output voltage were then read out and recorded. As the voltage values were fluctuating, two values were noted for each thermocouple and later an average was formed.

The thermocouples were then removed from the ice-bath. With a kettle, boiling water was prepared and poured into an insulated container. The temperature data was monitored with another mercury thermometer. The thermocouples were then held into the boiling water. Again, the voltage values were read out from LabVIEW with two data points for every thermocouple. The results were plotted and a straight line fit was assumed for the linear response of the thermocouples. One of the thermocouples that was to be used in the exhaust stream had to be calibrated to a much higher temperature, and for this a hot air gun was used rather than the hot water bath.

In order to calibrate the ignition timing, an ignition timing strobe [Gunson Xenon timing light and inductive pick-up] was used in conjunction with crank angle markings on the flywheel to determine the ignition timing. This could be compared to the set ignition timing in the LabVIEW VI and adjusted accordingly.

The pressure transducers for the exhaust and inlet were calibrated with the help of a mercury manometer. A calibration set-up was designed in which each transducer was connected with a T-junction to the manometer. Pressure was then induced with a glass gas syringe. With the

help of valves, the pressure could be brought up to 78 kPa. The voltage output in LabVIEW was recorded. Measurement points were taken along the way from positive to negative pressures, for which air was evacuated with another pump. Negative pressures of 75 kPa could also be achieved and the voltage outputs recorded. The data was collected and assessed on the computer. Plots were created and linear fitting applied to find a trend line.

The permanent airflow meter was calibrated in a similar fashion but instead of the mercury manometer a previously installed manometer [Type 504, Air Flow Developments Ltd] and a positive displacement flow meter were used. The flow meter allowed for a calibration of the manometer which in turn was used to calibrate the permanent airflow meter. The straight-line fit of the calibration can be seen in Figure 2.6.

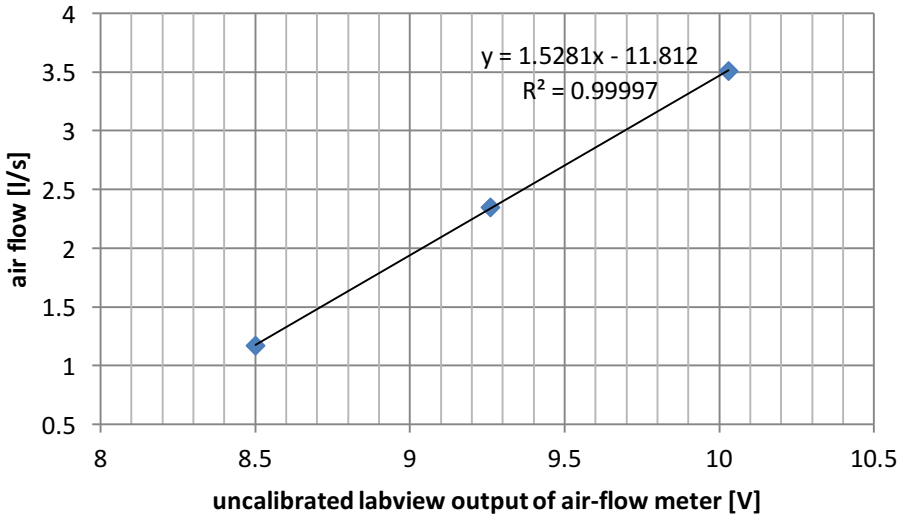

Figure 2.6. Calibration of permanent air flow meter

A digital displacement transducer [RDP DCTH 500C] was used to accurately determine the current compression ratio of the engine. The procedure for the calibration of the compression ratio is given from the original handbook [60].

The compression ratio (τ) is defined as:

$$\tau = \frac{V_{clearance} + V_{swept}}{V_{clearance}} \tag{2.1}$$

If a gauge with a thickness of 0.375" is inserted into the gap between the bottom face of the cylinder head flange and the crankcase, and the cylinder is lowered until the gauge is nipped, then the compression ratio is 12.23. This will correspond to a clearance volume of 45.15 cm^3, The calibration was then performed against the micrometer reading that is installed in the engine. A series of measurement points from the largest possible clearance (1.009") to the minimum at 0.116" was taken. This can be seen in Figure 2.7.

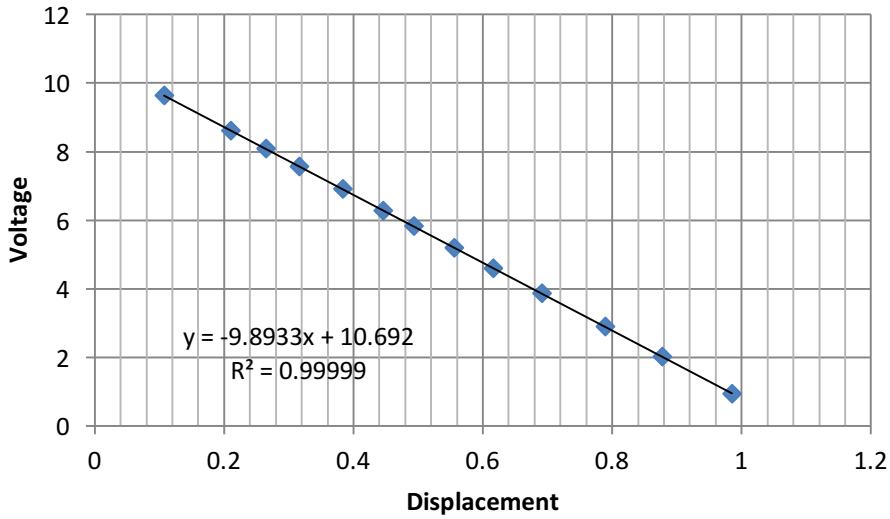

Figure 2.7. Displacement Transducer calibration (1/2)

The voltage was then calculated against the compression ratio as can be seen in Figure 2.8.

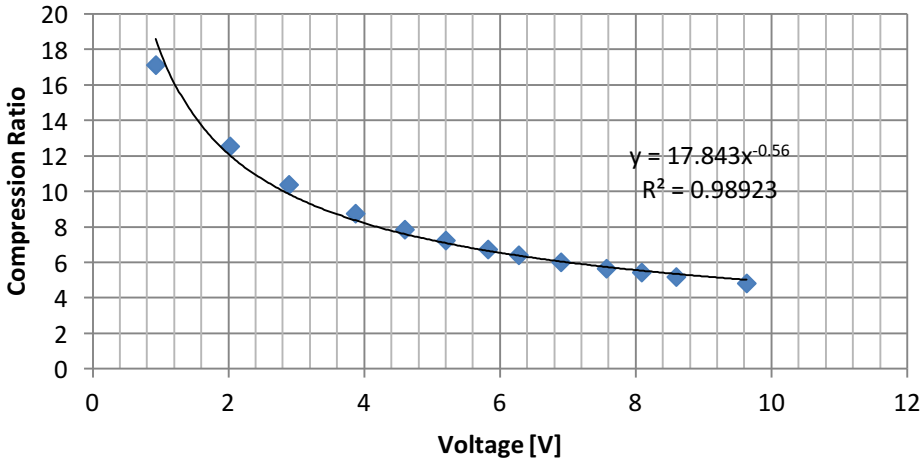

Figure 2.8. Displacement Transducer calibration (2/2)

For the calibration of the lambda sensor, the sensor was removed from the exhaust pipe and screwed into a manifold that is open on one side but can be connected to calibration gas bottles on the other. The voltage generated by the sensor was then recorded in LabVIEW for two gases that were exposed to the sensor.

(1) CO_2 14.06 %, CO 3.515 %, propane 1955 ppm, N_2 balance

(2) O_2 6.29%, N_2 balance

The flow ratio of the two gases was varied, and a linear correlation was found when the data was plotted and a straight line fitted (Figure 2.9). The R^2 value is 0.9971.

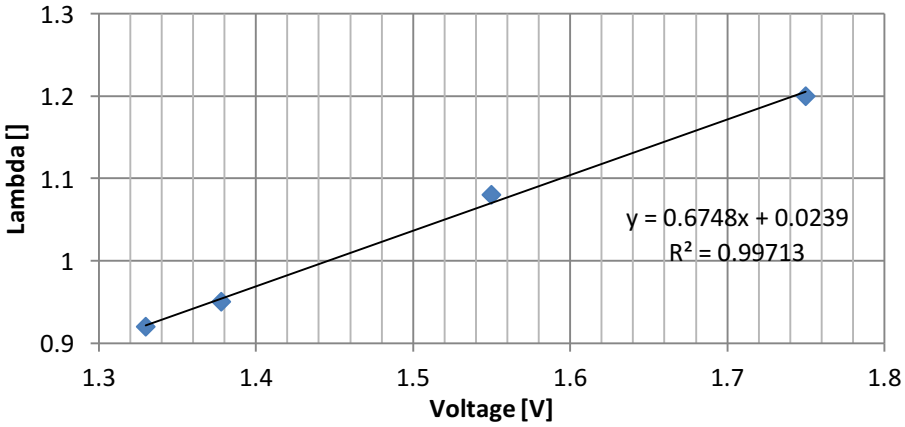

Figure 2.9. Lambda sensor calibration

It is important to note that experiments should not be conducted far outside the calibrated area (0.85 – 1.25) as there is a risk of saturating the sensor, so limits are imposed on the lambda values that can be demanded in the PID controller.

The load cell and an appropriate amplifier were connected to the LDAQ and LabVIEW and the output was monitored with an additional voltmeter for calibration. Weights were applied to the load cell and the output voltages were recorded. The weights pulled on the load cell while under firing engine conditions when the load cell was compressed. The torque T was calculated according to Equation 2.2.

$$T = mgl \tag{2.2}$$

With mass of the weights m, gravitational acceleration g and length of the arm l

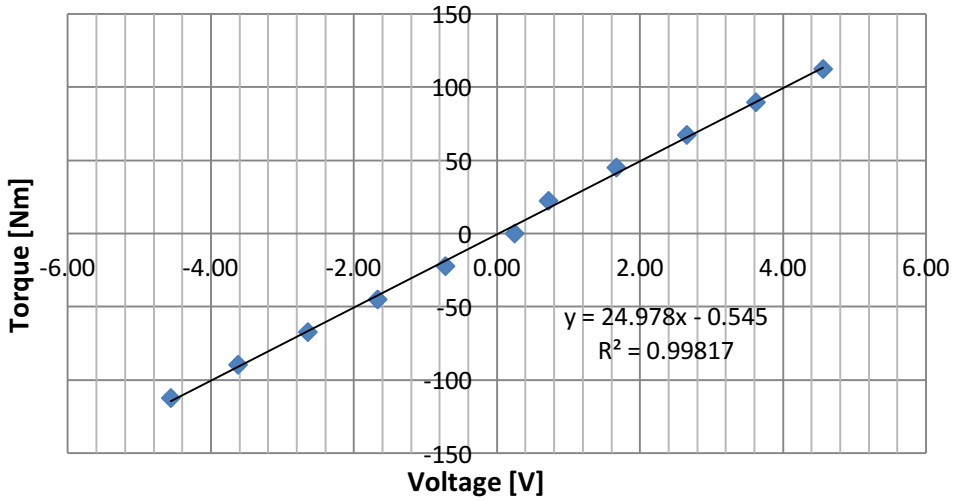

Figure 2.10. Load cell calibration

The signal from the load cell, as well as from the air flow meter, is of a pulsating nature during engine operation. As the sampling rate of LDAQ is low, a steady input is needed, so a smoothing amplifier unit was constructed and tested. The block diagram for the circuit can be seen in Figure 2.11.

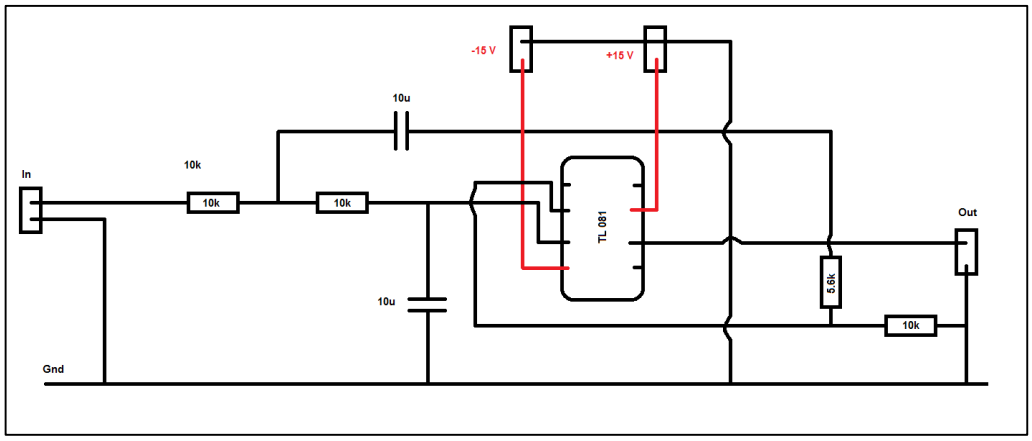

Figure 2.11. Filter block diagram

Figure 2.12 shows linear operation of the smoothing circuit. A steady output signal is produced that is proportional to the pulse width of the incoming signal.

The filter was calibrated for a range of pulse widths and the response was recorded. This can be seen in Figure 2.12.

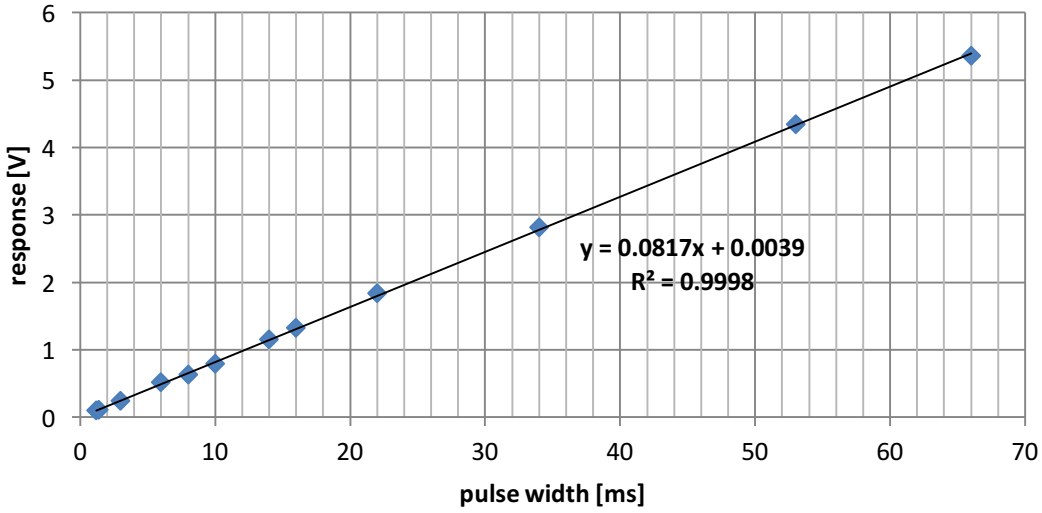

Figure 2.12. Filter calibration when tested with up to 70 ms period pulses.

All in-cylinder pressure sensors are [Kistler 6051A] or [Kistler 6517a17] piezo-electric pressure transducers. The output of these sensors is an electrical charge that, after being amplified externally, can be recorded directly with a LabVIEW VI. The output voltage is proportional to the pressure they measure. The calibration was performed using a dead weight calibration system. It relies on hydraulic pressure induced by weights on a piston that transfers the pressure to the transducer. The calibration data for one of the sensors [Kistler 6051A] is plotted in Figure 2.13. The other sensor calibrations showed similar linearity.

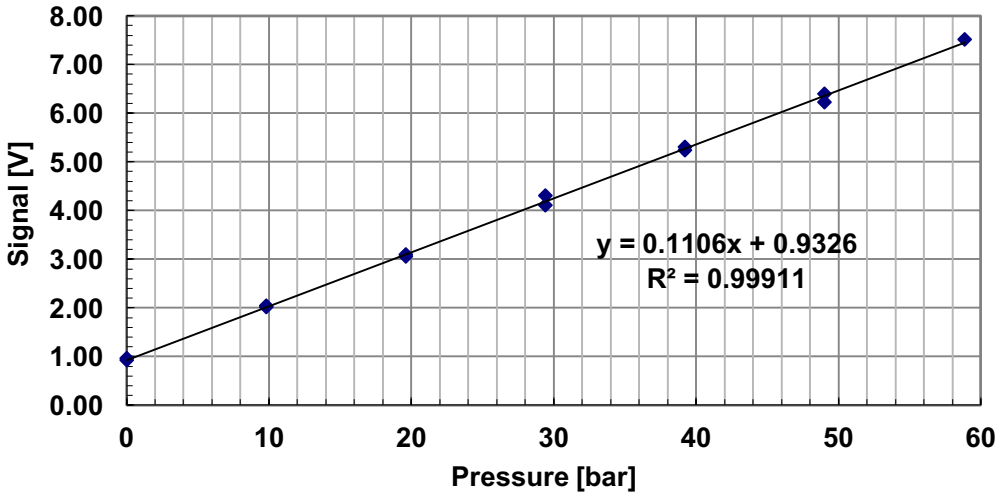

Figure 2.13. 6051A Pressure transducer calibration

2.4. Data Analysis

The combustion burn rate analysis code (COBRA) was deployed for data analysis. It was originally developed for an optical engine in Fortran [61]. Large parts of the code had to be rewritten to be able to process the data from the E6 engine in Matlab.

The code performs combustion analysis calculations based on in-cylinder pressure data and calculates important combustion parameters as outlined in Section 1.5. Of particular interest are the net indicated mean effective pressure (*IMEPn)*, the peak pressure p_{max}, the angle of the peak pressure Θ_{pMax} as well as the mass fraction burned (*mfb*) and the net heat release Q_N. The calculation of the peak pressure and the angle of peak pressure are straightforward. The other parameters are calculated according to the Equations 1.9 – 1.23.

The accuracy of the combustion analysis is dependent on an accurate crank angle phasing of the pressure data. The LabVIEW VI that operates the engine and logs engine data is therefore triggered to collect one sample of the pressure at every degree crank angle while logging the

crank flag signal to determine the position of the datum in relation to top dead centre (TDC). As described, the two data acquisition (DAQ) cards are deployed for this and the HDAQ is triggered at every rising edge of a crank angle signal to collect 360 readings per revolution and the LDAQ is triggered once per revolution by the crank flag. The pressure on the exhaust stroke was used to determine the atmospheric pressure to set a datum pressure.

3. The Influence of Humidity and Mixture Preparation on the Engine Operating Point and Knock

3.1. Introduction

This chapter covers the investigation of the engine operating point and the influence of humidity and vaporized fuel on the operation, combustion process and knock. A key requirement is to establish the appropriate ignition timing. For all things being equal, the ignition should be set to the Minimum Advance for Best Torque (MBT) timing, unless this lies after the onset of knock, in which case the ignition timing is set at the Knock Limited Spark Advance (KLSA). This implies that it is necessary to conduct a series of tests with different ignition timings, so an important question to answer is can the MBT ignition timing be found by using a fixed angle for the maximum cylinder pressure or a specified mass fraction burned?

Since the literature has not agreed on a single knock index, it is necessary to review the more commonly used knock indices and to identify their applicability and comparability. It is also necessary to review the physics of vaporization for the water and fuel, to analyse their effect on the engine and to avoid any unwanted condensation. The experimental equipment used for experiments in this chapter is set out below. Afterwards the experiments conducted and results obtained are explained and discussed.

3.2. Research Background

3.2.1. Engine Knock Indices

Knock can be detected and quantified with both direct and indirect measurements. The two approaches can be separated into in-cylinder pressure measurements on the one hand and analysis of the vibration of the engine on the other. In industrial applications, where

automobiles are produced and tested on a large scale, the indirect, non-intrusive vibration analysis with accelerometers is the approach of choice. It has the advantages of low cost and long durability. In research, nonetheless, direct in-cylinder measurements are preferred because of their higher accuracy. Other techniques such as methods based on measuring fluctuations in ion current in the spark gap have been deployed by researchers and are further investigated and discussed in Chapter 4 [62-64].

When knocking occurs, the combustion chamber gas vibrates at resonant frequencies. This leads to high frequency oscillations in the pressure trace. As described in Chapter 1, knock is a stochastic phenomenon and varies cycle to cycle. The pressure signal has to be filtered digitally before it can be analysed. Researchers are not consistent with what filter specifications they deployed, which is problematic as the filter type has an effect on the knock indices [47, 65, 66]. A finite impulse response (FIR) filter was implemented in MATLAB for the work in this thesis because it does not introduce a phase shift.

For the majority of spark ignition engines, the knocking in-cylinder pressure frequency range is between 4 and 25 kHz [47, 65, 66]. The ideal knock indicator would need little computational time, require a modest sampling frequency and give consistent results independent of the filtering technique. No common knock indicator is generally accepted in research, but several indices are more commonly used. Their names and physical background are outlined here.

The Maximum Amplitude of Pressure Oscillation (MAPO) is one of the most widely used methods of knock quantification [67]. The maximum amplitude of the band pass filtered pressure signal in the range of interest is considered:

$$\mathrm{MAPO} = \max\left(|\,\widetilde{p}\,|_{\theta_0}^{\theta_0+W}\right) \tag{3.1}$$

With: $\tilde{p}$ as the bandpass filtered pressure signal, θ_0 as the crank angle at the beginning of the knock interval and W is the duration of the knock window.

Integral of the Modulus of Pressure Oscillations (IMPO) sums the absolute values of the filtered pressure signal over the interval of interest [68].

$$IMPO = \sum_{\theta_0}^{\theta_0+W} |\tilde{p}| \mathrm{d}\theta \tag{3.2}$$

The Logarithmic Knock Index (LKI) uses the average energy of the filtered signal to describe knock intensity. This is appropriate given that the pressure oscillations are made up of many frequencies [69]. The average energy of a signal in the time domain is given by:

$$Average\ Energy = \frac{1}{N}\sum_{N=0}^{N-1} \tilde{p}^2(n) \tag{3.3}$$

The advantage of this method is its equivalence in the frequency domain and in the time domain. The complexity of the Fourier analysis in the frequency domain and the risk of spectral spreading means that the preferred choice is to evaluate the LKI value in the time domain as an 'average energy' calculation of the filtered pressure data [70].

$$LKI = \ln(C * Average\ Energy) \tag{3.4}$$

$$LKI = \ln\left(C\ \frac{\sum_{n=i}^{W} \tilde{p}(n)^2}{W} \right) \tag{3.5}$$

The constant C can be calibrated to give $LKI = 0$ for a knocking/non-knocking threshold as deemed appropriate for the respective experiment. W is the interval period over which the knock index is being evaluated [71].

The size of the window *W* over which the MAPO, IMPO and LKI are calculated is variable. Brunt et al. [72] suggest that a window from TDC to TDC+40 degrees crank angle should be adequate for knock analysis, however a tighter window can be used if processing time and data storage are limited.

The robustness of these knock parameters was assessed with the following method. The collected data is down-sampled and compared to the original data. Representative results are shown in Table 3.1.

Table 3.1. Down-sampled data for 1000 cycles collected at 200 ksamples/s that is used to compare three pressure-based knock indices: Maximum Amplitude of Pressure Oscillations (MAPO), Integral of the Modulus of Pressure Oscillations (IMPO) and Logarithmic Knock Index (LKI).

Knock Index	(Not Down-sampled)	Down-sampled Data			
		1,5,9...	2,6,10...	3,7,11...	4,8,12...
MAPO	1.38	1.35	1.39	1.39	1.38
IMPO	4.99	5.10	5.08	5.08	5.10
LKI	-3.19	-3.09	-3.10	-3.09	-3.07

Table 3.1 shows that the three methods (MAPO, IMPO, LKI) considered here appear to give equally good results, but there needs to be two notes of caution. Firstly, the results are an average of 1000 cycles, and secondly the conclusions may not be valid at lower sampling rates. At a lower sampling rate different values of the Maximum Amplitude of Pressure Oscillations (MAPO) would be identified for a given cycle, and when the results are averaged across many cycles variability in the MAPO will be masked. In the work in this chapter, which considers individual cycles, the Integral of the Modulus of Pressure Oscillations

(IMPO) and Logarithmic Knock Index (LKI) are preferred as they make more use of the information that is available and can be related to the intensity of the pressure fluctuations.

3.2.2. Intake Air Humidity

The effect of intake air humidity on the engine performance is well documented and ASTM [23] sets specific humidity limits for the RON and MON test from 0.00356 to 0.00712 [kg water/kg dry air]. It has been shown that higher levels of humidity lead to a smaller IMEP and reduced performance of the engine. The higher levels of humidity result in an elevated partial pressure of water vapour and a reduction in the dry air pressure. Hence there is less oxygen available for the combustion process [73, 74].

When it comes to the effect of humidity on knock, MacGregor et al [75] have demonstrated that that an increased humidity leads to a reduction in the severity of knock. This has been explained with regards to the reduced pressure in the combustion chamber.

Humidity is a measure of the water vapour content in air, but different humidity parameters are commonly used. These include the absolute humidity and the widely used relative humidity ϕ as defined in equation 3.6.

$$\phi = \frac{p'_s}{p_{sat}} \tag{3.6}$$

With: the partial pressure of water vapour p_s' and the equilibrium vapour pressure p_{sat}.

The relative humidity does not contain information about the fraction of water vapour in the air as it depends on the temperature. The specific humidity ω is a better measure as it

contains the ratio of the mass of water vapour to the mass of dry air. This is outlined in Equation 3.7.

$$\omega = \frac{m_s}{m_a} = \frac{p_s'}{p_a'}\frac{M_s}{M_a} \tag{3.7}$$

With: the mass of steam m_s, the mass of air m_a, the partial pressure of steam p'_s, the partial pressure of the air p'_a and the molar mass of steam M_s and air M_a.

For the experiments in which steam was to be introduced into the intake air, modelling was required to calculate the temperature that the water vapour had to be heated in order to avoid condensation upon mixing with the cooler dry air flow. The water vapour condenses if the partial pressure of the water p'_s in the air/vapour mixture exceeds the saturation pressure p_{sat} for a given mixture temperature T_m. A minimum required steam temperature depending on both the air temperature and the desired specific humidity ω was calculated with Equations 3.8 – 3.10:

Firstly, the partial pressure of the steam p'_s is calculated:

$$p'_s = \frac{x\, M_a p_a}{M_s(1-x) + x\, M_a} \tag{3.8}$$

With the steam mass fraction x which equals the specific humidity ω.

We then calculated the required mixture temperature using the Antoine vapour pressure equation [76].

$$T_m = -C + \frac{B}{A - \ln(p'_s)} \tag{3.9}$$

With the mixture temperature we can then calculate the required minimum steam temperature to avoid condensation.

$$T_s = \frac{(1-x)c_{pa}(T_m - T_a) + x c_{ps} T_m}{x\, c_{ps}} \text{-273.15K} \tag{3.10}$$

The results for the required steam temperature to avoid condensation for a range of steam mass fractions and five different air temperatures can be seen in Figure 3.1.

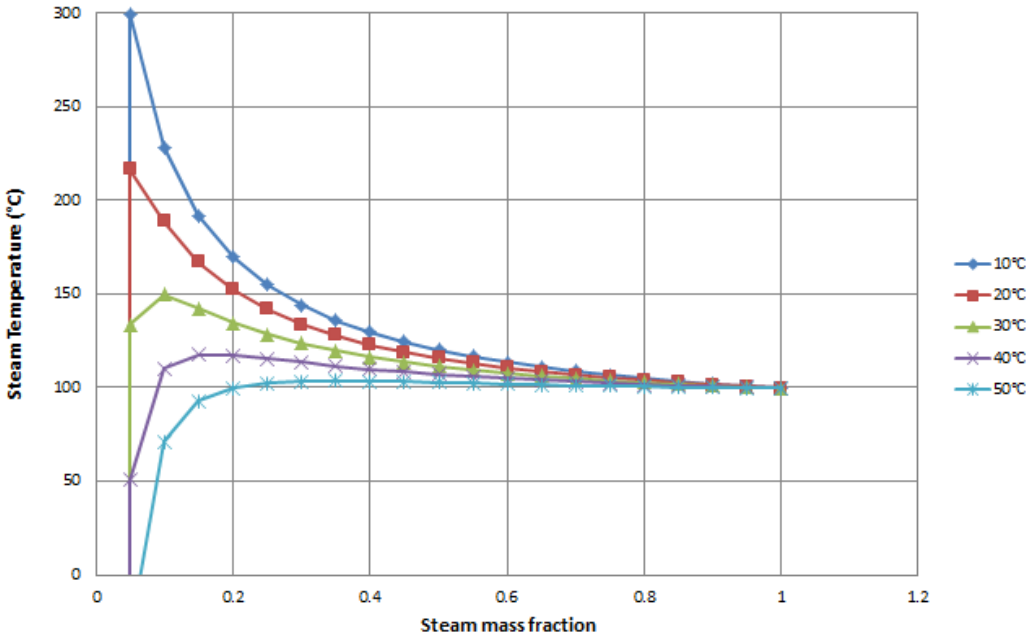

Figure 3.1. Required steam temperature to avoid condensation with different air temperatures at 1 bar ambient pressure.

It can be seen from Figure 3.1 that the higher the air temperature the more moderate can the temperature of the steam be for lower levels of specific humidity (or steam mass fraction).

The humidity of the air of the laboratory has to be taken into account. With the help of a wet-and-dry-bulb thermometer and a psychrometric chart (Figure 3.2) the specific humidity could be estimated.

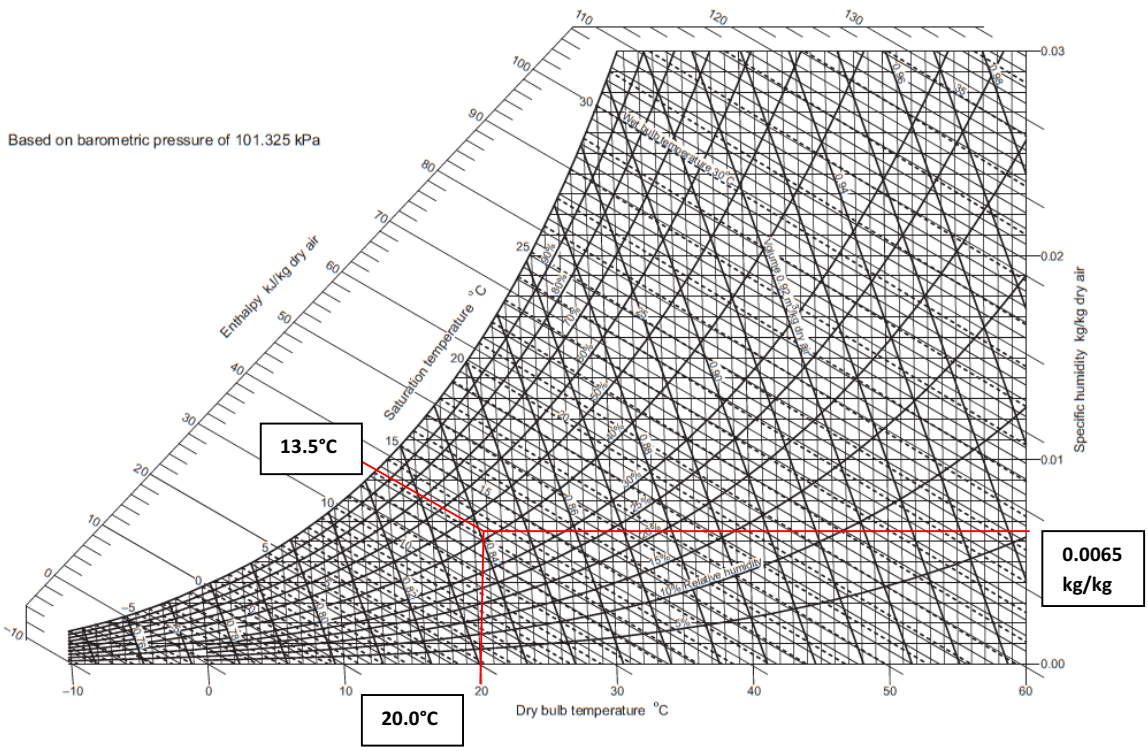

Figure 3.2. Psychrometric chart, adapted from [77].

In the psychrometric chart, the dry bulb temperature is found on the bottom axis and the wet bulb temperature is the saturation temperature on the left hand side. At the intercept of the two lines, the specific humidity can be read out on the right hand side and the calculations for the required humidity of the intake air can be adjusted accordingly. In Figure 3.2, the data points for a typical experiment have been included to illustrate how the psychrometric chart can be used. This is for a dry bulb temperature of 20°C and a wet bulb temperature of 13.5°C which result in a specific humidity of 0.0065 kg/kg dry air.

3.2.3. Fuel Vaporization Characteristics

As described in Chapter 1, the evaporation characteristics of fuels can have a large impact on engine performance and on knock. The RON and MON tests do not take appropriate account of the real world behaviour in this regard [56]. The evaporative cooling can have a positive

effect on the anti-knock quality of the fuel. However this effect is eradicated in the MON test and tests of this cooling effect on knock are in order.

The evaporative cooling (V_{evap}, kJ/kg$_{air}$) can be calculated with the following formula:

$$V_{\mathrm{evap}} = \frac{\widetilde{h_{\mathrm{fg}}}}{R_{AF}\ M_{\mathrm{air}}} \tag{3.11}$$

With the enthalpy of vaporisation of the fuel $\widetilde{h_{\mathrm{fg}}}$, the molar mass of dry air M_{air} and the molar air fuel ratio R_{AF}. Table 3.2 shows the difference in evaporative cooling for a range of fuels.

Table 3.2. Evaporative cooling of selected fuels at 298.15 K

Fuel	**Evaporative cooling V_{evap} [kJ/kg$_{Air}$]**
Iso-Octane	20.4
n-Heptane	24.1
Toluene	30.9
Ethanol	97.7

The evaporative cooling in this list is largest for ethanol and smallest for iso-octane.

Modelling was performed to investigate to what temperature the fuel has to be heated up to keep it fully vaporized while mixing with cooler air. This process is equivalent to the procedure for calculating the threshold value to avoid condensation with steam (Equations 3.10 – 3.12). However, the heat capacity c_p has to be calculated separately as it depends on the fuel and the stoichiometry. In the following c_p was modelled for a range of different fuels in stoichiometric/rich/lean combustion with air according to Equation 3.12.

$$c_p = K_a + K_b T + K_c T^2 + K_d T^3 \tag{3.12}$$

Where K_a, K_b, K_c, K_d are constants to calculate the isobaric heat capacity [78].

In Figure 3.3, c_p has been plotted for lean/rich heptane combustion and in Figure 3.4, c_p is plotted for different fuels at stoichiometric conditions. It can be seen that $c_{p,mix}$ increases gradually with temperature.

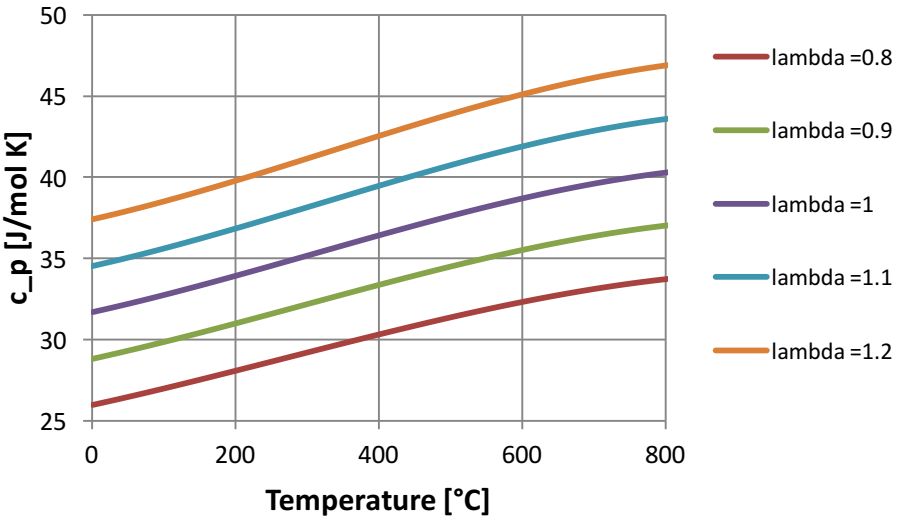

Figure 3.3. Mixture heat capacity $c_{p,mix}$ for n-heptane/air mixtures with different air/fuel ratios.

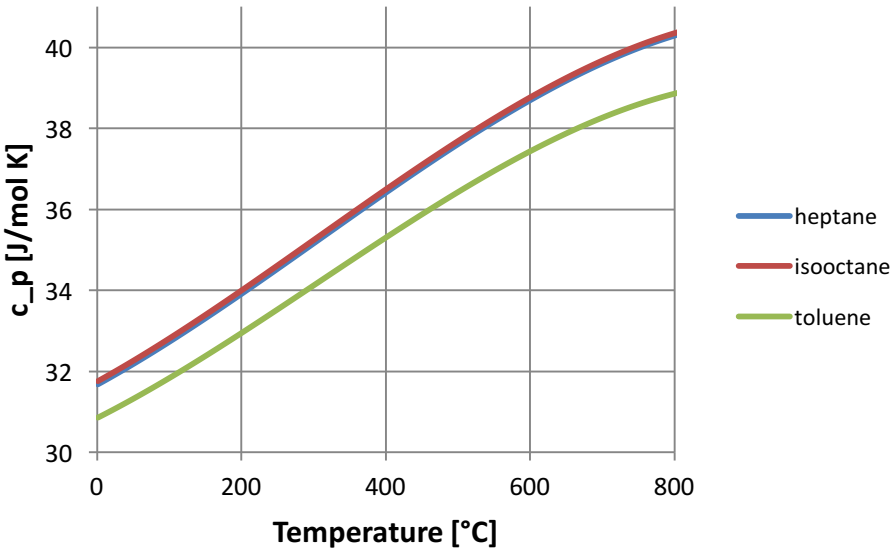

Figure 3.4. Mixture heat capacity $c_{p,mix}$ for different fuels at stoichiometric conditions

With the variation of the heat capacity established, the required vapour temperature to avoid condensation was calculated according to Equation 3.10. The modelling for a range of fuel vapour mass fractions and air temperatures is shown in Figure 3.5.

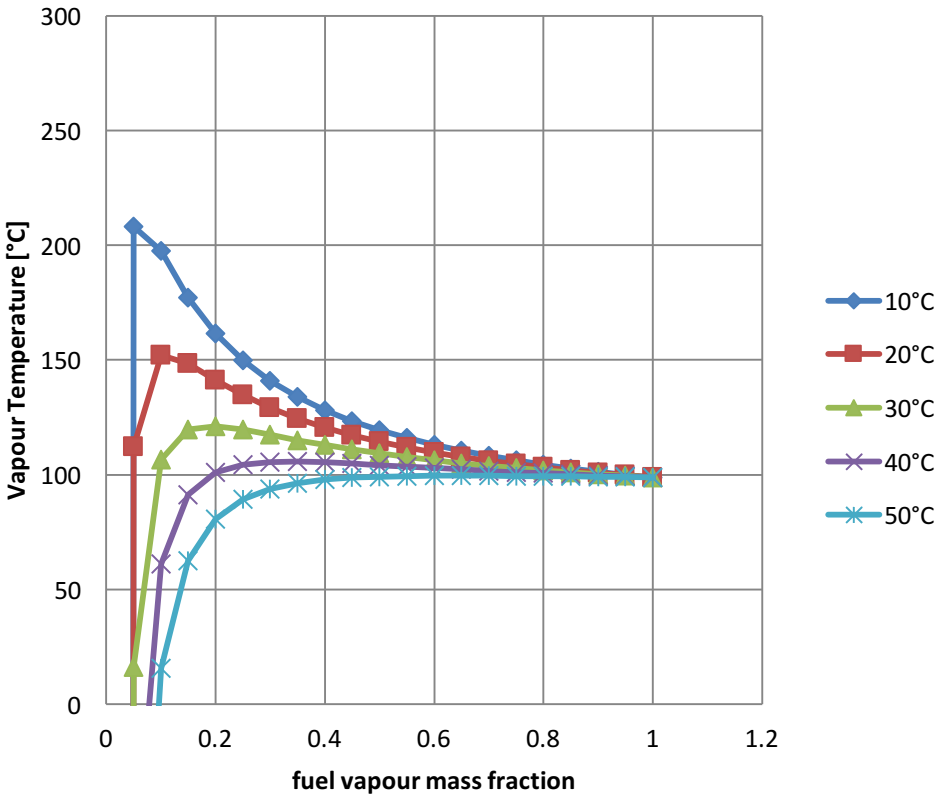

Figure 3.5. Required fuel vapour temperature to avoid condensation with different air temperatures at 1 bar for iso-octane

It can be seen in Figure 3.5 that the higher the air temperature, the lower is the required fuel vapour temperature to avoid condensation. The resulting mixture temperature can be calculated in respect to the air fuel ratio with Equation 3.13.

$$T_m = \frac{c_{pa}\, m_a T_a + c_{pv}\, m_v\, T_v}{c_{pa}\, m_a + c_{pv}\, m_v} \tag{3.13}$$

With $m_v = 1$ and $m_a = \lambda * R_{AF}$

3.3. Experimental Equipment

3.3.1. Humidifier

A humidifying unit to control the humidity of the intake air was constructed and mounted on the air plenum of the E6 engine. A drawing of the unit, mounting equipment and air plenum can be seen in Figure 3.6

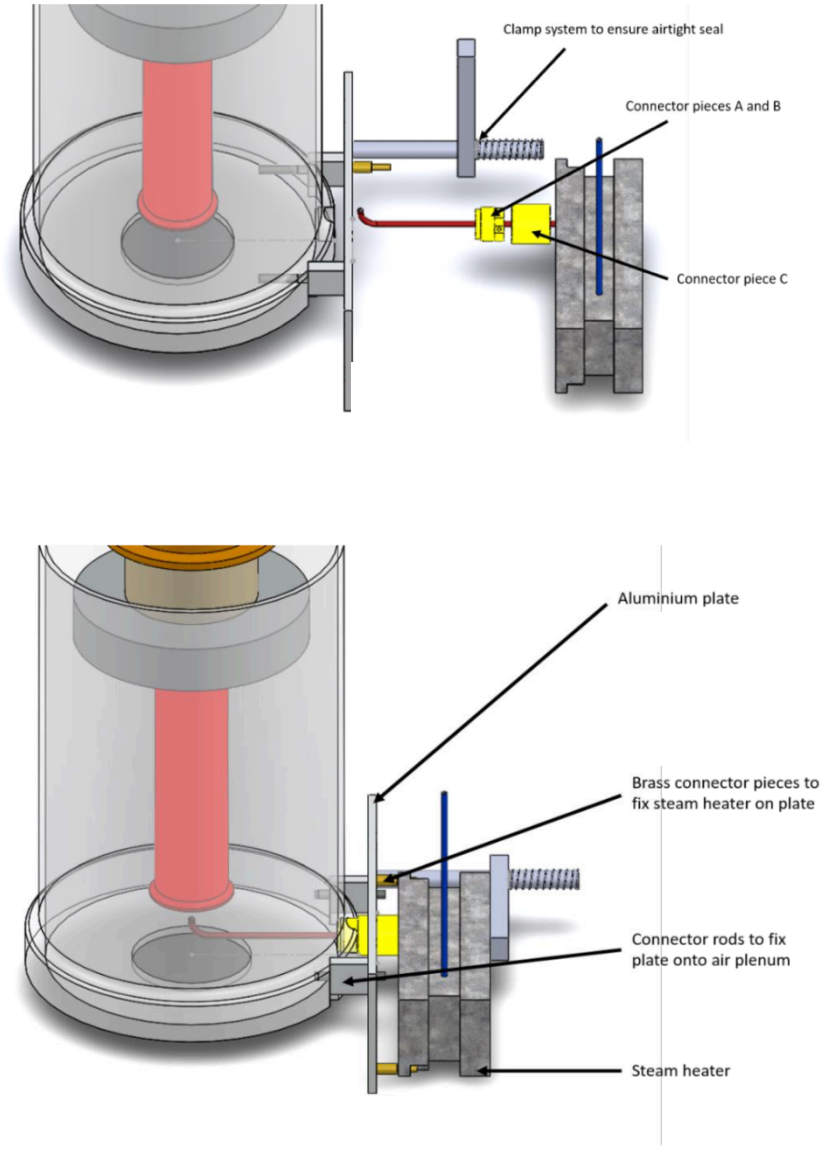

Figure 3.6. Drawings of humidifier/steam heater detached and attached to the air plenum

The humidifying unit can be quickly attached and detached from the air plenum. Two Tufnol connector pieces are screwed together around the output copper pipe (red pipe in Figure 3.6) forming a cylindrical component. Fitted with an outer and inner o-ring, they seal the air plenum when the humidifier is mounted. A clamp system ensures air-tight sealing. This is essential as the humidifying unit has to be warmed up before experiments to ensure vapour-only output and thence to avoid the injection of liquid water into the combustion chamber. When the humidifier is removed, the hole to the air plenum is sealed with a rubber bung.

For the experiments with elevated humidity, the air heater inside the air plenum (large red tube in Figure 3.6) was modified to heat air as it enters the plenum rather than at the exit of the plenum. The deionized water supply for the humidifying unit was secured through a peristaltic pump.

The heater used for the humidifier is a cartridge heater. A flow of water in a copper pipe is heated up sufficiently to evaporate the water into steam. The heater has a power of 450 W. This power was selected as the relative humidity in our experiments was not going to exceed 60% at 50°C. For this experimental condition, we would then require a water flow of 0.1 g/s at an engine speed of Ω = 600 RPM. For steam, at 150°C, this would require a heat of 280 W in the heater, well below our selected heater power.

A peristaltic pump was chosen over other types of pumps because of its high accuracy at small flow rates, resistance to backflow, low maintenance requirements and low susceptibility to contamination. The pump has a power of 24 W and a speed range of 0.1 to 200 RPM can be selected with different tubes in a range of 0.5 to 4.8 mm tube diameter. This allows for a flow range of 0.002 mL/min to 170 mL/min.

It was of great importance that the humidifying unit was emitting a constant flow of steam because an intermittent and pulsating output of steam could have led to poor mixing with the

air and therefore lead to an unstable and unreliable humidity level in the engine. To test this, a schlieren imaging test was performed.

Schlieren photography is a widely used method to visualize flows of fluids. An optical system is used to photograph a flow. The different densities in the flow can be made visible as they lead to gradients in the refractive index n according to Equation 3.14

$$n = 1 + k\rho \tag{3. 14}$$

With the density ρ and Gladstone-Dale coefficient k [79]

The schlieren system relies on a point light source that is used to create a collimated beam that passes through the target flow and subsequently on to a converging lens that focuses the light on a knife edge. The ray curvature then varies according to differences in the refractive indices of the flow. While positive fluid density gradients result in an upwards deflection beyond the peak of the knife edge, a negative fluid density gradient leads to a downward deflection that will be blocked by the knife edge. A camera with a CCD detector behind the knife edge collects the upwards deflected light beams as bright spots while the downward reflected beams leave dark spots on it. A test result for our humidifying unit for a typical output (2.87 mL/min flow at 100°C) can be seen in Figure 3.7.

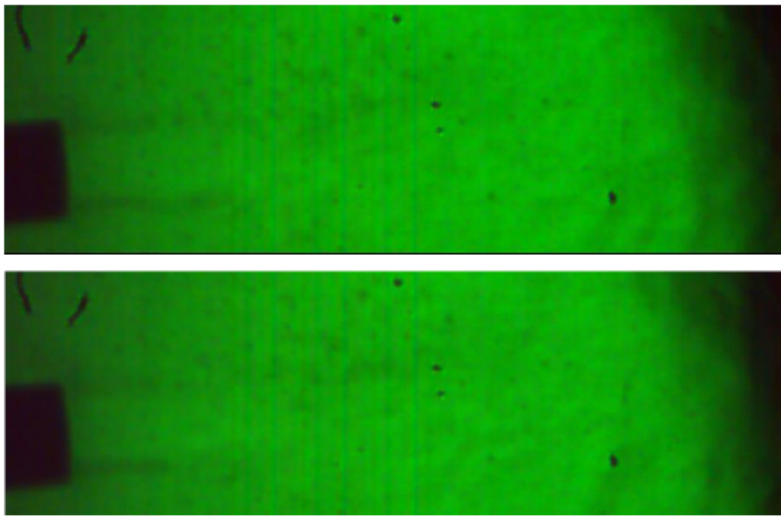

Figure 3.7. Schlieren photographs of the output of the vaporization unit taken at different time points. 2.87 mL/min water supply and saturated steam at 100°C (power of heater: 128 W). For scale: Outside diameter of pipe = 4 mm

The peristaltic pump was also tested for accuracy for two different tube sizes over a range of speeds. The expected flow rates (according to the manual) were compared to the measured flow rates. This can be seen in Table 3.3.

Table 3.3. Testing of the peristaltic pump

Tube bore size (mm)	Pump Speed (RPM)	Expected Flow Rate (mL/min)	Measured Flow Rate (mL/min)	Calculated Error (%)
1.6	26	3.00	2.99	0.33
1.6	148	17.00	17.02	0.12
1.6	200	23.00	23.00	0.00
2.4	49	12.00	12.00	0.00
2.4	98	24.00	24.01	0.04
2.4	151	37.00	36.99	0.02

It can be seen in Table 3.3 that the measured flow rates are nearly identical to the expected flow rate. The maximum calculated error was small (< 0.33%).

For the experiments with elevated humidity, a fixed air-steam mixture temperature of 50°C was selected. Rather than operating at 30°C like in most previous tests, this allowed for a more moderate humidifying unit requirement (Figure 3.1).

3.3.2. Fuel Vaporization Unit

In order to conduct experiments with fully vaporized fuel, the humidifying unit was later adapted for use as a fuel vaporizer. An additional in-line fuel injector was installed at the inlet to the vaporising/humidifying unit (Figure 3.6). The copper pipe leading into the plenum was oriented downwards rather than upwards so as to spray the fuel directly to the combustion chamber. This also meant that the vaporization unit could be used during its warm-up, as any droplets of unvaporised fuel would enter the engine directly. With the original injector still in place, it was now possible to switch between the two types of injector without stopping the engine.

While the heater was used as a humidifying unit it had been controlled with closed-loop PID through LabVIEW. Preliminary fuel vaporization tests showed that this form of control was insufficient to provide a constant flow of fuel vapour. This is because the fuel flow is much smaller and due to the pulsed nature of the injector it was much more periodic than the vapour flow in the humidifier. This led to unstable temperature cycling of the heater between every fuel injection. We therefore decided to control the heater manually with a Variac.

Calculations to estimate the approximate power required to fully vaporize the fuel were performed.

The mass flow m_f of the fuel is described as:

$$m_f = \frac{m_a \, \rho_a}{R_{AF} \, M_f} \tag{3.15}$$

With mass of air m_a, air fuel ratio, R_{AF}, density of the air ρ_a and molar mass of the fuel M_f

The required energy E is given by:

$$E = \Big(H + \big(c_p \, \Delta T\big)\Big) m_f \tag{3.16}$$

With H as enthalpy of vaporization of the fuel, c_p in (MJ/kmol K) and ΔT as the temperature between cold fuel temperature and the temperature at which it evaporates. The Variac was then adjusted to provide a 20% higher heating value, so as to provide a margin for extraneous heat transfer.

3.4. Results and Discussion

3.4.1. Investigation of Engine Operating Point

In this set of experimental sequences the MBT engine operating point (see Chapter 1) was determined for a range of experimental conditions. While the most straightforward way to conduct such an analysis is to run ignition timing sweeps, the hypothesis that it is also possible to determine the ideal engine operating point with a study of the angle of of p_{max} and the angle of the *mfb* was tested in this section.

At first, the *IMEPn* and 0-50%*mfb* were determined for experiments with a range of ignition timings. In this experimental sequence, the effect of a sweep of compression ratio was tested as can be seen in Figure 3.8.

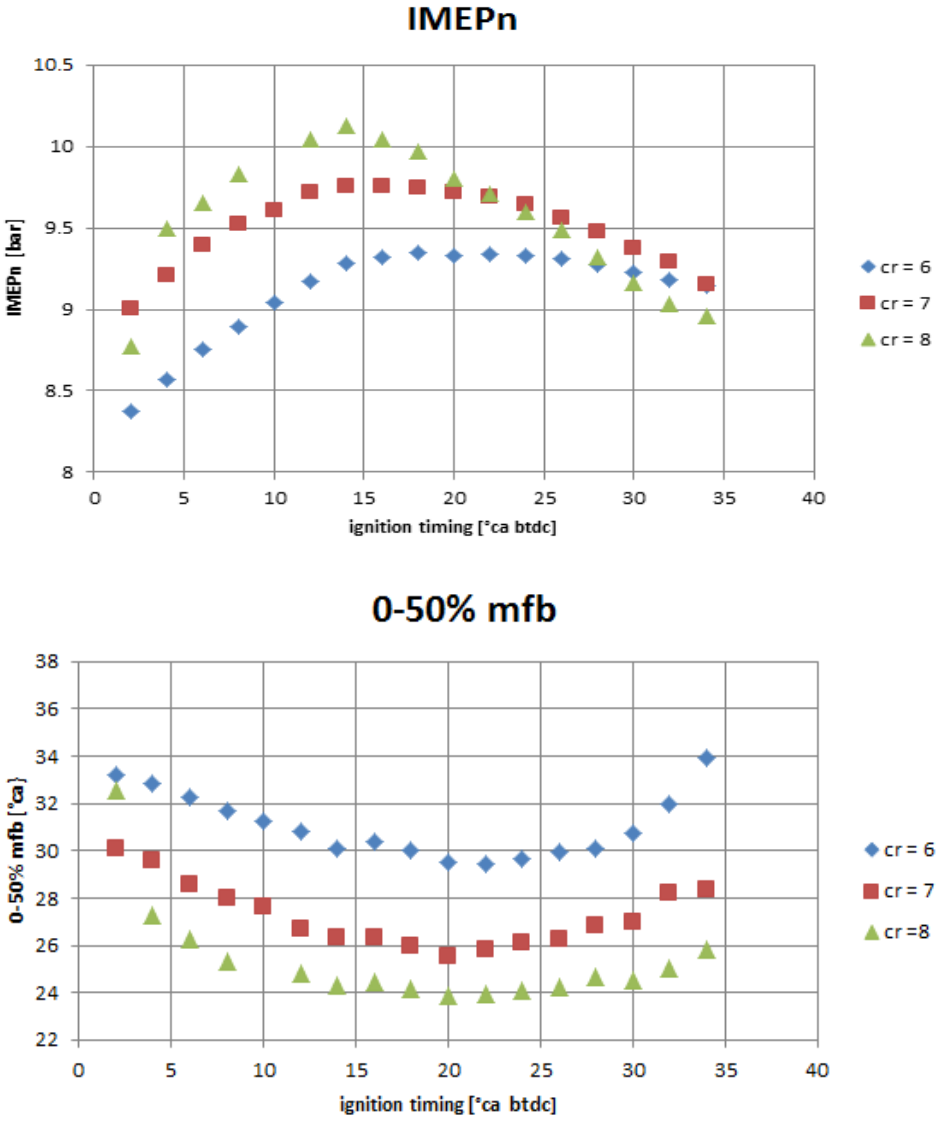

Figure 3.8. Compression ratio sweep. *Fuel: i*so-octane, Θ_i = 2-34°ca bTDC, λ = 1 , τ = 6-8, T_c = 80°C, T_a = 30°C, Ω = 600 RPM

Figure 3.8 shows that as the compression ratio increases, θ_{MBT} is increasingly less advanced and IMEPn is increased. The burn duration decreases with an increasing compression ratio because the associated higher temperature leads to faster combustion. This effect can be seen in Figure 1.3. To explain the shape of the *0-50%mfb* curves, two effects have to be

considered. If the ignition is happening too early, the volume of the combustion chamber is large and the pressure and temperature remain low. This means that the laminar burning velocity is low. If the mixture is ignited too late, the volume is increasing, pressure is falling and the flame is following the piston. Again, this leads to a reduced laminar burning velocity. The fastest combustion therefore occurs in between these two regimes.

In a second experimental sequence, the effect of a sweep of lambda was tested. This is shown in Figure 3.9.

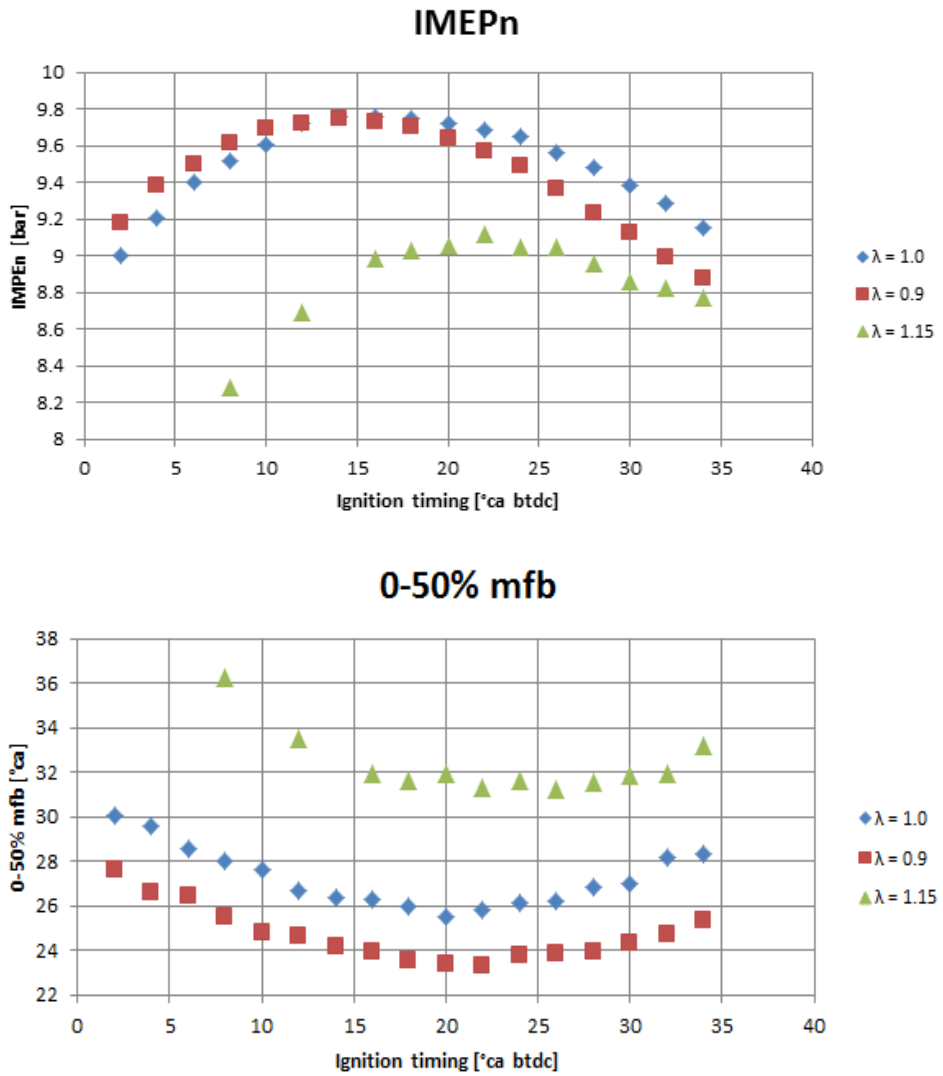

Figure 3.9. Lambda sweeps. *Fuel:* iso-octane, Θ_i = 2-34°ca bTDC, λ = 0.9 – 1.15, τ = 7, T_c = 80°C, T_a = 30°C, Ω = 600 RPM

It can be seen in Figure 3.9 that the rich mixture is burning faster, the *0-50%mfb* is the fastest for the rich mixture ($\lambda = 0.9$) and slowest for weak mixture ($\lambda = 1.15$). This effect is a direct consequence of a change in laminar burning velocities.

COBRA (see Section 2.4) was deployed to analyse the data. The resulting *IMEPn* curves were then taken to determine the *MBT* timing with polynomial fitting. Again, the *MBT* value was calculated as the *IMEPn* value - that is 99.9% of the maximum *IMEPn*. From the *0-50%mfb* curves, the corresponding *0-50%mfb* values at *MBT* ignition timing for the lambda and compression ratio sweeps were calculated.

In Figure 3.10 three *mfb* values are compared over sweeps of ignition timing, compression ratio and lambda.

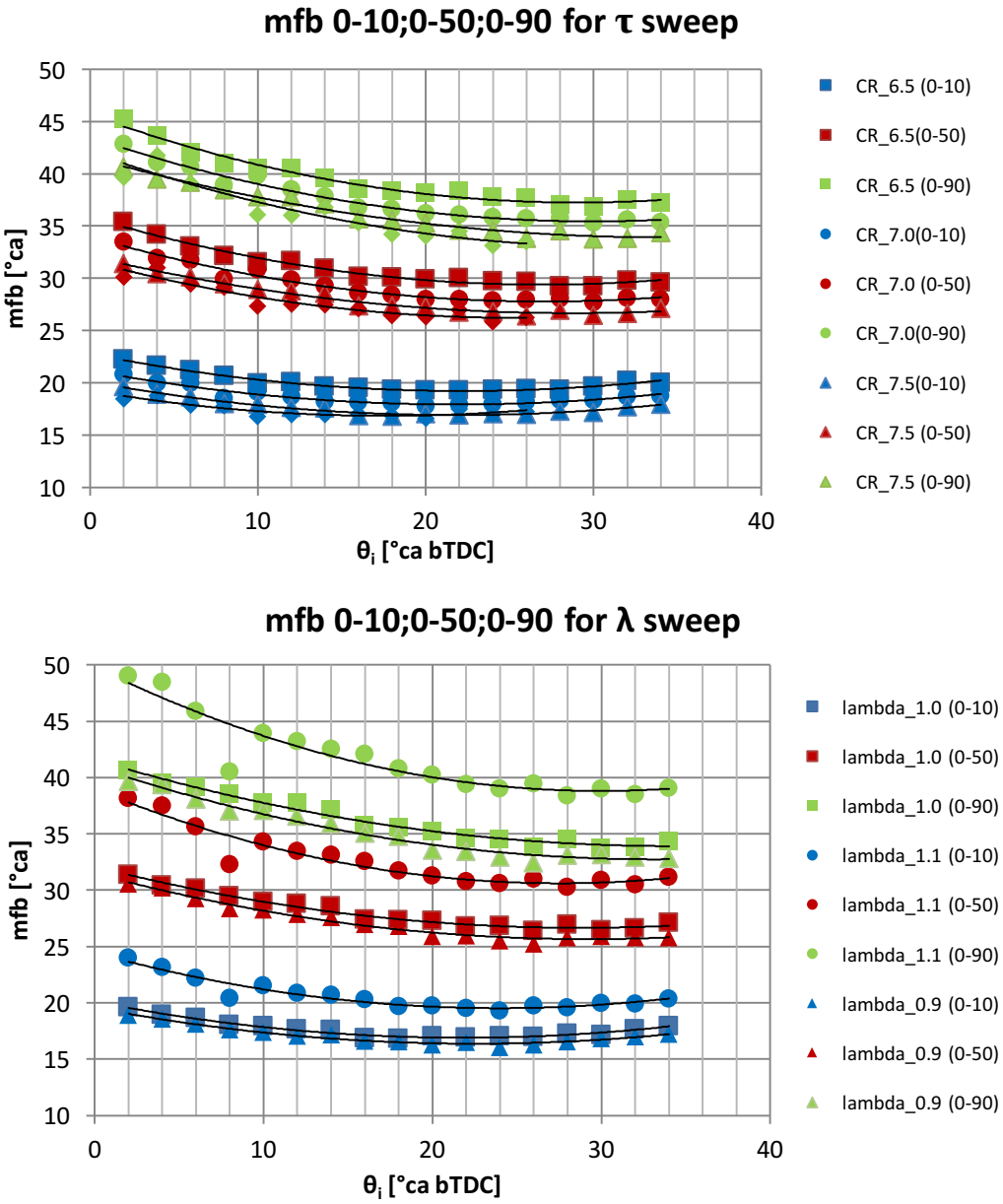

Figure 3.10. *0-10%mfb, 0-50%mfb, and 0-90%mfb* plot of compression ratio (constant λ = 1.0) and Lambda (constant τ = 7.5) sweep. *Fuel:* iso-octane, Θ_i = 2-34°ca bTDC, λ = 0.9 – 1.1, τ = 6.5-7.5, T_c = 80°C, T_a = 50°C, Ω = 600 RPM

Figure 3.10 shows that the trends for the three different *mfb* are displaced laterally for the ignition timing, compression ratio and lambda sweeps. It is therefore a valid assumption that the *0-50%mfb* is representative for the other two indicators. The experiments with τ = 8 could not be run under the same advanced ignition timings as severe knock limited the spark advance.

In the next experimental sequence, additional ignition timing, lambda and compression ratio sweeps were conducted. The lambda sweep covers a wider range and the compression ratio sweep more resolution than the test conducted in the first part of this section. With COBRA, the trends for θ_{Pmax} were calculated and can be seen in Figure 3.11.

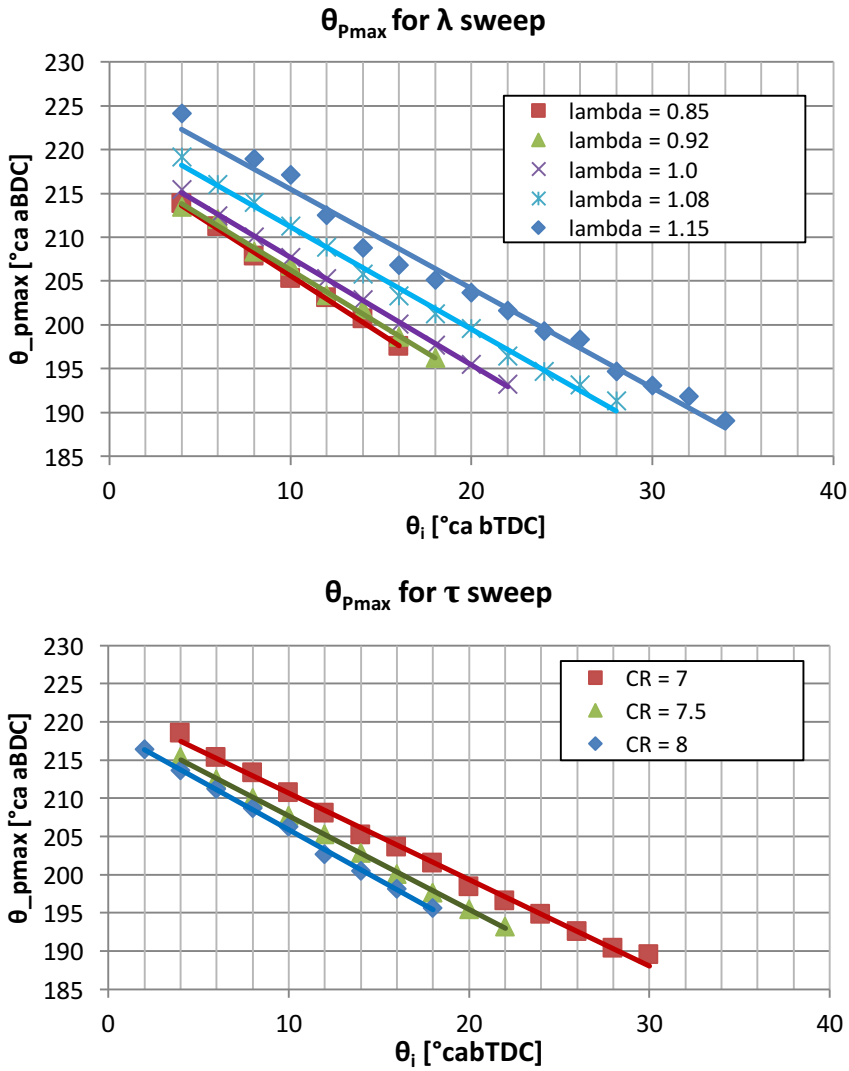

Figure 3.11. Θ_{pmax} [°ca aBDC] plot of compression ratio (λ = 1.0) and Lambda (τ = 7.5) sweeps. *Fuel*: 92% iso-octane + 8% n-heptane, Θ_i = 2-34°ca bTDC, λ = 0.85–1.15, τ = 7-8, T_c = 80°C, T_a = 30°C, Ω = 600 RPM

Figure 3.11 shows that the maximum pressure occurs earlier for richer mixtures and later for weaker mixtures. It also shows that an increased compression ratio leads to an earlier occurrence of the maximum pressure.

In the next step, it was analysed to what degree the information for the *0-50%mfb* and the Θ_{pmax} can be used to identify the ideal engine operating point (MBT) without having to undertake an ignition timing sweep. The results of this are shown in the two subsequent plots.

The first possibility is to aim for a particular angle of p_{max}. The target angle of the p_{max} value is that of the *MBT* igniting timing of the stoichiometric mixture as determined with the ignition timing sweep. The p_{max} values at this target ignition timing are then plotted for the rich and weak mixtures and lines are fitted to them. This can then be compared to the *MBT* data points for the respective rich and weak experiments. The results can be seen for a sweep of compression ratios in Figure 3.12.

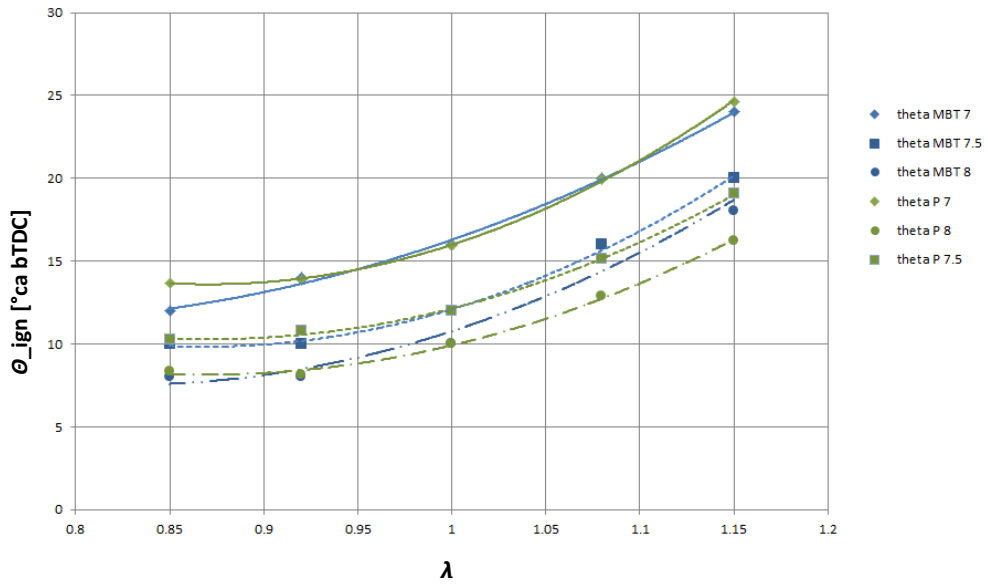

Figure 3.12. MBT and p_{max} ignition timing for τ-sweep. *Fuel*: 92% i-octane, 8% n-heptane. T_c = 80°C, T_a = 50°C, Ω = 600 RPM

Figure 3.12 shows that there is good agreement between the data points and trend lines of the Θ_{pmax} and and MBT points at their respective matching compression ratios. The largest discrepancy is about 2 degrees crank angle. The data points at λ = 1 are, by definition, identical for every compression ratio. The findings suggest that this method can be applied to find the MBT ignition timing and so avoid the lengthy ignition timing sweeps.

The second possible way to identify Θ_{MBT} without the ignition timing sweeps is to aim for a particular θ_{mfb50} (the ignition timing to give a specific *0-50%mfb* angle of occurrence). The target θ_{mfb50} value is the MBT timing of the stoichiometric mixture. The results can be seen in Figure 3.13 which also shows the data from the p_{max} method from Figure 3.12 for comparison.

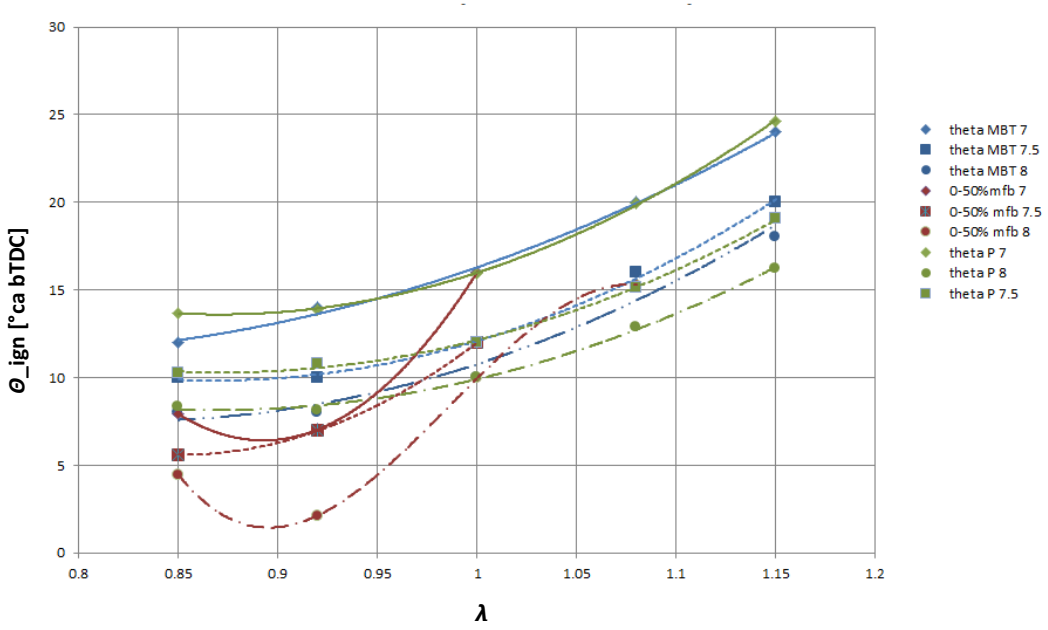

Figure 3.13. *MBT*, p_{max} and *0-50%mfb* ignition timing for τ -sweep. *Fuel*: 92% i-octane, 8% n-heptane. T_c = 80°C, T_a = 50°C, Ω = 600 RPM

The relevant data points for most of the weak experiments could not be calculated. This is because the *mfb* results in convex curves over ignition timing (see Figure 3.10). The target value at the stoichiometric case often lies below these curves for weaker experimental sequences. But independently from that, from the available data in Figure 3.13 it can be seen that fixing the ignition timing for *0-50%mfb* is not a feasible method to estimate MBT timing as the trend lines show poor agreement with the MBT trend lines.

It was therefore decided to disregard the *mfb* method and to proceed with the p_{max} method and test it for a fuel sweep. The fuels are listed in Table 3.4 along with their octane numbers and the compression ratios used for subsequent experiments.

Table 3.4. Fuel compositions. Colours correspond to the data points in the subsequent plots for improved orientation

Fuel #	iso-octane	n-heptane	toluene	ethanol	RON	MON	τ
1	100	0	0	0	100	100	9
2	92	8	0	0	92	92	8
3	20	20	60	0	92	80	9
4	80	20	0	0	80	80	7.5
5	18	18	54	10	-	-	9

Compression ratios for these experiments were selected to cause knocking combustion at moderate ignition timings. The results for the fuel sweep with the p_{max} method are shown in Figure 3.14. An average value between the two calculated MBT ignition timings for every fuel and stoichiometry was formed and trend lines fitted. This allows for a more straightforward overview of the data in a single plot.

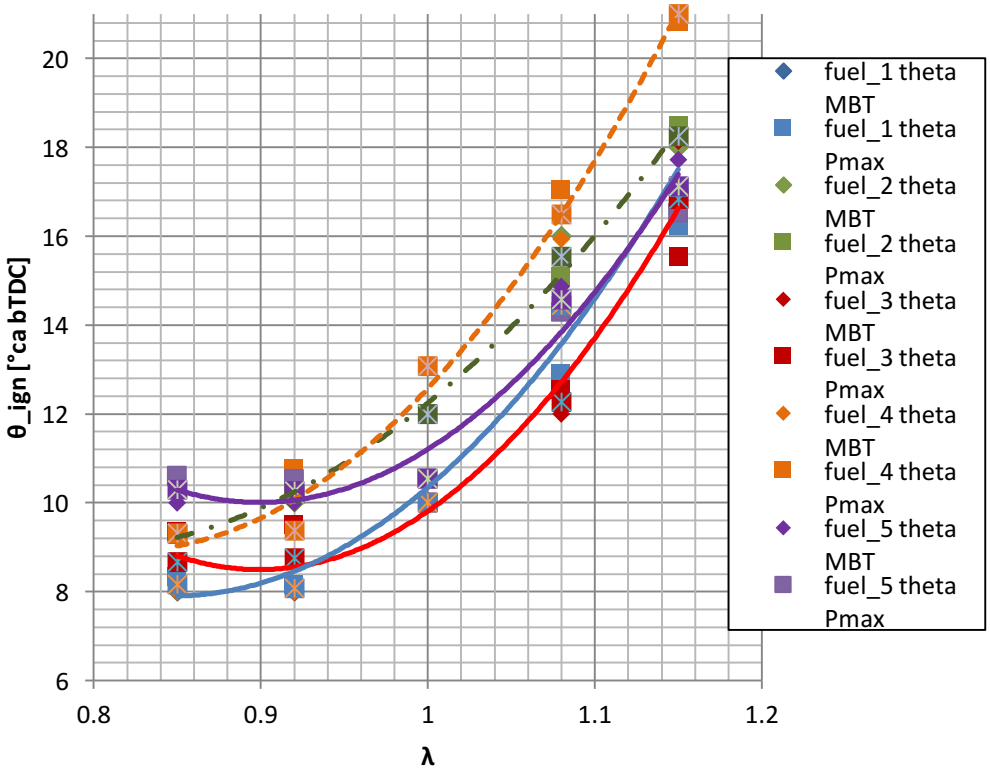

Figure 3.14. Fuel compositions and compression ratios as defined in Table 3.4. Trend lines fitted for mean of Θ_{MBT} *and* Θ_{Pmax}. Dashed lines to indicate different compression ratios. Θ_i = 2-34°ca bTDC, λ = 0.85– 1.15, τ = 7.5-9, T_c = 80°C, T_a = 30°C, Ω = 600 RPM

As in Figure 3.12, the angle for θ_{Pmax} has been found for the stoichiometric mixtures in Figure 3.14, and this angle has then been used as the target value for p_{max} by varying the ignition timing. It can be seen from Figure 3.14 that the two calculated MBT ignition timings show good agreement for most fuels and levels of stoichiometry. In no instance are two data points more than 2 degrees crank angle apart. The plot further shows that at stoichiometric conditions there is a large difference in the MBT ignition timings depending on the fuel and compression ratio used. This is further influenced by knock which will be analysed more in Section 3.4.2.

The hypothesis that it is also possible to determine the ideal engine operating point with a study of the angle of of p_{max} or the angle of the *0-50%mfb* was tested in this section. While good agreement was found when using the p_{max} method, the method was not found to be precise enough for further studies. Only if an agreed schedule of ignition timings as a function of compression ratio for every fuel could be agreed on might this method be used.

3.4.2. Engine Knock - Fundamental Tests

In this section, the engine was deliberately run at conditions that initiated auto-ignition and knock. The three knock indicators that were outlined in Equations 3.1 – 3.5 were tested for a range of experimental conditions and efforts undertaken to compare them to each other to be able to continue the analysis with a single representative knock indicator.

For an ignition timing and lambda sweep, the knock parameters MAPO, IMPO and LKI are shown in Figure 3.15.

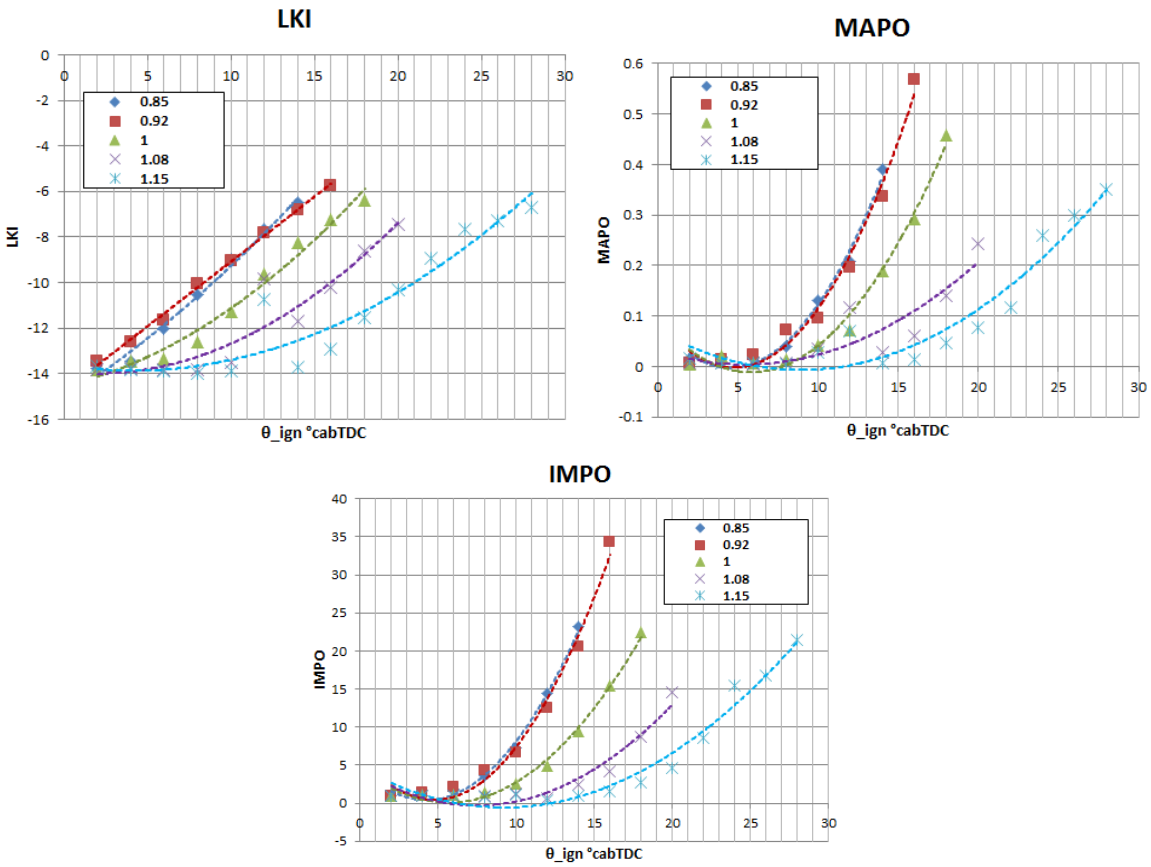

Figure 3.15. Plots for *LKI*, *MAPO* and *IMPO* for an ignition timing and lambda (in legend) sweep. *Fuel*: 92% iso-octane + 8% n-heptane, Θ_i = 2-34°ca bTDC, λ = 0.85–1.15, τ = 7.5, T_c = 80°C, T_a = 30°C, Ω = 600 RPM

It can be seen from Figure 3.15 that the knock data shows clear trends only beyond a certain threshold. Cycles below this threshold can be considered as non-knocking. Several different thresholds were considered for the three knock indicators. Two sets of thresholds (*IMPO* = 2.5, *LKI* = -11.3, *MAPO* = 0.05 and *IMPO* = 5, *LKI* = -11, *MAPO* = 0.1) are shown in Figure 3.16 for comparison. Figure 3.16 also shows the data points and trend lines for an average of the ignition timings of the knock thresholds as well as data points and trend lines for the MBT ignition timings for the respective lambdas. MBT occurs before the second set of knock thresholds and the engine is thus limited by knock.

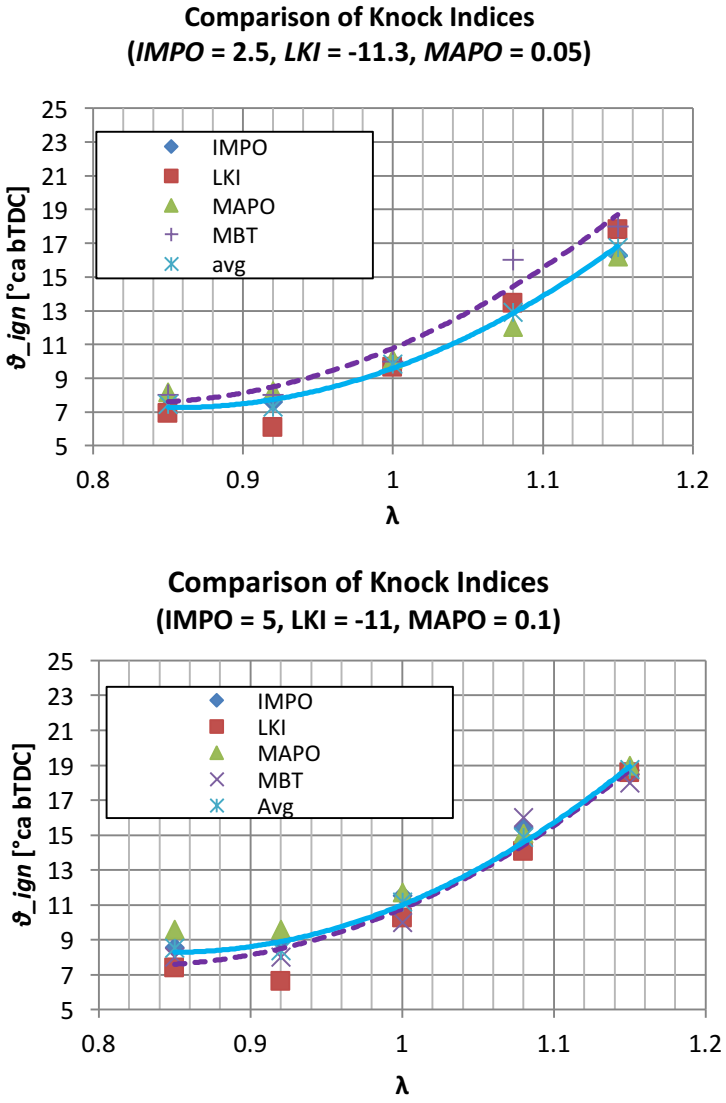

Figure 3.16. Comparison of knock indices. Broken lines represents *MBT* data, continuous lines represent averages of ignition timings at the knock threshold. *Fuel*: 92% iso-octane + 8% n-heptane, Θ_i = 2 -34°ca bTDC, λ = 0.85– 1.15, τ = 7.5, T_c = 80°C, T_a = 30°C, Ω = 600 RPM

Figure 3.16 shows that with suitably selected knock thresholds, there is very good agreement between the KLSA ignition timings using the three knock indicators, and that this holds at different levels of knock intensity. We therefore proceeded to mostly rely on using the LKI to determine the severity of knock in subsequent experiments. As a threshold for knock onset a *LKI* of -11.3 (*IMPO* = 2.5, *MAPO* = 0.05) was selected.

The comparison of the data points for the average knock ignition timing and the data points for MBT show a difference in the two plots of Figure 3.16. In the first set of knock thresholds (*LKI* = -11.3) the average knock timing is less advanced than the MBT. In the second plot (*LKI* = -11) the average knock timing is nearly identical to the MBT timing and with the rich mixture the MBT ignition timing is less advanced than the knock threshold. This means that, according to our definition, the engine was limited by knock for rich experiments when the threshold factor (*LKI* = -11) was deployed.

To better illustrate how the engine can be limited by knock, Figure 3.17 is a plot of both the IMEPn and the LKI data for an ignition timing and lambda sweep.

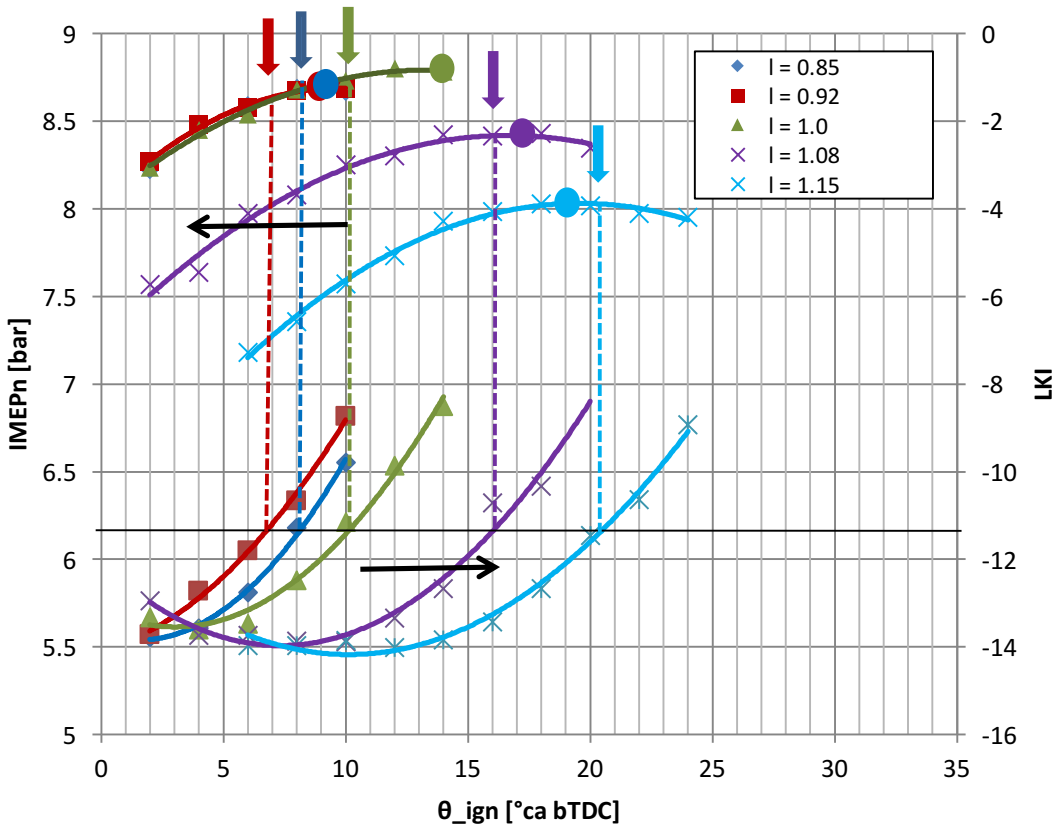

Figure 3.17. Plots of IMEP and LKI. Circles to indicate Θ_{MBT}, arrows to indicate KLSA for *LKI* = -11.3. *Fuel*: 92% iso-octane + 8% n-heptane, Θ_i = 2-34°ca bTDC, λ = 0.85– 1.15, τ = 7.5, T_c = 80°C, T_a = 30°C, Ω = 600 RPM

In Figure 3.17 it can be seen that the weaker the mixture, the lower the IMEPn and the less prone to knock is the engine. MBT is reached at 99.9% of the maximum IMEPn. Defining the onset of knock at *LKI* = -11.3, knock occurs at or just before MBT and the engine is therefore limited by knock under these experimental conditions.

The other fuels and experimental conditions listed in Table 3.4 were further analysed for their knock tendency and operating point for a sweep of lambda. Figure 3.18 contains plots holding information about the Θ_{MBT} and Θ of the knock threshold (LKI and IMPO).

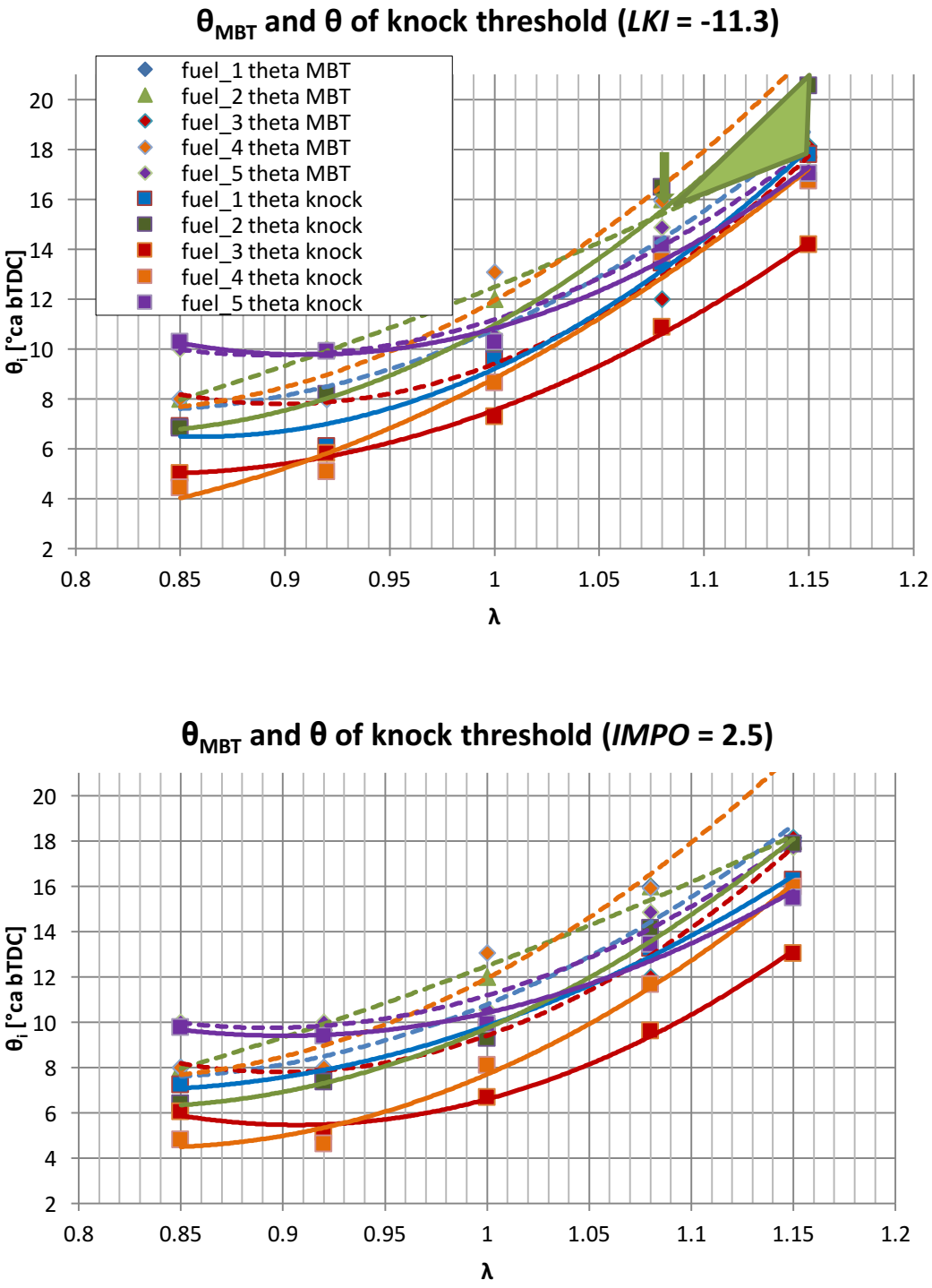

Figure 3.18. Comparison of Θ_{MBT} (dashed lines) and Θ of knock threshold (LKI and IMPO; continuous lines), green area to indicate knock limitation, Θ_i = 2-34°ca bTDC, λ = 0.85 – 1.15, T_c = 80°C, T_a = 30°C, Ω = 600 RPM

It can be seen in Figure 3.18, that with one exception, for every experiment the dotted Θ_{MBT} trend lines lie above the continuous trend lines for the angle of knock. This means that the

knock thresholds were reached after MBT and the engine was therefore not limited by knock. The green area in the LKI plot is a notable exception and indicates limitation by knock for fuel 2 in the weak area. The green arrow indicates the *KLSA*. The weak mixture is burning more slowly and this allows for auto-ignition mechanisms to start. For a weaker mixture and for a given pressure, the temperature in the unburned gas is higher. That said, p_{max} is lower compared to a richer mixture and the question is whether the auto-ignition or the flame propagation mechanism is prevalent.

3.4.3. The Effect of Humidity on the Engine Operating Point and on Knock

For the next section of experiments, the engine was equipped with the humidifying unit as described in Section 3.2. In a first experimental sequence, a compression ratio sweep at stoichiometric conditions was performed for a range of ignition timings and two levels of humidity. These were the dry 0.005 kg/kg (‘off’) humidity of the engine lab and the wet, humidifier-elevated 0.05 kg/kg (‘on’) humidity. In Figure 1.19 both the IMEPn (left axis) and the LKI (right axis) were calculated.

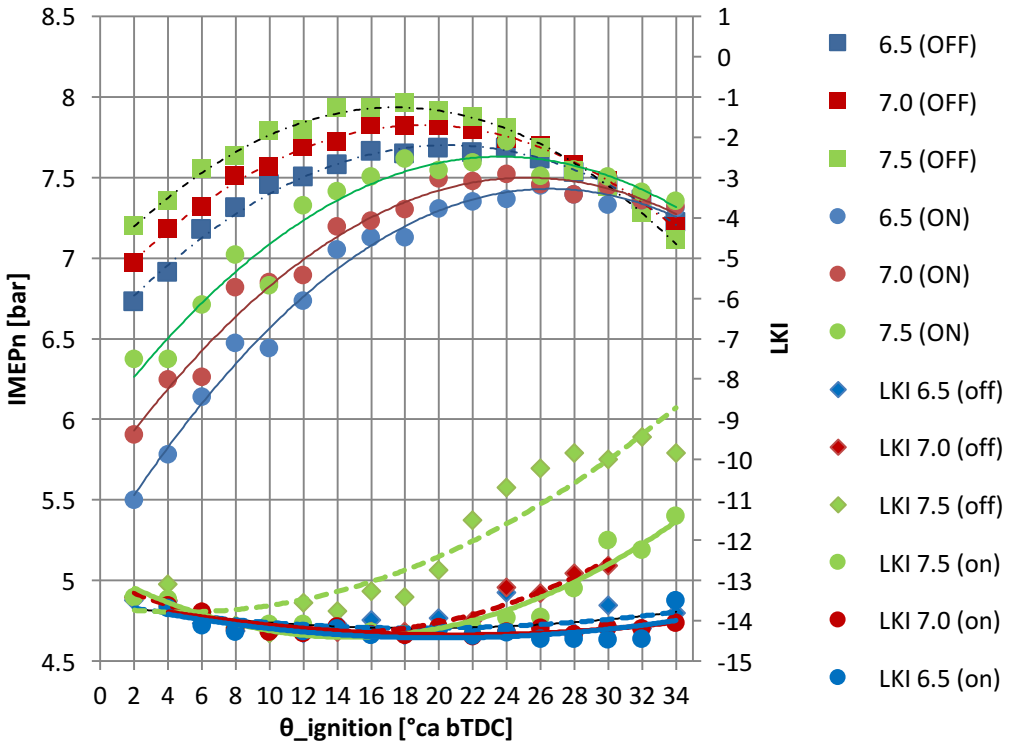

Figure 3.19. Compression ratio sweep. *Fuel:* iso-octane, Θ_i = 2-34°ca bTDC, λ = 1.0, τ = 6.5-7.5, T_c = 80°C, T_a = 50°C, Ω = 600 RPM, humidity: 0.005 kg/kg ('off'), 0.05 kg/kg ('on')

It can be seen that the experiments with low humidity showed a higher IMEPn compared to the tests with elevated humidity. This is because more air can enter the engine when the inlet stream is not diluted with the steam from the humidifier. More air in the engine chamber allows for more fuel and hence a higher IMEPn. The theoretical reduction in IMEPn at MBT for the experiment with increased humidity is 7%. The measured reduction in IMEPn was found to be between 5-7% for the three compression ratios tested here. It can further be seen that there is more scatter in the data with the increased humidity and this was attributed to the unsteady, pulsating flow of the air/steam.

Knock remains low in this experimental sequence. The engine operating points were not limited by knock. Only for the highest compression ratio and most advanced ignition timings does a trend become visible. It can be seen that the knock intensity is much smaller for the

experiments with increased humidity. Humidity here has a significant effect on reducing knock.

In the next experimental sequence, a lambda ratio sweep at a fixed compression ratio ($\tau = 7.5$) was performed for a range of ignition timings and two levels of humidity. These were the dry 0.005 kg/kg ('off') humidity of the engine lab and the wet, humidifier-elevated 0.05 kg/kg ('on') humidity. Both IMEPn and LKI were calculated and plotted in Figure 3.20.

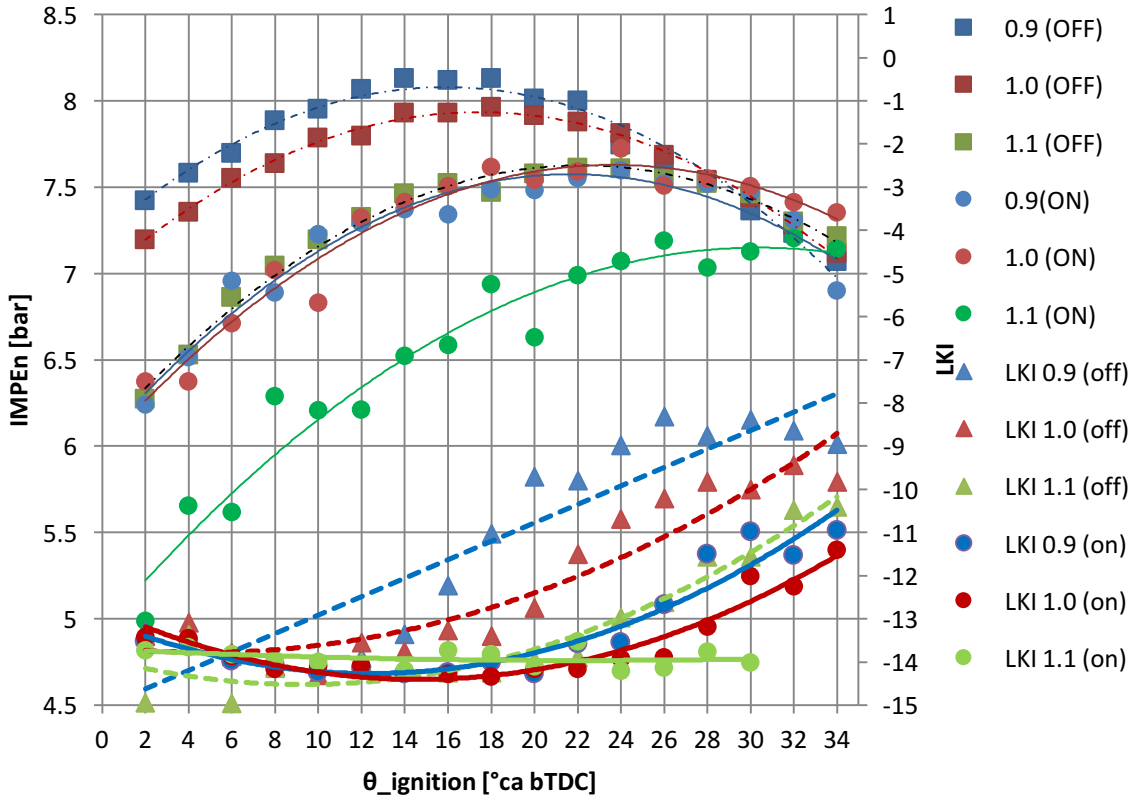

Figure 3.20. IMEPn plot of Lambda sweep. *Fuel*: iso-octane, Θ_i = 2-34°ca bTDC, λ = 0.9 – 1.1, τ = 7.5, T_c = 80°C, T_a = 50°C, Ω = 600 RPM, humidity: 0.005('off'), 0.05 ('on')

The findings for the lambda sweep are similar to the findings from the compression ratio sweep in Figure 3.19. An increased humidity decreases IMEPn. Unsurprisingly, this is

particularly pronounced for the experiment with the weak mixture which requires the most air. This data set further provides the least smooth curve.

Knock was found to be significantly smaller for the experiments conducted with increased humidity. The operation with humid air required a significantly more advanced ignition timing for MBT.

In a next step, the effect of humidity on the mass fraction burned was analysed. Firstly, the *0-50%mfb* was calculated and plotted for both the compression ratio and lambda sweep from figures 3.19 und 3.20. The results are plotted in Figure 3.21 and 3.22.

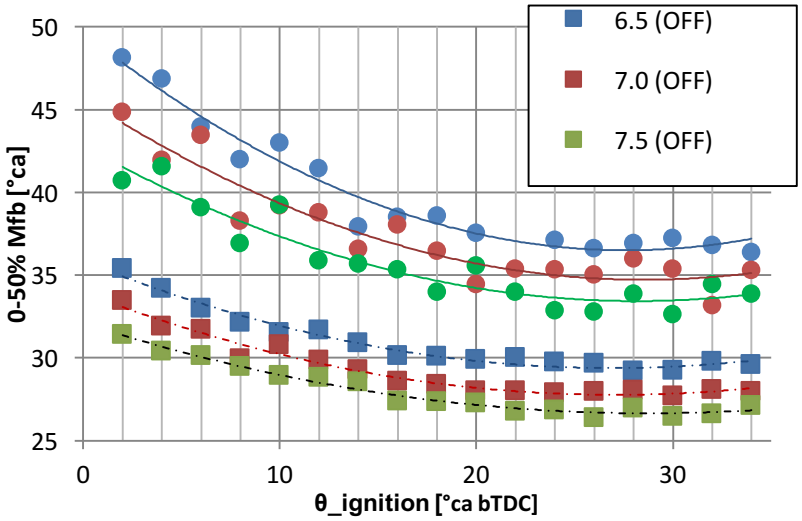

Figure 3.21. *0-50%mfb* plot of compression ratio sweep. *Fuel:* iso-octane, Θ_i = 2-34°ca bTDC, λ = 1.0, τ = 6.5-7.5, T_c = 80°C, T_a = 50°C, Ω = 600 RPM, humidity: 0.005(‘off’), 0.05 (‘on’)

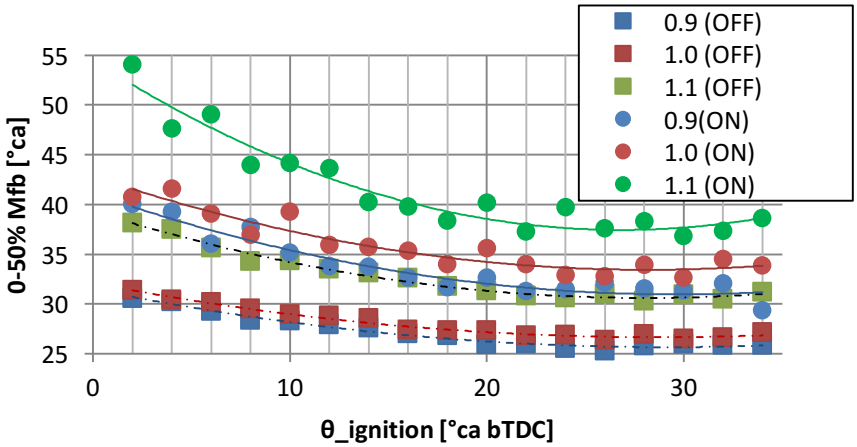

Figure 3.22. *0-50%mfb* plot of Lambda sweep. *Fuel*: iso-octane, Θ_i = 2-34°ca bTDC, λ = 0.9 –1.1, τ = 7.5, T_c = 80°C, T_a = 50°C, Ω = 600 RPM, humidity: 0.005('off') - 0.05 ('on')

It can be seen from Figure 3.21 and 3.22 that the elevated humidity in one half of the experimental sequences increased the duration of the *0-50%mfb* significantly. This was again especially pronounced for the weak mixture. The higher heat capacity of the moist air that enters the engine leads to a lower flame temperature and slower combustion.

The θ_{MBT} and *0-50%mfb* at θ_{MBT} are plotted in Figure 3.23 for the compression ratio sweep.

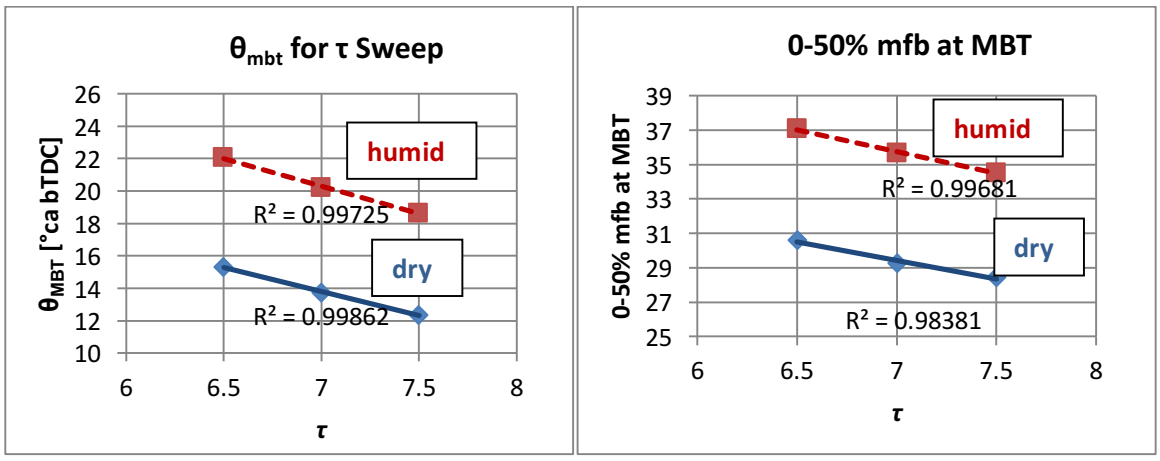

Figure 3.23. 0-50% Mfb and θ_{MBT} plot of compression ratio sweep. *Fuel:* iso-octane, Θ_i = 2-34°ca bTDC, λ = 1.0, τ = 6.5-7.5, T_c = 80°C, T_a = 50°C, Ω = 600 RPM, humidity: 0.005('dry') - 0.05 ('humid')

It can be seen that there is a linear negative trend for both plots. The larger the compression ratio, the less advanced is the ignition timing for MBT, and the smaller is the duration of the *0-50%mfb*. It can be concluded that MBT is reached at a much more advanced ignition timing for an elevated humidity and that in this case the *0-50%mfb* will be much higher at MBT. This is independent of the compression ratio and has an important implication when knock is considered. While the increased humidity reduces knock, if the engine is to be operated at MBT then some of this reduction is lost due to the more advanced ignition timing of the humid MBT. This is illustrated with the orange lines in Figure 3.24.

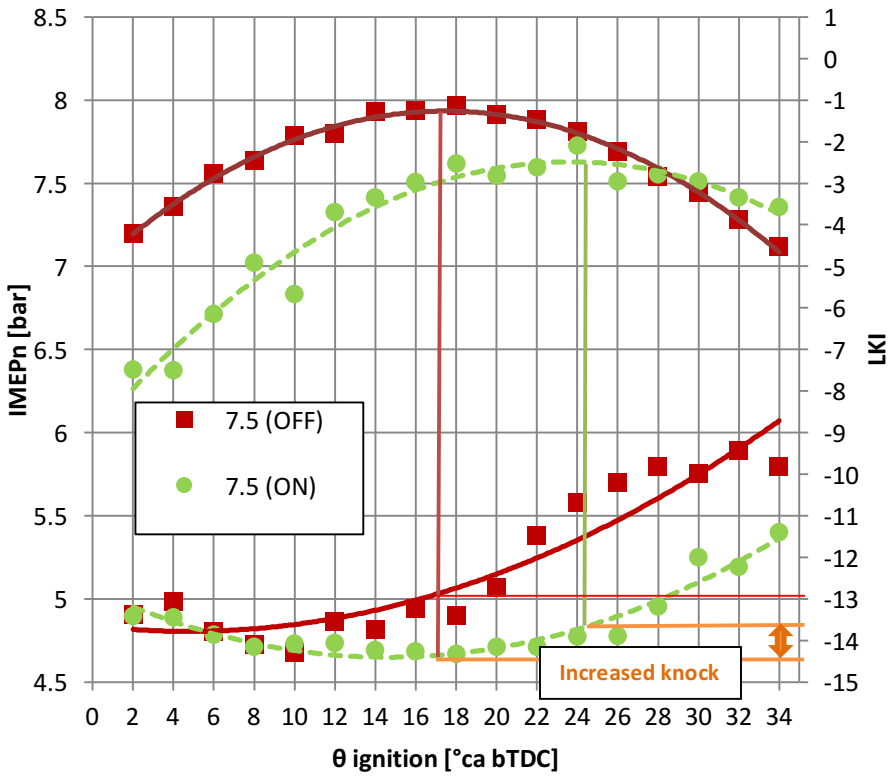

Figure 3.24. Humidity sweep with indication in 'loss of knock reduction'. *Fuel:* iso-octane, Θ_i = 2-34°ca bTDC, λ = 1.0, τ = 7.5, T_c = 80°C, T_a = 50°C, Ω = 600 RPM, humidity: 0.005 kg/kg ('off'), 0.05 kg/kg ('on')

Figure 3.25 shows θ_{MBT} and *0-50%mfb* at θ_{MBT} for the lambda sweep.

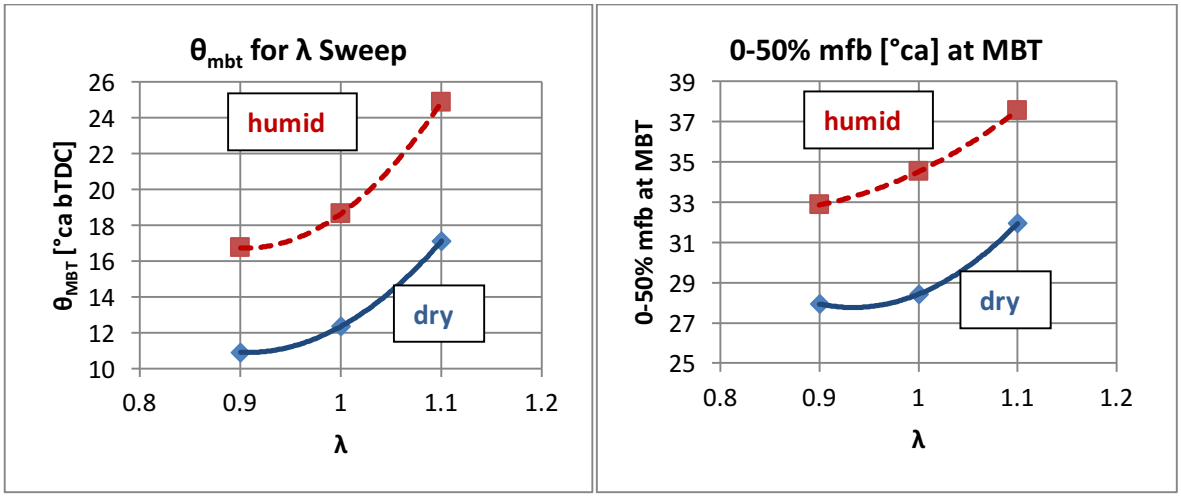

Figure 3.25. *0-50%mfb* and θ_{MBT} plot of Lambda sweep. *Fuel*: iso-octane, Θ_i = 2-34°ca bTDC, λ = 0.9 – 1.1, τ = 7.5, T_c = 80°C, T_a = 50°C, Ω = 600 RPM, humidity: 0.005('dry') - 0.05 ('humid')

Figure 3.25 shows that the ignition timings for MBT and the duration of *0-50%mfb* have an exponential dependence on lambda. The richer the mixture, the less advanced is the ignition timing for MBT and the smaller is the duration of the *0-50%mfb*. The humidity trends are analogous to the trends with the compression ratio as outlined in Figure 3.23.

The experiments described here depend on extensive ignition timing sweeps to find the engine operating point. As described in Section 3.4.1, the crank angle of the maximum cylinder pressure can be used to set the MBT ignition timing. Figure 3.26 outlines this p_{max} method to find MBT for a sweep of humidity.

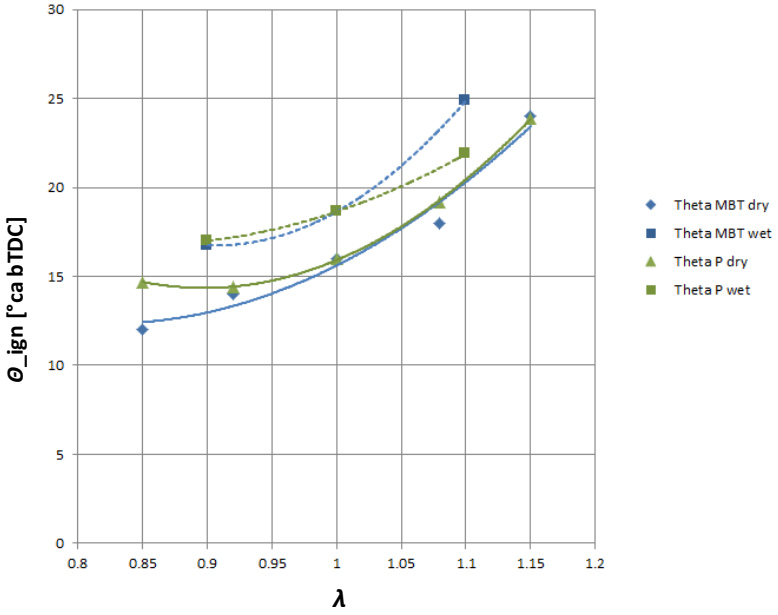

Figure 3.26. MBT and p_{max} ignition timing for humidity sweep. *Fuel*: iso-octane. T_c = 80°C, T_a = 50°C, Ω = 600 RPM, τ = 7.5 humidity: 0.005 kg/kg ('dry') - 0.05 kg/kg ('wet')

It can be seen in Figure 3.26 that the p_{max} method is a valid alternative to an ignition timing sweep. The data points for the rich mixture are nearly identical with those calculated from the ignition timing sweep. The weak mixture data points are 3°ca apart and this can be attributed to the scatter in the data as seen in Figure 3.20.

3.4.4. The Effect of Vaporised Fuels on the Engine Operating Point and on Knock

In this section, the vaporization unit (as described in Section 3.3) was used to fully vaporize the fuel before the injection into the engine. A range of iso-octane/ethanol blends was tested alongside pure iso-octane and ethanol. The fuels were tested for a range of knock-relevant ignition timings under both liquid and fully vaporized fuel conditions. The results can be seen in Figure 3.27.

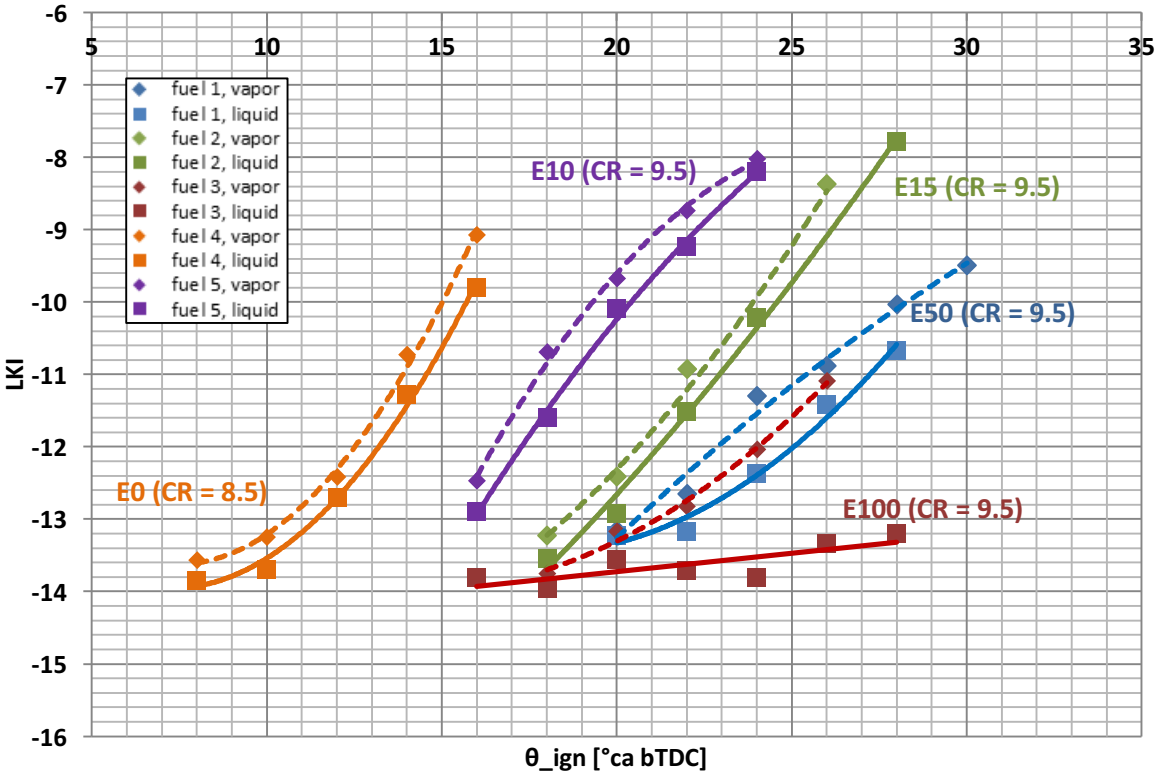

Figure 3.27. LKI plot of ignition timing and fuel sweep and effect of vaporization of fuel. Squares and solid lines for liquid fuels, diamonds and broken lines for vaporized fuels. *Fuel*: Iso-octane/ethanol blends, Θ_i = 8-30°ca bTDC, λ = 1.0, τ = 8.5-9.5, T_c = 80°C, T_a = 50°C, Ω = 600 RPM.

It can be seen in Figure 3.27 that the higher the ethanol content of the tested fuel, the less prone to knock is the fuel. This is illustrated by a shift to the right hand side of the plot where more advanced ignition timings are required to achieve the same knock characteristics as a fuel with a lower or no ethanol content. Further, it can clearly be seen in Figure 3.27 that when a given fuel is vaporized, the knock intensity is increased. Both results have been expected as the cooling effect of the enthalpy of vaporization decreases the knocking tendency of an injected liquid fuel. If the fuel has been vaporized before injection, this effect disappears and from Figure 3.27 it can be concluded that this approximately has the same positive effect on knock as advancing the ignition timing by 1°ca for low ethanol content (0-15%) and significantly more for higher ethanol contents (50-100%). Note that the iso-octane

tests had to be conducted at a reduced compression ratio. The findings ion Figure 3.27 are further summarized in Figure 3.28 where the ignition timing at the knock threshold (*LKI* = -11.3) has been plotted against ethanol content of the fuels.

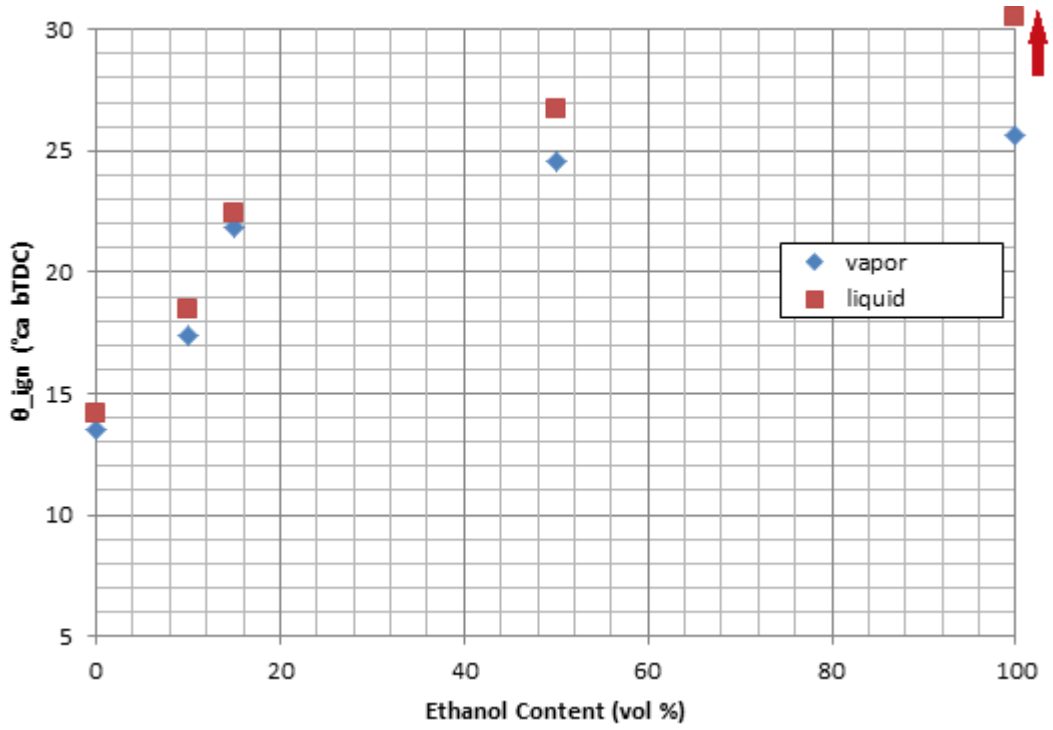

Figure 3.28. Ignition timing at knock threshold (*LKI* = -11.3) of fuel sweep. *Fuel*: Iso-octane/ethanol blends, $\lambda = 1.0$, $T_c = 80°C$, $T_a = 50°C$, $\Omega = 600$ RPM.

The liquid fuels and fuel blends tested in Figure 3.27 were analysed for their mixture temperature before entering the engine. The results are shown in Figure 3.29.

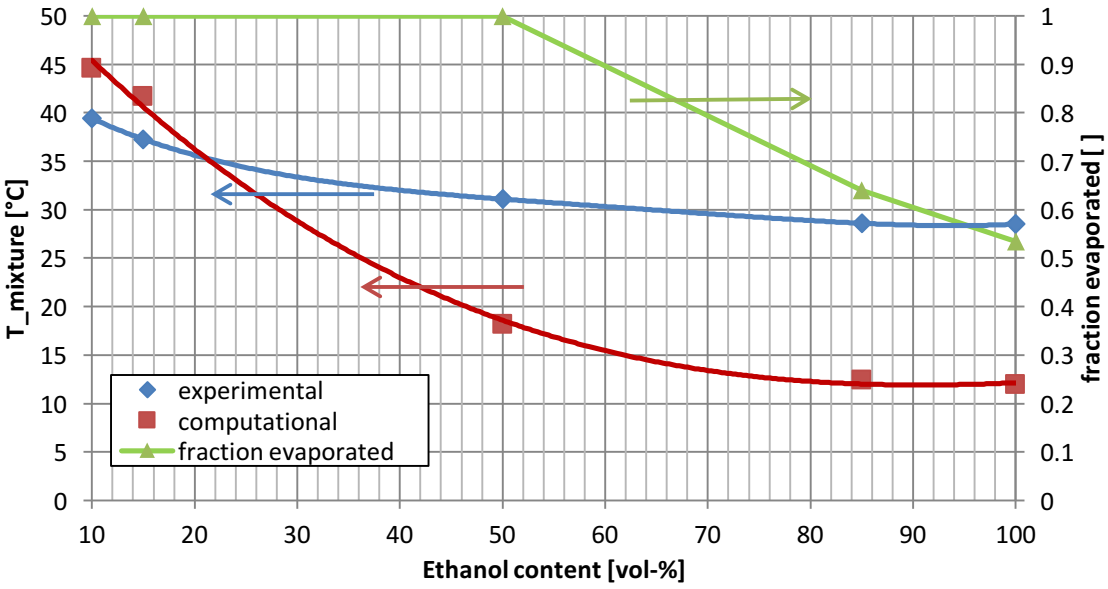

Figure 3.29. Mixture temperature of fuel sweep. *Fuel*: iso-octane/ethanol blends, $\lambda = 1.0$, $T_c = 80°C$, $T_a = 50°C$, $\Omega = 600$ RPM.

It can be seen in Figure 3.29 that the measured mixture temperature decreases with an increase in ethanol content. The reason for this is the increasing enthalpy of vaporization and its cooling effect on the mixture.

The temperature of the mixture was also calculated assuming that the ethanol component fully evaporates. However, with an initial air temperature of $T_a = 50°C$ and a fuel temperature of $T_f = 20°C$ it was found that fuels with higher levels of ethanol do not fully evaporate. The partial pressure of the fuel exceeds the saturation pressure. This is indicated in Figure 3.29 with the fraction evaporated data on the secondary axis.

In the next test, the effect of a sweep of compression ratio was analysed for a 90% iso-octane, 10% ethanol blend (E10). The results for knock intensity and IMEPn can be seen in Figure 3.30.

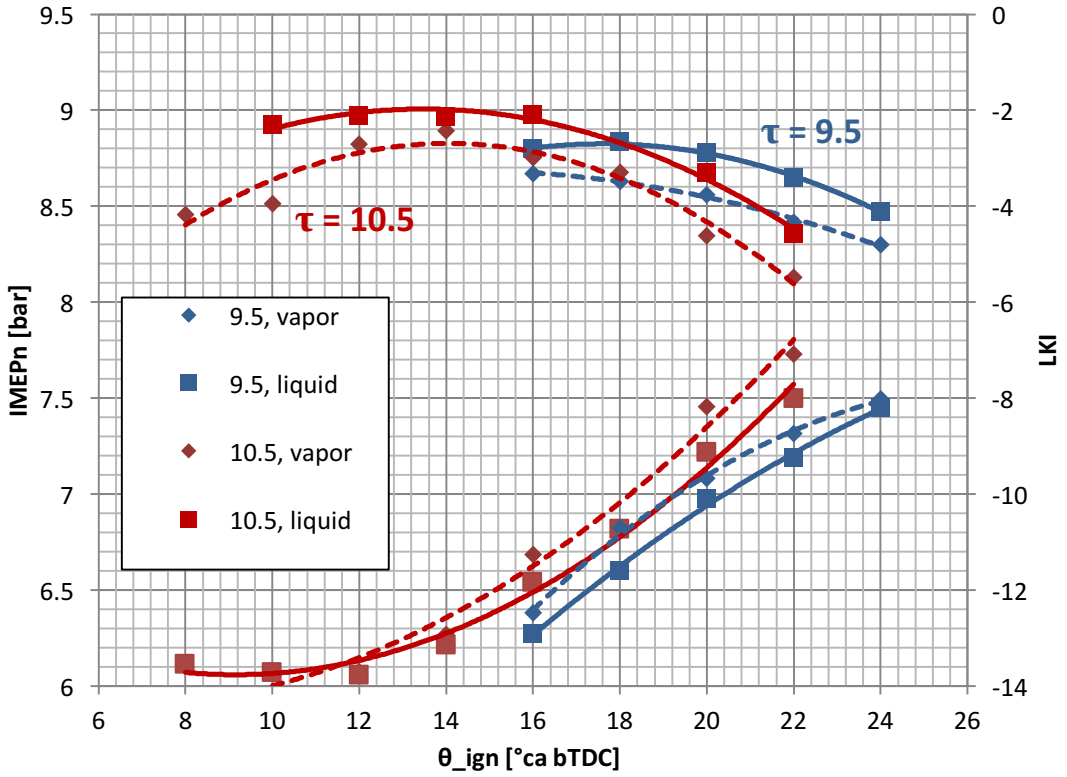

Figure 3.30. IMEPn and LKI plot of ignition timing and compression ratio sweep and effect of vaporization of fuel. *Fuel:* E10, Θ_i = 8-24°ca bTDC, λ = 1.0, τ = 9.5-10.5, T_c = 80°C, T_a = 50°C, Ω = 600 RPM.

Figure 3.30 confirms the trend previously seen that for vaporized (low ethanol-content) fuels the knock tendency is increased by about the same effect as an ignition advance of 1°ca as compared to a fuel injected in liquid form. The compression ratio sweep further shows that a fully vaporized fuel at a compression ratio of 9.5 has a near identical knock characteristic as a liquid fuel at a compression ratio of 10.5. This shows that in the MON test, which specifies a mixture temperature in which the fuel would be fully vaporised, then the contribution of the enhanced evaporative cooling from the alcohol is not accounted for.

As can be seen on the IMEP curves in Figure 3.30, this means that the MBT is approximately 3% lower and θ_{MBT} is occurring at a much more advanced igniting timing. This is proof that the practise of heating up the fuel and denying the engine the positive cooling effect in the

MON test is a most inappropriate practice. If not limited by knock, the difference in IMEPn for vaporized/liquid fuel is about 4 percent for both compression ratios.

Figure 3.31 shows the effect of a lambda sweep for both liquid and vaporized ethanol.

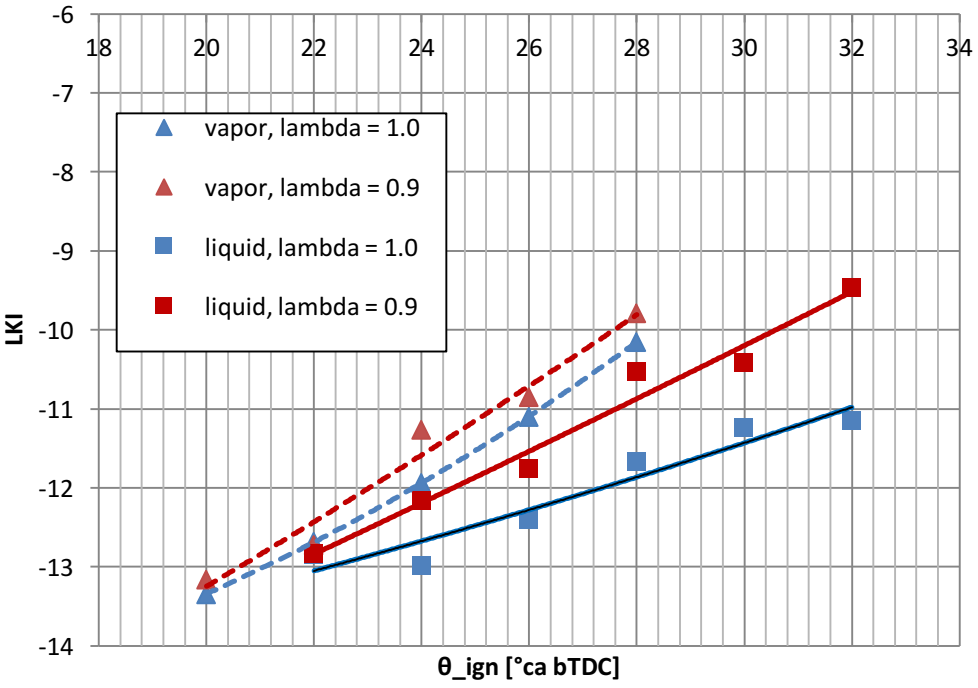

Figure 3.31. LKI plot of ignition timing lambda sweep and effect of vaporization of fuel. *Fuel:* ethanol, Θ_i = 20-32°ca bTDC, λ = 1.0, τ = 9.5, T_c = 80°C, T_a = 50°C, Ω = 600 RPM.

It can be seen in Figure 3.31 that the rich mixture has a higher knock tendency as compared to the weak mixture. This has been seen before but the plot also shows that the trend is the same for vaporized and liquid fuel. The data here suggests that switching from liquid to vaporized fuel is equivalent to an ignition advance of up to 6°ca. The difference between the two lambdas is smaller for the vaporized fuel as it is for the liquid fuel and interestingly the two trend lines are parallel rather than opening up. This means that the difference in knock intensity between the two lambdas is less dependent on the ignition timing for the vaporized fuel.

Figure 3.32 shows a sweep of three lambdas in vaporized methanol combustion. An additional experiment for liquid methanol at stoichiometric conditions was conducted to provide a comparison. The chosen functional form for the fits here is arbitrary.

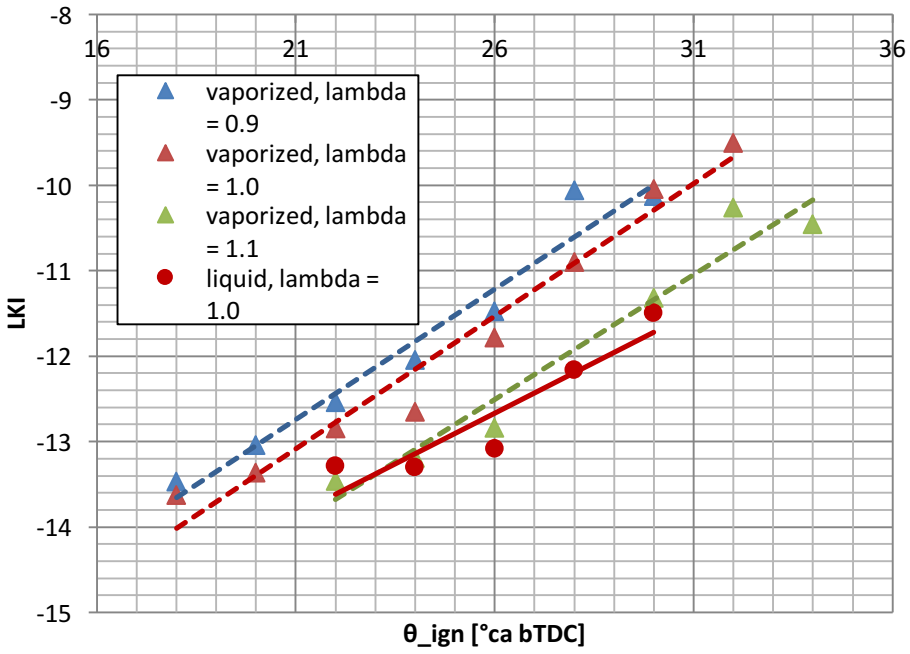

Figure 3.32. LKI plot of ignition timing lambda sweep and effect of vaporization of fuel. *Fuel:* methanol, Θ_i = 18-34°ca bTDC, λ = 1.0, τ = 9, T_c = 80°C, T_a = 70°C, Ω = 600 RPM.

Similar to the ethanol data in Figure 3.32, the rich experiment with methanol shows a higher knock intensity compared to the weak mixture then the stoichiometric compared to the weak mixture. Again, the trend lines are parallel, suggesting that the vaporized fuel has a reduced dependence on the ignition advance.

To investigate the influence of the air temperature on the knock tendency of vaporized fuel, an experiment with methanol was conducted and results plotted in Figure 3.33.

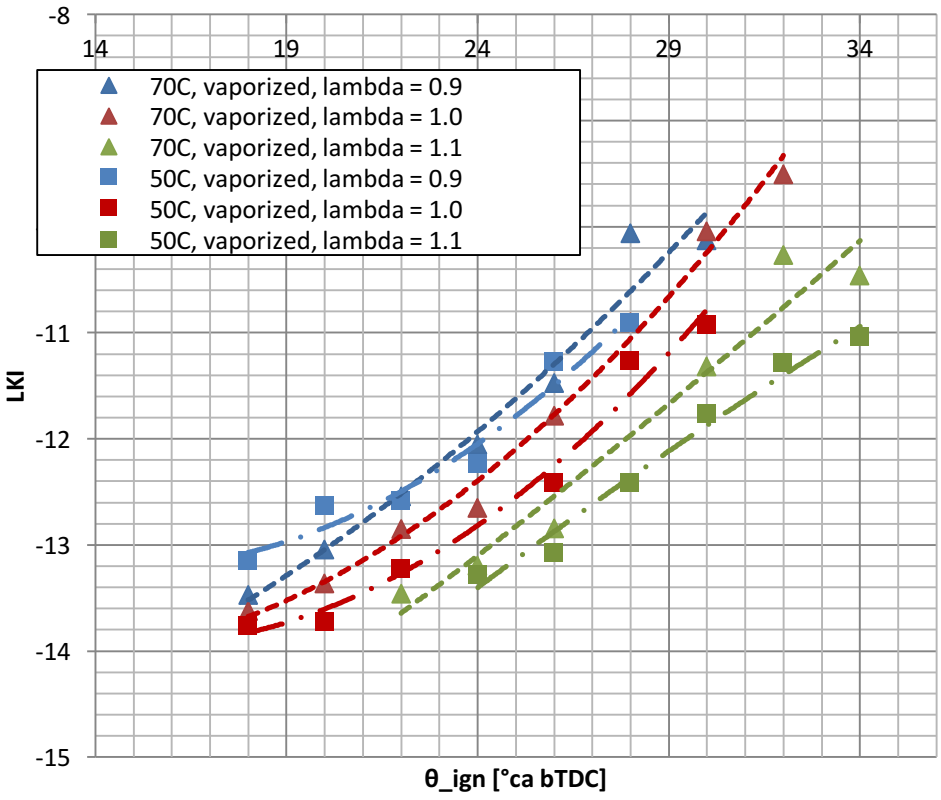

Figure 3.33. LKI plot of ignition timing lambda sweep and effect of different air temperatures. *Fuel:* methanol, Θ_i = 18-34°ca bTDC, λ = 1.0, τ = 9, T_c = 80°C, T_a = 50-70°C, Ω = 600 RPM.

Figure 3.33 shows how a decreased air temperature leads to a decreased knocking tendency for all three lambda values tested here for methanol. A hypothesis that parts of the vaporized fuel is condensing in the colder air stream was found to be untrue, as modelling of the mixture temperature (Figure 3.34) excluded the possibility that condensation occurred at the air fuel temperatures used in these experiments. Condensation occurs when the partial pressure of the vapour p'_v exceeds the saturation pressure p_{sat} at a mixture temperature of T_m = 34°C, well below the experimental conditions in Figure 3.33.

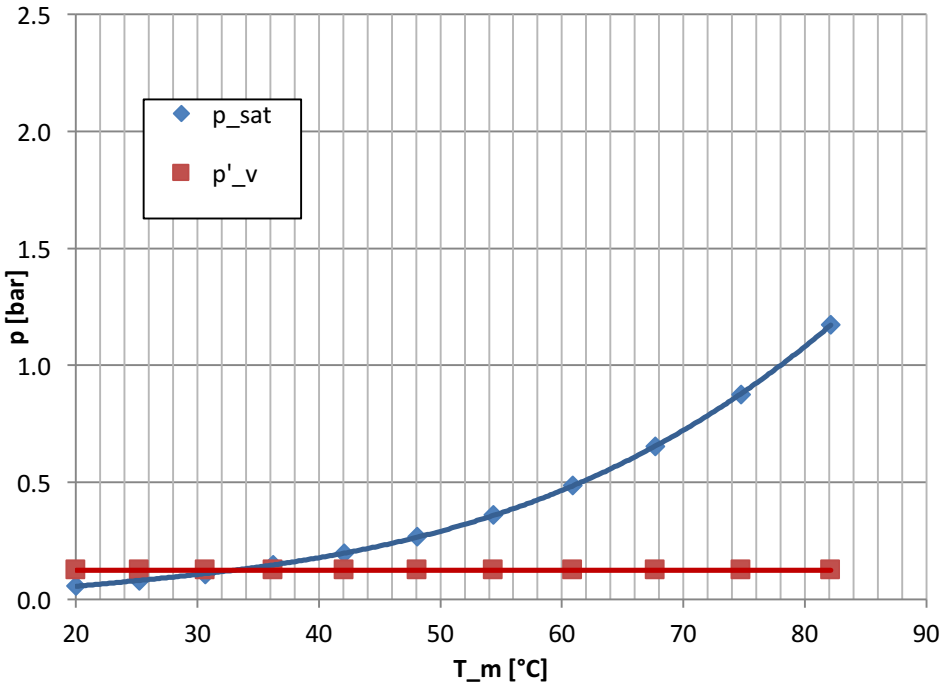

Figure 3.34. Modelling of mixture temperature. *Fuel:* methanol, Θ_i = 18-34°ca bTDC, λ = 1.0, τ = 9, T_c = 80°C, T_a = 50°C, T_f = 70°C Ω = 600 RPM.

3.5. Conclusions

The identification of the ideal engine operating point and the influence of intake air humidity and mixture preparation on knock have been analysed in this chapter. Knock indices and the influence of humidity and the effect of evaporative cooling of fuels on knock were discussed. Modelling to avoid condensation of steam and fuel vapour was presented. A custom built humidifying unit with a peristaltic pump water supply was built. Continuous output of steam was confirmed with schlieren imaging. The humidifying unit was also found suitable for vaporization of fuel. Experiments were then conducted for a range of conditions as outlined below.

Firstly, the hypothesis that the ideal engine operating point can be identified with a study of maximum pressure and mass fraction burned was tested.

- A sweep of ignition timing, lambda and compression ratio was conducted.
- Comparisons between three different mass fraction burned ranges revealed linear trends. We therefore decided to conduct future experiments with the single mfb range of *0-50%mfb*.
- While the p_{max} method serves as a reasonable substitute (error < 2°ca) for finding the MBT engine, a *mfb* based technique proved unfeasible.
- Overall, both methods were considered too imprecise to replace the ignition timing sweep studies in this work.

Secondly, the response of the engine to knock was assessed.

- Ignition timing sweeps were analysed for three knock indices and it was found that beyond a 'knock-onset' threshold, linear trends of knock intensity over advancing ignition timing were apparent.
- This threshold was then defined for all three knock indices and it could be shown that the ignition timing of the knock onset is independent of the knock index; this allowed us to proceed with just a single knock indicator for which the LKI was selected.
- A sweep of fuels and lambda values was conducted and, with one exception, it could be shown that the engine was not limited by knock because the MBT ignition timings were reached at ignition timings less advanced than the knock threshold.

The effect of humidity on the engine operating point, IMEPn and knock was investigated next.

- Experimental sequences of sweeps of ignition timing and compression ratios for two levels of humidity were analysed.
    - A reduced humidity was found to lead to an increased value of IMEPn in the respective experiments. This was expected as some of the combustible air is

replaced with water vapour. The calculated reduction of 7% was confirmed by the experiments.

  - The scatter of the data was increased when humidity was increased and this was considered to be caused by the unsteady air/steam flow.
  - Experiments with elevated humidity showed a significantly reduced knock tendency.

- An experimental sequence with a sweep of ignition timing, lambda and two levels of humidity showed similar results.
  - Increased levels of humidity had a reduction effect on the IMEPn and this effect was especially pronounced for weak mixtures where the water vapour had an increased effect.
- The results of the two experimental sequences (compression ratio and lambda sweeps) were then analysed to calculate the *0-50%mfb*.
  - It was found that an elevated humidity advances the position of MBT significantly and the *0-50%mfb* is longer. This effect was reported for both the compression ratio and lambda sweep.
  - This led to the conclusion that while humidity has a decreasing effect on knock, if the engine is to be operated at its ideal operating point, the required ignition advance to achieve this in turn makes knock more probable.

The last experimental section in this chapter was a study of the effect of mixture preparation on the engine operating point, on the IMEPn and on knock.

- A range of fuel blends of iso-octane and ethanol was tested for sweeps of ignition timing for both liquid and vaporized fuel. Two results were observed:

  - The higher the content of iso-octane of the test blend, the more prone to knock was the experiment.
  - For all vaporized fuels, the knock intensity was increased compared to liquid fuels. The enthalpy of vaporization makes knock less probable for liquid fuels due to its cooling effect. It can be confirmed here and it has been seen in detail in Chapter 1 that this effect disappears when the fuel is injected in a vaporized state.

- An analysis of the mixture temperature for the liquid fuels tested in the study showed that the mixture temperature decreased with increasing content of ethanol in the fuel. Modelling showed that these fuels did not fully evaporate.

The effect of mixture preparation on the engine's IMEPn followed next. A compression ratio sweep showed a reduced MBT for the vaporized fuel.

- The engine could be operated at a higher compression ratio with a liquid fuel and this provides further evidence of the fact that the practice of using fully vaporized fuels in the MON test can have a significant effect on underestimating the real-engine performance of fuels.

Experiments with sweeps of the lambda for ethanol and methanol showed that an engine operated with liquid fuel can operate at up to 6°ca more advanced ignition timing compared to vaporized fuel.

An experiment of a sweep of air temperatures for vaporized methanol showed that higher air temperatures led to more knock than lower air temperatures.

- Modelling showed that no fuel condensation was possible at the tested experimental conditions.

4. Surface Pre-Ignition in Internal Combustion Engines

4.1. Introduction

As explained in Chapter 1, the means to increase the efficiency of spark-ignition engines include downsizing, turbocharging and supercharging and these measures increase the chance for surface pre-ignition with potentially destructive consequences for the engine. Surface pre-ignition is therefore a topic of high importance and further research is needed to better understand the phenomenon.

Pre-ignition is the technical term given to ignition prior to the occurrence of the ignition spark. In the past this was only associated with surface ignition. Conventionally, pre-ignition referred to the ignition of the fuel/air mixture by a hotspot such as a part of the spark plug, combustion deposits or an exhaust valve. This is termed 'surface pre-ignition' in this thesis, so as to avoid any ambiguity with ignition in the bulk of the compressed unburned mixture, caused by the auto-ignition of, for example, a lubricant droplet. A recent comprehensive review by Wang et al [14] discusses this form of auto-ignition and the related phenomenon of 'super knock'. The maximum pressures observed during pre-ignition are higher and occur earlier than during normal combustion as the earlier start of the combustion compresses the end gas more [53, 80].

4.2. Research Background

Combustion analysis of surface pre-igniting cycles has shown that flames appeared before the spark ignition timing, and this has been confirmed in optical and flame ionization studies. Here, the rate of the heat release is in the same range as during normal spark ignition experiments which is significantly below the heat release rate during auto-ignition; surface pre-ignition and auto-ignition are distinct phenomena [13, 53, 81].

To establish surface pre-ignition a source of ignition must be present in the engine. This is a hotspot such as combustion deposits or a hot part of the cylinder wall (e.g. overheated spark plugs or valves). The increased pressure during surface pre-igniting cycles leads to magnified negative work during the compression stroke, and this reduces the efficiency of the engine. The earlier ignition means the pressure during combustion is increased, so the pressure and temperature of the unburned gas is higher. The raised unburned gas temperature can lead to auto-ignition of the remaining unburned gas and to a very rapid pressure rise that leads to audible knock. The rapid pressure rise is also associated with an increased heat flux so component temperatures will rise. This will be explained in more detail in Chapter 5. If there is auto-ignition as a consequence of pre-ignition, then the higher component temperatures will mean earlier pre-ignition and thence more intense auto-ignition in subsequent cycles. This leads to runaway knock and an increased likelihood of structural damage to the engine (see Figure 4.1) [80]; retarding or turning off the spark ignition will, of course, have no benefit.

Figure 4.1. Surface pre-ignition damage on a piston, adapted from [82]

As described in the introduction, pre-ignition can also be caused by droplets of fuel/oil blends. These can form on the cylinder wall and have significantly lower octane numbers than the fuel [14]. The droplets have a smaller surface tension than the oil film and can be blown away from the wall where they vaporize during the compression stroke and self-ignite. The ignition source can then heat up a localized small volume that can ignite a flame. For successful pre-ignition the ignition delay (τ_i) must be sufficiently small. The fuel/oil droplets were found to have sufficiently low ignition delays to be the cause of pre-ignition in the unburned gas [80, 81]. Catalytic effects of oil additives are poorly understood but empirical studies found that lower levels of metallic additives, such as barium, in the oil lead to reduced surface pre-ignition tendencies [81, 83, 84]. In this thesis only the pre-ignition by a hotspot on the cylinder wall or engine component is considered [50].

Surface pre-ignition occurs if two criteria are met: the ignition criterion and the propagation criterion.

The initiation criterion dictates that after ignition, a flame must grow to a critical size in order to propagate further when the ignition source has disappeared. The hotspot has to provide enough energy for the flame kernel to reach this critical size. If the flame size is too small, the rate of heat loss to the surroundings outweighs the rate of heat release from the chemical reaction and the flame extinguishes [13].

Zeldovich's flame ball concept suggests that a spherical flame has to have a critical radius R_f in order to self-sustain. If the radius is smaller than R_f, the flame extinguishes. R_f depends on the Zeldovich number β and laminar flame thickness δ as described in Equation 4.1 [85].

$$\frac{R_f}{\delta} = \exp\frac{1}{2}\beta\left(1 - \frac{1}{Le}\right) \tag{4.1}$$

R_f is greater than δ when Le > 1 and smaller when Le < 1. Independently of the Lewis number, a larger laminar flame thickness δ means that the critical radius R_f is larger which makes flame propagation harder and therefore surface pre-ignition less likely.

δ depends on the thermal diffusivity D and the laminar burning velocity S_L.

$$\delta = \frac{D}{S_L} \tag{4.2}$$

Under the assumption of a unity Prandtl number, $D = \mu/\rho$ with the dynamic viscosity μ. The laminar flame thickness δ can then be expressed as:

$$\delta = \frac{\mu}{\rho\, S_L} \tag{4.3}$$

It can be seen that the larger S_L, the more likely it is for the engine to surface pre-ignite.

S_L depends on pressure and temperature and is modelled empirically according to:

$$S_L = S_{LO} \left(\frac{T}{T_0}\right)^n \left(\frac{p}{p_0}\right)^{-m} \tag{4.4}$$

With datum values of pressure p_0 and temperature T_0, and the laminar burning velocity S_{L0}, as well as the fuel-dependent exponents m and n. For iso-octane, the coefficients were identified as $n = 1.01$ and $m = 0.282$ [13, 86].

Further, from the ideal gas law with ρ_0 as the density at the datum point:

$$\frac{p}{p_0} = \frac{T}{T_0}\frac{\rho}{\rho_0} \tag{4.5}$$

And with the dynamic viscosity μ at the datum point:

$$\frac{\mu}{\mu_0} = \left(\frac{T}{T_0}\right)^{0.5} \tag{4.6}$$

Combining Equations 4.3 - 4.6 ,Equation 4.7 can then be formulated for the laminar flame thickness δ:

$$\delta = \left(\frac{\mu_o}{\rho_0 S_{\mathrm{L}0}}\right)\left(\frac{P}{P_0}\right)^{m-1}\left(\frac{T}{T_0}\right)^{1.5-n} \tag{4.7}$$

4.2.1. Influence of Operating Conditions and Fuels on Pre-Ignition

Engines have been shown to be more susceptible to surface pre-ignition when operated under higher pressures (e.g. when turbocharged). This can be deduced from Equation 4.7. While the temperature remains constant and with a typical positive value for $m < 1$, an increased pressure leads to a reduced flame thickness δ as compared to the datum case. As explained, this enhances the chance of surface pre-ignition [13].

While there are established industrial standards for the ranking of fuels towards their auto-ignition or knock behaviour using the research and motor octane numbers (RON and MON), there is no common surface pre-ignition rating for fuels.

The most comprehensive data on the pre-ignition properties of pure fuel components is the work of Downs and Theobald [53] who tested 21 components.

The technique to rank fuels according to their surface pre-ignition rating follows a similar approach as with the octane tests. A study was conducted on a single cylinder engine with surface pre-ignition induced through a glow-plug [53]. It was recorded how much energy the glow-plug required to bring the engine to surface pre-igniting conditions with $\lambda = 0.9$. This rich air fuel ratio was taken because at this condition the maximum laminar burning velocity S_{Lmax} was to be expected. The tests were then executed for a wide range of fuels. Two 'primary reference fuels' were identified with fuel 1 that needed the least glow-plug heat for surface pre-ignition (cyclohexane) and fuel 2 which needed the hottest glow-plug for surface pre-ignition (iso-octane). These reference fuels were then assigned a 'surface pre-ignition resistance' (PR) number of 0 and 100. The other fuels were assigned PR numbers in between on a scale from 0-100 and this can be seen in Table 4.1 [53, 80].

Table 4.1. Surface pre-ignition rating PR, maximum laminar burning velocity S_{Lmax}, *RON* and *MON* of selected fuels [53].

Fuel	***PR***	$\boldsymbol{S_{Lmax}}$	***MON***	***RON***
1-hexene	-20	0.835	74	76.4
cyclohexane	0	0.78	78	83
ethyl benzene	18	0.77	97.9	109
benzene	26	0.84	97	105
2-methylbutene	50	0.71	82	98
cyclopentane	70	0.782	85.7	102.8
iso-pentane	75	0.662	93	93.5
toluene	93	0.68	102	117
p-xylene	95	0.615	100.6	113
iso-octane	100	0.667	100	100
o-xylene	120	0.615	88.8	105.4
m-xylene	125	0.56	101.3	117

A large PR number indicates that more energy was required from the glow-plug to achieve the same surface pre-igniting behaviour as a fuel with a lower PR number. Therefore, the higher the PR, the more resilient to surface pre-ignition is the fuel. In the third column of Table 4.1 there is information about the maximum laminar burning velocity $S_{Lmax.}$ According to Equation 4.1, the larger S_L, the smaller the flame thickness δ and according to Equation 4.1, the more prone to surface pre-ignition is the fuel. That this hypothesis is plausible can be seen in Figure 4.2.

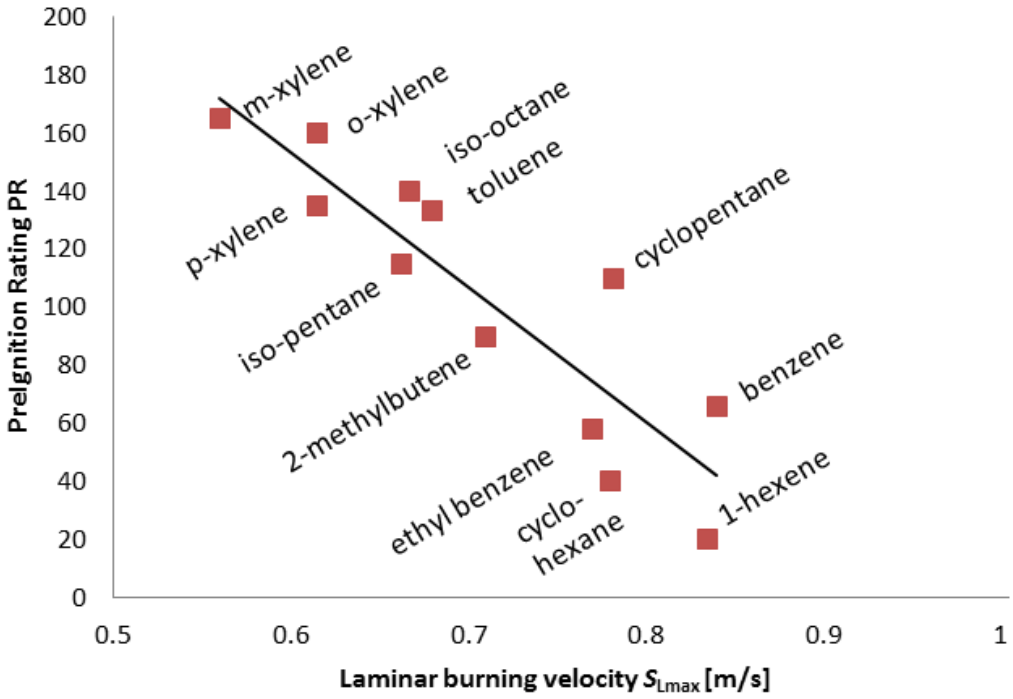

Figure 4.2. Correlation between *PR* and S_{Lmax} [53].

At the same time there is no correlation between PR and the octane numbers RON and MON. This can be seen in Figure 4.3.

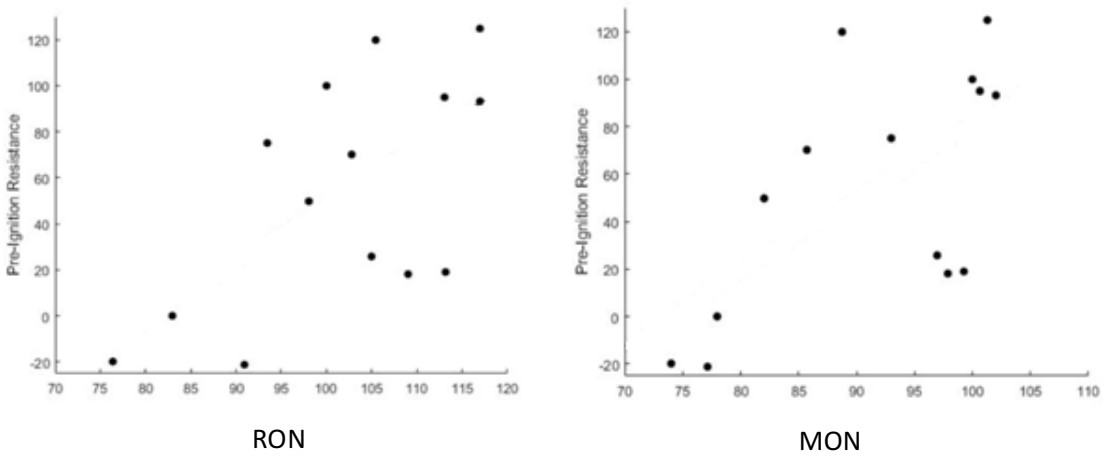

Figure 4.3. Correlation between PR and RON and MON [13]

Downs and Theobald [53] did not report data for oxygenates. This work is now over 50 years old and did not have the benefit of modern data acquisition systems that allow statistical analysis of data from many engine cycles. The proposed method of rating surface pre-ignition by means of the heat input to the glow-plug is questionable, as it does not allow for an absolute measurement. Nor is it independent of the engine and heater geometry. As pre-ignition is a highly stochastic process, then this placed high demands on the test operator in determining a threshold for pre-ignition. The comparison of this data with other data is very difficult as it depended on the heat input to the glow-plug. Data on the temperature of the heater was reported and will be discussed later in this chapter.

There are different ways of inducing surface pre-ignition and reporting the susceptibility of a fuel to surface pre-ignition.

Guibet and Duval [83] used two methods: a heating element and spark plugs with different temperature ratings. In both cases the temperature was used to characterise the pre-ignition rating. Of particular interest was how the metallic additives in oil and fuel led to deposits that catalysed pre-ignition. These effects were quantified by how long the engine had to be run before pre-ignition occurred.

Menrad et al. [84] also used spark plugs with different heat ratings and materials to quantify the pre-ignition rating of different alcohol gasoline blends with a particular focus on methanol because of its susceptibility to pre-ignition. They used the spark plug as an ionisation detector. A typical ionization probe consists of two narrowly spatially separated electrodes that are fitted into a combustion chamber. When a hydrocarbon flame is present between the electrodes, charged ions are present and these ionization effects can be measured by applying a voltage that causes a current to flow. This can be used as an indicator for combustion [88]. If this signal is then amplified and appropriate pulse logic is applied, it is possible to see if a flame is present in the combustion chamber before the spark plug has fired which indicates surface pre-ignition [53, 83, 84]. Menrad et al. [84] increased the temperature of the sparkplug by retarding the ignition timing and reported their results in terms of this critical ignition timing.

Another approach to identifying a pre-igniting cycle is reported by Luef et al. [89] who considered the angle of occurrence of the 5% mass fraction burned (*mfb*) in 200 consecutive cycles. If the observed angle of *5%mfb* was earlier than the predefined limit, set at $\xi - 2\sigma$ of the *5%mfb* point for spark-ignited combustion then pre-ignition had occurred. Tests with a similar pre-ignition criterion were also undertaken with a heated glow-plug and the temperature for pre-ignition was reported for a range of alcohols blended with iso-octane.

Alternatively, surface pre-ignition can be detected by means of an in-cylinder pressure analysis. Comparisons of normal and surface pre-igniting cycles show that surface pre-igniting cycles have higher peak pressures than spark-igniting cycles. This can be seen in Figure 4.4 where a retarded ignition timing has been used and surface pre-ignition was induced with a glow plug.

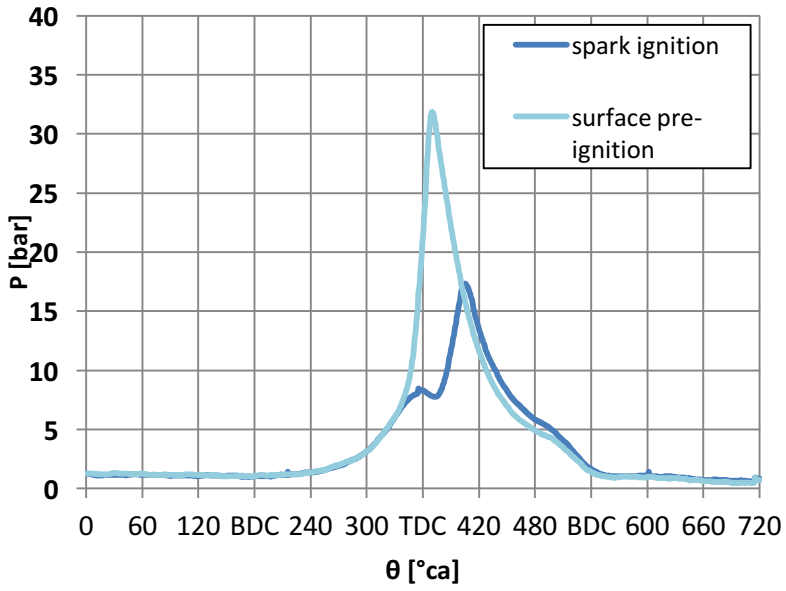

Figure 4.4. Surface pre-igniting and spark-igniting cycles. Θ_i = 5°ca bTDC, τ = 6, *Fuel*: iso-octane, T_{gp} = 850°C surface pre-ignition cycle, T_{gp} = 550°C spark-ignition cycle, λ = 1.0, T_c = 80°C, T_a = 30°C, Ω = 600 RPM

The cycles with elevated maximum pressures can then be counted and compared to the overall number of cycles to calculate a ratio of surface pre-igniting to spark-igniting cycles [90].

4.2.2. Simulations of Unburned Gas Temperature

Modelling of the unburned gas temperature was performed with the in-house ISIS code and results were plotted in Figure 4.5.

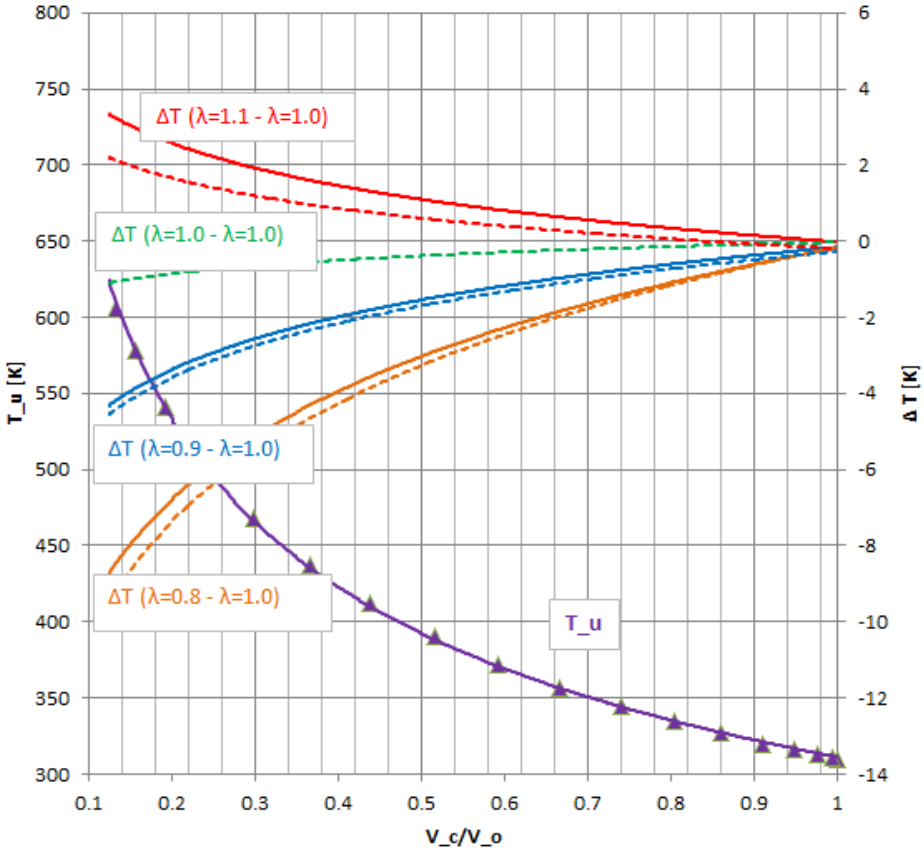

Figure 4.5. Unburned gas temperatures for lambda and humidity sweep. Dotted lines: humidity=0.05 kg/kg, continuous lines: humidity=0.006 kg/kg, $\tau = 8$, iso-octane, $T_c = 80°C$, $T_a = 50°C$, $\Omega = 600$ RPM

Figure 4.5 shows the results of modelling of the unburned gas temperature over a fractional cylinder volume for both weak and rich mixtures assuming fully vaporized fuel. TDC is located on the left of the x-axis. Further, different levels of humidity were tested. The temperature differences ΔT are shown. T_u is representing the datum temperature at a particular volumetric compression ratio for the stoichiometric, dry case. It can be seen that weaker mixtures result in higher unburned gas temperatures and richer mixtures lead to reduced unburned gas temperatures. The effect is more pronounced for rich mixtures. The reason for the difference is in the ratio of heat capacities γ as shown in Figure 4.6.

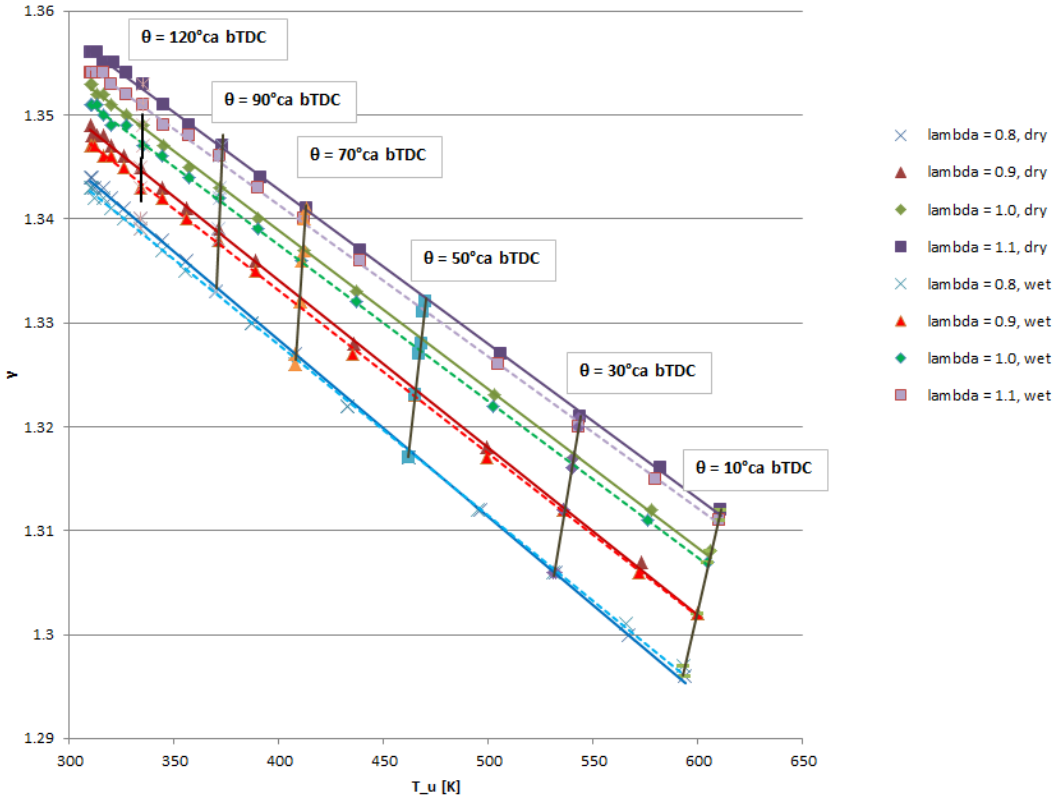

Figure 4.6. Ratio of heat capacities over unburned gas temperature. Dotted lines: humidity=0.05 kg/kg, continues lines: humidity=0.006 kg/kg, $\tau = 8$, iso-octane, $T_c = 80°C$, $T_a = 50°C$, $\Omega = 600$ RPM

The ratio of heat capacities γ varies over the unburned gas temperature and with humidity. As the unburned gas temperature increases, γ becomes smaller. This effect is stronger for richer mixtures. It can be seen that a larger humidity reduces the value of γ and this effect is more pronounced for weaker mixtures.

4.3. Experimental Equipment

An experimental set-up was designed to assess the susceptibility of different fuels to surface pre-ignition under a range of different experimental conditions when triggered with a closed-loop temperature controlled glow-plug and measured with a flame ionization sensor or an in-

cylinder pressure analysis. As with the work of Downs and Theobald [53] the Ricardo E6 variable compression ratio engine was used for the surface pre-ignition tests**.**

4.3.1. Surface Pre-Ignition Probe

An experimental probe was constructed that consists of a glow-plug with an externally welded-on thermocouple and a flame ionization detector. The glow-plug acts as hotspot to cause surface pre-ignition according to the ignition criterion (Section 4.2). The attached thermocouple records the temperature of the glow-plug for closed-loop control in LabVIEW. The ionization probe takes advantage of the ionization effect in a flame to detect when a flame is present between its electrodes.

Figure 4.7 shows drawings and a picture of the adaptor that holds the glow-plug, thermocouple and ionisation probe. The larger hole contains the glow-plug and the smaller holes hold the thermocouple and the ionization probe.

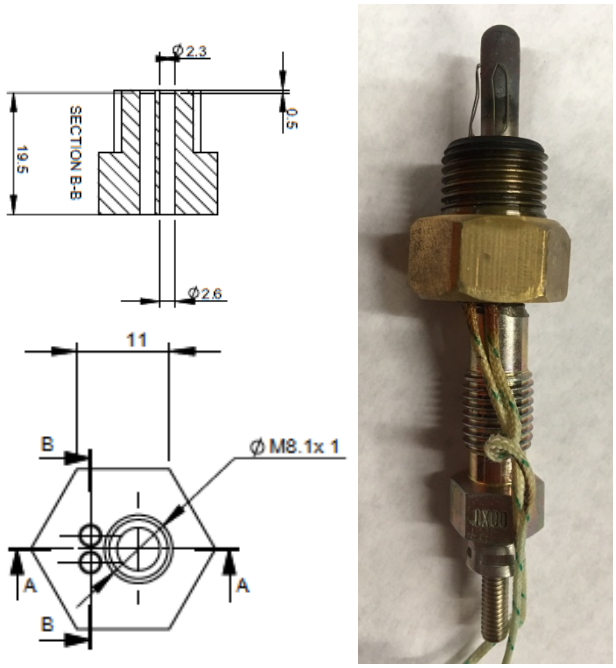

Figure 4.7. The surface pre-ignition sensor adaptor with holes for sensors and glow-plug

The ionization probe is made up of K-Type thermocouple wires that act as electrodes and are set to be 1 mm apart. One wire is charged with +15 V and the other with -15 V.

The K-Type electrode wires are fitted into two holes of a 3 mm ceramic tube which is then glued into one of the smaller holes of the adaptor. An identical ceramic tube is fitted into the other small hole of the adaptor and also contains two holes for the thermocouple wires that measure the temperature of the glow-plug.

The Ricardo E6 variable compression ratio engine has two bores on opposite sides of the upper combustion chamber wall (Figure 4.8). One of these is used for the spark plug and it also holds a Kistler piezoelectric pressure transducer. The other bore is available to be used for the surface pre-ignition sensor.

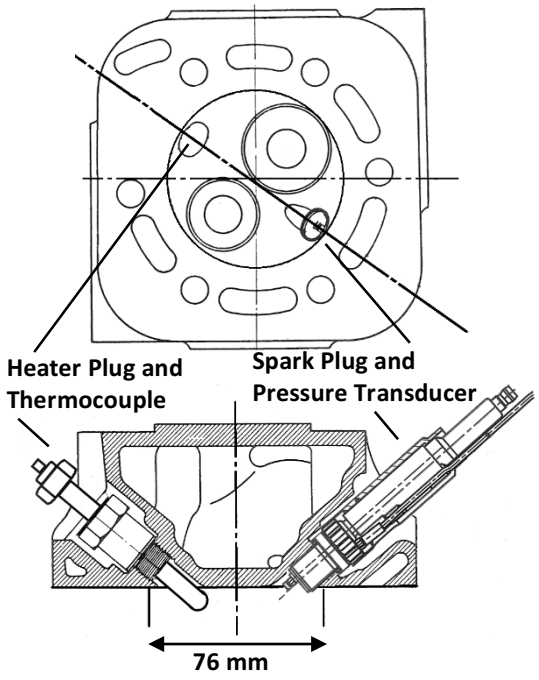

Figure 4.8. Set-up of the surface pre-ignition probe and spark plug; similar to set-up of previous surface pre-ignition studies [53].

The cross-section drawings in Figure 4.8 show the position of the two bores in the E6 engine. The lengths of the glow-plug and ionization probe were selected to be short enough not to interfere with the rising piston at compression ratios (τ) of up to $\tau = 10$.

4.3.2. Glow-Plug Temperature Control

As the glow-plug requires a high current at a voltage of 12 V (e.g. 23 A to heat to 300°C), a mains-operated power supply was not feasible, so a lead acid battery, identical to the unit that supplies the ignition system, was deployed. The downside of using a battery is that the voltage cannot be regulated so our approach to control the temperature of the plug is to pulse width modulate the power supply by turning it on and off frequently. This required extensive hardware.

A pulse width modulation (PWM) system was used to convert the analogue demand signal (0-1 V) from LabVIEW to a TTL pulse that was sufficiently high (0-5 V) to operate a power MOSFET operated with the 12 V supply.

In order to monitor and control the temperature of the glow-plug, a K-type thermocouple was welded on the glow-plug. This thermocouple was connected to an AD595 amplifier that incorporates thermocouple cold junction compensation. The thermocouple amplifier gives a 10 mV/°C analogue signal that feeds directly into the SLDAQ (USB-6525) and into a LabVIEW VI. This LabVIEW VI was created to monitor and control the temperature of the glow-plug. A PID controller was programmed to set the temperature of the glow-plug to the value of interest. Sensitive initial manual tuning (Ziegler Nichols Method [59]) gave approximate values for the PID terms. Subsequent auto-tuning was applied for a more precise response. A user-defined alarm range showed a red light when the glow-plug was too hot. This was particularly useful to quickly alert the user about runaway surface pre-ignition.

For the tests and experiments, operating conditions of engine speed Ω = 600 RPM, coolant temperature T_c = 80°C and air temperature T_a = 30°C were chosen. Previous tests in the literature have been performed at these conditions [53, 84].

The pre-ignition experiments were conducted with a spark-ignition timing of 5°ca bTDC. This retarded timing was selected so that when pre-ignition occurred, it would not immediately lead to knock.

4.4. Data Analysis

Various criteria based on a flame ionization system and combustion analysis derived from the pressure record were considered. The latter included the angle of *0-50%mfb* and the heat release rate. Eventually, it was concluded that these had no advantage over the most direct measurement – the maximum cylinder pressure. But even with the maximum cylinder pressure there are different criteria that can be used. All methods are outlined and discussed in this section.

4.1.1. Ionization Probe Based Surface Pre-Ignition Detection

The data logic used for the ionization sensor detection can be seen in Figure 4.9.

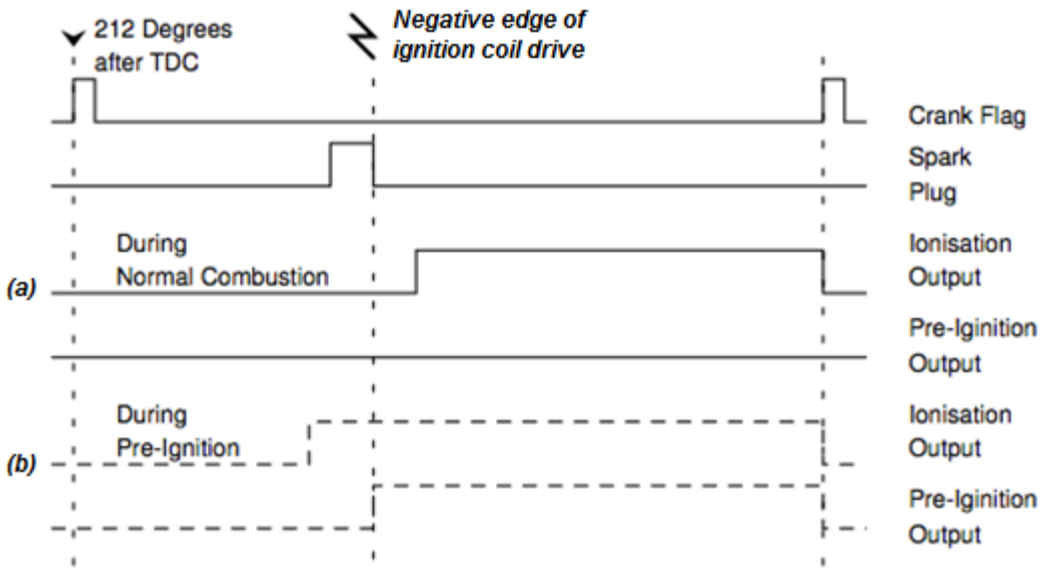

Figure 4.9. Data logic to assess normal combustion (a) and surface pre-ignition (b)

Figure 4.9 shows how the surface pre-ignition output channel forms a pulse if the ionisation output channel goes high before the spark plug channel goes low (firing event). All channels are reset at the next crank flag event. The output of the surface pre-ignition channel was recorded with a DAQ card and processed in LabVIEW. Here, a ratio of surface pre-ignition events over a total number of cycles in a given experiment was calculated and used as an indicator for the severity of surface pre-ignition.

After initial experiments it became apparent that the temperature of the glow-plug was prone to strong variations at severe surface pre-ignition conditions. The response time of the PID was two orders of magnitude slower than the average cycle. Variations of +-20 K were possible and occurred frequently. Temperature averaging was used to remove the most serious oscillations. At a later stage, the methodology was further developed to use a cycle-by-cycle pressure and temperature measurement approach.

This system was also monitored on an oscilloscope. The upper screenshot in Figure 4.10 shows a normal combustion event with retarded ignition timing as can be seen by the operator on the oscilloscope.

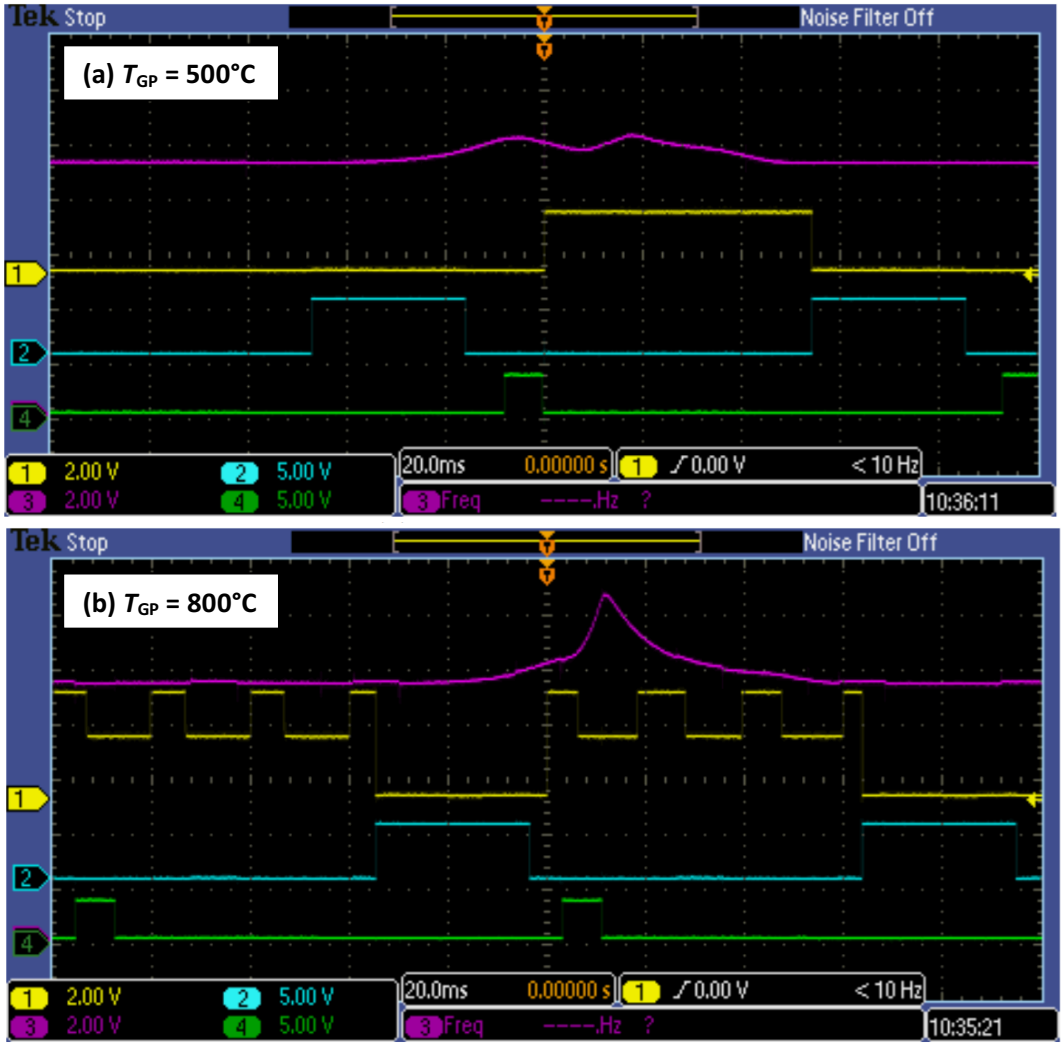

Figure 4.10. Oscilloscope screenshots from the ionization probe system; Red: in-cylinder pressure, yellow: ionization signal, blue: extended crank flag, green: ignition pulse. Θ_i =5°ca bTDC, τ = 6, *Fuel*: iso-octane, λ = 1.0, T_c = 80°C, T_a = 30°C, Ω = 600 RPM

The upper screenshot (spark-igniting cycle) shows that the yellow ionization pulse appears immediately after the spark plug has fired (falling edge of the green pulse). In the bottom screenshot the engine is surface pre-igniting which can be seen by the elevated pressure on the red signal and by the advanced appearance of the yellow ionization pulse relative to the spark.

Extensive testing of the ionization device was performed and several problems surfaced that eventually led to disregarding this technique.

The resistance of the ionization probe is the resistance between the electrodes of the ionization sensor along with a pull-up resistor form a potential divider. The pull-up resistor's resistance can be adjusted to change the sensitivity of the probe during experiments. The variable resistor that sets the threshold level for the ionization detector had to be adjusted constantly, very precisely and within a narrow band. If an inaccurate resistance was selected, either no signals or erroneous signals (combustion on exhaust stroke, see bottom screen shot of Figure 4.10) were detected. It had to be re-set constantly as the engine was warming-up because the resistance depended on the operating temperature. While all experiments were conducted at an elevated coolant temperature of 80°C, surface pre-ignition caused the engine temperature to rise for short intervals, and it was not possible to adjust the resistor in real time for this. Cycle-by-cycle variations and misfiring cycles added to the problem.

Further, the signal was prone to interference from the glow-plug and fluctuated instead of giving a steady 5 V output. This can be seen in the bottom screen shot of Figure 4.10. An amplifier was deployed to remove interference and a NAND-Gate latch system was used to extend the ionization pulse. While this worked satisfactorily, it was realized that the response time of the system was too long for accurate measurements. The ionization system was found to be unreliable for the surface pre-ignition study and disregarded.

While an optical measurement of the flame front with a fibre optic was considered, the approach of assessing surface pre-ignition through elevated pressure traces was chosen as a replacement technique. This required the application of the COBRA combustion analysis code in Matlab. As introduced in Chapter 2, the COBRA code performs combustion analysis calculations based on in-cylinder pressure data and calculates important combustion parameters. Of particular interest for us in this chapter are the peak pressure p_{max}, the angle of the peak pressure Θ_{pMax} as well as the mass fraction burned *mfb* and the net heat release Q_N.

The PIA (pre-ignition analysis) code was designed to process the combustion burn rate analyses data for our purposes of assessing the severity of surface pre-ignition.

4.4.2. Pressure-Based Surface Pre-Ignition Detection

When surface pre-ignition is induced by means of increasing the temperature of the glow-plug above a certain level the engine moves towards surface pre-ignition conditions which can be detected by an increased maximum pressure. This can be seen in Figure 4.11 where the pressure traces of two spark igniting and two surface pre-igniting cycles are shown.

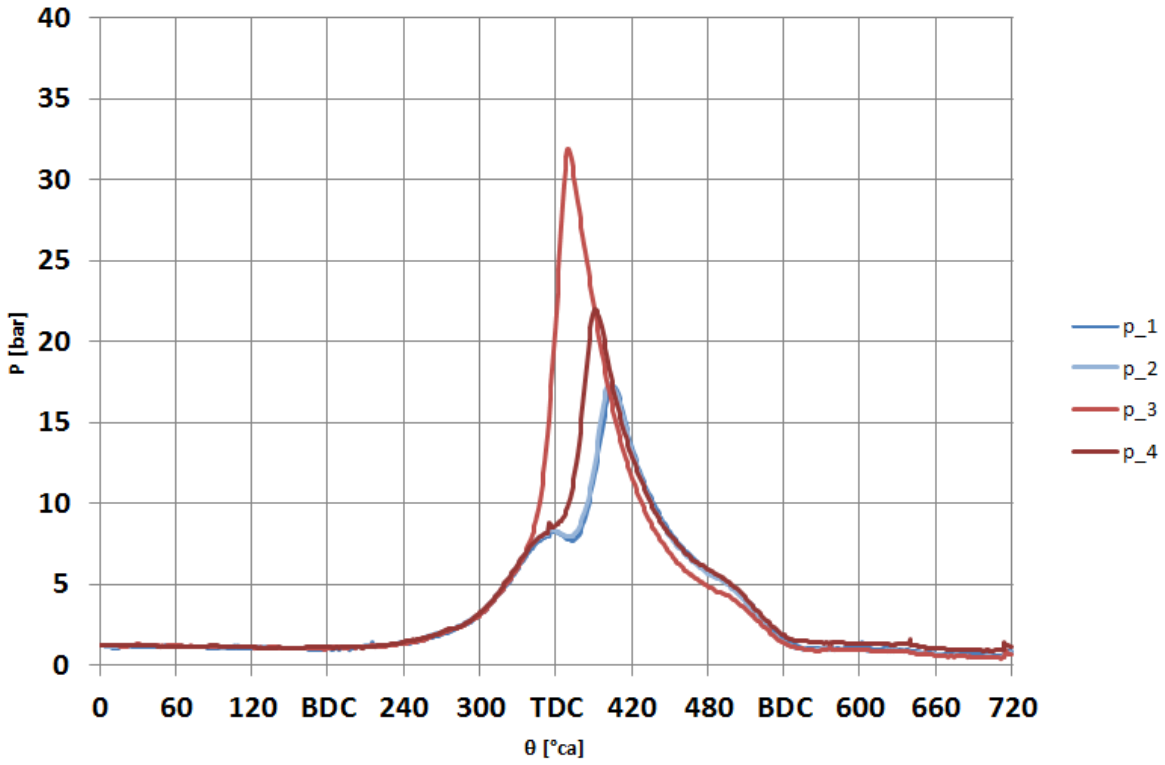

Figure 4.11. Pressure curves of spark-igniting cycles (blue, 1&2, T_{GP} = 850°C) and surface pre-igniting (red, 3&4, Glowplug disabled) Θ_i = 5°ca bTDC, τ = 6, *Fuel*: iso-octane, T_c = 80°C, T_a = 30°C, Ω = 600 RPM

The amplified Kistler piezoelectric pressure sensor data was logged in LabVIEW for subsequent analysis through COBRA. The peak pressure data was then further analysed to

find an appropriate measure to define surface pre-ignition and create a ranking for the severity of surface pre-ignition.

The script PIA used the p_{max} data and formed histograms with normal distribution curves. For one test sequence, four sets of peak pressure data were obtained which can be seen in Figure 4.12.

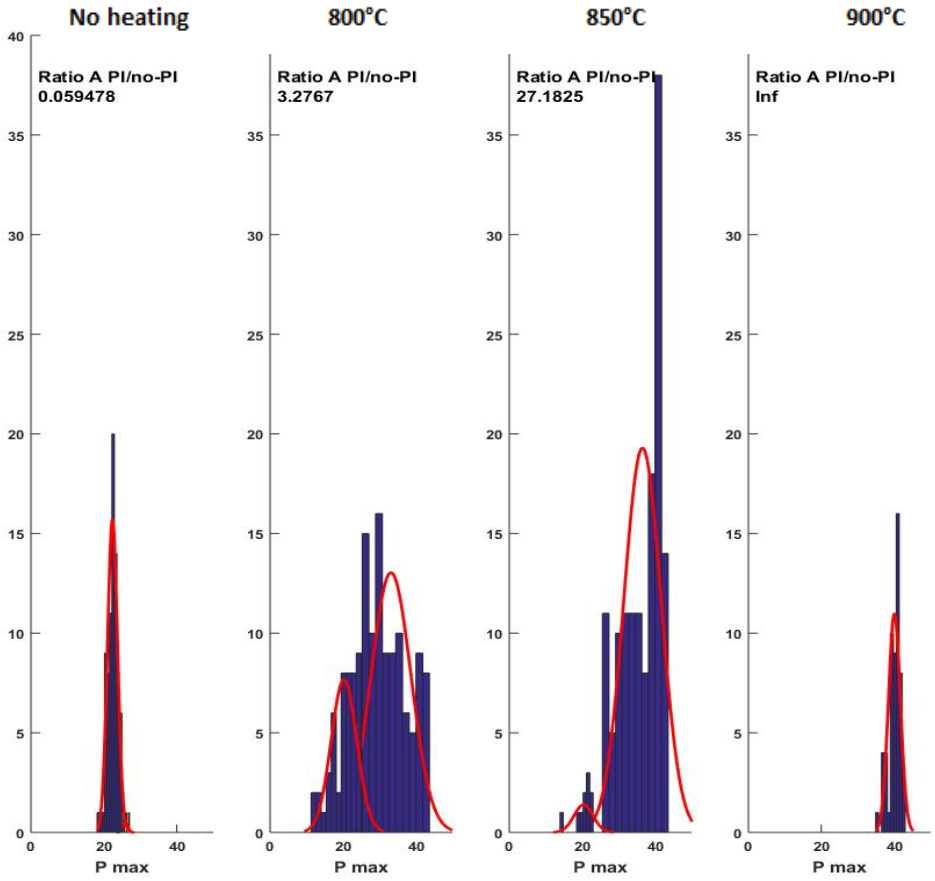

Figure 4.12. Histograms of p_{max} at different glow-plug temperatures (T_{gp}); Θ_i = 5°ca bTDC, τ = 6, *Fuel*: iso-octane, λ = 1.0, T_c = 80°C, T_a = 30°C, Ω = 600 RPM

The first data set was taken at normal spark-igniting conditions when the glow-plug was turned off. This led to a glow-plug temperature of about 530°C for iso-octane at standard conditions. For the second test, the glow-plug was set to 800°C and it can be seen that a

significant number of the cycles have much higher pressures, indicating that they surface pre-ignited. For the third experiment, the glow-plug was heated to 850°C and two discernible pressure regimes (spark-igniting and surface pre-igniting) are visible. At the last experiment the temperature was high enough (T_{GP} = 900°C) for all cycles to surface pre-ignite.

A bimodal distribution was observed in Figure 4.12. with Experiments 2 (T_{GP} = 800°C) and 3 (T_{GP} = 850°C) when there are peaks in the histogram at pressures that indicate spark-ignition and another peak at elevated pressures caused by surface pre-ignition. A combined bimodal distribution has a minimum in between these two peaks. Finding this minimum allowed a threshold to be defined for spark-igniting and surface pre-igniting cycles that was set at 25 bar in this experiment. When the histograms are summed on either side of the threshold to find the ratio between the number of surface pre-igniting and spark-igniting cycles this can be used as a ranking for surface pre-ignition severity. At T_{gp} = 800°C in Figure 4.12, the value for this ratio was 3.3, while at T_{GP} = 850°C 27.2 times as many cycles surface pre-ignited as compared to spark-ignited cycles.

In order to find a measure to quantify the severity of the surface pre-ignition two individual normal density functions were created, separated by the surface pre-ignition threshold. The curves were then integrated to find the area they encompass. The ratio of the areas r_{PI} is then calculated. This ratio increases from 0 to infinity as the glow-plug temperature increases. This measure for surface pre-ignition severity was found to not have a significant advantage over the ratio derived from the total number of the different ignition events.

More detailed tests (Figure 4.13) in the temperature range of highest interest show a clear trend as the temperature of the glow-plug is increased gradually and surface pre-ignition becomes more and more prevalent.

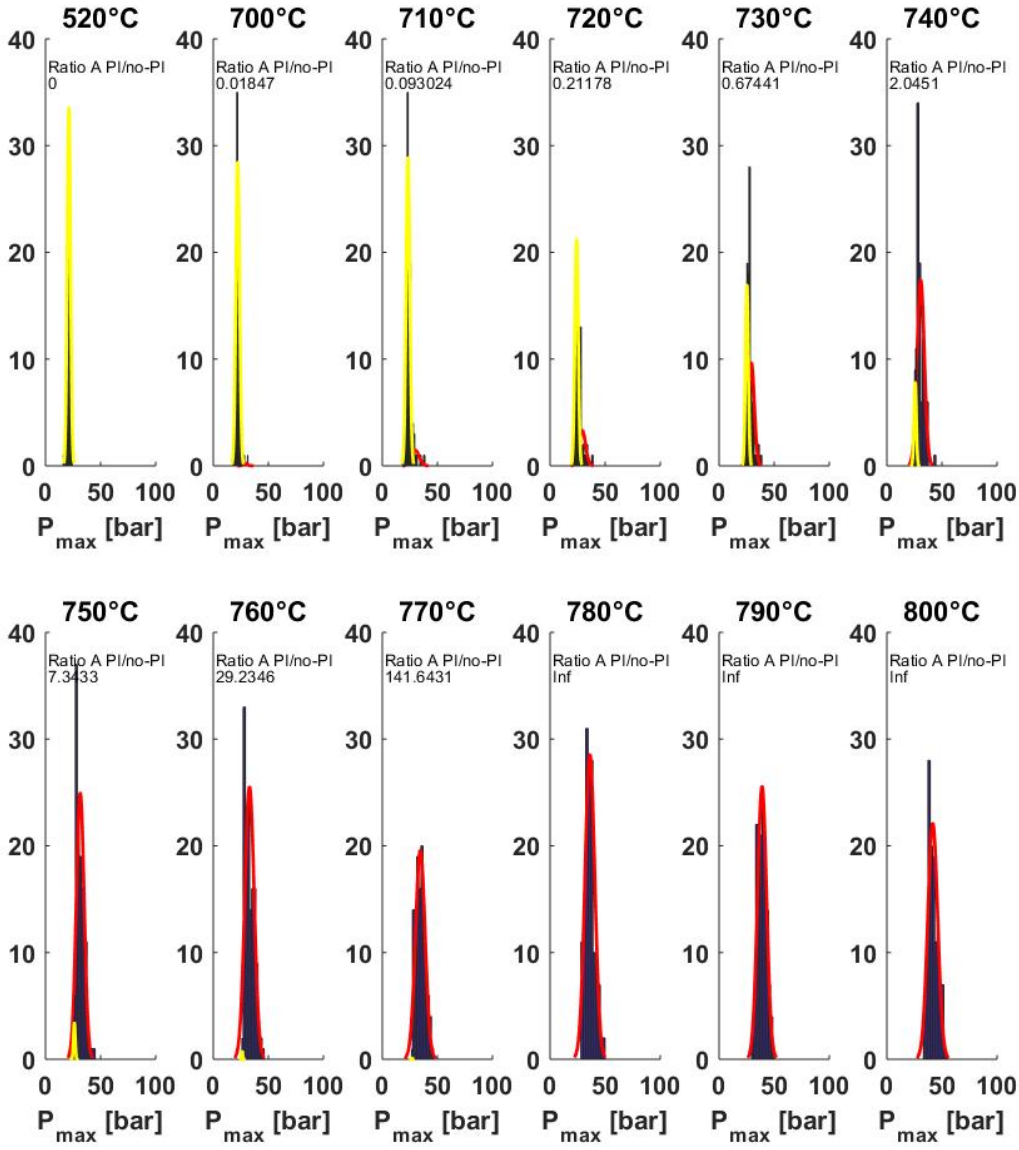

Figure 4.13. Histograms of p_{max} to form ratios at a threshold of 28.5 bar; T_{gp} 520 - 800°C, Θ_i = 5°ca bTDC, τ = 6, *Fuel*: iso-octane, λ = 1.0, T_c = 80°C, T_a = 30°C, Ω = 600 RPM

A reference case in a spark-igniting experiment in which the glow-plug is disabled allows for finding a threshold for surface pre-ignition. It can be set 1 bar higher than the highest pressure measured during this reference case, as it can be assumed that during subsequent

experiments none of the spark-igniting cycles reach this pressure and cycles with pressures beyond this are surface pre-igniting cycles.

Given that for every experiment the spark spark-igniting p_{max}-distribution looks different, it was important to find a more repeatable and automated way to determine the threshold. For this the normal distribution of the p_{max} histograms of the reference case (exclusively spark-igniting cycles) is considered. The mean ξ and the standard deviation σ of this distribution are calculated. It was then decided to set the threshold t_{PI} of surface pre-ignition for the following experiments in relation to a threshold factor x_{PI}.

$$t_{PI} = \xi + x_{PI}\,\sigma \tag{4.8}$$

Several threshold factors x_{PI} have been tested and plotted in Figure 4.14.

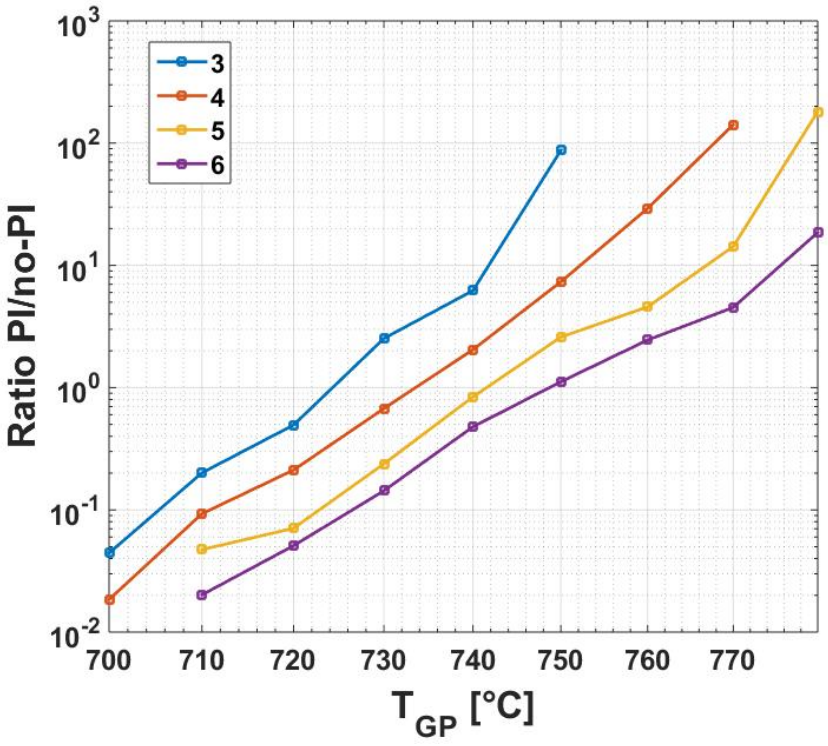

Figure 4.14. Different threshold factors x_{PI} (multiplier of the standard deviation as defined in Equation 4.8) to form surface pre-ignition thresholds t_{PI}; Θ_i = 5°ca bTDC, τ = 6, *Fuel*: iso-octane, λ = 1.0, T_c = 80°C, T_a = 30°C, Ω = 600 RPM

As would be expected, the higher the threshold factor (x_{PI}) in Figure 4.14, then the higher the required glow-plug temperature for a given incidence of pre-ignition. When there are only a few either pre-igniting or spark-igniting cycles, then calculating the ratio of the pre-igniting to the spark-igniting cycles will be less accurate. The accuracy will be greatest when there is a unity ratio ($r_{PI} = 10^0$) of pre-igniting to spark-igniting cycles, and Figure 4.14 shows that with this ratio, then the mean glow-plug temperature for pre-ignition rises with the threshold factor (x_{PI}) from 724°C ($x_{PI} = 3$) to 750°C ($x_{PI} = 6$). The trends plotted in Figure 4.14 are essentially linear, and as this is a log-linear plot, this implies that the incidence of pre-ignition has an exponential dependence on temperature.

The data points for a lambda sweep were plotted again in Figure 4.15. They are compared to the threshold factors x_{PI} in a range from 2 to 3.

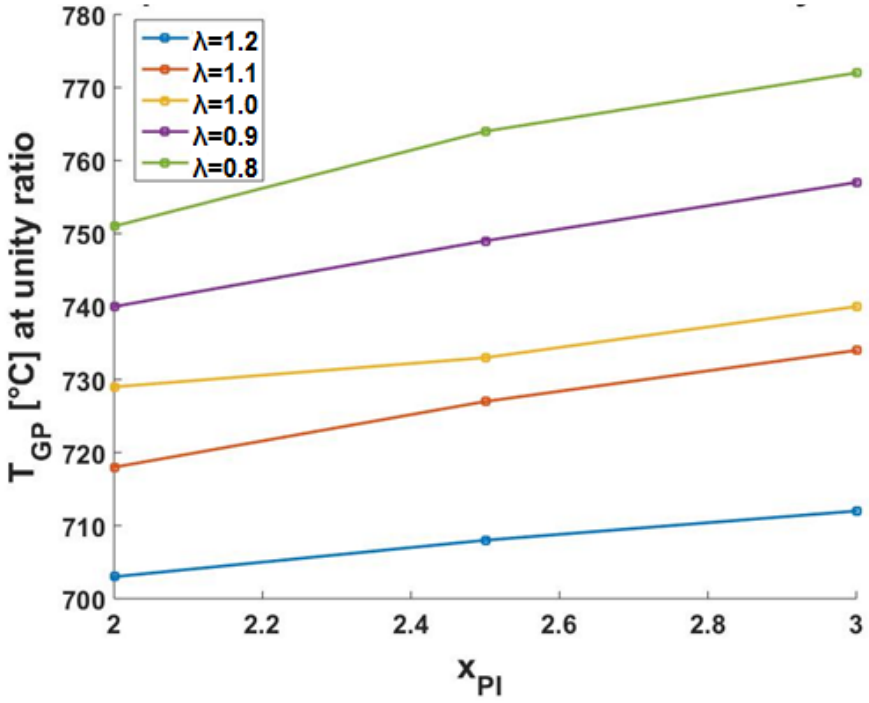

Figure 4.15. Plots of $r_{PI} = 1$ over threshold factor x_{PI} as defined in Equation 4.8; $\Theta_i = 5$°ca bTDC, $\tau = 6$, *Fuel*: iso-octane, $T_c = 80$°C, $T_a = 30$°C, $\Omega = 600$ RPM

It can be seen in Figure 4.15 that none of the threshold lines are overlapping for the different air fuel ratios and are nearly parallel to each other. This indicates that independently of the threshold for surface pre-ignition t_{PI}, the method is well able to analyse the influence of different experimental conditions, even when the differences are small.

4.4.3. Discontinued Pressure-Based Methods

While the maximum pressure was chosen as the most straightforward method, other techniques were examined and tested for accuracy and feasibility. The results give additional validation to the maximum pressure method.

The mass fraction burned (*mfb*) parameters of *0-10%mfb* and *0-50%mfb* and 50% mfb °ca aTDC (*mfb50*) were calculated and analysed with COBRA and PIA. Histograms were created and for every experiment, two normal distributions formed. For one set of experiments, this can be seen in Figure 4.16.

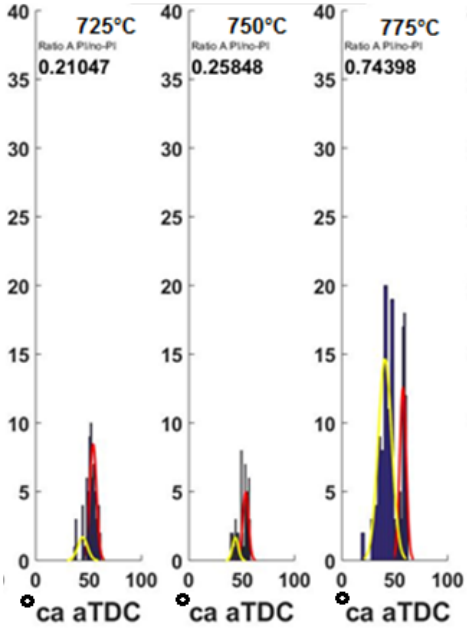

Figure 4.16. Histograms of *mfb50* (°ca aTDC); Θ_i = 5°ca bTDC, τ = 6, *Fuel*: iso-octane, λ = 1.0, T_c = 80°C, T_a = 30°C, x_{PI} = 2.5, Ω = 600 RPM

Figure 4.16 shows the data sets plotted as histograms for three experiments for *mfb50*, similar to the previous experiments with p_{max}. The absolute values plotted on the vertical axis are now degrees crank angle rather than pressure values. Again, a reference case (not displayed here) was taken and a threshold factor of $x_{PI} = 2.5$ determined. Ratios between surface pre-igniting cycles and spark-igniting cycles were formed. Note that unlike with p_{max}, surface pre-ignition actually makes the *mfb50* value smaller, so here the yellow curves indicate surface pre-igniting cycles. Red lines indicate spark combustion. Examination of Figure 4.16 shows that there is now much less distinction between the distribution of the surface pre-igniting and spark igniting cycles. Furthermore, the glow-plug temperature appears to have an impact on all of the burn durations.

The net heat release per degree crank angle $Q_{n\Theta}$ was also considered as a surface pre-ignition criterion. In Figure 4.17, $Q_{n\Theta}$ is plotted over a range of 90 degrees crank angle.

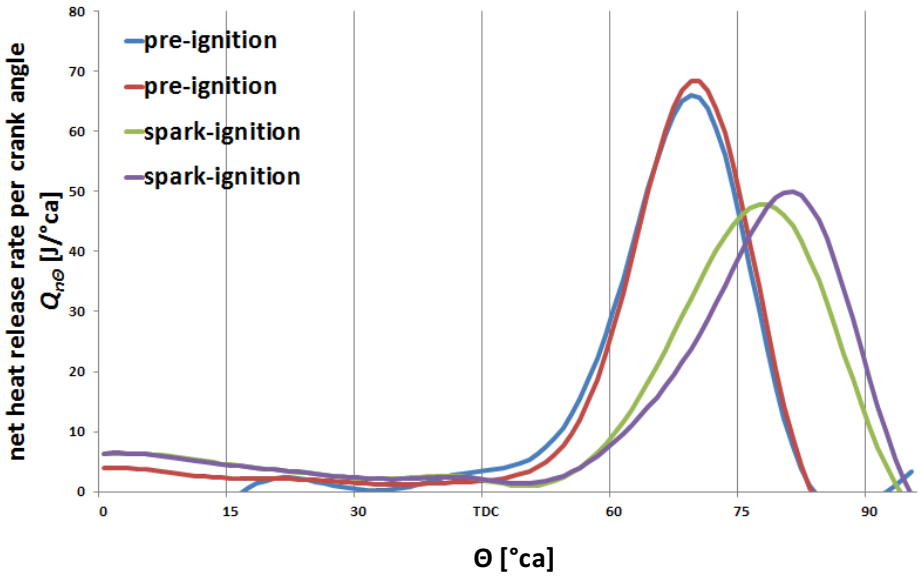

Figure 4.17. Net heat release rate per degree crank angle $Q_{n\Theta}$. $\Theta_i = 5$°ca bTDC, $T_{gp} = 780$°C surface pre-ignition cycles, $T_{gp} = 550$°C spark-ignition cycles, $\tau = 6$, *Fuel*: iso-octane, $\lambda = 1.0$, $T_c = 80$°C, $T_a = 30$°C, $\Omega = 600$ RPM, $x_{PI} = 2$

Figure 4.17 shows two data sets each for surface pre-igniting and spark-igniting cycles. The more advanced, higher curves indicate surface pre-ignition. In order to develop a method to rank these cycles, there are several possibilities which include a function that separates all cycles that reach a threshold of (say) 60 J/°ca from those who stay below that threshold. However, cycle-by-cycle variations make this a challenging approach. It was therefore decided to base the analysis on the heat release rate at 8°ca aTDC which forms two normal distributions. The method is then identical to the one used for the $p_{\max}$ and *mfb50* analyses. Histograms are plotted and two normal distributions are fitted with the help of a threshold.

Very similar to the trends obtained from the p_{max} and *mfb50* anlyses, the $Q_{n\Theta}$ analysis shows that the pre-igniton tendency increases with weaker mixtures. The threshold temperature for surface pre-igniting mixtures in the regime of stoichiometric are similar to the temperatures extracted using the maximum pressure criterion. However, the results using the heat release method will obviously depend on the crank angle chosen for analysing the heat release rate (8 °ca aTDC) and to some extent on the details of the net heat release calculation method, and the method for calculating the ratio of heat capacities for different stoichiometric levels.

4.4.4. Pressure-Based Method with Cycle-Resolved Temperature Determination

The surface pre-ignition occurred in ‘waves’ at intermediate temperatures - once a cycle surface pre-ignites, then a number of subsequent cycles are likely to surface pre-ignite as well, but then the engine reverts to spark-ignition as the glow-plug and cylinder wall have cooled down sufficiently for the surface ignition criterion to cease to be fulfilled. This is shown in Figure 4.18 where the temperature of the glow-plug is presented on the secondary vertical axis.

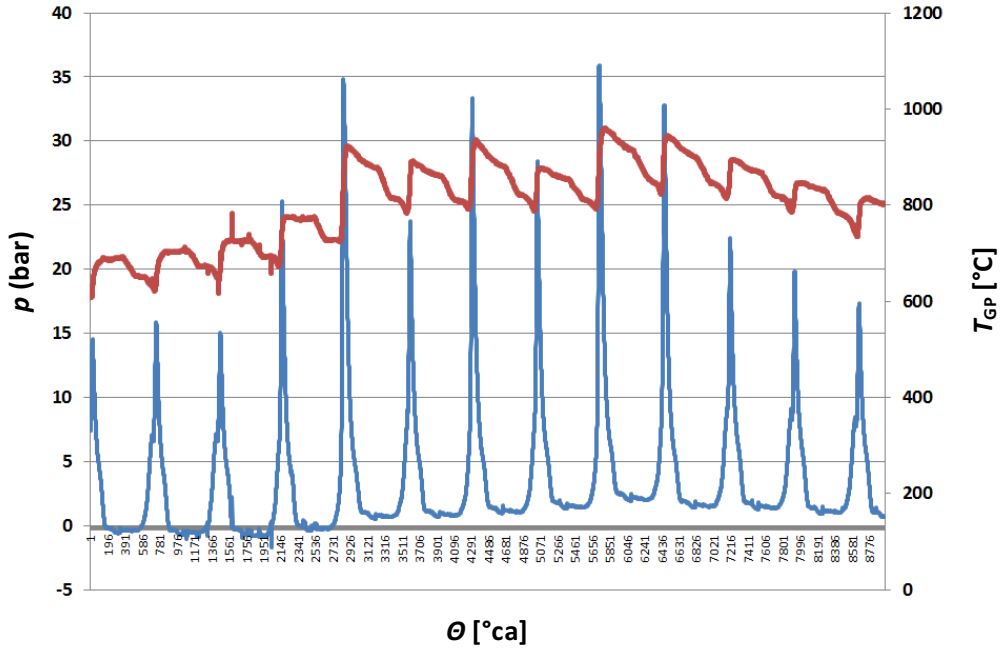

Figure 4.18. In-cylinder pressure and glow-plug temperature during surface pre-ignition when the PID controller was set to T_{GP} = 800°C. Θ_i = 5°ca bTDC, τ = 6, *Fuel*: iso-octane, T_c = 80°C, T_a = 30°C, x_{PI} = 2.5, Ω = 600 RPM

This suggests that the method of using average temperatures over the range of a whole experiment might produce an inaccurate picture of the real surface pre-ignition behaviour. It was therefore decided to analyse the glow-plug temperature data on a cycle-by-cycle basis.

To explain the new methodology, in Figure 4.19, four cycles are plotted. These are two consecutive spark-igniting cycles in blue and two consecutive surface pre-igniting cycles (T_{GP} = 850°C) in red. The in-cylinder pressure is displayed along with the respective temperature curves.

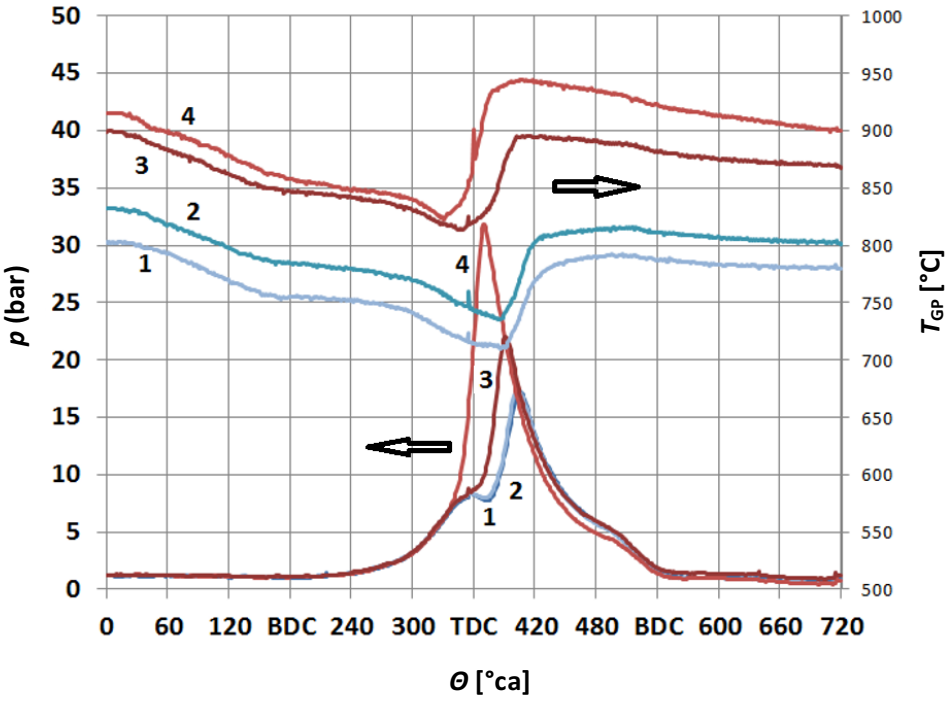

Figure 4.19. Pressure and temperature curves for surface pre-igniting (red) and spark igniting (blue) cycles. Θ_i = 5°ca bTDC, τ = 6, *Fuel*: iso-octane, T_c = 80°C, T_a = 30°C, x_{PI} = 2.5, Ω = 600 RPM, T_{GP} = 850°C.

For the new method to assess pre-ignition, an average of the glow-plug temperature was formed between $TDC_{exhaust}$ and TDC_{firing} for every cycle.

Figure 4.20 shows the results from a lambda sweep, with a scatter plot showing the maximum pressure and window-averaged glow-plug temperature for every cycle with a range of different average glow-plug temperatures.

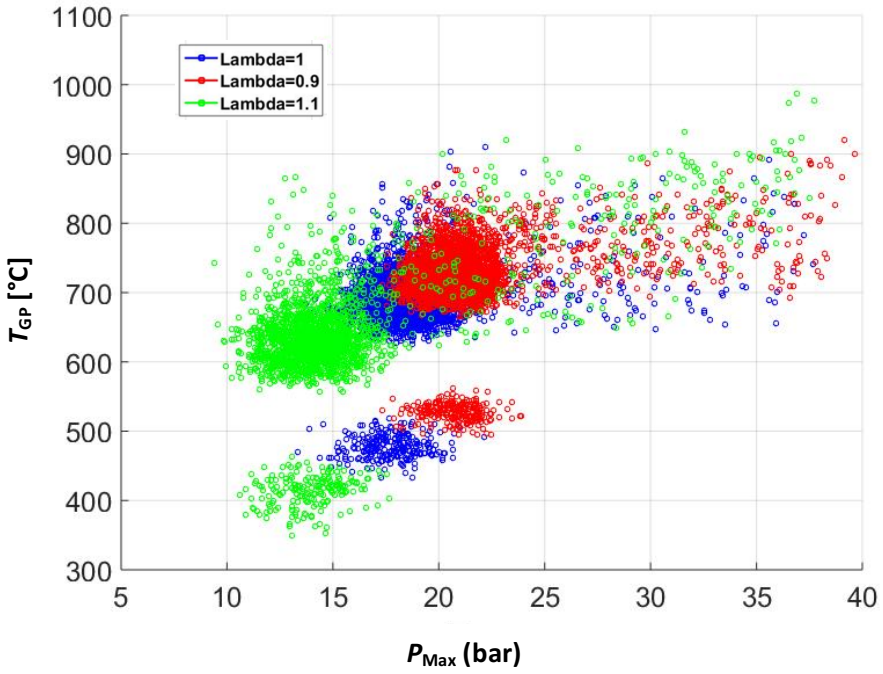

Figure 4.20. Window-averaged glow-plug temperatures and maximum pressure for every cycle (scatter plot for lambda sweep). Θ_i = 5°ca bTDC, τ = 6, *Fuel*: iso-octane, T_c = 80°C, T_a = 30°C, x_{PI} = 2.5, Ω = 600 RPM

Reference cycles were recorded when the glow-plug was turned off and no surface pre-ignition was induced. These are the regimes in Figure 4.20 with the lower temperatures and pressures. They are crucial for the analysis as they are used to determine the threshold for surface pre-ignition according to Equation 4.8. As expected, richening the mixture led to higher temperatures and pressures. Above this region sits the area of cycles which are spark-igniting while the glow-plug is hot. At these higher temperatures to the right are cycles with higher pressures that have surface pre-ignited.

In order to form ratios of surface pre-ignition to spark ignition it is necessary to consider temperature bands or 'bins'. Figure 4.21 shows a subset of the stoichiometric data from Figure 4.20 with a temperature bin of 690°C to 710°C, and the pre-ignition pressure threshold set at 2.5 standard deviations above the mean maximum pressure value during spark ignition.

Ratios can then be calculated by counting the cycles above and below the pressure threshold for surface pre-ignition.

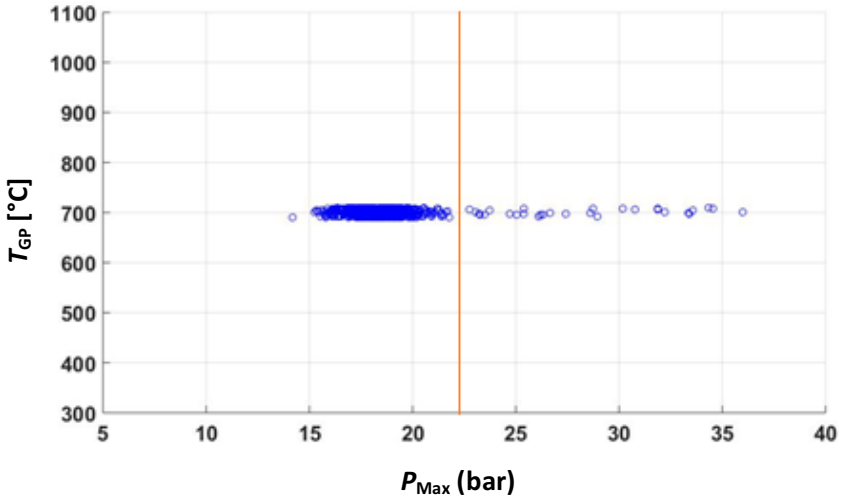

Figure 4.21. Subset of the window-averaged glow-plug temperatures and maximum pressure for every cycle from Figure 4.20 to illustrate a temperature bin of 690°C to 710°C with a surface pre-ignition pressure threshold (t_{PI}) of 22 bar. λ=1, Θ_i = 5°ca bTDC, τ = 6, *Fuel*: iso-octane, T_c = 80°C, T_a = 30°C, x_{PI} = 2.5, Ω = 600 RPM

To refine the method, parametric studies were conducted, to vary the width of the temperature bin, the number of cycles to be analysed, the standard deviation multiplication factor (x_{PI}) and the minimum number of events for a spark ignition or pre-ignition bin to be valid.

- Firstly this involves the size of the temperature bin. The effect of a varying size of that bin can be seen in Figure 4.22 where the data set of λ=1 from Figure 4.20 has been selected.

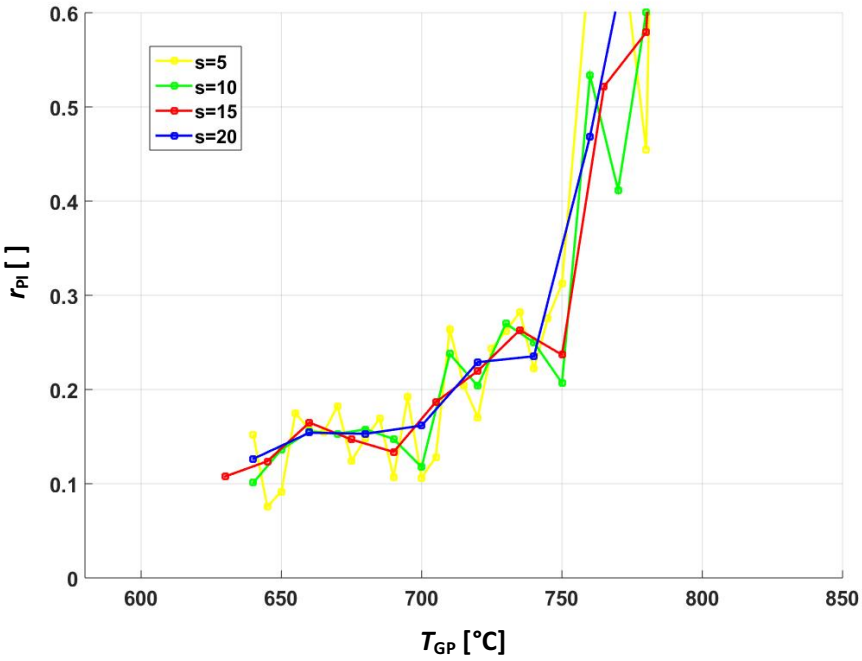

Figure 4.22. Effect of bin size, s [K], N = 1000 cycles, n > 5, Θ_i = 5°ca bTDC, τ = 6, λ = 1.0, *Fuel*: iso-octane, T_c = 80°C, T_a = 30°C, x_{PI} = 2.5, Ω = 600 RPM

It can be seen that the larger the temperature band, the smoother is the curve. This is to be expected given that more data points go into the analysis as the bin width increases which removes variances. However, if the selected bin width is too large, much of the resolution of the data is lost so a bin size of 15 K was chosen as the most appropriate bin width.

- Secondly, it was necessary to assess how many cycles should be analysed in a given experiment. Four different sample sizes were tested and the results plotted in Figure 4.23. This again is the data set of λ = 1 from Figure 4.20.

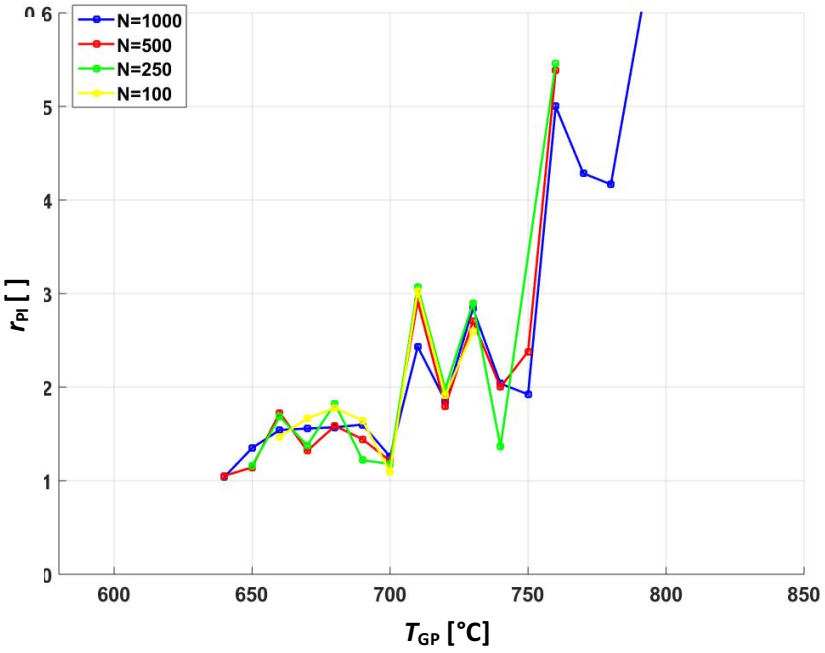

Figure 4.23. Effect of sample size N [ ], s =10 K, n > 5, Θ_i = 5°ca bTDC, τ = 6, λ = 1.0, *Fuel*: iso-octane, T_c = 80°C, T_a = 30°C, x_{PI} = 2.5, Ω = 600 RPM

It can be seen that a larger sample size makes variances smaller. It is therefore advisable to make the sample size as large as possible. The sample size of 1000 cycles per experiment was selected for all future experiments. At Ω = 600 RPM this corresponds to 200 s of data.

- Thirdly a cut-off size rule was introduced to specify the minimum number of events in a bin. When looking at Figure 4.20, it can be seen that in some temperature bands, there would be only very few cycles to be identified as either spark-igniting or pre-igniting. This is particularly an issue with low temperature surface pre-igniting cycles and high temperature spark-igniting cycles. Calculating the ratio of spark-igniting to surface pre-igniting cycles in these areas can skew the analysis. Figure 4.24 shows a sweep of different cut-off sizes to propose a minimum number of data points to be selected in any given temperature band.

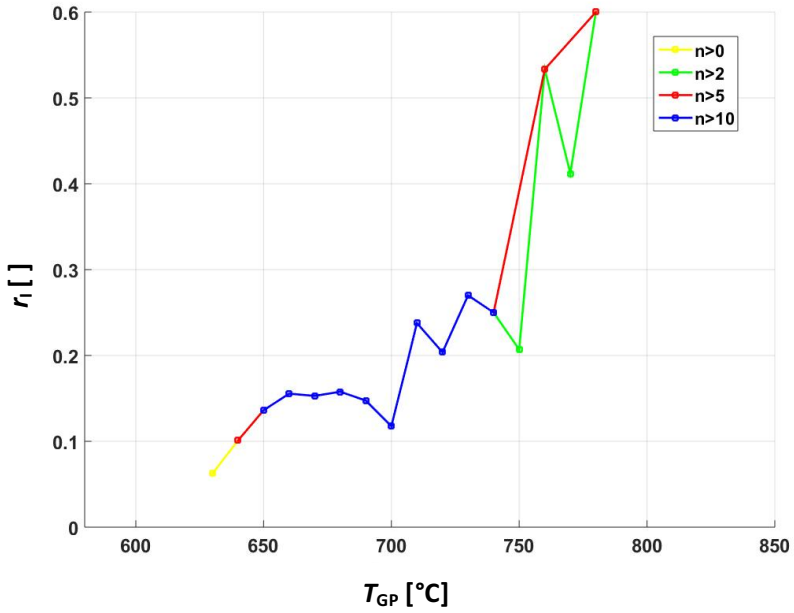

Figure 4.24. Effect of 'cut-off size'(n) sweep. N = 1000, s =10 K, Θ_i = 5°ca bTDC, τ = 6, λ = 1.0, *Fuel*: iso-octane, T_c = 80°C, T_a = 30°C, x_{PI} = 2.5, Ω = 600 RPM

It can be seen in Figure 4.24 that a larger cut-off size reduces the variances and improves the smoothness of the graph. It however also reduces the length of the useable data and there should therefore be a compromise which was selected to be of a cut-off size of larger than 5.

The parameters from the parametric study are summarized in Table 4.2.

Table 4.2. Parameters used in defining the pre-ignition temperature

Parameter	**Range examined**	**Value used**
Width of the temperature bin [K]	5-20	15
Number of cycles to be analysed	100-1000	1000
Standard deviation multiplication factor (x_{PI})	2-6	2
Minimum number of events in a spark -ignition or pre-ignition bin to be valid	2-10	5

As an alternative to the p_{Max} method, the pressure at TDC was analysed and a p_{TDC} (firing) method was assessed as a measure for a surface pre-ignition rating on a cycle by cycle basis. Figure 4.25 shows the scatter plot of individual cycles for p_{TDC} for a lambda sweep which show a narrower distribution for the firing cycles.

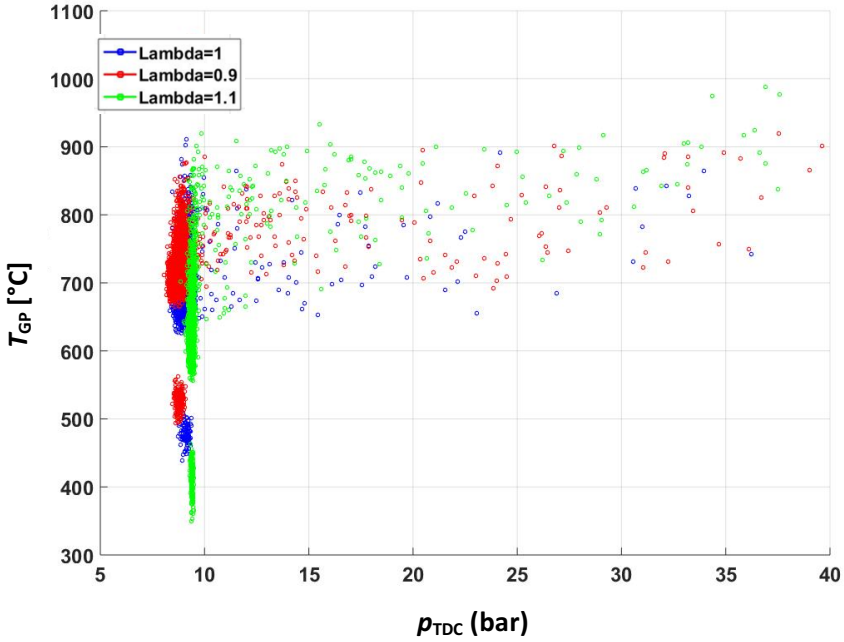

Figure 4.25. Scatter plot for lambda sweep. Window-averaged glow-plug temperatures plotted against pressure at TDC for every cycle. Θ_i = 5°ca bTDC, τ = 6, *Fuel*: iso-octane, T_c = 80°C, T_a = 30°C, x_{PI} = 2.5, Ω = 600 RPM

Figure 4.25 shows the distributions of pressure and cycle-averaged temperature at TDC for spark-igniting and surface pre-igniting cycles. The richer mixture shows lower pressures at TDC than the weaker mixtures as this pressure rise is dominated by compression instead of combustion and the ratio of heat capacities will be lowest for the rich mixture (Section 4.2.2.). This can be seen in Figure 4.26.

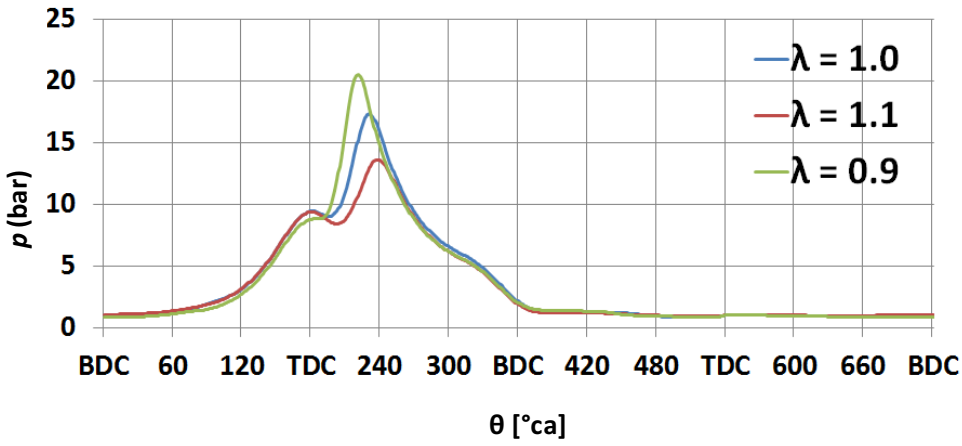

Figure 4.26. Ensemble-averaged pressure for 400 spark igniting cycles. Θ_i = 5°ca bTDC, τ = 6, *Fuel*: iso-octane, T_c = 80°C, T_a = 30°C, x_{PI} = 2.5, Ω = 600 RPM

Figure 4.26 shows the extended ensemble averaged pressure for 400 cycles at spark igniting conditions. The richer mixture is burning faster than the weaker mixture to give a higher maximum pressure despite a lower pressure at TDC. The temperature at TDC can be calculated with Equation 4.9:

$$T_{TDC} = T_{IVC} \frac{p_{TDC} V_{TDC}}{p_{IVC} V_{IVC}} \tag{4.9}$$

The comparison between pressure and temperaure at TDC and at inlet valve closure (IVC) with an assumed $T_{IVC} = T_C$ = 353K, allows for a calculation of T_{TDC}. The results are plotted in Figure 4.27.

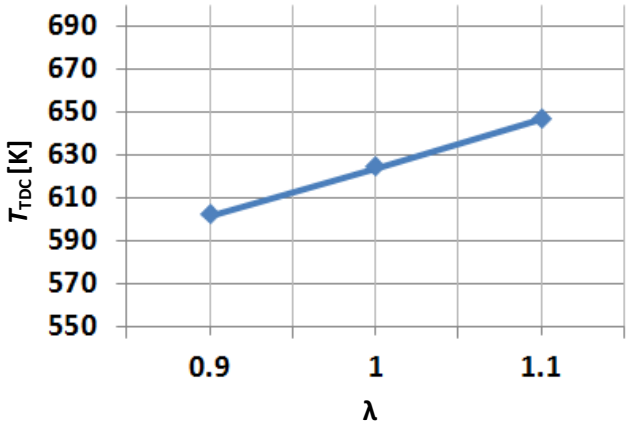

Figure 4.27. Calculated Temperature at TDC. Θ_i = 5°ca bTDC, τ = 5.5, *Fuel*: iso-octane, T_c = 80°C, T_a = 30°C, Ω = 600 RPM, x_{PI} = 2

Similar to the p_{TDC} a clear upwards trend of the temperature of T_{TDC} from rich to weak mixtures is visible. This helps to explain why the weak mixtures have a lower surface pre-ignition temperature.

Figure 4.27 shows that an assessment of the p_{max} is more appropriate compared to $p_{TDC.}$ The maximum pressure criterion is the simplest and least ambiguous to implement and as there are no advantages in using analyses based on combustion analysis, then it seems simplest to use the maximum pressure criterion.

4.5. Results and Discussion

4.5.1. Surface Pre-Ignition Experiments without Humidity

A range of different experimental variables were tested and analysed with the cycle averaged p_{max}-based method where 600 cycles were analysed for every data point. The effect of ignition timing Θ_i on the surface pre-ignition behaviour can be seen in Figure 4.29.

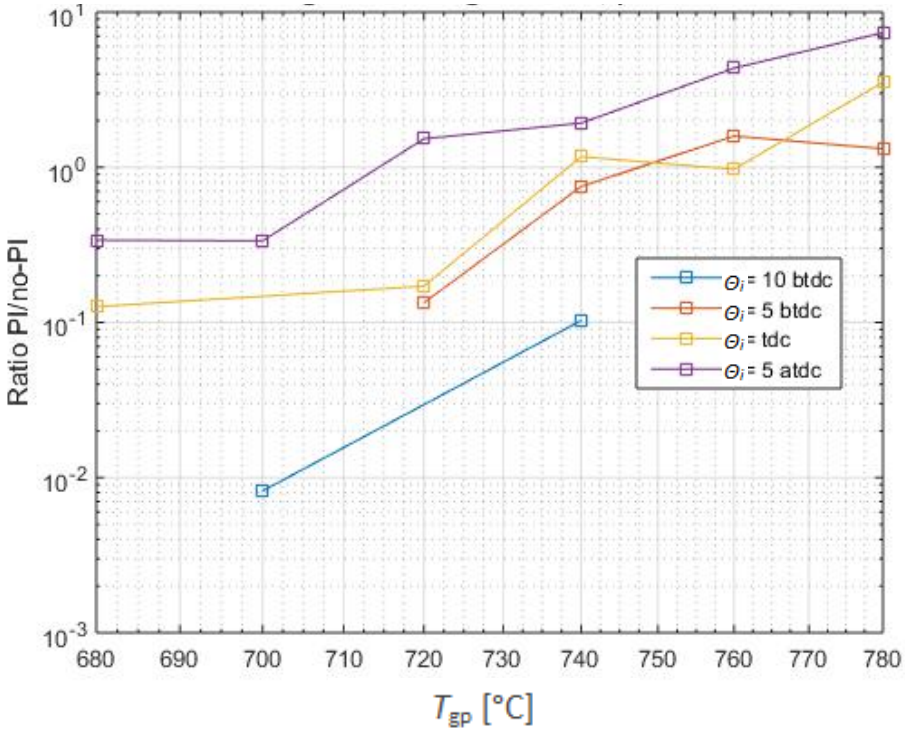

Figure 4.29. Ignition timing effect on ratio of surface pre-ignition; $\tau = 6$, *Fuel*: iso-octane, $\lambda = 1.0$, $T_c = 80°C$, $T_a = 30°C$, $\Omega = 600$ RPM, 600 cycles per ignition timing, $x_{PI} = 2.5$

It can be seen that a more retarded ignition timing brings with it a stronger surface pre-ignition tendency. More cycles are surface pre-igniting at the same glow-plug temperatures when ignition is retarded or a lower glow-plug temperature is necessary to achieve the same surface pre-ignition behaviour at a retarded ignition timing. This can be explained with retarded ignition because there is more time for pre-ignition to occur and the engine parts will be hotter. Namely the exhaust valve and the spark plug are heated up more during combustion. This enhances pre-ignition as can be seen in Figure 4.29.

Next, the effect of lambda variation was analysed as can be seen in Figure 4.30.

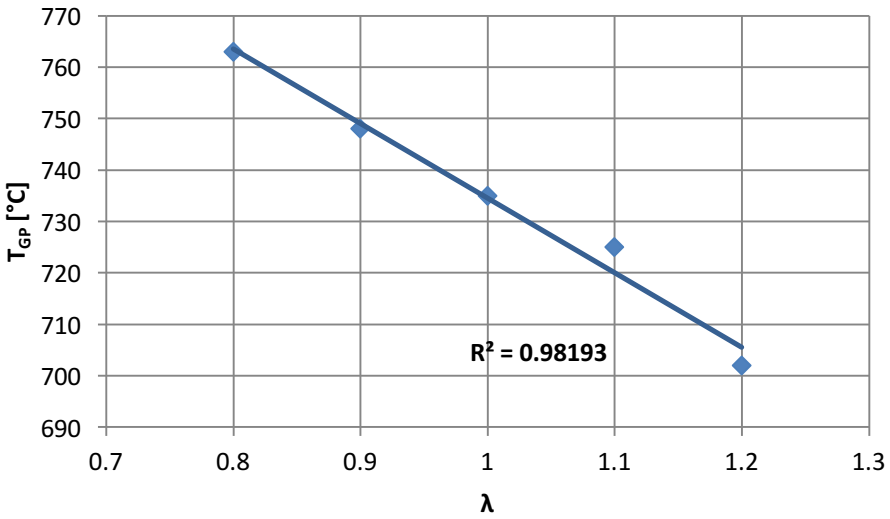

Figure 4.30. Temperature of glow-plug to achieve unity ratio r_{PI} = 1 Lambda sweep; Θ_i = 5°ca bTDC, τ = 6, *Fuel*: iso-octane, T_c = 80°C, T_a = 30°C, Ω = 600 RPM, 600 cycles per data point, x_{PI} = 2.5

In Figure 4.30 it can be seen that the necessary glow-plug temperature to cause a unity ratio of surface pre-ignition and spark ignition decreases with higher values for lambda. This makes it apparent that the surface pre-ignition tendency increases with weaker mixtures. In other words: the weaker the mixture, the lower the temperature of the glow-plug necessary to achieve the same surface pre-ignition rate as for a richer mixture. This contradicts earlier work [53]. The tests were thus repeated with the cycle-by-cycle method.

As described in the previous section, the cycle-averaged analysis is prone to errors so all subsequent tests were analysed with the p_{max} cycle-by-cycle method. A lambda sweep was performed for iso-octane and the results can be seen in Figure 4.31.

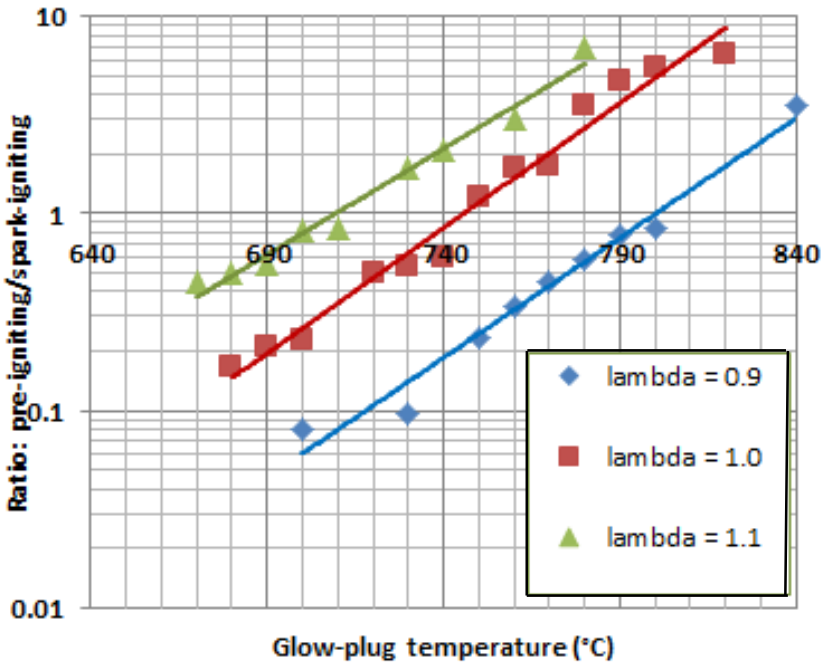

Figure 4.31. The influence of glow-plug temperature on the incidence of pre-ignition for a Lambda sweep. Θ_i = 5°ca bTDC, τ = 5.5, *Fuel*: iso-octane, T_c = 80°C, T_a = 30°C, Ω = 600 RPM, x_{PI} = 2.

Figure 4.31 confirms the unexpected trend – as the mixture is richened then a higher glow-plug temperature is needed for pre-ignition; the same trend was found with toluene. One explanation is that the weaker mixture will have a higher compression index (as the ratio of heat capacities will be higher), and a lower specific heat capacity. The higher compression index will mean higher compression temperatures, and the lower specific heat capacity will mean that less heat needs to be transferred from the glow-plug to further raise the mixture temperature; this agrees with the modelling in Figures 4.5 and 4.6. This confirms the trends that have been seen before with the scatter plot data in Figure 4.24 and adds additional insights to the work by Downs and Theobald [53].

A sweep of compression ratio showed no discernible differences in pre-ignition temperature

Figure 4.32 shows the influence of the glow plug temperature on the incidence of pre-ignition for a fuel sweep (chain structured molecules = parafins, olefins, oxygenates) under stoichiometric conditions.

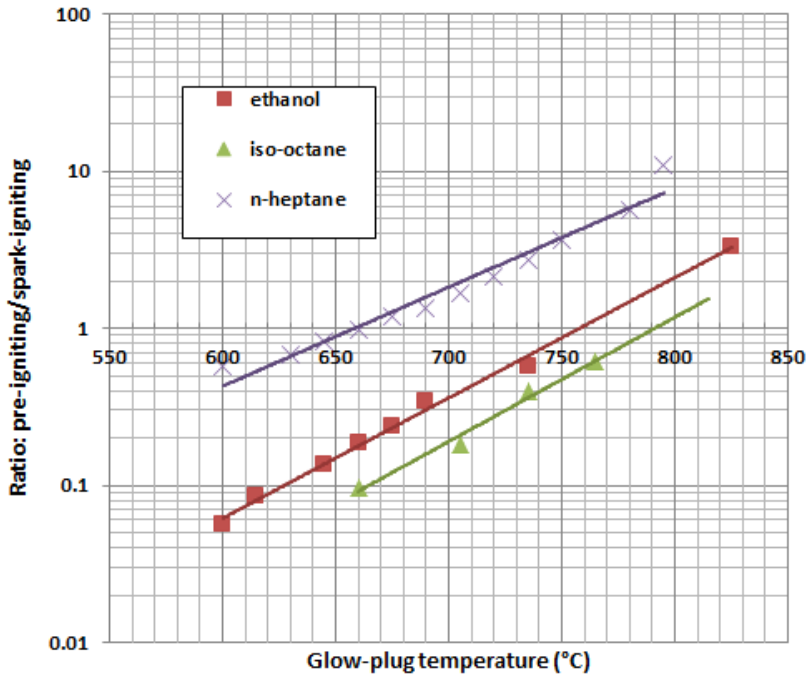

Figure 4.32. The influence of glow-plug temperature on the incidence of pre-ignition for stoichiometric tests; the straight lines are exponential fits. Fuel sweep. Θ_i = 5°ca bTDC, λ = 1.0, τ = 5.5, T_c = 80°C, T_a = 30°C, Ω = 600 RPM, x_{PI} = 2

As would be expected, Figure 4.32 shows that the incidence of pre-ignition increases with temperature, and the straight lines on the logarithmic plot show that there is an exponential dependence on temperature.

Figure 4.33 presents data for cyclic compounds that in general have higher pre-ignition temperatures than the non-cyclic compounds reported in Figure 4.32.

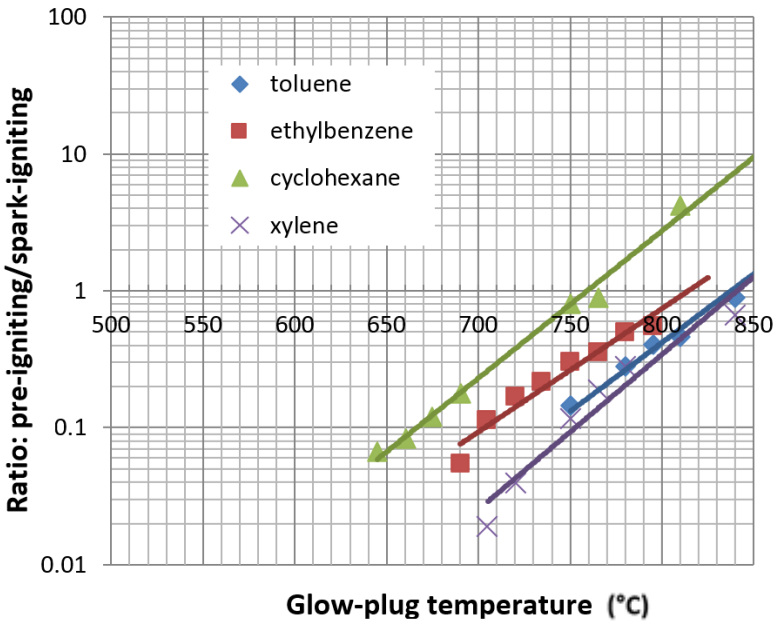

Figure 4.33. The influence of glow-plug temperature on the incidence of pre-ignition for stoichiometric tests of cyclic compounds; Fuel sweep (molecules with ring structures) $\Theta_i = 5$°ca bTDC, $\lambda = 1.0$, $\tau = 5.5$, $T_c = 80$°C, $T_a = 30$°C, $\Omega = 600$ RPM, $x_{PI} = 2$

Figure 4.33 shows that the aromatic compounds have higher pre-ignition temperatures than the cycloalkane, and as the length of the side chain on the aromatic increases, then the pre-ignition temperature is reduced.

Figure 4.34 compares n-pentane with iso-pentane and (as might be expected from the data in Figure 4.32) the branched isomer has a higher pre-ignition temperature than its straight-chain isomer.

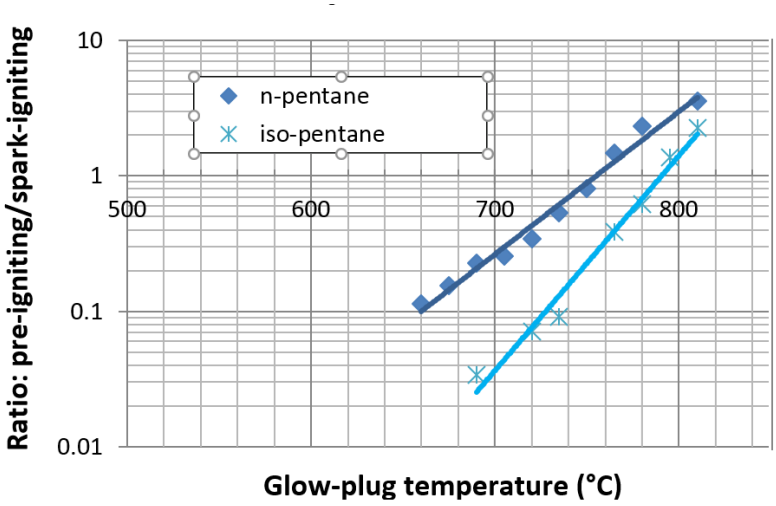

Figure 4.34. The influence of glow-plug temperature on the incidence of pre-ignition for stoichiometric tests of pentane isomers; Θ_i = 5°ca bTDC, λ = 1.0, τ = 5.5, T_c = 80°C, T_a = 30°C, Ω = 600 RPM, x_{PI} = 2

Figure 4.35 shows that methanol is more susceptible to pre-ignition than ethanol.

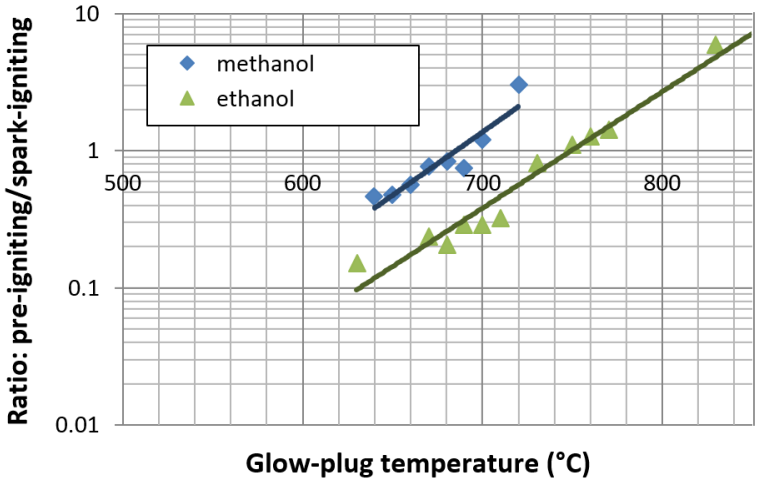

Figure 4.35. The influence of glow-plug temperature on the incidence of pre-ignition for stoichiometric tests of methanol and ethanol; Θ_i = 5°ca bTDC, λ = 1.0, τ = 5.5, T_c = 80°C, T_a = 30°C, Ω = 600 RPM, x_{PI} = 2

Studies show that an increased ethanol content led to more surface pre-ignition, and this is in line with the findings here, as ethanol is more susceptible to surface pre-ignition than iso-octane [89].

If the unity ratio of pre-igniting to spark-igniting cycles is used to define the pre-ignition temperature, then the results are as shown in Table 4.3 along with the MON and RON values, and the Pre-ignition Resistance (PR) values from Downs and Theobald [53].

Table 4.3. Heater temperature for a unity ratio of pre-igniting to spark-igniting cycles compared with the Pre-ignition Resistance (PR) of Downs and Theobald [53].

fuel	Surface Pre-ignition Temperature (°C)	MON	RON	Pre-ignition Resistance [53]	Heater Temperature [53] (°C)
n-heptane	660	0	0		
methanol	685	88.6	108.7		
n-pentane	755	61.9	62		
ethanol	758	89.7	108.6		
cyclohexane	760	78	83	0	1071
iso-octane	790	100	100	100	1175
iso-pentane	790	93	93.5	73	1120
ethyl benzene	815	97.9	109	15	1025
toluene (methyl benzene)	838	100.6	117	91	1125
xylene (dimethyl benzene)	842	115	118	118	1165

Downs and Theobald [53] reported their data (summarised here in Table 4.3) for conditions slightly rich (0-10%) of stoichiometric, while the surface pre-ignition temperature in the current work is for stoichiometric operation. Downs and Theobald also note that the heat input required for pre-ignition reduced when the compression ratio and speed were increased. The corresponding heater temperature reported by Downs and Theobald [53] seem very high and indeed temperatures of around 900°C were reported. With disabled heating these measurements come from a heater that was made by butt welding a pair of thermocouple materials, and the temperature was derived by filtering the dc component from the ac heating current to find the temperature. As no details of the technique are reported it is hard to explain these results. Given that the reported heater temperatures are higher than our results,

one possible explanation is that their data was collected in Kelvin (K) and wrongfully reported as Celsius (°C).

Figure 4.36 shows a plot of the RON and MON values with the surface pre-ignition temperature of the fuels stated in Table 4.3.

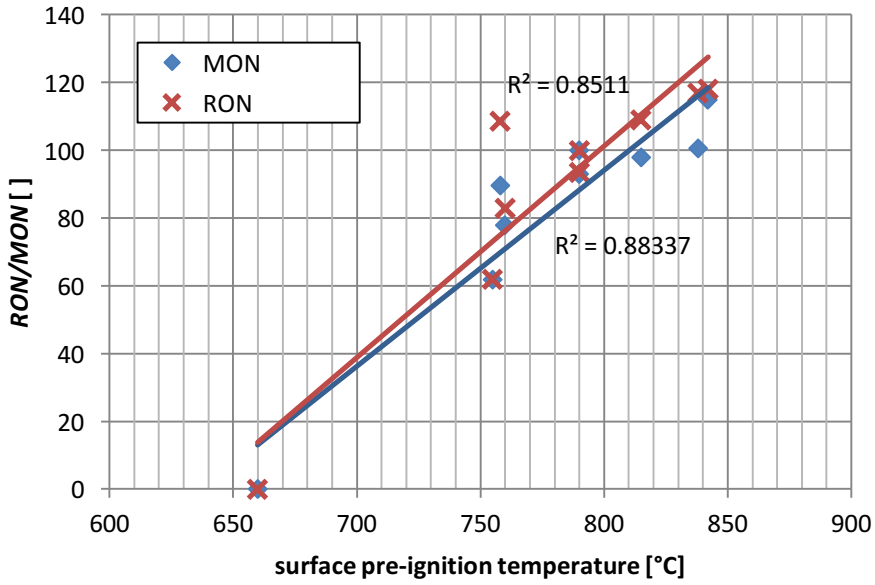

Figure 4.36. Correlations of RON and MON with surface pre-ignition temperature.

Figure 4.36 shows that there is only a poor correlation between the RON and MON values and the surface pre-ignition temperature. This is further evidence to the fact that the pre-ignition tendency is independent of the octane performance of a fuel.

The effect of fuel blending was analysed and results can be seen in Figure 4.37.

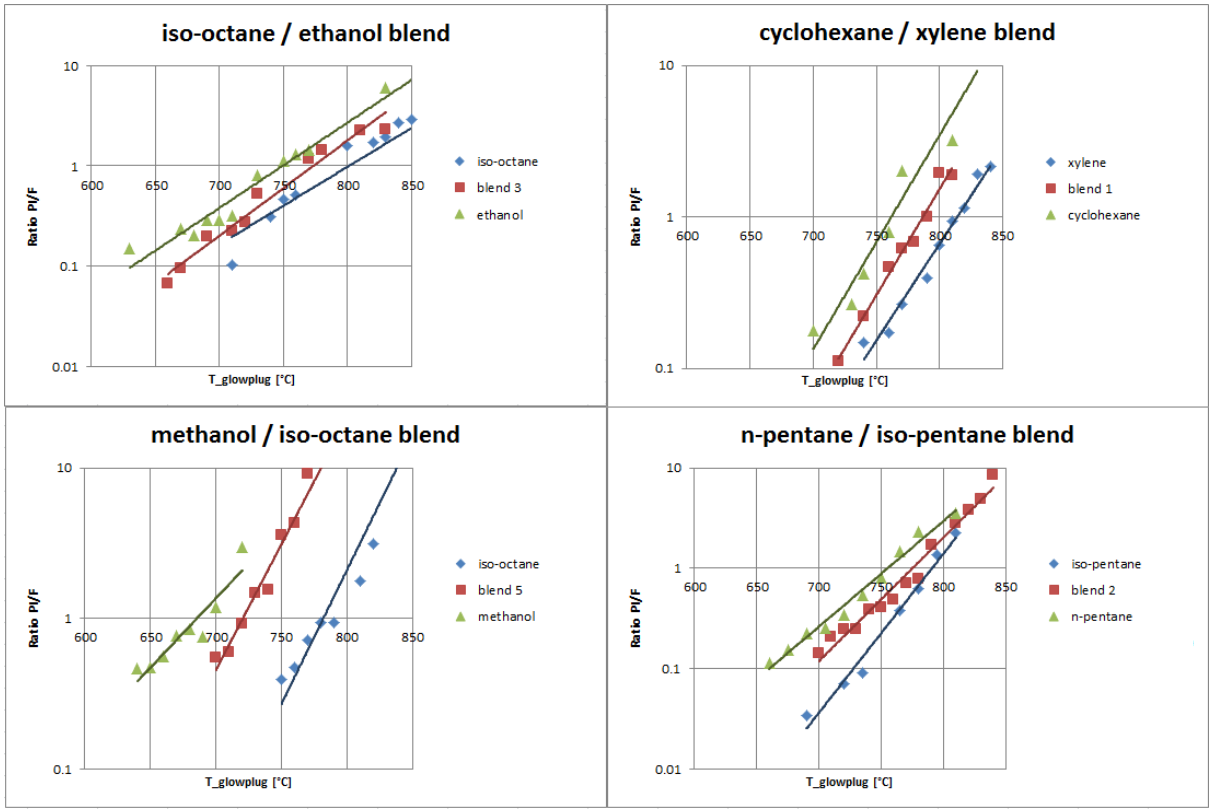

Figure 4.37. The influence of glow-plug temperature on the incidence of pre-ignition for stoichiometric fuel mixtures (volumetric 50%:50%) compared with their pure components. Θ_i = 5°ca bTDC, λ = 1.0, τ = 5.5, T_c = 80°C, T_a = 30°C, Ω = 600 RPM, x_{PI} = 2

Blends of volumetric 50%:50% n-pentane and iso-pentane (blend 2), cyclohexane and xylene (blend 1) as well as ethanol and iso-octane (blend 3) were tested for their pre-ignition susceptibility and compared to results of their unblended components. The data in Figure 4.37 for volumetric 50% mixtures suggests a linear mixture rule between the volumetric based composition and the surface pre-ignition behaviour, except for the methanol and iso-octane mixture. The repeat of the ethanol data shows good agreement with the data plotted in Figure 4.35.

The reported data includes several repeats of iso-octane at identical conditions. These were summarized in Figure 4.38 to give an indication of the repeatability of our experimental method.

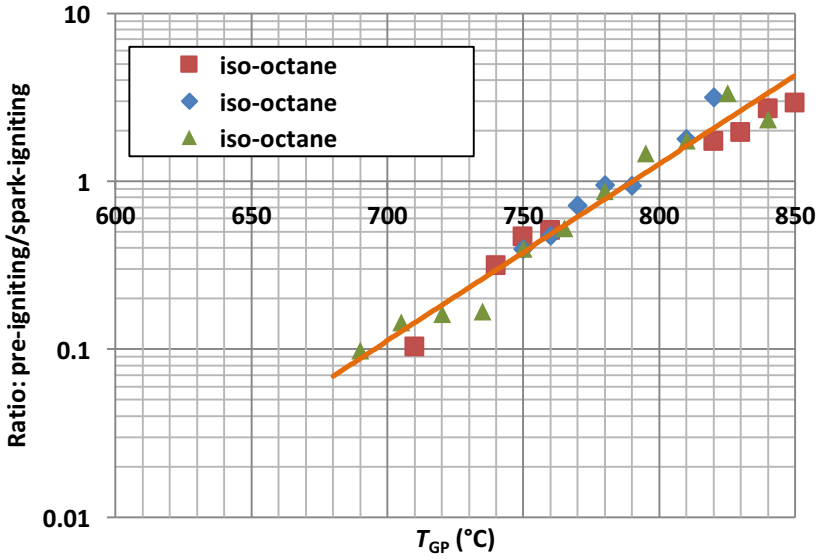

Figure 4.38. Comparison of all iso-octane data to show repeatability. Dotted orange line shows mean of three data sets. Θ_i = 5°ca bTDC, λ = 1.0, *Fuel*: iso-octane, τ = 5.5, T_c = 80°C, T_a = 30°C, Ω = 600 RPM, x_{PI} = 2

As can be seen in Figure 4.38, there is good agreement with the three iso-octane data sets. The surface pre-ignition temperature (ratio of pre-igniting/spark igniting cycles r_{PI} = 1) varies only slightly between 785°C and 795°C indicating very good repeatability of our tests.

4.5.2. The Effect of Humidity on Surface Pre-Ignition

The humidifying unit (introduced in Chapter 3) was used to increase the relative humidity of the intake air of the engine and to study the influence of humidity on surface pre-ignition in the E6 engine.

A sweep of three levels of humidity was performed and this can be seen in Figure 4.39.

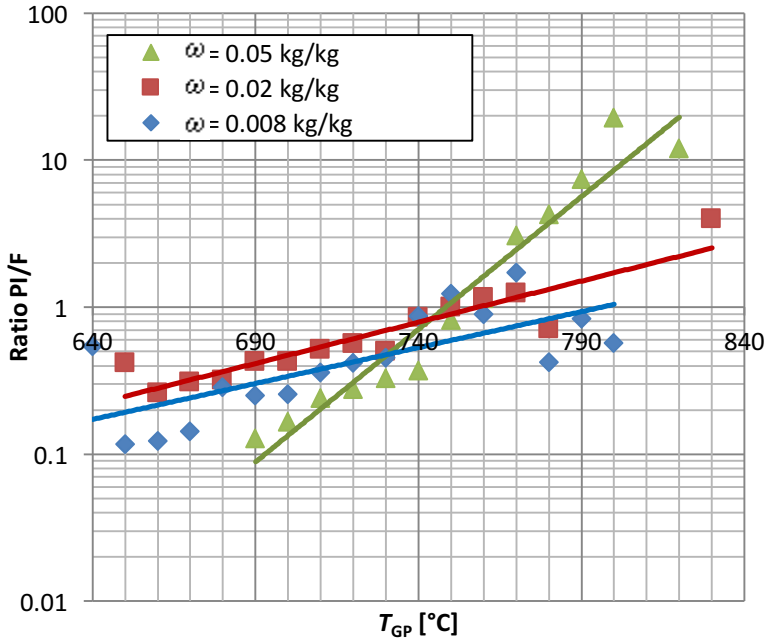

Figure 4.39. Effect of air intake humidity on surface pre-ignition. *Fuel*: iso-octane, $\Theta_i = 5$°ca bTDC, $\lambda = 1.0$, $\tau = 5.5$, $T_c = 80$°C, $T_a = 50$°C, $\Omega = 600$ RPM, $x_{PI} = 2$

Figure 4.39 shows no clear trend in the surface pre-ignition tendency for the sweep of humidity at this stoichiometric experiment. The relative humidity of 0.05kg/kg equals 100% (relative) humidity at 43°C which is very much an upper limit for a real world application.

In the next experiment we tested the effect of two humidity levels on iso-octane at three different mixture strengths. The results can be seen in Figure 4.40.

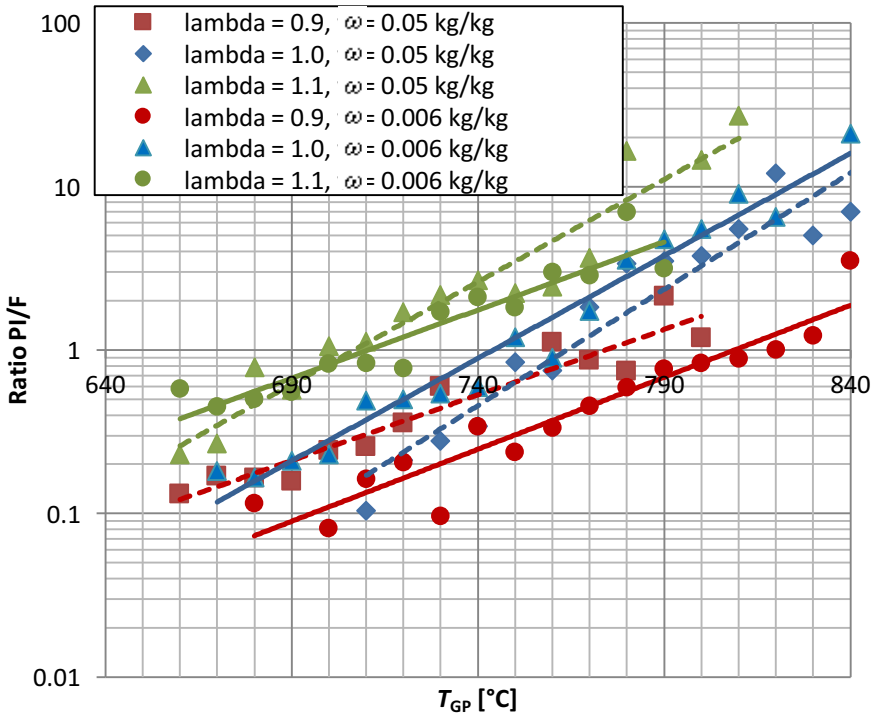

Figure 4.40. Effect of air intake humidity on surface pre-ignition. *Fuel:* iso-octane, Θ_i = 5°ca bTDC, τ = 5.5, T_c = 80°C, T_a = 50°C, Ω = 600 RPM, x_{PI} = 2**, '***on'*: humidity=0.05 kg/kg, '*off*': humidity=0.006 kg/kg

There is a rather clear trend in Figure 4.40 for both the rich and the weak mixtures, that an increased humidity increases the surface pre-ignition tendency. It is an unexpected result as one would assume that the increased humidity leads to a smaller γ which should bring the surface pre-ignition tendency down. The trend seen for the rich and weak mixtures can not be confirmed in repeated tests at stoichiometric conditions where there is an overlap in the humidity data.

In a further test toluene was analysed at stoichiometric conditions for two levels of humidity.

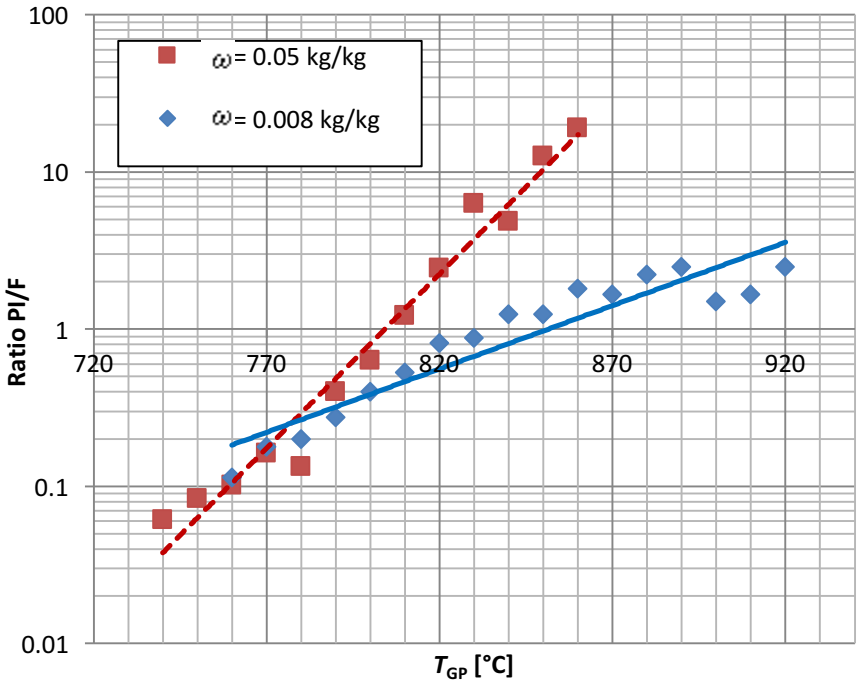

Figure 4.41. Effect of air intake humidity on surface pre-ignition. *Fuel:* toluene, $\Theta_i = 5$°ca bTDC, $\tau = 5.5$, $T_c = 80$°C, $T_a = 50$°C, $\Omega = 600$ *RPM*, $x_{PI} = 2$

It can be seen in Figure 4.41 that similar to the tests with iso-octane, a trend for higher levels of humidity to increase the surface pre-ignition tendency only becomes clear at higher temperatures.

The effect of humidity on an internal combustion engine can be compared to the effect of exhaust gas recirculation (EGR). The water in the air reduces the heating value per unit mass of mixture and subsequently reduces the adiabatic flame temperature. This leads to a proportional reduction in laminar burning velocity that was found to be independent of the equivalence ratio of mixture, pressure and temperature [91]. So, for an increased humidity we would expect to see a slower combustion but most of our results show that pre-ignition is more likely with increased humidity. This is the opposite of what we expected.

In any case, given that the lower, more realistic levels of humidity that were tested here had no discernible effect on pre-ignition, the conclusion to this investigation is that surface pre-ignition is not a function of humidity in a real-world road setting.

4.6. Summary

The objective of this chapter was the investigation of surface pre-ignition in a spark-ignition internal combustion engine. A closed loop temperature controlled glow-plug was fitted into a variable compression ratio research engine to control the incidence of surface pre-ignition. Attached to the glow-plug was a flame ionization sensor. A humidifying unit to control the humidity of the intake air was also deployed. The chapter considered several techniques of surface pre-ignition analysis.

- Flame ionization sensor and appropriate pulse logic
- In-cylinder pressure analysis, based on:
    - Maximum pressure
    - Pressure at TDC
    - Mass fraction burned
    - Net heat release rate

The in-cylinder maximum pressure was used to obtain statistical data on the incidence of pre-ignition compared with spark ignition. The surface pre-ignition temperature was window-averaged on a cycle-by-cycle basis with appropriate parameters.

A sweep of lambda and compression ratio was conducted for iso-octane, and the tendency for surface pre-ignition was recorded when surface pre-ignition was induced with the glow-plug and retarded spark timing.

A range of pure fuel components was tested for their susceptibility to surface pre-ignition. This included six chain-structured molecules (n-heptane, ethanol, n-pentane, iso-octane and iso-pentane) and four ring structured molecules (cyclohexane, ethyl-benzene, toluene and xylene). Some of these were selected as they had been tested in previous studies. From these fuels, four 50:50 blends by volume were selected and also tested for their surface pre-ignition tendency.

With the help of a humidifying unit the humidity of the intake air could be increased and the effect on surface pre-ignition of iso-octane and toluene was assessed under a range of stochiometries.

Key results are:

- A higher glow-plug temperature is needed for pre-igniting stoichiometric or rich mixtures compared to weak mixtures, and this was attributed to the weaker mixture having a higher compression index and a lower specific heat capacity.
- Alkanes and alcohols were found to be rather susceptible to surface pre-ignition.
- Straight chain molecules such as n-heptane, ethanol and n-pentane have a higher pre-ignition tendency than branched chain molecules such as iso-octane and iso-pentane.
- The pre-ignition tendency of ring-structured components depends on the length of the attached chain. Shorter side-chain molecules (xylene, toluene) are less susceptible to pre-ignition than longer side-chain molecules like ethyl-benzene; cyclohexane was more susceptible to pre-ignition than any of the aromatic fuels.
- For most of the fuel blends tested in this study (n-pentane and iso-pentane, cyclohexane and xylene, ethanol and iso-octane), a linear correlation between composition and surface pre-ignition tendency was observed. With methanol and iso-

octane the pre-ignition temperature for a 50:50 by volume mixture was closer to that of methanol than iso-octane.

- The effect of the intake air humidity on the surface pre-ignition tendency of the fuels tested at the operational experimental parameters was not significant but the pre-ignition tendency increased for high levels of humidity.

5. Knock and Heat Flux

5.1. Introduction

The previous chapters have expressed that knock can lead to failure of engine components and this damage is caused by the increased pressure but also, more importantly, by thermal stresses on the material. The thermal strains induced at the surface of the cylinder are proportional to the temperature gradients, which are directly related to the instantaneous heat flux. For this reason, further research into quantifying the effect of knock on in-cylinder heat transfer is of great importance to engine manufacturers. Relating the change in heat flux to knock parameters that are based on in-cylinder pressure measurements is the approach chosen in this chapter.

5.2. Previous Research Relating Knock Intensity and Heat Flux

Several researchers have sought correlations between surface heat flux and knock intensity [92-95]. Grandin and Denbratt [95] conducted their research on a single cylinder optical engine and concluded that severe knock intensities more than doubled the heat flux compared to a non-knocking cycle. They suggest that this is due to the increased charge motion and subsequent increase in Reynolds number as a result of auto-ignition. However, they did not define their knock index and reported only limited details of their heat flux probe. Figure 5.1 shows a plot of their surface temperature, cylinder pressure and heat flux. The temperature plots are very ‘smooth’, so it is possible that there is too much filtering/smoothing, or the transducer time constant is too long.

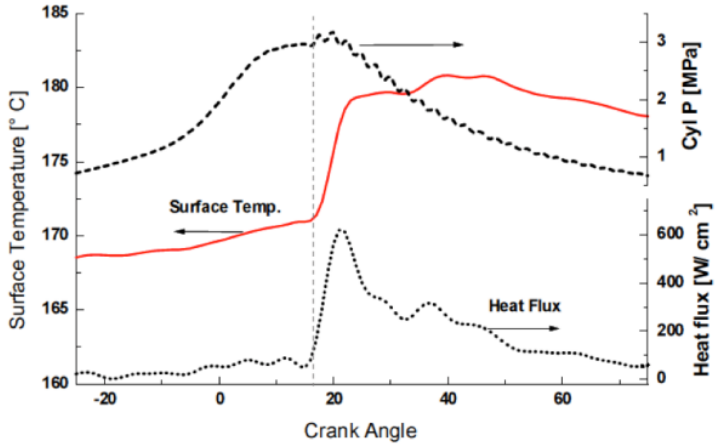

Figure 5.1. Surface temperature, pressure and heat flux. Data from Grandin and Denbratt [95] that appears to have been smoothed.

Syrimis *et al*. [94] also found that under light knocking conditions, the ensemble-averaged peak heat flux was increased for locations near the end gas, and for heavy knock, the ensemble-averaged peak heat flux increased significantly throughout the piston crown. The pressure data was filtered to 3 kHz and then analysed using a net heat release analysis, which is shown in Figure 5.2. A spike at about Θ = 20°ca aTDC is attributed to auto-ignition, but this is somewhat later than is usually encountered; one explanation is that their digital filter has introduced a phase lag.

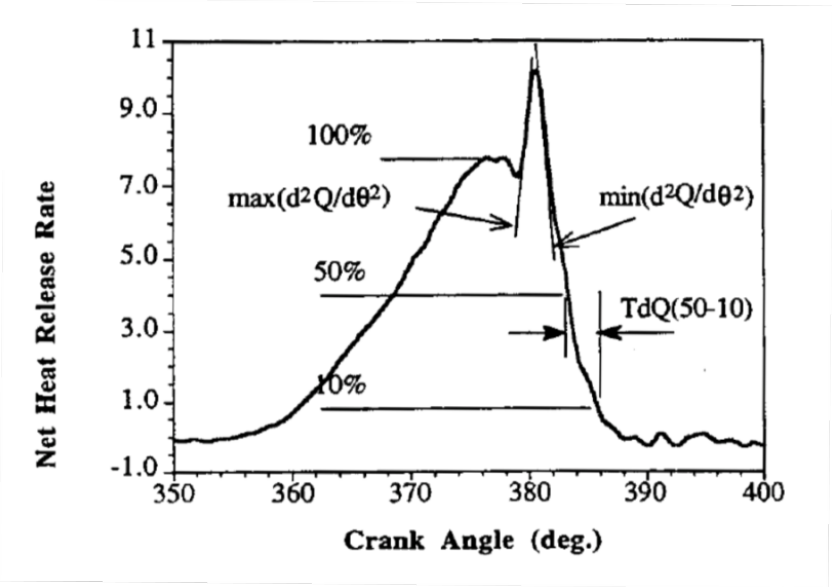

Figure 5.2. Results from Syrimis et al. [94] in which the knock event (~380 °ca) is late, possibly a consequence of filtering the pressure data to 3 kHz, which might have introduced a phase lag.

Syrimis *et al.* [94] sought to find correlations between the peak heat flux and various knock parameters. The results in Figure 5.3 are the most promising, but do not show any strong evidence of a correlation between the heat flux and knock intensity.

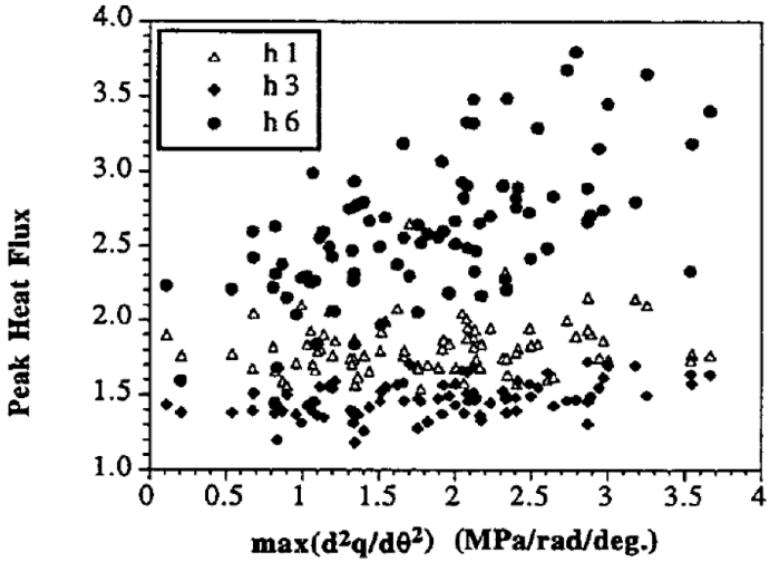

Figure 5.3. A scatter plot from Syrimis et al. [94] that records the heat flux at three different locations.

Correlations have been reported on an averaged basis between the heat flux and the knock intensity. Since it is known that there will be spatial variations in the pressure history within the combustion chamber, then in order to obtain comparisons on a cycle-by-cycle basis it will be important to co-locate the pressure transducer and heat flux sensor. Comparisons on a cycle-by-cycle basis will be seen to be important as there appears to be a threshold of knock intensity above which there is a rapid increase in heat flux. Knock indicators have been introduced in Section 3.2.1 and corresponding indicators for the heat flux are discussed after a description of the experimental equipment.

5.3. Experimental Equipment

Most of the experiments were conducted on the Ricardo E6 variable compression ratio engine, which has the same disc-shaped combustion chamber as the Cooperative Fuel Research (CFR) engine. Additional tests were conducted with a Smart Car engine. The engine specifications can be found in Table 5.1.

Table 5.1. Engine Specifications

	Ricardo E6	**Smart Car**
Engine Type	Single Cylinder, Naturally Aspirated	Three Cylinder, Turbocharged
Fuel Injection Type	Port Fuel Injection	Port Fuel Injection
Bore	76.2 mm	66.5mm
Stroke	111.1 mm	67.0 mm
Swept Volume	507 cm^3	698 cm^3
Compression Ratio	4.5 – 20	9

While the Ricardo E6 engine was equipped with three fuel tanks, so that operation could be readily switched between different fuels, the Smart Car engine operated with a single fuel tank. The smart car engine speed was regulated by a dynamometer, and had a lambda sensor for controlling the air fuel ratio. The Smart Car engine relied on its thermostat to regulate the

coolant temperature, while the Ricardo E6 had closed loop control of both the coolant (at T_c = 80°C) and inlet air temperature (at T_a = 30°C). Both engines were operated at Ω = 1000 RPM, with additional testing of the Smart Car engine at Ω = 2000 RPM.

5.3.1. Fuels

Four different blends of iso-octane, n-heptane and toluene were tested, along with an unleaded gasoline (ULG). The composition of the fuel blends is given in Table 5.2, and the Research Octane Number (RON) and Motor Octane Number (MON) values are taken from the work by Smallbone et al [96]. The properties of the ULG are given in Table 5.3, and this was the only fuel used in the Smart Car engine.

Table 5.2. Composition of the fuel blends (volume %).

Fuel	iso-octane	n-heptane	toluene	RON	MON
1	100	0	0	100	100
2	92	8	0	92	92
3	20	20	60	92	80
4	80	20	0	80	80

Table 5.3. Properties of the unleaded gasoline (ULG) used in this study.

RON	97.0
MON	87.7
Density @ 15°C	0.744 kg/L
DVPE @ 37.8°C	60.0 kPa
Aromatics % v/v	29.0
Olefins % v/v	1.8
Saturates % v/v	69.2

5.3.2. Heat Flux Probe

The heat flux probe consisted of a co-fitted heat flux sensor and pressure sensor and had similar thermal properties to the cylinder wall. As described in Section 5.2, co-location can allow for a novel spatially resolved comparison of the pressure and temperature data.

The cylinder pressure was measured by a flush-mounted Kistler 6051A piezo-electric pressure transducer and charge amplifier that were calibrated as a pair. The transducer can be seen in Figure 5.4. The pressure data, a reference flag and the surface temperature measurement from the heat flux probe were sampled at 100 ksamples/s with 12 bit resolution.

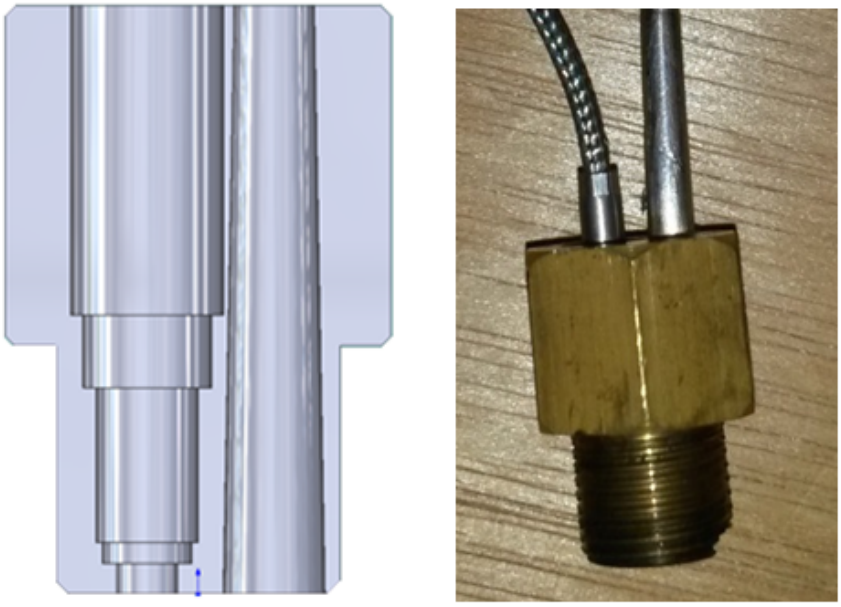

Figure 5.4. M14x1.25 adaptor for holding the pressure transducer and the heat flux probe (in the tapered hole).

Two separate thermometer types were considered for the heat flux probe. A thin film platinum resistance thermometer and a Nanmac eroding type thermocouple (chromel/alumel). The first type of sensor applies a thin layer of platinum as a resistor between two wires. Platinum has a linear temperature coefficient of resistance and is often used for accurate temperature measurement. The advantage over the thermocouple is that the output voltage is much higher so that less amplification is necessary and therefore less noise occurs when recorded. However, the eroding type thermocouple was chosen for its greater durability.

The heat flux probe has a surface Nanmac eroding thermocouple type and a reference thermocouple junction 4.76 mm from the surface thermocouple. This was tested to be sufficiently far from the surface for the temperature to be steady. The location of the thermocouples on the sensor can be seen in Figure 5.5.

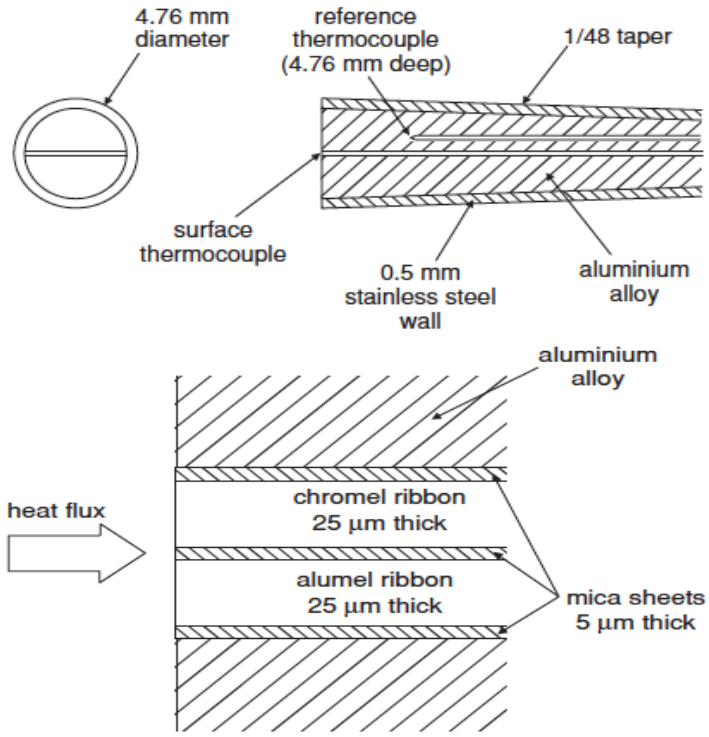

Figure 5.5. Cross section of the heat flux probe with a surface thermocouple and a reference junction, and a detailed view of the surface thermocouple cross section.

Figure 5.5 also shows how the thermocouple ribbons are separated by an extremely thin sheet of mica insulation. The 'hot' measuring junction is formed by abrading the exposed ends of the thermocouple. The dielectric insulation between the Chromel and Alumel elements is so thin that in the process of eroding the surface, metallic 'whiskers' bridge the gap and form a junction [97].

To avoid the need for cold junction compensation, it was the difference between the surface and reference temperatures that was amplified. As the thermocouple output is only about 40 µV/K, a high gain instrumentation amplifier (gains up to 25 000) was used. The surface temperature fluctuations were as high as ΔT = 80 K during heavy knock, and this is in contrast to normal combustion for which the surface temperature fluctuations would be less than ΔT = 10 K.

A LabVIEW system for control and low speed data acquisition was used on the Ricardo E6 engine, while the Smart Car Engine used a Sierra CP Cadet system. The SHDAQ (1.25 Msamples/s) was used for the experiments to collect data from inside the combustion chamber. The signals for pressure, surface temperature and TDC flag pulse were recorded with 100 ksamples/s using LabVIEW and then analyzed in MATLAB. The interface can be seen in Figure 5.6. The two plots show pressure and temperature relative to the flag pulse.

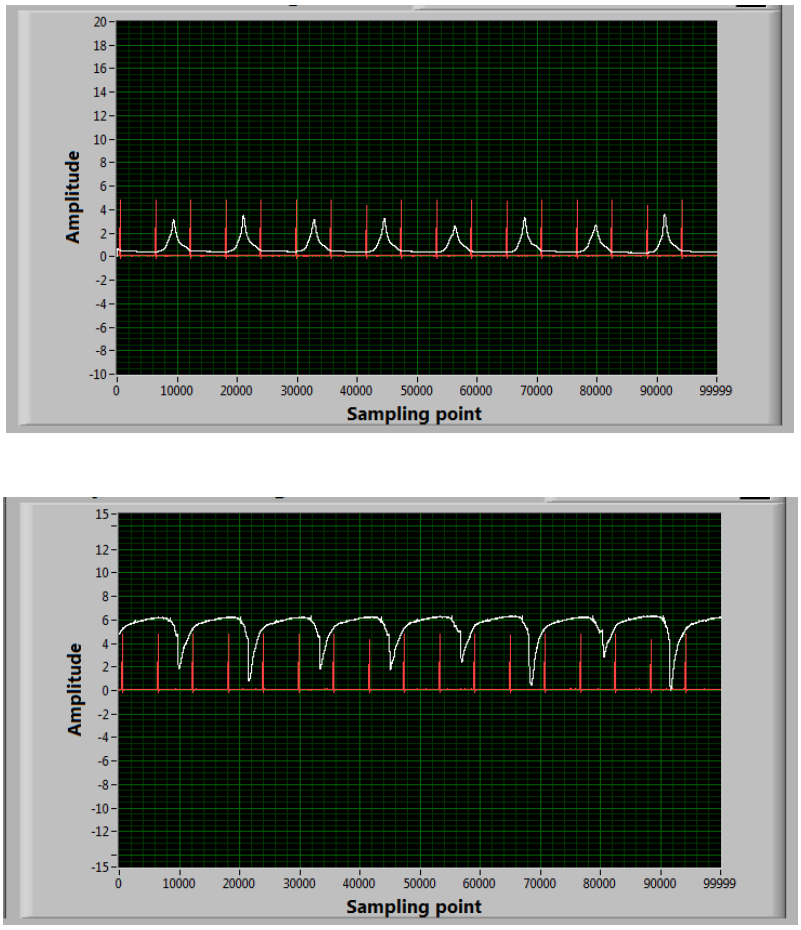

Figure 5.6. LabVIEW user interface, pressure and flag on the top, temperature and flag on the bottom.

5.4. Data Analysis

The unsteady heat flow equation is a partial differential equation that can be expressed in finite difference form by using Taylor expansions. The finite difference equations were solved using an explicit formulation, with boundary conditions from the experimental data. The following analysis is for one-dimensional heat transfer.

$$\frac{\partial T}{\partial t} = \alpha \frac{\partial^2 T}{\partial x^2} \tag{5.1}$$

With the thermal diffusivity $\alpha = \frac{k}{\rho c_p}$, k is the thermal conductivity [W/m K], ρ is the density [kg/m^2]

Using a Taylor expansion, the first and second derivatives from equation 5.1 are approximated as shown below (note that these equations are shown in the time domain but apply equally to the space domain as used later):

$$T(x,t)_{t+\Delta t} \approx T(x,t)_t + \Delta t\, T'(x,t) + \frac{\Delta t^2}{2} T''(x,t) \tag{5.2}$$

$$T(x,t)_{t-\Delta t} \approx T(x,t)_t - \Delta t\, T'(x,t) + \frac{\Delta t^2}{2} T''(x,t) \tag{5.3}$$

Equation 5.2 is rearranged to give the forward difference approximation (Equation 5.4), assuming the higher order Δt terms are negligible. In the same way, the backward difference method can be obtained from equation 5.3.

$$\frac{\partial T}{\partial t} \approx \frac{T(x,t)_{t+\Delta t} - T(x,t)_t}{\Delta t} \tag{5.4}$$

A central difference approximation is used for the second derivative in the space domain:

$$\frac{\partial^2 T}{\partial x^2} \approx \frac{T(x,t)_{x+\Delta x} - 2T(x,t)_x + T(x,t)_{x-\Delta x}}{\Delta x^2} \tag{5.5}$$

These approximations are then substituted into equation 5.1 to give:

$$\frac{T(x,t)_{t+\Delta t} - T(x,t)_t}{\Delta t} \approx \alpha \frac{T(x,t)_{x+\Delta x} - 2T(x,t)_x + T(x,t)_{x-\Delta x}}{\Delta x^2} \tag{5.6}$$

Finally, rearranging to solve for the temperature distribution at the new time step gives:

$$T(x,t)_{t+\Delta t} \approx T(x,t)_t + r\,[T(x,t)_{x+\Delta x} - 2T(x,t)_x + T(x,t)_{x-\Delta x}] \tag{5.7}$$

where $r = \frac{\alpha\,\Delta t}{\Delta x^2}$ is the Fourier number

This method is an iterative process since at every time step (t+Δt), the temperature distribution is found by solving Equation 5.7 for each grid point using the values from the time step (t). This is an explicit formulation as only known values are used to calculate the new temperature distribution. The grid in Figure 5.7 can be used to visualise each time step.

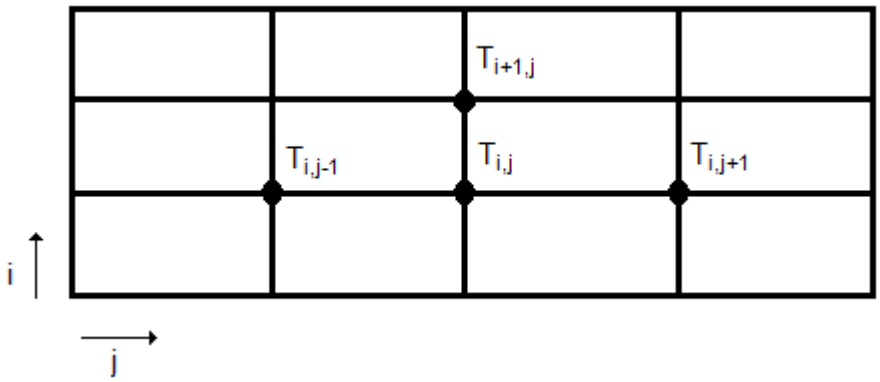

Figure 5.7 Visualisation of the explicit finite difference method. The i-direction represents the time steps and the j-direction represents the spatial grid

Once the temperature distribution is found, the instantaneous heat flux is calculated using a discretized version of Fourier's law:

$$\dot{q} = k\,\frac{T_s - T_1}{\Delta x} \tag{5.8}$$

Where T_S is the surface temperature,

T_1 is the temperature of the first grid element

Δx is the grid step size

A disadvantage of using an explicit finite difference method is that there is a constraint on the size of the time step Δt and grid spacing Δx such that $r \leq 0.5$ for a stable solution [77]. For a given sampling rate and thermal diffusivity, an upper limit on the number of grid points, *N*, is given by:

$$N = L\sqrt{\frac{r}{\alpha \Delta t}} \tag{5.9}$$

where *L* is the length between the surface and the reference point in metres.

Implicit methods, such as the Crank-Nicholson method, guarantee stability. However, they require the solution of several simultaneous equations at each time step and so are more complex and computationally costly. Applying the technique to the experimental equipment on the E6 engine, the cylinder surface temperature data provides the surface boundary condition, and the reference temperature provides the other boundary condition. Data from a cycle is read into the code, the reference temperature is constant and the initial temperature distribution between the boundaries is assumed to be linear. At each iteration, a new temperature distribution is found using the solution from the last step. This process continues by looping through the data from an individual cycle until the difference between two consecutive iterations is below $\Delta T = 0.005$ K, at which point the solution has converged. For all subsequent cycles the initial temperature distribution is that at the end of the previous cycle. The thermal properties of alumel were used, as this was the recommendation of Wang et al [97] when a 1D unsteady solution is being used. The code was validated by assuming a sinusoidal temperature variation, for which the analytical solution could be used for comparison.

Figure 5.8 shows the solution for the temperature distribution at a representative operating point.

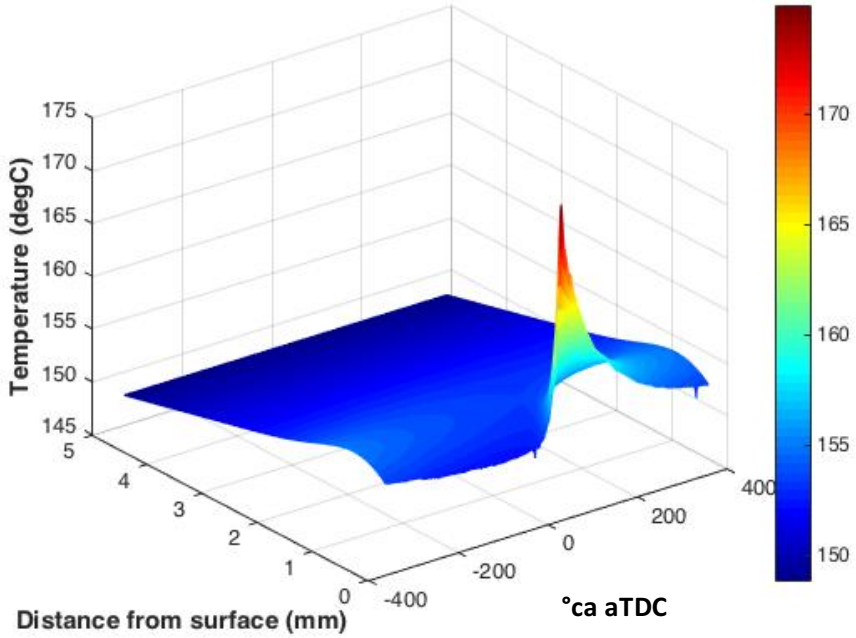

Figure 5.8. Temperature distribution between surface and reference thermocouples for one cycle. *Fuel*: iso-octane. Θ_i = 28°ca bTDC, λ = 1.0, τ = 8, T_c = 80°C, T_a = 30°C, Ω = 1000 RPM

The surface temperature increases very quickly slightly after TDC as the flame front reaches the cylinder wall. The variation in temperature damps out within 1.5-2 mm of the surface. This can be seen in Figure 5.9. Because of the cycle-by-cycle variation 100 cycles were averaged.

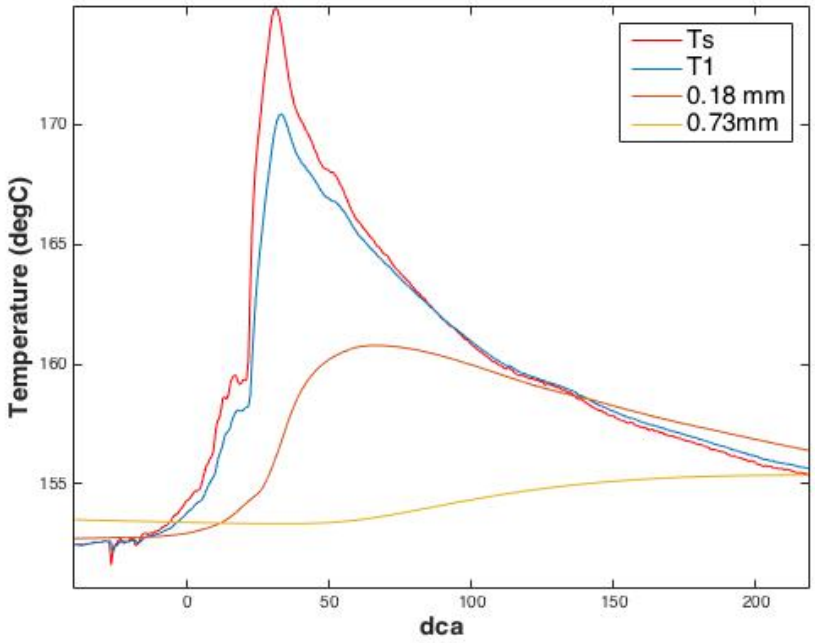

Figure 5.9. Temperature at different distances from the surface, *Fuel*: iso-octane. Θ_i = 28°ca bTDC, λ = 1.0, τ = 8, T_c = 80°C, T_a = 30°C, Ω = 1000 RPM

Once the temperature distribution is known, the heat flux can then be calculated from the temperature gradient at the surface. Figure 5.10 shows results from 20 consecutive cycles. Interference from the spark (Θ_i =28°ca bTDC) has to be rejected.

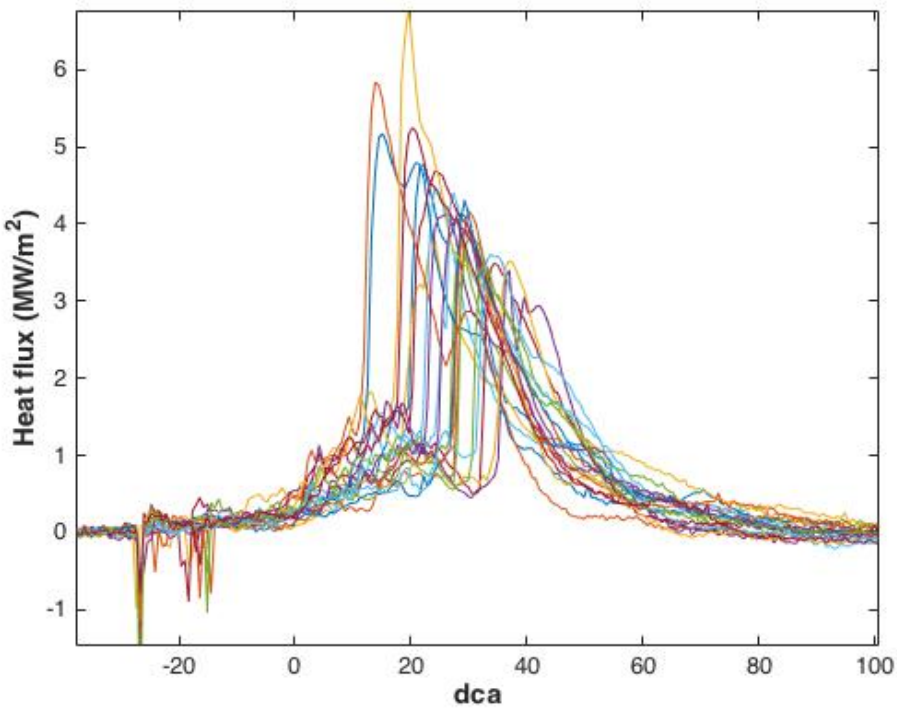

Figure 5.10. Plot of the surface heat flux for 20 consecutive cycles. *Fuel*: iso-octane. Θ_i = 28°ca bTDC, λ = 1.0, τ = 8, T_c = 80°C, T_a = 30°C, Ω = 1000 RPM.

In-cylinder pressure based knock indices are extensively used in research [98]. An introduction to pressure-based knock intensity parameters is given in Section 3.2.1. As described, no single indicator of knock intensity is universally accepted so for this study several different indicators were used. These could then be compared to three proposed heat flux based knock indices as outlined here.

Peak heat flux. The peak heat flux is the maximum value of the surface heat flux over one cycle. The peak heat flux events are the most disproportionally damaging.

$$\dot{q}_{\max} = \max\left[\dot{q}\right] \tag{5.1}$$

Integral of heat flux. Similar to the Integral of the Modulus of Pressure Oscillations index (*IMPO*), this index sums the heat flux over a given integral.

$$\dot{q}_{\mathrm{int}} = \sum_{\mathrm{tdc}-W}^{\mathrm{tdc}+W} \dot{q}\,\mathrm{d}\theta \tag{5.2}$$

For this index an interval of 0-60°ca aTDC is appropriate and therefore differs from the range for the pressure based indices.

Angle of peak heat flux. When knocking, the peak heat flux occurs earlier than in a non-knocking cycle because there is additional fuel consumed in the auto-ignition process. The crank angle at which the maximum heat flux occurs is therefore advanced and can be an indicator for knock.

$$\dot{q}_{\mathrm{ang}} = angle\left[\max(\dot{q})\right] \tag{5.3}$$

5.5. Results and Discussion

5.5.1. Results on a Cycle-by-Cycle Basis

Due to the close proximity of the pressure transducer and the thermocouple, the instantaneous heat flux accurately reflects the knock intensity on a cycle-by-cycle basis. For all three fuels tested here, it was found that there was a very weak relationship between the peak heat flux and knock intensity under light knocking conditions. Figure 5.11 shows scatter plots of the peak heat flux ($\dot{q}_{\mathrm{Max}} = Q_{\mathrm{max}}$) against *MAPO*, *IMPO* and *LKI* for Fuel 2 for a range of ignition timings.

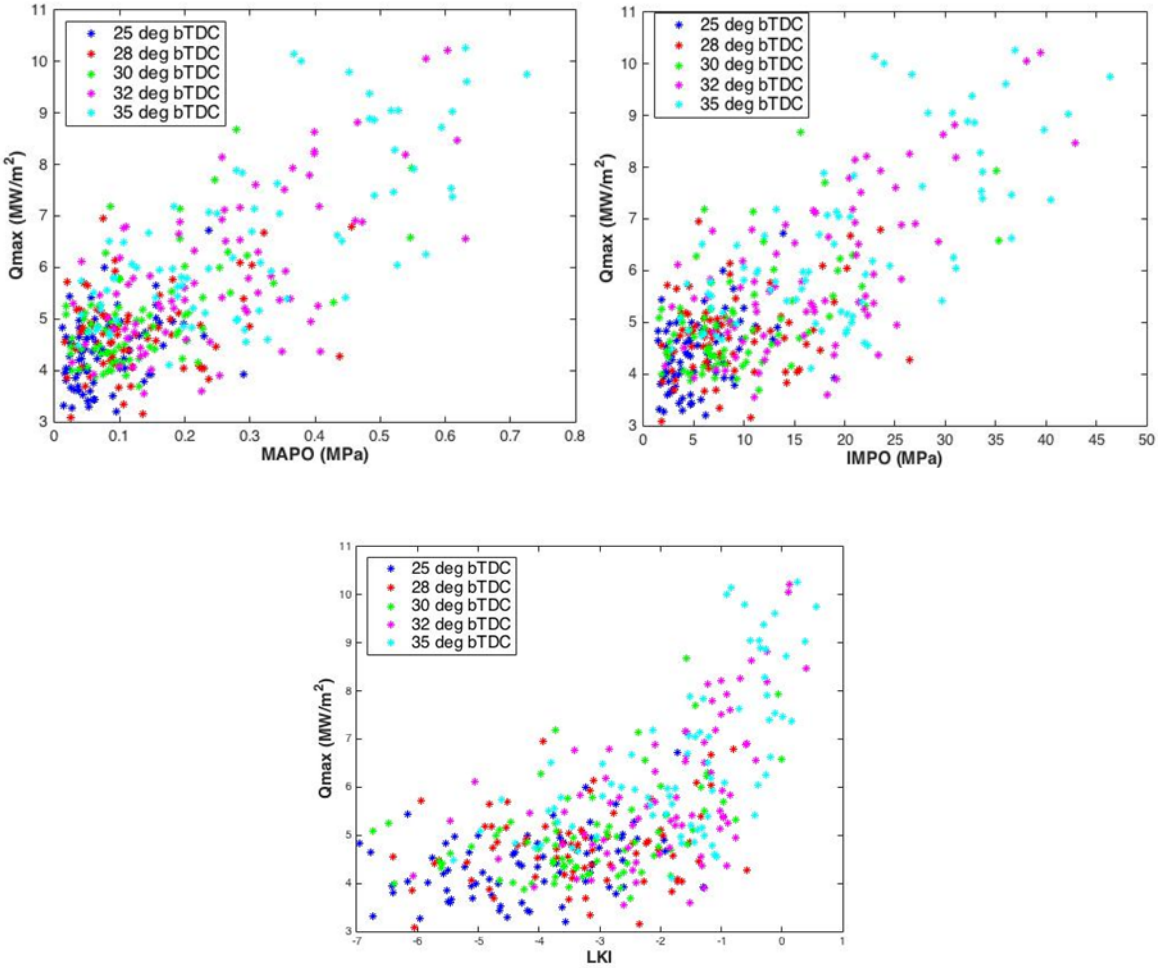

Figure 5.11. Scatter plots of $\boldsymbol{Q}_{\mathrm{max}}$ against *LKI*, *MAPO* and *IMPO* for 86 consecutive cycles. E6 Engine, *Fuel*: 2. Θ_i = 25-35°ca bTDC, λ = 0.9, τ = 7, T_{c} = 80°C, T_{a} = 30°C, Ω = 1000 RPM

It can be seen in Figure 5.11 from the plots of Q_{max} against *MAPO* and *IMPO*, that at ignition timings of Θ_i = 25°ca bTDC to Θ_i = 30°ca bTDC, there is very little correlation between the peak heat flux and knock intensity. However, for the more advanced ignition timings, Q_{max} increases almost linearly with knock intensity. The plot of Q_{max} against *LKI* shows that for cycles with an *LKI* < -1, knock intensity appears to have little effect on the peak heat flux. However, above this value (*LKI* > -1), the correlation between Q_{max} and *LKI* becomes much stronger.

Figure 5.12 shows a sweep of compression ratio for a fixed ignition timing. Q_{max} is being compared to three pressure based knock indices.

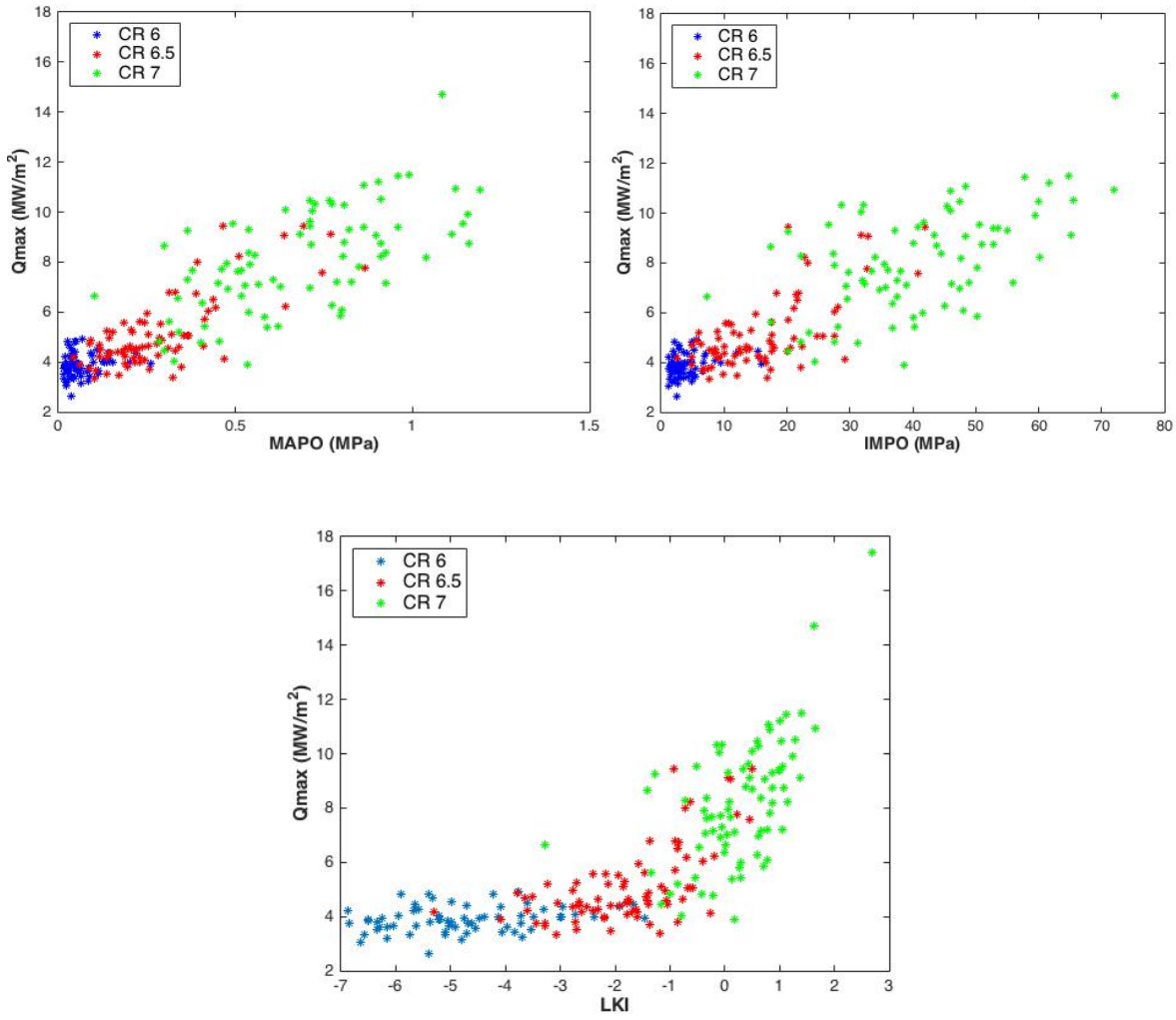

Figure 5.12. Scatter plots of peak heat flux against *LKI*, *MAPO* and *IMPO* for 87 consecutive cycles. E6 Engine, *Fuel*: 3. Θ_i = 30°ca bTDC, λ = 1, τ = 6-7, T_c = 80°C, T_a = 30°C, Ω = 1000 RPM

Figure 5.12 compares Q_{max} with *MAPO*, *IMPO* and *LKI* using Fuel 3 for compression ratios of 6, 6.5 and 7 at 30°ca bTDC and a stoichiometric (λ = 1) mixture. The progression from very light knock to heavy knock was well defined, which is reflected in the average values of *LKI*, which were $\overline{LKI}$ = -5.72, $\overline{LKI}$ = -1.78 and $\overline{LKI}$ = 0.26 respectively. From all three plots it can be seen that there is little relationship between the peak heat flux and knock intensity for very light knock at a compression ratio of τ = 6. For some cycles at a compression ratio of τ = 6.5, knock had an effect on Q_{max}. However, for a compression ratio of τ = 7, the plots of

Q_{max} against *MAPO* and *IMPO* show a stronger correlation between Q_{max} and knock intensity. Similarly with the plot of Q_{max} against *LKI*, there is a clear progression for each compression ratio, with the strongest relationship at *LKI* > -1.

An alternative to using the peak heat flux is to integrate the heat flux ($\dot{q}_{int} = Q_{int}$ as in Equation 5.2 over a time window). When the same data reported in Figure 5.11 is analyzed in this way the results (Figure 5.13) show broadly the same trends as in Figure 5.12.

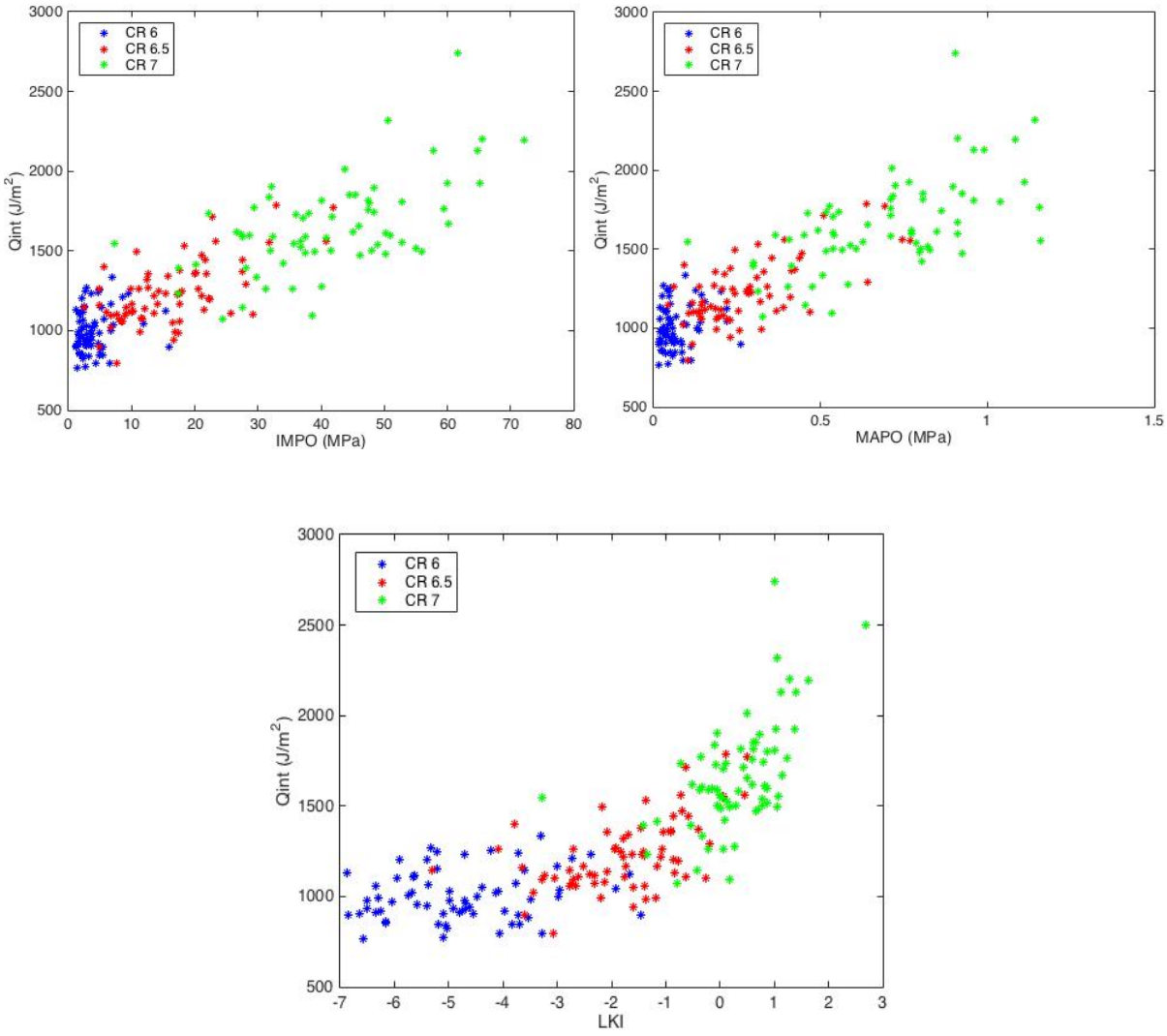

Figure 5.13. Scatter plots of integrated heat flux against *LKI*, *MAPO* and *IMPO* for 87 consecutive cycles. E6 Engine, *Fuel*: 3. Θ_i = 30°ca bTDC, λ = 1, τ = 6-7, T_c = 80°C, T_a = 30°C, Ω = 1000 RPM

Plots of the angle of occurrence of the peak heat flux ($\dot{q}_{ang} = Q_{ang}$ Equation 5.3) against the knock parameters showed the expected trends – namely the more intense the knock the earlier the angle at which the peak heat flux occurs. This can be seen in Figure 5.14.

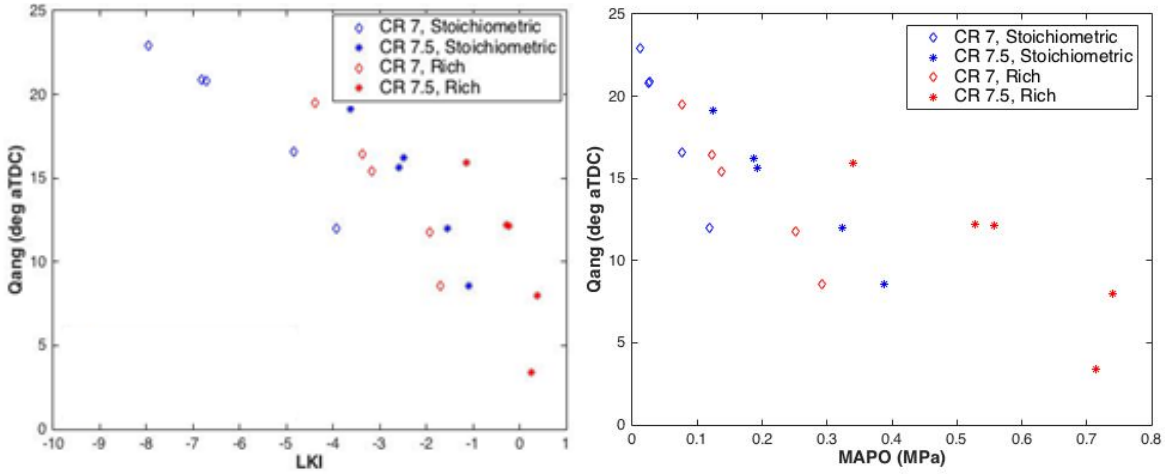

Figure 5.14. Angle of peak heat flux and knock indices *LKI* and *MAPO*. E6 Engine, *Fuel*: 2. Θ_i = 25-35°ca bTDC, λ = 0.9-1, τ = 7-7.5, T_c = 80°C, T_a = 30°C, Ω = 1000 RPM

The angle of peak heat flux can further be compared directly to the angle of knock occurrence. This can be seen in Figure 5.15.

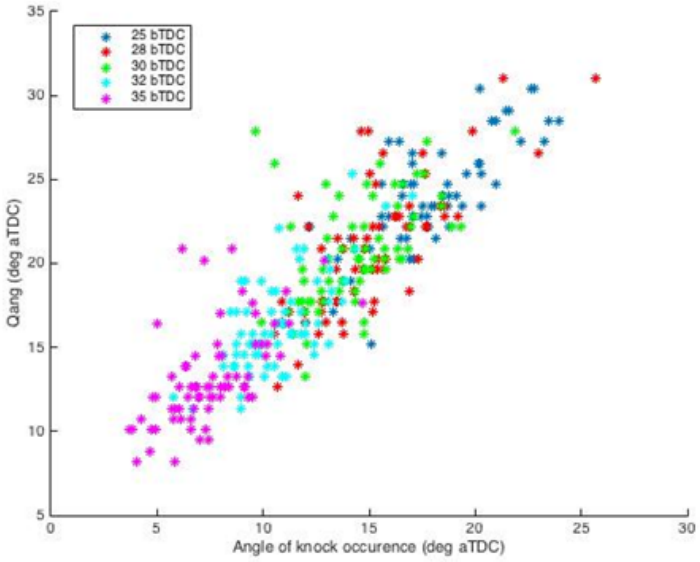

Figure 5.15. Angle of peak heat flux versus angle of knock occurrence. E6 Engine, *Fuel*: 2. Θ_i = 25-35°ca bTDC, λ = 0.9-1, τ = 7, T_c = 80°C, T_a = 30°C, Ω = 1000 RPM

A strong correlation can be seen in the analysis of the angle of peak heat flux and the angle of knock occurrence. This indicates good comparability of the pressure and heat flux based method. The next set of experiments was conducted on the Smart Car engine. The Smart Car engine has a squish region unlike the simple disc shaped combustion chamber of the Ricardo E6. The squish region generates significant turbulence; the burn rate in the Smart Car engine is estimated to be about double that of the Ricardo E6 engine. Figure 5.16 shows a sweep of ignition timing on the Smart Car engine.

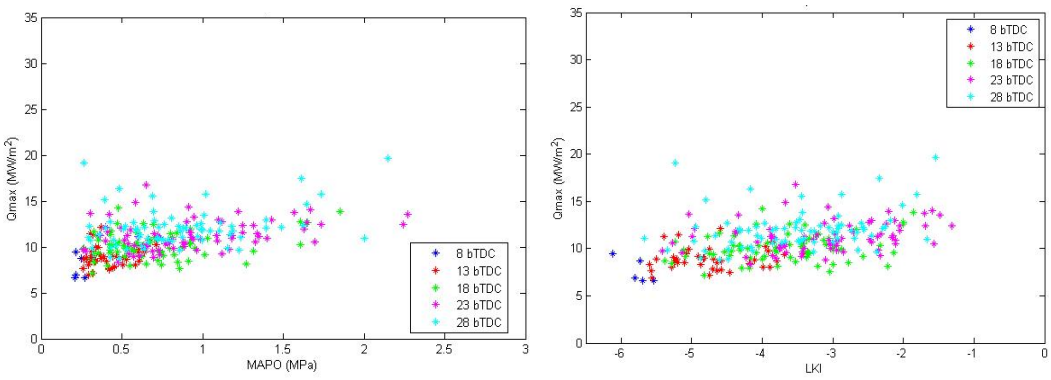

Figure 5.16. Scatter plots of peak heat flux against *MAPO* and *LKI* for 87 consecutive cycles. Smart car engine, *Fuel*: gasoline. Θ_i = 8-28°ca bTDC, λ = 1, τ = 9, Ω = 1000 RPM

Figure 5.16 shows a scatter plot of the peak heat flux against *MAPO* and *LKI* for 87 consecutive cycles using unleaded gasoline at λ = 1 for a range of ignition timings in the Smart Car engine at Ω = 1000 RPM. Compared to the Ricardo E6 engine, the heat flux is about twice as high for a given value of *LKI*, and this can be explained by the higher level of turbulence that increases the burn rate, and the higher compression ratio leading to higher in-cylinder pressures and temperatures. Similar results were found at Ω = 2000 RPM except that there was more scatter in the data and the trend line was about 30% higher, which again can be explained by the higher level of turbulence. The *MAPO* data showed a similar difference

for the two engine speeds. At both speeds concerns over the increased levels of heat flux during knocking combustion limited the extent of the ignition advance compared with the test in the Ricardo E6.

5.5.2. Results on a Cycle-Averaged Basis

Figure 5.17 shows cycle-averaged results for sweeps of compression ratio, stoichiometry and ignition timing.

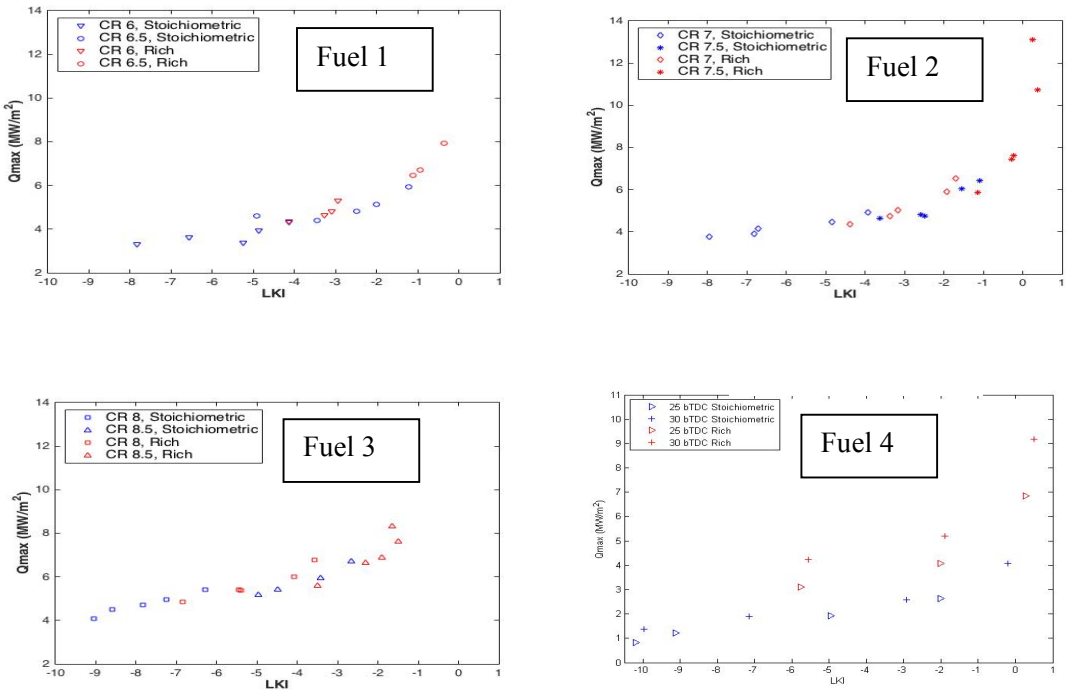

Figure 5.17. Scatter plots of the average peak heat flux against *LKI*. E6 Engine, *Fuel*: 1-4. Θ_i = 25-35°ca bTDC, λ = 0.9-1, τ = 6-8.5, T_c = 80°C, T_a = 30°C, Ω = 1000 RPM

Figure 5.17 shows scatter plots of the average peak heat flux against *LKI* for a range of ignition timings from Θ_i = 25°ca bTDC to Θ_i = 35°ca bTDC and varying compression ratios and mixture strengths. For Fuels 1-3 in each dataset, the data points refer to ignition timings Θ_i = 25°ca bTDC to Θ_i = 35°ca bTDC sequentially from left to right, as advancing the spark timing increased the knock intensity. Fuel 4 was tested at τ = 6 and less advanced ignition

timings (Θ_i = 25-30°ca bTDC) because of the lower octane rating (*RON* = *MON* = 80). The lower in-cylinder pressures account for the generally lower values of heat flux.

As would be expected, the cycle averaged results for different fuels in Figure 5.17 show the same trends, and it is possible to show data from a wider range of test conditions in single plots. As with the cycle-by-cycle results, there is a marked increase in the heat flux once *LKI* > -1. The corresponding results from Fuels 1-3 of Figure 5.17 for the maximum amplitude of pressure oscillation (*MAPO*) are combined and plotted in Figure 5.18 where the trends seen with LKI can be confirmed. The data points refer to the legends in Figure 5.17.

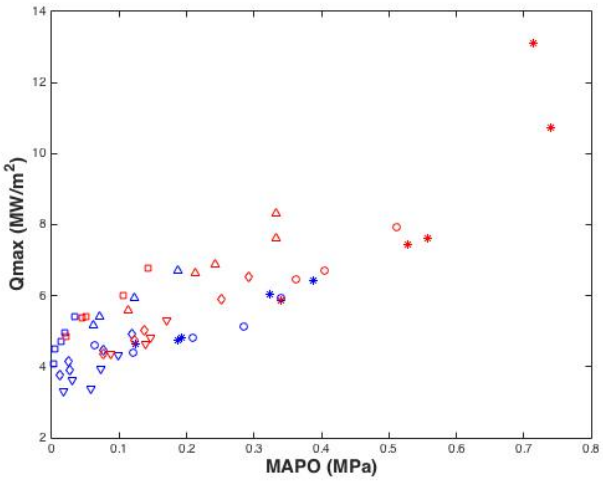

Figure 5.18. Scatter plot of the average peak heat flux against maximum amplitude of pressure oscillation (*MAPO*). E6 Engine, *Fuel*: 1-3. Θ_i = 25-35°ca bTDC, λ = 0.9-1, τ = 6-8.5, T_c = 80°C, T_a = 30°C, Ω = 1000 RPM

The corresponding plot to Figure 5.18 for the Smart Car engine is Figure 5.19 which shows a scatter plot of the average peak heat flux against *LKI* and *MAPO* for 87 consecutive cycles using unleaded gasoline at λ = 1 for a sweep of ignition timing at Ω = 1000 RPM. Compared with the results in the Ricardo E6 engine, the heat flux in the Smart Car engine is about 30% higher for a given *MAPO*, and this is attributed to the higher compression ratio, different fuel and higher level of in-cylinder turbulence.

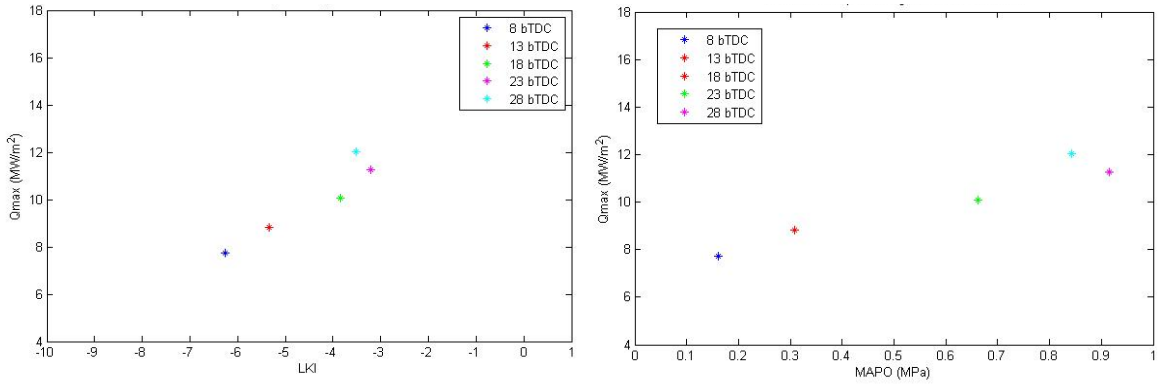

Figure 5.19. Scatter plot of the average peak heat flux against LKI and MAPO for 87 consecutive cycles. Smart Car Engine, *Fuel*: gasoline. Θ_i = 8-28°ca bTDC, λ = 1, τ =9, T_c = 80°C, T_a = 30°C, Ω = 1000 RPM

The data in Figure 5.20 addresses the question of the added benefit of measuring the heat flux rather than the steady metal temperature, which would be much simpler to measure.

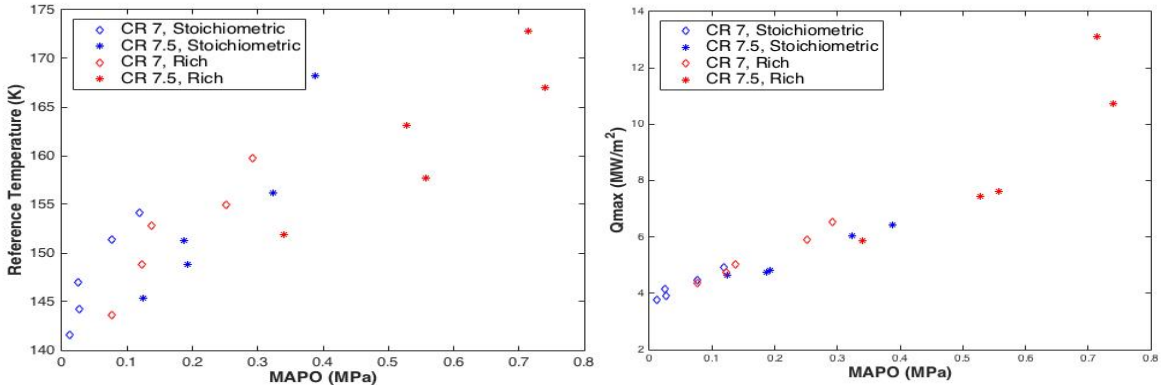

Figure 5.20. Scatter plot of the (left) reference temperature and (right) average peak heat flux against maximum amplitude of pressure oscillation (*MAPO*). E6 Engine, *Fuel*: 2. Θ_i = 25-35°ca bTDC, λ = 0.9-1, τ = 7-7.5, T_c = 80°C, T_a = 30°C, Ω = 1000 RPM

In Figure 5.20 the greater scatter in the data for the reference temperature compared with the data for Q_{max} when plotted against *MAPO* indicates that the reference temperature is a less precise technique than the heat flux measurement. Furthermore, the instantaneous heat flux is linked to the thermal stresses that cause the engine damage.

5.6. Summary

The aim in this chapter was to investigate the effect that combustion knock has on the instantaneous heat flux at the surface of the combustion chamber in spark ignition engines. A pressure transducer and eroding-type thermocouple were placed in close proximity in the end-gas region of two different spark ignition engines (E6 engine and Smart Car engine) to measure the in-cylinder pressure and surface temperature during knocking combustion. The heat flux was calculated from the surface temperature data using a one-dimensional finite difference method in MATLAB. The knock indices *MAPO*, *IMPO* and *LKI* were used as references to investigate the effect that knock had on the surface heat flux. Three knock intensity parameters were evaluated from the heat flux data: the peak heat flux (Q_{max}), the integral of heat flux over a given window (Q_{int}) and the crank angle at which peak heat flux occurs (Q_{ang}). These were then compared to the pressure based knock indices on a cycle-by-cycle and cycle-averaged basis. The in-cylinder pressure and surface temperature were recorded for a range of compression ratios, ignition timings and air-fuel ratios in the Ricardo E6 engine, using four fuels with different octane ratings. The key findings from the cycle resolved measurements in the Ricardo E6 engine are summarized first.

- For all four fuels, it was found that there was little correlation between the instantaneous surface heat flux and knock intensity under very light knocking conditions on a cycle-by-cycle basis.
- The knock intensity was increased by advancing the ignition timing, increasing the compression ratio, using a lower octane rating fuel or using a richer mixture. Under the resulting heavier knocking conditions a correlation between heat flux and knock intensity was found for all four fuels.
- For $LKI > -1$, Q_{max} and Q_{int} increased almost linearly with *LKI*.

- The crank angle at which peak heat flux occurred was found to decrease as knock intensity increased.

Similar trends were reflected in the analysis of the cycle-averaged results. The relationship between peak heat flux and knock intensity was largely independent of the conditions in the Ricardo E6 engine used to achieve a given knock intensity.

The tests with the Smart Car engine showed that as the speed was increased from Ω = 1000 to Ω = 2000 RPM, there was a significant increase in the maximum heat flux for fixed values of *MAPO* (30% higher peak heat flux) and *LKI* (approximately double the peak heat flux). The increase in heat flux can be accounted for by an increase in the turbulence intensity, resulting from the squish design in Smart Car engine. Further, the higher compression ratio also accounts for higher values of heat flux at Ω = 1000 RPM in the Smart Car engine.

The reference temperature just below the surface was found to increase at a higher rate under heavy knocking conditions. Measuring a single temperature of the cylinder to assess potential damage to the engine would be much simpler than evaluating the instantaneous heat flux, but the correlation between this metal temperature and the knock intensity showed significantly increased scatter compared to the correlation of heat flux and knock intensity. Furthermore, it is the differential thermal strain that leads to thermal stresses and these will depend on the temperature gradient, which is directly related to the instantaneous heat flux.

6. Conclusions and Future Work

6.1. Originalities of this Thesis

- A novel method of identifying the engine MBT operating point by means of a study of maximum pressure was successfully demonstrated. A similar proposed method concerned with mass fraction burned was proven to be unfeasible. Relationships of the humidity of the intake air as well as status of mixture preparation on the engine operating point and knock tendency could be demonstrated for the Ricardo E6 engine.
- With the work on surface pre-ignition, we were able to outline the feasibility of a wide range of measurement techniques which will prove valuable for future research in this field. Further, we demonstrated a previously unknown relationship of stoichiometry on surface pre-ignition. A rich mixture had a lower susceptibility to surface pre-ignition than a weak mixture. Further, a minor influence of humidity on surface pre-ignition was demonstrated. A repeat of experiments from an important publication from Downs and Theobald with an improved measurement technique revealed a possible misreport in temperature units.
- The study on the effect of knock intensity on the instantaneous heat flux provided data to demonstrate that there is a correlation between the heat flux and the knock-intensity derived from a pressure measurement. The associated publication is the first paper to show such a correlation on a cycle-by-cycle basis since the pressure transducer and heat flux probe were co-located; previous work had only shown a relation on a cycle-average basis. Given that it is the individual peak heat flux events that are disproportionally relevant for subsequent auto-ignition and damage to the engine, a cycle-by-cycle resolution is crucial for understanding the impact of this phenomenon.

6.2. Summary and Conclusions

6.2.1. Overview and Integration of Research

This thesis project involved the experimental investigation of abnormal combustion phenomena in spark ignition internal combustion engines and was begun in October 2014. The research was aimed at providing greater understanding of the influence of operating conditions including compression ratio, ignition timing, engine operating temperature, air intake conditions (temperature and humidity), fuel (composition, temperature, degree of vaporization) and hot spots on abnormal and potentially harmful combustion events. The development of new engines that, while being more efficient than older models, are more prone to these abnormal combustion events has put such research into the spotlight. It is relevant for both the automotive and the petroleum industry and the research was supported by BP (p.l.c.).

6.2.2. Summary of Literature Review

A review of the relevant literature revealed that albeit with the steady improvement of electric cars, internal combustion engines will remain the prevalent powertrain for vehicles for the foreseeable future. The majority of these engines are spark ignition engines which were briefly introduced and separated from compression ignition engines due to environmental concerns. Car manufacturers are investing in increasing the efficiency of their spark ignition engines. Practical engines in vehicles are run in part-load operation with large throttling losses for most of their lifetime as the engine size is determined by the occasionally-demanded peak power. Downsizing and turbocharging are measures to remove this

discrepancy and to increase the efficiency at part load. However, this comes with an increased chance of auto-ignition, knock and subsequent pre-ignition at high load.

The physical backgrounds of these abnormal combustion phenomena, including potential damage, influence on operating point and reduction of engine efficiency were introduced next. It was explained what engine factors influence auto-ignition and this included the potential countermeasures. The fuel was identified as a key feature here and the method by which industrial fuels are rated according to their auto-ignition tendency with the bi-component RON/MON octane scales was explained in detail. Problems with the octane scale were highlighted with the introduction of the operating condition variable K that has historically moved away from the octane test conditions for practical engines. The fact that both the automotive and petroleum industries rely heavily on an inadequate and deceptive octane scale for the development of engines and fuels became obvious and is further supported in subsequent sections and chapters of this thesis. An alternative test method is required urgently and a toluene reference number test scale was presented as one such possibility.

This thesis aims to improve the understanding of abnormal combustion with the goal of helping to develop a new test method for industrial fuels that is more suitable to modern engines.

This required additional in-depth review of the physics of knock and auto-ignition. This included an introduction of the Livengood-Wu integral and the influence of temperature, pressure and lambda on auto-ignition. The two roots of pre-ignition, the surface pre-ignition and the pre-ignition through fuel/oil droplets were discussed and the latter disregarded for the work in this thesis as it does not directly relate to auto-ignition. The supressing effect of fuel evaporation on auto-ignition was discussed and it was elaborated how this effect is

unfortunately disregarded in the MON test. Several engine performance parameters were introduced and it was discussed how these are influenced by lambda and the engine operating point. It was explained how these can be affected and limited by knock. The work in this thesis took advantage of a burn rate analysis and this was introduced for key parameters such as the mass fraction burned and the heat release rate. Finally, PID controllers were introduced to provide the reader with an understanding of these crucial control devices for engine operation as can be seen in the next section.

6.2.3. Summary of Crucial Experimental Equipment

A variable compression engine facility has been developed with extensive measurement and control equipment being installed, commissioned, and calibrated. With a LabVIEW VI and an interface control box, temperatures, pressures and other relevant variables could be monitored while at the same time injection duration and several heaters could be controlled with closed-loop PID controllers. Further equipment included sensor probes for in-cylinder pressure, heat flux on the cylinder wall and flame ionization. A custom built ignition system allowed for control of the engine operating point. A humidifying unit, a fuel vaporization unit and a closed-loop controlled glow plug have been constructed. Data acquisition was facilitated with four DAQ cards of different sampling rates that were connected to LabVIEW on two computers. Data analysis was conducted using an in-house-build combustion burn rate analysis software in Matlab and was deployed for all experiments. Additional in-house built software packages were created for the study of pre-ignition and heat flux.

The E6 engine and equipment can be seen in Figure 6.1.

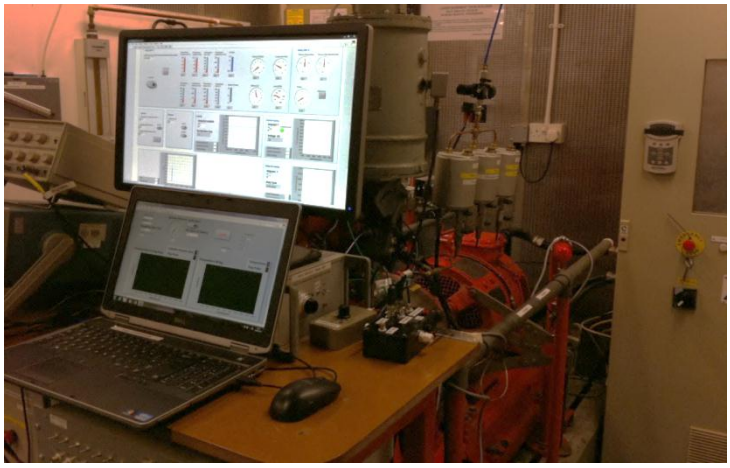

Figure 6.1. E6 engine, experimental equipment and LabVIEW control system.

6.2.4. Conclusions of the Study of the Engine Operating Point, Knock, Humidity and Mixture Preparation

This chapter was concerned with the identification of the ideal engine operating point and the influence of intake air humidity and mixture preparation on knock. Knock indices were introduced and reviewed. The influence of humidity on knock was discussed and modelling was performed so to avoid condensation when water vapour is introduced to the engine. It was further explained how the evaporative cooling of fuels can inhibit the occurrence of knock and how this is disregarded in the MON test. Modelling to avoid condensation of fuel vapour was presented.

A humidifying unit was custom built and can readily be attached to the engine's air plenum. The water supply is through a peristaltic pump and the humidifier's continuous output stream was confirmed with schlieren imaging. With only minor modifications, the humidifying unit could be used to fully vaporize the fuel.

A first experimental sequence was dedicated to the hypothesis of the possibility of finding the ideal engine operating point with a study of maximum pressure or mass fraction burned rather than with ignition timing sweeps. At first, this required several ignition timing sweeps for ranges of lambda and compression ratio. A comparison between three different mass fraction burned ranges revealed linear trends allowing us to continue with a single *mfb* range (*0-50%mfb)*. Further data analysis showed that the p_{max} method can serve as a good substitute (error < 2°ca) for finding the ideal engine operating point. The same could not be said for the *mfb* based method which was not feasible in the weak regime and inaccurate (error ~ 6°ca) in the rich regime. A fuel sweep was then conducted to validate the p_{max} method under knocking conditions and it was concluded, that the method lacks precision and so ignition timing sweeps were conducted throughout this thesis work to obtain the ideal engine operating points.

The response of the engine to knock was tested in a second experimental sequence. Ignition timing sweeps were analysed for the three common knock indices and linear trends of knock intensity over advancing ignition timing could be reported beyond a 'knock-onset' threshold. This threshold was then defined properly for all three knock indices and it could be shown that the ignition timing of the knock onset is independent of the knock index. This allowed us to proceed with our analysis with just a single knock indicator. The *LKI* was selected for most subsequent experiments to express the engine knock severity. A fuel and lambda sweep was conducted and it was shown that (with one exception) the knock thresholds were reached at ignition timings more advanced than *MBT*. This means that the engine was not operated in the KLSA region, so the experiments were not limited by knock.

The effect of humidity on the engine operating point, power output and knock was under investigation next. Experimental sequences of ignition timing sweeps for a range of

compression ratios and two levels of humidity were conducted first. The experiments with reduced humidity had a higher *IMEPn* compared to those with increased humidity. This can be explained with the reduced amount of combustible air that is present when replaced with water vapour. A theoretical reduction in *IMEPn* of 7% at a 10-fold increased humidity could be confirmed experimentally. The data curves show more scatter when the humidity is increased. This can be explained with the pulsating nature of the air/steam flow. It could be shown that knock was reduced significantly when the humidity was increased. A second experimental sequence with a sweep of ignition timing, humidity and lambda showed similar trends. Knock was more pronounced in these experiments as they were done at at a higher compression ratio. Again, it could be shown that an increased humidity has a negative effect on the *IMEPn*. As expected, this was particularly pronounced for the weak mixture as the water vapour has an increased effect here. The data sets of the two experimental sequences (compression ratio and lambda sweep) were further analysed for *mfb*. Conclusions from this include that an elevated humidity will push *MBT* to a more advanced ignition timing and the 0-50% *mfb* is higher. This was found to be independent of the compression ratio and lambda. It can be concluded that while an increased humidity decreases knock, if the engine is to be operated at *MBT*, the required ignition advance will in turn make knock more probable. The positive effect of humidity is reduced.

The last part of this chapter concerned itself with the effect of mixture preparation on the engine operating point, IMEPn and knock. The vaporization unit was deployed and different fuel blends of iso-octane and ethanol were tested for sweeps of ignition timing for both liquid and vaporized fuel. Two expected results were observed. Firstly, the higher the content of ethanol of the test fuel, the less prone to knock was the fuel. Secondly, the knock intensity increased when a given fuel was vaporized. The cooling effect of the enthalpy of vaporization makes liquid fuels less susceptible to knock. This effect disappears when the fuel is injected

in a state of vapour. This effect can be quantified as the liquid fuel allows for an approximate $\Delta\Theta_i$ = 1°ca (iso-octane) further ignition advance to reach the same knocking tendency as a vaporized fuel. This advance grows with increasing content of ethanol. The enthalpy of vaporization for ethanol is approximately five times higher than that of iso-octane.

The mixture temperature was found to decrease steadily with increasing ethanol content for liquid fuels. An analysis of *IMEPn* for a compression ratio sweep showed that a vaporized fuel results in a smaller *MBT*. A vaporized fuel at compression ratio τ = 9.5 has a near identical knock intensity as a liquid fuel at compression ratio τ = 10.5. Consequently, if the engine was limited by knock, the engine could be operated at a higher compression ratio if a liquid rather than a vaporized fuel was to be used. The *MBT* would then be 3 % higher and occur 2°ca later. The fact that the high mixture temperatures in the MON test require fuels to be fully vaporized therefor has an effect on the operating conditions.

Lambda sweeps for ethanol and methanol showed that a liquid fuel allows for up to $\Delta\Theta_i$ = 6°ca of advanced ignition timing compared to vaporized fuel. The difference in knock intensity for the vaporized ethanol for two lambdas is less dependent on the ignition timing than the liquid ethanol. A sweep of air temperatures was conducted for vaporized methanol. A lower air temperature led to less knock for three lambdas and fuel condensation could be excluded as a reason for this with modelling of the mixture temperature.

6.2.5. Conclusions to the Study of Surface Pre-Ignition

An investigation of surface pre-ignition in a spark-ignition internal combustion engine was conducted. Surface Pre-ignition is the ignition of the air/fuel mixture before the spark plug has fired. It can have destructive consequences for the engine as it is linked to auto-ignition and knock. An auto-igniting cycle causes an augmented heat flux on the cylinder wall which can serve as a hot spot for surface pre-ignition in a subsequent cycle. This then has the same effect as an over-advanced spark which aggravates auto-ignition and can lead to run-away knock. Literature shows no correlation of surface pre-ignition tendency to the RON/MON octane tests.

A closed loop temperature controlled glow-plug was fitted into a variable compression ratio research engine to control the incidence of surface pre-ignition. Attached to the glow-plug was a thermocouple and a flame ionization sensor. A humidifying unit to control the humidity of the intake air was also deployed. Two major techniques of surface pre-ignition analysis were tested and discussed.

Firstly, a flame ionization sensor and appropriate pulse logic were considered. This was the intended measure for surface pre-ignition and consequently it was revised and optimized several times. An ionization probe can take advantage of the ionization effect of a hydrocarbon flame and can detect such a flame when it is present between two electrodes. The technique had to be disregarded eventually as it was demonstrated that a reliable response time was highly dependent on the fluctuating temperature of the combustion chamber.

Secondly, a range of in-cylinder cycle-by-cycle pressure-based analyses were considered. These included an assessment of the pressure at TDC, the mass fraction burned, the net heat release and the method of choice: the maximum pressure method. All four techniques show

significant differences between surface pre-igniting and spark-igniting cycles. Thresholds between the distributions of the two ignition regimes could be established and this enabled separation of the surface pre-igniting and spark-igniting cycles. A comparison between the four pressure-based methods showed that the most straight-forward method of the maximum pressure has no disadvantages over the other methods and was therefore selected as the method of choice. The temperature of the glow plug was recorded and window-averaged on a cycle-by-cycle basis. This average temperature could then be compared to the maximum pressure for every cycle and this made it possible to define a 'surface pre-ignition temperature' at the unity ratio between surface pre-igniting and spark-igniting cycles. The method was refined with parametric studies.

Experiments were conducted and analysed with a cycle-averaged maximum pressure method. In a sweep of ignition timing, it was found that the more retarded the ignition timing, the stronger is the surface pre-ignition tendency. This was explained with the fact that a retarded ignition timing allows for more time for surface pre-ignition to occur. All subsequent experiments were conducted at a (retarded) ignition timing of Θ_i = 5°ca bTDC for repeatability, to minimise the risk of run-away knock.

An analysis of a cycle-averaged lambda sweep showed that the pre-ignition tendency increased with leaner mixtures. This was an unexpected trend and was repeated for a cycle-by-cycle analysis for two fuels and the same results were reported. The explanation is that the higher compression index of the weaker mixture results in higher compression temperatures and the lower specific heat capacity of the weaker mixture means that less heat has to be transferred from the glow plug to increase the temperature of the mixture.

A sweep of compression ratios revealed that there is no dependence of the surface pre-ignition tendency on the compression ratio.

Conclusions and Future Work

A range of pure fuel components was tested for their susceptibility to surface pre-ignition and the selection was based on comparable data in the literature. This included six chain-structured molecules (n-heptane, ethanol, n-pentane, iso-octane and iso-pentane) and four ring structured molecules (cyclohexane, ethyl-benzene, toluene and xylene).

It could be demonstrated that alkanes and alcohols were rather susceptible to surface pre-ignition. The straight chain molecules of n-heptane, ethanol and n-pentane were found to have a higher pre-ignition tendency as the branched chain molecules of iso-octane and iso-pentane. The ring structured components' surface pre-ignition tendency was found to be dependent on the length of the attached chains. Toluene and xylene are less susceptible to surface pre-ignition compared to ethyl-benzene as the latter has a longer side chain than the former. Cyclohexane was shown to be more susceptible to surface pre-ignition than the aromatic fuels. A comparison of the surface pre-ignition temperature and the octane numbers revealed that there is no correlation.

Further, the effect of fuel blending on the surface pre-ignition tendency was tested experimentally. 50%:50% (volumetric) blends of n-pentane and iso-pentane, cyclohexane and xylene, and ethanol and iso-octane as well as methanol and iso-octane were selected. It could be shown that linear correlations exist between the blending strength and the pre-ignition tendency in all cases with the exception of the iso-octane/methanol blend where methanol disproportionally increased the pre-ignition tendency of the blend. Excellent repeatability of the experimental results was demonstrated with several repeats of iso-octane tests.

The effect of humidity on the intake air was analysed with a humidifying unit. Several fuels and lambdas were tested. Only when the humidity was increased to levels beyond what is realistic in real-world operation did a trend become apparent. The unexpected trend that an increased humidity increases the surface pre-ignition tendency was demonstrated.

6.2.6. Heat Flux Study Conclusions

Thermal stresses on the material of the combustion chamber are one of the major causes of damage by auto-ignition. Further, the augmented temperature of parts of the cylinder wall can provide the hot spots for surface pre-ignition. An investigation of the effect of auto-ignition and knock on the instantaneous heat flux at the surface of the combustion chamber in a spark ignition engine was in order.

While other researchers have addressed this topic, no data has been reported for a correlation between knock intensity and heat flux on a cycle-by-cycle basis. A cycle-by-cycle based analysis is crucial, as it is the peak heat flux events that are disproportionally damaging. A pressure transducer and heat flux probe were co-fitted in the end gas region of the combustion chambers of both the E6 engine and a contemporary 3 cylinder Smart Car engine. The heat flux was calculated from the temperature data using a one-dimensional finite difference method. Three knock intensity parameters were proposed from the heat flux data: the peak heat flux (Q_{max}), the integral of heat flux over a given window (Q_{int}) and the crank angle at which peak heat flux occurs (Q_{ang}). These could then be linked to the pressure based knock indices: *MAPO*, *IMPO* and *LKI*.

Results were reported on a cycle-by-cycle and cycle-averaged basis. Four fuels with different octane ratings and sensitivities were used on the Ricardo variable compression ratio engine.

It was found that the correlation between heat flux and knock was weak for light knocking conditions compared to heavy knocking conditions on a cycle-by-cycle basis. The knock intensity was subsequently increased by means of advancing the ignition timing, increasing the compression ratio, using a lower octane rating fuel or using a richer mixture. It could then be demonstrated that for heavier knocking conditions the correlation between heat flux and

knock intensity was stronger for all four fuels on both a cycle-by-cycle and cycle-averaged basis. This was independent of the way the heavier knock was achieved.

For a $LKI > -1$, Q_{max} and Q_{int} rose almost linearly with LKI. It was also found that Q_{ang} was more advanced as the knock intensity increased. When comparing Q_{ang} directly with the (pressure-based) angle of knock occurrence, a linear relation became apparent.

The Smart Car engine was operated on a standard gasoline. A sweep of speed from $\Omega = 1000$ RPM to $\Omega = 2000$ RPM showed an explicit rise in the heat flux for fixed values of pressure based knock indices (30-100%). The stark difference in heat flux can be accounted for by the higher turbulence intensity at higher speeds. The heat flux in the Smart engine was much higher as compared to the E6 engine and this is attributed to the higher turbulence due to the squish region as well as operation at a higher compression ratio.

It was further found that an assessment of the reference temperature shows similar results compared to the heat flux. However, the heat flux should remain the method of choice for such analyses as the scatter is significantly reduced compared to the steady metal temperature. Additionally, it is the heat flux that is directly related to the differential thermal strains that lead to the damaging thermal stresses.

6.3. Possible Extension Work

- The E6 Engine is fully equipped like a CFR engine. This allows for a wide range of additional tests on the MON and RON test procedures including effects of vaporized fuel and air intake humidity. A snatch sampling valve can be used to take samples of the composition of the end gas during knocking combustion.
- Knocking combustion disrupts the boundary layer at the surface of the combustion chamber, but the mechanism by which the pressure oscillations from knocking cycles affect the thermal boundary layer remains unclear. It is a very complex area as the

flows are highly unsteady, turbulent and compressible. It would be interesting work for future projects to investigate how the boundary layer is influenced under light and heavy knocking conditions. As automotive companies continue to downsize engines, knock is a major concern not only as a barrier to performance and efficiency but also due to the fact that knocking cycles are more severe under the conditions found in highly boosted engines. Therefore, it would be useful to investigate the instantaneous heat flux under conditions that would cause component failure.

6.4. Publications Relating to this Thesis

- *The Effect of Combustion Knock on the Instantaneous Heat Flux in Spark Ignition Engines;* J Mutzke, B Scott, R Stone, J Williams; SAE Paper, 2016-01-0700, 2016 Presented at the SAE Congress, Detroit 2016
- *Surface Pre-Ignition Measurements of Fuel Components and their Mixtures;* J Mutzke, R Stone, J Williams; *currently under review*
- *The Influence of Humidity and Mixture Preparation on the Engine Operating Point in Knocking Spark-Ignition Engines;* J Mutzke, R Stone, J Williams; *currently in preparation*

7. References

1. *Webpage: iea.org/publications/worldenergyoutlook/publications/weo-2011/ - World Energy Outlook 2011*. [cited November 2014].
2. *Webpage: bp.com/en/global/corporate/energy-economics/energy-outlook.html - BP Energy Outlook 2035*. [cited November 2017].
3. Hoefer, C., *Echte Herausforderung fuer's Stomnetz.* Fraenkische Allgemeine Zeitung, 2017: p. 24.
4. European Federation for Transport and Environment. *How to Avoid an Electric Shock. Electric Cars from Hype to Reality* 2014 [cited December 2014].
5. Smil, V., *Energy Myths and Realities: Bringing Science to the Energy Policy Debate.* American Enterprise Institute, AEI Press, Washington DC, 2010.
6. Appel, H. and L. Weber, *Elektro Wagen.* Frankfurter Allgemeine Zeitung, 2017.
7. *Webpage: shell.com/energy-and-innovation/the-energy-future/scenarios/new-lenses-on-the-future - Shell Energy Scenarios to 2050*. [cited October 2016].
8. *Webpage: shop.dena.de/fileadmin/denashop/media/ Downloads_Dateien/verkehr/ 9059_MOB_Studie_Ungeliebt_aber_unentbehrlich.pdf - Deutsche Energie Agentur (DENA)* [cited October 2017].
9. Stone, R., *Introduction to internal combustion engines.* Basingstoke, UK, 1999.
10. Heywood, J.B., *Internal combustion engine fundamentals*. Vol. 930. 1988: Mcgraw-hill New York.
11. Dinkelacker, F. and A. Leipertz, *Einfuehrung in die Verbrennungstechnik.* Esytec Verlag, Erlangen, 2012. Volume 3.
12. Zhao, H., *Advanced Direct Injection Combustion Engine Technologies and Developement, Gasoline and Gas Engines*. ISBN 1 84569 389 2. 2015, Woodhead Publishing LtD and CRC Press.
13. Kalghatgi, G. T., *Fuel/engine interactions.* SAE International, 2014. Volume 1

References

14. Wang, Z., H. Liu, and R.D. Reitz, *Knocking Combustion in Spark-Ignition Engines.* Progress in Energy and Combustion Science, 2017. 61: p. 78.
15. Konig, G. and C.G.W. Sheppard, *End gas autoignition and knock in a spark ignition engine*. 1990, SAE Technical Paper - 902135.
16. Griffiths, J.F. and J.A. Barnard, *Flame and Combustion*. 1995, Chapman and Hall, London.
17. Semenov, N.N., *Chemical Kinetics and Chain Reactions*. 1935, Oxford, U.K: Oxford University Press.
18. Westbrook, C.K., *Chemical Kinetics of Hydrocarbon Ignition in Practical Combustion Systems;* Proceedings of the Combustion Institute, 2000. Volume 28: p. 1563-1577.
19. *Webpage: bmwmotorcycletech.info/pinging-detonation.htm*. [cited September 2015].
20. Ricardo, H. and J. Hempson, *The High-Speed Internal Combustion Engine - Blackie and Son*. 1955, Ltd.
21. Lichty, L.C., *Combustion Engine Processes* 1967: McGraw-Hill.
22. Lovell, W.G., *Knocking Characteristics of Hydrocarbons* Industrial & Engineering Chemistry Research, 1948. 40: p. 2388 - 2438.
23. ASTM, *E-05, Standard Test Method for Measurement of Fracture Toughness. Annual Book of Astm Standards*. 2006, American Society for Testing and Materials, Philadelphia, Pa, USA.
24. Jones, R. and W.S. Farren, *Henry Thomas Tizard. 1885-1959.* Biographical Memoirs of Fellows of the Royal Society, 1961. 7: p. 313-348.
25. Shenghua, L., Clemente E. R. C., Tiegang, H., Yanjv, W. *Study of Spark Ignition Engine Fueled with Methanol/Gasoline Fuel Blends.* Applied Thermal Engineering, 2006. Volume 27: p. 1904-1910.
26. Kalghatgi, G. T., *An Alternative Method Based on Toluene/n-Heptane Surrogate Fuels for Rating the Anti-knock Quality of Practical Gasolines.* SAE technical Paper 2014-01-2609, 2014.
27. Kalghatgi, G.T., *Auto-ignition quality of practical fuels and implications for fuel requirements of future SI and HCCI engines*. 2005, SAE Technical Paper 2005-01-0239.

References

28. Kalghatgi, G. T., *Fuel anti-knock quality-Part I. Engine studies*. 2001, SAE Technical Paper 2001-01-3584

29. Kalghatgi, G.T., *Fuel anti-knock quality-Part II. Vehicle Studies-how relevant is Motor Octane Number (MON) in modern engines?* 2001, SAE Technical Paper 2001-01-3585.

30. Kalghatgi, G.T., Nakata, K., Mogi, K., *Octane appetite studies in direct injection spark ignition (DISI) engines*. 2005, SAE Technical Paper 2005-01-0244.

31. Bell, A., *Modern SI engine control parameter responses and altitude effects with fuels of varying octane sensitivity*. 2010, SAE Technical Paper - 2010-01-1454.

32. Mittal, V. and J.B. Heywood, *The relevance of fuel RON and MON to knock onset in modern SI engines*. 2008, SAE Technical Paper - 2008-01-2414.

33. Amer, A., Babiker, H., Chang, J., Kalghatgi, G., *Fuel effects on knock in a highly boosted direct injection spark ignition engine*. 2012, SAE Technical Paper - 2012-01-1634.

34. Davies, T., Cracknell, R., Lovett, G., Cruff, L., Fowler, J., *Fuel effects in a boosted DISI engine*. 2011, SAE Technical Paper - 2011-01-1985.

35. Morgan, N., Smallborne, A., Bhave, A., Kraft, M., *Mapping surrogate gasoline compositions into RON/MON space.* Combustion and Flame, 2010. 157(6): p. 1122-1131.

36. Smallbone, A.J., Morgan, N., Bhave, A., Kraft, M., *Simulating combustion of practical fuels and blends for modern engine applications using detailed chemical kinetics*. 2010, SAE Technical Paper 2010-01-0572

37. Kalghatgi, G., H. Babiker, and J. Badra, *A Simple Method to Predict Knock Using Toluene, N-Heptane and Iso-Octane Blends (TPRF) as Gasoline Surrogates.* SAE paper, 2015(2015-01-0757).

38. Westbrook, C.K., *Chemical kinetics of hydrocarbon ignition in practical combustion systems.* Proceedings of the Combustion Institute, 2000. 28(2): p. 1563-1577.

39. Livengood, J. and P. Wu. *Correlation of autoignition phenomena in internal combustion engines and rapid compression machines*. in *Symposium (International) on Combustion*. 1955. Elsevier.

References

40. Gauthier, B.M., D.F. Davidson, and R.K. Hanson, *Shock tube determination of ignition delay times in full-blend and surrogate fuel mixtures.* Combustion and Flame, 2004. 139(4): p. 300-311.

41. Fikri, M., Herzler, J., Starke, R., Schulz, C., Roth, P., *Autoignition of Gasoline Surrogate Mixtures at Intermediate Temperatures and High Pressures* Combustion and Flame, 2008. 152: p. 276-281.

42. Herzler, J., Fikri, M., Hitzbleck, K., Starke, R., Schulz, C., *Shock Tube Study of the Ignition of N-Heptane/Toluene/Air Mixtures at Intermediate Temperatures and High Pressures.* Combustion and Flame, 2007. 139: p. 25-31.

43. Eng, J.A., Leppard, W.R., Najt, P.M., Dreyer, F.L., *The interaction between nitric oxide and hydrocarbon oxidation chemistry in a spark ignition engine*. 1997, SAE Technical Paper - 972889.

44. Risberg, P., Johansson, D., Andrae, J., Kalghathi, G., *The Influence of NO on the Combustion Phasing in an HCCI Engine*. 2006, SAE Technical Paper - 2006-01-0416.

45. Burluka, A.A., Liu, K., Sheppard, C.G.W., Smallbone, A.J., *The influence of simulated residual and NO concentrations on knock onset for PRFs and gasolines*. 2004, SAE Technical Paper - 2004-01-2998.

46. Chevalier, C., H. Melenk, and J. Warnatz, *Automatic Generation of Reaction Mechanisms for Description of Oxidation of Higher Hydrocarbons* ZIB, 1990. preprint, SC 90-8.

47. Leppard, W.R., *The chemical origin of fuel octane sensitivity*. 1990, SAE Technical Paper.

48. Bradley, D. and C. Morley, *Autoignition in spark-ignition engines.* Comprehensive Chemical Kinetics, 1997. 35: p. 661-760.

49. Cowart, J.S., Keck, J.C., Heywood, J.B., Engine knock predicitions using a fully-detailled and a reduced chemical kinetic mechanism. Proceedings of the Combustion Institute, 1990. 23: p. 1055-1062

50. Kalghatgi G.T., Bradley, D., *Pre-Ignition and Super-Knock in Turbocharged Spark Ignition (SI) Engines.* International Journal of Engine Reserach, 2012(13(4)): p. 399-414.

References

51. Dahnz, C., Han, K.M., Spicher, U., Magar, M., *Investigation on Pre-Ignition in Highly Supercharged Engines* SAE technical paper - 2010-01-0355, 2010.

52. Amann, M., D. Mehta, and T. Alger, *Engine operating condition and gasoline composition effects on low-speed pre-ignition in high performance spark ignited engines.* SAE paper - 2011-01-0342, 2011.

53. Downs, D. and F.B. Theobald, *The Effect of Fuel Characteristics and Engine Operating Conditions on Pre-ignition.* Proceedings of the Institution of Mechanical Engineers (Auto Division), 1963(178(2A)): p. 89-102.

54. Bradley, D., *Autoignitions and detonations in engines and ducts.* Phil.Trans.R.Soc 2012. 370:: p. 689-714.

55. Peters, N., B. Kerschgens, and G. Paczko, *Super-knock prediction using a refined theory of turbulence.* SAE technical paper - 2013-01-1109, 2013.

56. Reinhard Luef, P.G., Helmut Eichlseder, *Development of a New Test Procedure to Determine Fuel and Oil Impact on Irregular Combustion Phenomena with Focus on Highly Boosted Downsized S.I. Engines.* 23rd Aachen Colloquium Automobile and Engine Technology 2014 1169.

57. Rassweiler, G.M., Lloyd Withrow, *Motion pictures of engine flames correlated with pressure cards.* SAE Technical Paper, 1938(No. 380139).

58. Liang, K., *A Novel Linear Electromagnetic-drive Oil-free Refrigeration Compressor* in *Engineering Science*. 2014, University of Oxford.

59. Ziegler, J.G. and N.B. Nichols, *Optimum Settings for Automatic Controllers* ASME, 1042.

60. Ricardo, *E.6/T Variable Compression Engine a MILL1122iLi*.

61. Stone, R., *Cobra, the Combustion Burn Rate Analysis Code. User Manual*. University of Oxford, Parks Road, Oxford.

62. Puzinauskas, P.V., *Examination of methods used to characterize engine knock*. 1992, SAE Technical Paper 920808.

63. Zhen, X., Wang, Y., Xu, S., Zhu, Y., tao, C., Xu, T., Song, M., *The engine knock analysis–an overview.* Applied Energy, 2012. 92: p. 628-636.

References

64. Collings, N., S. Dinsdale, and D. Eade, *Knock detection by means of the spark plug*. 1986, SAE Technical Paper - 860635.

65. Gao, X., *Real Time Knock Detection for Spark Ignition Engines*. 1994, Brunel University.

66. Andersson, I., *Cylinder pressure and ionization current modeling for spark ignited engines.* Linkopings Universitet, SE, 2002. 581: p. 83.

67. Shu, G., J. Pan, and H. Wei, *Analysis of onset and severity of knock in SI engine based on in-cylinder pressure oscillations.* Applied Thermal Engineering, 2013. 51 (2013) 1297 1306.

68. Brecq, G., J. Bellettre, and M. Tazerout, *A new indicator for knock detection in gas SI engines.* International Journal of Thermal Sciences 2003. 42 (2003) 523-532.

69. Hudson, C., X. Gao, and C.R. Stone, *Knock measurement for fuel evaluation in spark ignition engines.* Fuel, 2001. 80.

70. Checkel, M. and J. Dale, *Computerized knock detection from engine pressure records*. 1986, SAE Technical Paper 860028.

71. Brunt, M.F., C.R. Pond, and J. Biundo, *Gasoline engine knock analysis using cylinder pressure data*. 1998, SAE Technical Paper - 980896.

72. Luef, R., Grabner, P., Eichsleder, H., *Development of a New Test Proceduce to Determine Fuel and Oil Impact on Irregular Combustion Phenomena with Focus on High Boosted Downsized S.I. Engines.* 23rd Aachen Colloquium Automobile and Engine Technology, 2014.

73. Gardiner, A., *Atmospheric Humidity and Engine Performance.* SAE technical Paper 290033, 1929.

74. Lin, C., *Influences of Charge Air Humidity and Temperature on the Performance and Emission Characteristics of Diesel Engines.* Journal of Ship Research, 1996. 40: p. 172-177.

75. MacGregor, J.R., *The Influence of Humidity on Knock Ratings.* SAE Technical Paper 370152, 1937.

76. Antoine, C., *Tensions des Vapeurs, nouvelle relation entre les tensions et les temperatures.* comptes renus des seances de l'academie des sciences, 1888. 107.

77. Howatson, A.M., P.G. Lund, and J.D. Todd, *Engineering Tables and Data*. 2009.

78. Reid, R.C., J.M. Prausnitz, and B.E. Polling, *The properties of Gases & Liquids, fourth edition* Mcgraw-hill, 1987.

79. Marshall, S.P., Stone, R., Heghes, C., *High Pressure Laminar Burning Velocity Measurements and Modelling of Methane and n-Butane.* Combustion Theory and Modelling, 2010. 14(4).

80. Ricardo, H.R. and J.G.G. Hempson, *The High-Speed Internal-Combustion Engine*. Fifth Edition 1968: Blackie & Son London.

81. Zahdeh A., R.P., *Fundamental Approach to Investigate Pre-Igniton in Boosted SI-Engines.* SAE International, 2011(2011-01-0340).

82. Webpage: sdsefi.com/meltdown.htm, W. [cited January 2015].

83. Guibet, J.C. and A. Duval, *New Aspects of Preignition in European Automotive Engines.* SAE technical Paper - 720114, 1972.

84. Menrad, H., M. Haselhorst, and W. Erwig, *Preignition and Knock Behaviour in Alcohol Fuels.* SAE technical paper - 821210, 1982.

85. Zeldovich Y. B., B.G.I., Librovich V.B., Makhviladze G.M. , *Combustion and Explosions.* 1985.

86. Bradley, D., *Molecular Effects On Laminar Burning Velocities At Elevated Temperature And Pressure.* SAE technical paper - 2004-01-2936, 1998.

87. Farrell, J., R. Johnston, and I. Androulakis, *Molecular Structure Effects On Laminar Burning Velocities At Elevated Temperature And Pressure.* SAE technical paper - 2004-01-2936, 2004.

88. Holm, T., *Aspects of the mechanism of the flame ionization detector.* Journal of Chromatography A, 1999(842): p. 221 - 227.

89. Luef, R., Grabner, P., Eichsleder, H.,, *Development of a New Test Procedure to Determine Fuel and Oil Impact on Irregular Combustion Phenomena with Focus on Highly Boosted Downsized S.I. Engines.* Aachen Colloquium Automobile and Engine Technology 2014, 2014.

References

90. Manz P.W., D.M., Jippa K.N., Willand J., *Pre ignition in highly turbo charged engines analysis procedure and results.* 8th international symposium on internal combustion diagnostics, 2008.

91. Rhodes, D.B. and J.C. Keck, *Laminar Burning Speed Measurements of Indolene-Air-Mixtures at High Pressures and Temperature.* SAE technical paper - 850047, 1985.

92. Lu, J., Ezekoye, D., Liyama, A., Greif, R., Sawyer, R.F., *Effect of Knock on time-resolved Engine Heat Transfer.* SAE paper - 890158, 1989.

93. Harigaya, Y., Toda, F., Ohyagi, S., Tsuji, H., *Surface temperature and Wall heat flux in a Spark Ignition Engine under Knocking and non-Knocking Conditions.* SAE technical paper 891795

94. Syrimis, M., K. Shigahara, and D. Assanis, *Correlation between Knock Intensity and Heat Transfer Under Light and Heavy Knocking Conditions in Spark Ignition Engines.* SAE technical paper 960495.

95. Grandin, B. and I. Denbratt, *The Effect of Knock on Heat Transfer in SI Engines.* SAE technical paper - 2002-02-0238, 2002.

96. Smallborne, A.J., Morgan, N., Bhave, A., Kraft, M., *Simulating Combustion of Practical Fuels and Blends for Modern Engine Applications Using detailed Chemical Kinetics.* SAE technical Paper 2010-01-0572, 2010.

97. Wang, X., Stone, R., Stevens, R., Arita, Y., Buttsworth, D., *Finite Element Analysis of Eroding Type Surface thermocouple with Application to Engine Heat Flux Measurement* Thermal Fluid Sciences, 2006.

98. Zhen, X., Wang, Y., Xu, S., Zhu, Y., Tao, C., Xu, T., Song, M., *The engine knock analysis - An overview.* Applied Energy, 2012. 92(628-636).